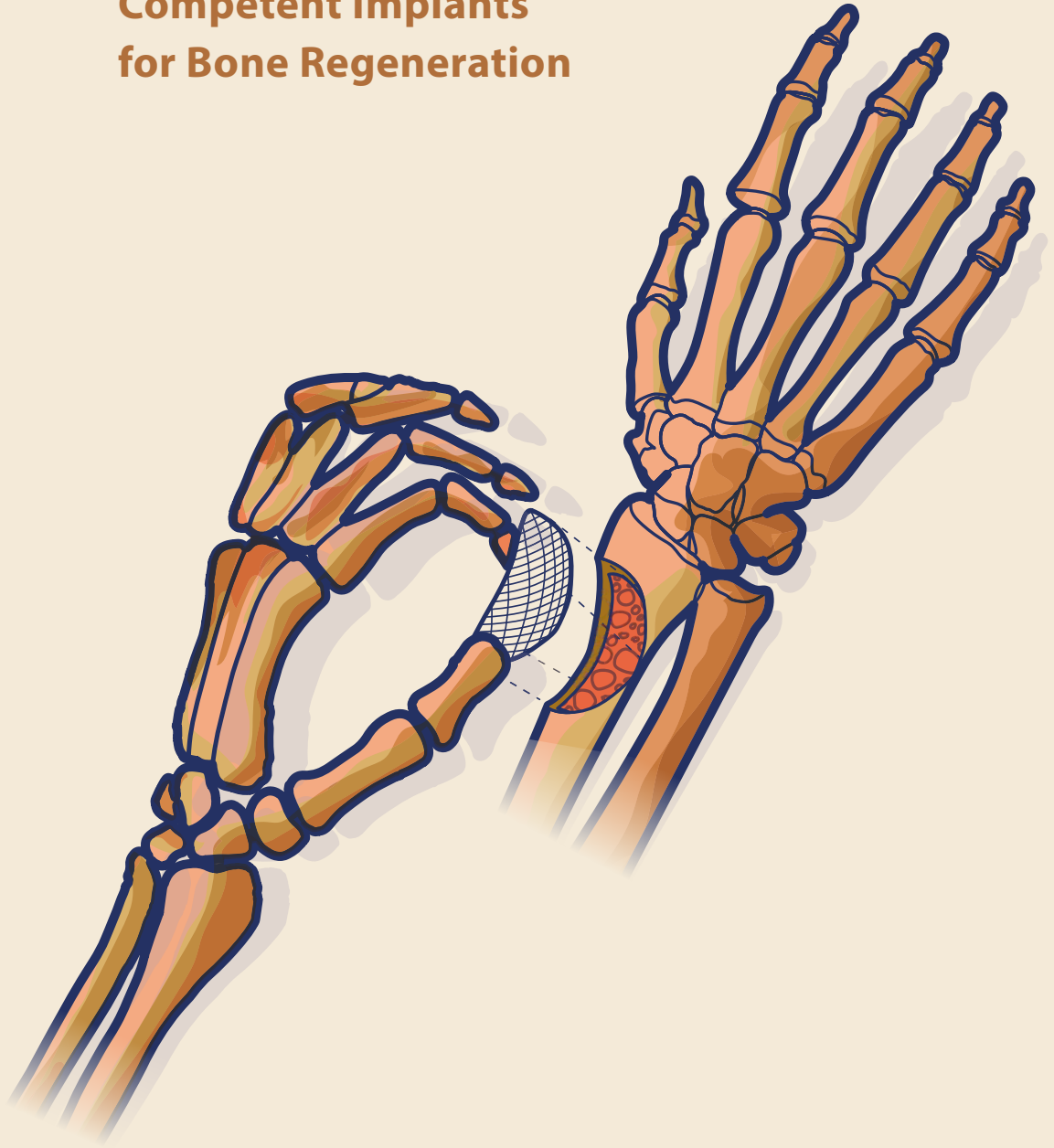


Towards 3D Fabrication of MgP-based Mechanically Competent Implants for Bone Regeneration



Nasim Golafshan

Towards 3D Fabrication of MgP-based Mechanically Competent Implants for Bone Regeneration

Nasim Golafshan

Towards 3D fabrication of MgP-based mechanically competent implants for bone regeneration

PhD Thesis Utrecht University

ISBN: 978-94-93315-60-0

Author: Nasim Golafshan

Cover design: Guus and Nasim

Layout and printing: Guus Gijben, Proefschrift All In One (AIO)

The research in this thesis is financially supported by the European Research Council (ERC) under grant agreement 647426 (3D-JOINT) and RegMED XB project.

Financial support for printing this thesis was kindly provided by Materialise NV and Anna Fonds te Leiden.

Copyright © 2023. All rights reserved. No parts of this thesis may be reproduced, stored in a retrieval system of any nature, or transmitted in any form or by any means, without prior written consent of the author. The copyright of the articles that have been published has been transferred to the respective journals.

Towards 3D Fabrication of MgP-based Mechanically Competent Implants for Bone Regeneration

Naar 3D-fabricage van MgP-gebaseerde mechanisch competente implantaten voor botregeneratie

(met een samenvatting in het Nederlands)

Proefschrift

ter verkrijging van de graad van doctor aan de
Universiteit Utrecht
op gezag van de
rector magnificus, prof.dr. H.R.B.M. Kummeling,
ingevolge het besluit van het college voor promoties
in het openbaar te verdedigen op

woensdag 31 mei 2023 des ochtends te 10.15 uur

Door

Nasim Golafshan

geboren op 25 september 1990
te Esfahan, Iran

Promotor:

Prof. dr. J. Malda

Copromotor:

Dr. M. Dias Castilho

Beoordelingscommissie:

Prof. dr. ir. S.C.G. Leeuwenburgh

Prof. dr. J.M. Beekman (voorzitter)

Prof. dr. F.C. Oner

Prof. dr. B.P. Meij

Dr. S. Hofmann

When you do things from your soul, you feel
a river moving in you, a joy.

Rumi

Table of contents

CHAPTER 1	
Introduction, research aims and thesis outline	9
CHAPTER 2	
Combinatorial Fluorapatite bioceramic substituted with strontium, magnesium and silicon ions for mending bone defects	21
CHAPTER 3	
Tough magnesium phosphate-based 3D-printed implants induce bone regeneration in an equine defect model	39
CHAPTER 4	
3D-printed regenerative magnesium phosphate implant ensures stability and restoration of hip dysplasia	67
CHAPTER 5	
A gap-filling, regenerative implant for open-wedge osteotomy	93
CHAPTER 6	
Influence of osmotic swelling restriction on load bearing properties and neo-cartilage matrix formation on osteochondral implant	111
CHAPTER 7	
Composite graded melt electrowritten scaffolds for regeneration of the periodontal ligament-to-bone interface	139
CHAPTER 8	
General discussion	167

Appendices

Annex I

Scaling up from osteochondral plug to patient-specific condyle resurfacing: fabrication, <i>in vitro</i> characterization, and mechanical characterization under physiological conditions of clinically relevant osteochondral implants	179
---	-----

Annex II

Evaluation of the residual solvent concentrations in the MgP-based bioceramic biomaterial after the sterilization process	203
---	-----

References	207
------------	-----

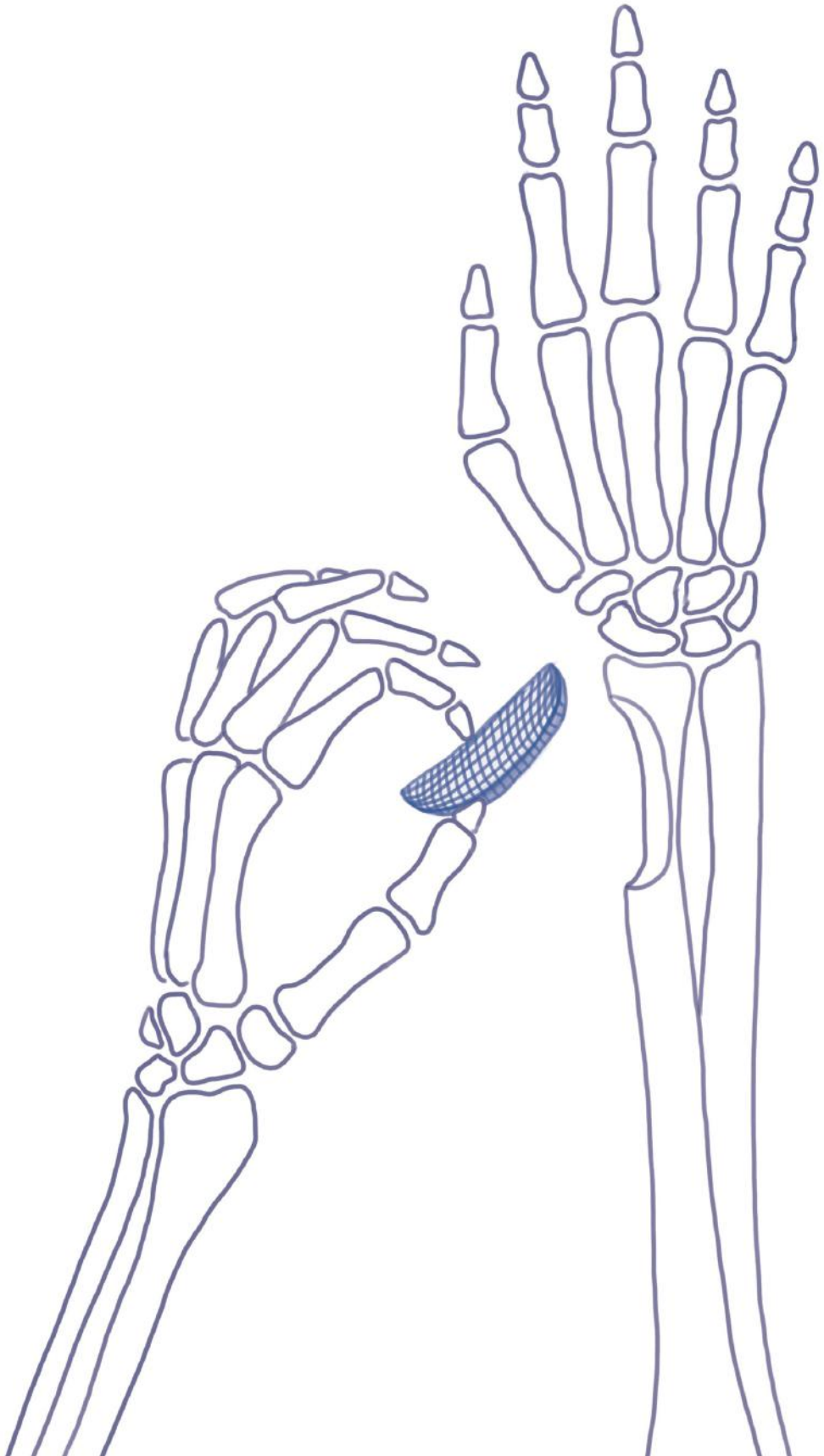
List of Abbreviations	225
-----------------------	-----

Summary, Samenvatting, Persian Summary	229
--	-----

Acknowledgments	243
-----------------	-----

Publications	249
--------------	-----

Curriculum Vitae	255
------------------	-----



CHAPTER 1

Introduction, research aims
and thesis outline

Bone structure

Bone is a complex tissue in which both hard and soft materials (*i.e.* type-1 collagen, non-collagenous proteins and carbonated apatite) interact to form a well intertwined and unique hierarchical structure (Fig. 1) ^[1-3]. The human skeletal system consists of more than 200 different bones and depending on the type of bone (cortical or trabecular), and location in the body, bone tissue has a specific organization^[4]. In the majority of the bones, a very dense shell (cortical bone) protects the inner, more porous, core of trabecular bone. Both cortical and trabecular bone are arranged in small unit blocks called lamellae (Fig. 1). These lamellae consist of multiple mineralized collagen fibrils that are, in turn, composed of well intertwined collagen, apatite crystals and a small amount of non-collagenous proteins. Both organic and inorganic phases together provide bone with its unique combination of compressive strength and resilience, typically ranging from 130-200 MPa and 0.1-16 MPa, for cortical and trabecular bone, respectively^[5]. Due to the intricate and hierarchical organization of bone tissue over different length scales, replication of bone structure, composition and respective properties has proven extremely difficult, and this remains an open challenge in the field of bone regeneration.

Bone injuries and disorders

Bone injuries and disorders represent a serious clinical problem that affect nearly 2 million people worldwide every year^[7]. The clinical presentation is very diverse amongst which infantile craniofacial anomalies, trauma, bone abnormality, congenital disorders and cancer are the most common (Fig. 2) ^[7-10]. Although bone loss is not a life-threatening health condition, it has dramatic consequences and impact on patients' quality of life, making bone, after blood, the second most transplanted tissue^[7-10]. Although small fractures and bone defects usually heal spontaneously, larger (*i.e.*, ³ 10 mm) and more complex bone defects have limited regenerative capacity. Typically, bone defects heal via a process called, indirect or secondary, fracture healing. This healing process results in the formation of a callus around the bone defect region and involves three main phases; the inflammatory, reparative and remodeling phase^[11]. Altogether, the fracture healing process can take months to years to fully complete. In some cases, however, bone non-unions are not capable of healing, and do require further surgical intervention and treatment^[12,13]. This surgical intervention involves the stabilization of the bone fracture with a permanent implant, typically composed of metals, and the use of bone substitutes to fill bone gap and promote its regeneration ^[14]. Different types of transplants and synthetic materials have been explored as bone substitutes or fillers to aid the healing.

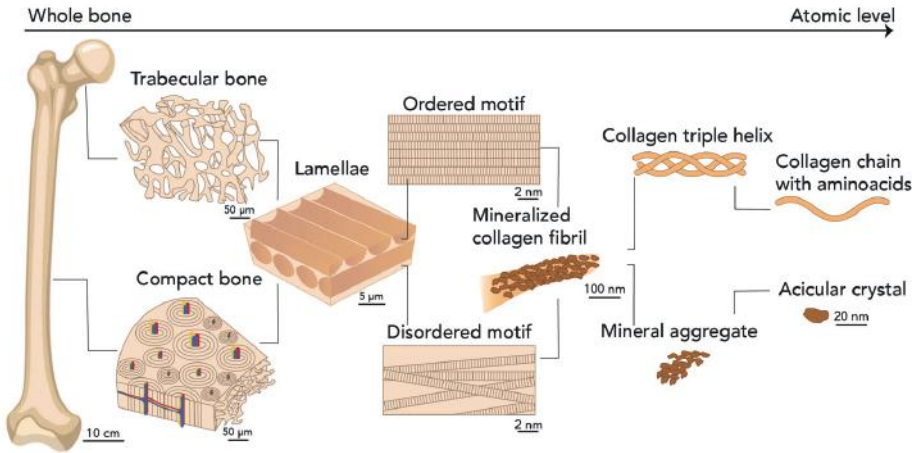


Figure 1. Schematic representation of bone composition and hierarchical structure. Adapted from Wegst *et al.* [6].

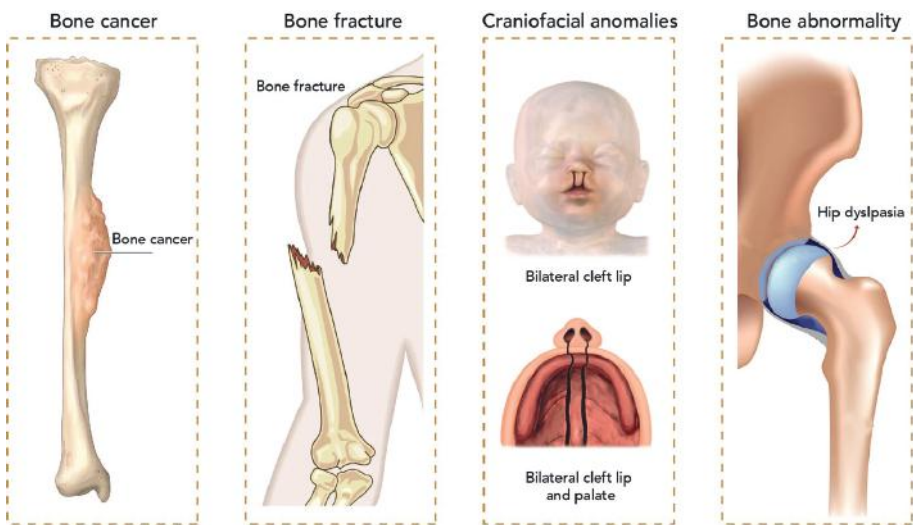


Figure 2. Some examples of the bone diseases and injuries which require surgical intervention. The images are adapted from [15–18].

Bone substitutes

The current golden standard for treating bone non-unions involves the autologous transplantation of bone from one location (typically the iliac crest) to the defect site. Although autologous bone possesses unique osteoinductive (ability to promote new bone formation) and osteoconductive properties (ability to support and guide bone growth), the major drawback is that its application requires two surgical procedures and comes with the increased risks of infection, nerve damage, and blood clot formation^[19]. Alternatives to autologous bone are transplants from another source, *i.e.*, allografts, extracted from a human donor, or xenografts, extracted from a donor of non-human origin^[20]. Despite these different options, no transplant has proven itself to be free of limitations. Hence, several synthetic materials have been developed as alternative bone substitutes. Titanium (Ti) has become a popular metallic material because of its biocompatibility and biomechanical properties. It is still the most widely used synthetic implant material for segmental bone defects^[21]. However, metals like Ti lack biodegradation properties and can thus not be replaced by new bone, which is associated with different challenges. For example, in children and young adults where skeleton is still developing, eventual removal and replacement of the metallic implants is usually needed. This requires additional surgical efforts, which obviously is also associated with pain and infection risks, without mentioning the increase in healthcare costs^[22,23]. To overcome these limitations, biodegradable polymers and ceramics, and combinations thereof, have been explored^[24]. Among these, polymer like, polycaprolactone (PCL)^[25–28] and poly(lactic-co-glycolic acid) (PLGA)^[29–32] have been the most widely used due to their biodegradation and mechanical properties. Despite promising, polymeric implants typically lack osteopromotive properties. As an alternative, bioceramics like calcium phosphates^[29] or silica-based materials like bioglass^[33] can directly interact with the bone tissue, either supporting tissue growth or inducing new tissue regeneration. The typical advantages and disadvantages of these main classes of materials are highlighted in Figure 3.

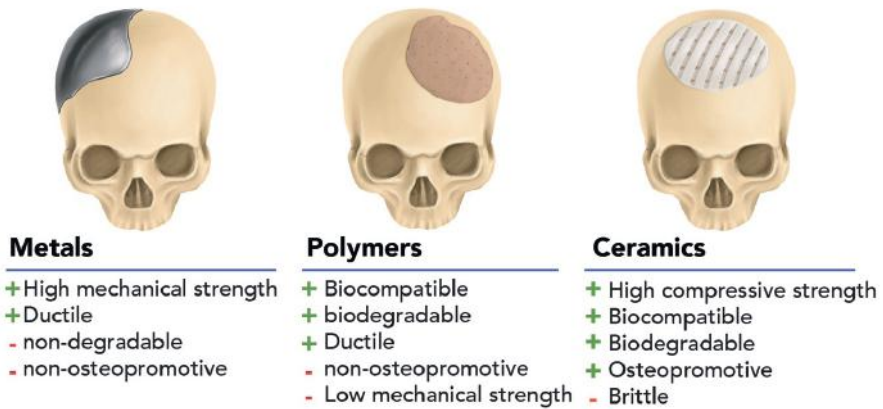


Figure 3. Summary of benefits and drawbacks of the main classes of materials used for bone replacement and regeneration.

Bioceramics and bioceramic composites

A variety of synthetic ceramic bone substitutes are currently used as an alternative to the traditional allo- and autografts with hydroxyapatite (HA) and tricalcium phosphate (TCP)^[34]. Although TCP is chemically degradable *in vivo* compared to HA, it presents only limited osteoinductivity^[35]. To overcome this limitation, magnesium phosphate (MgP)-based formulations, such as struvite ($\text{NH}_4\text{MgPO}_4 \cdot 6\text{H}_2\text{O}$), newberyite ($\text{Mg}(\text{PO}_3\text{OH}) \cdot 3\text{H}_2\text{O}$), and trimagnesium phosphate ($\text{Mg}_3(\text{PO}_4)_2$) have been introduced^[36–38]. MgP can stimulate osteogenesis by releasing magnesium (Mg^{2+}) ions^[39–41].

In addition, the release of metal or metalloid ions has shown a great promise for stimulating both osteogenesis (ability to promote bone formation)^[42], and angiogenesis (ability to promote blood vessel formation)^[43]. In particular, ions such as silicon, zirconium, copper, or strontium have attracted great attention. For example, silicon incorporated into CaPs has been shown to improve osteogenic properties of CaP grafts^[44]; while strontium has been used for treatment of osteoporosis, due to its capacity to inhibit osteoclast activity (bone resorption)^[45,46].

Nevertheless, the common drawback to all bioceramics remains their brittleness and unpredictable failure, which largely limit their clinical use in load-bearing locations^[47]. Several approaches have been explored to overcome these limitations, including combination with synthetic polymers, such as polycaprolactone (PCL)^[48], PLGA^[25] and polymethylmethacrylate (PMMA)^[49]; reinforcement with carbon nanotubes^[50],

or even development of dual setting cement systems^[51]. The inspiration for these strategies is mostly based on the fact that bone tissue itself, is a composite material composed of a ceramic and polymeric phase. However, independently of the strategy explored to combine the organic and inorganic phases, important challenges persist. Several studies have shown that methods to combine bioceramics with polymer compromise the osteoconductive nature of the bioceramics due to the polymeric masking of the ceramic phase, and that the composite material lacks the required interconnectivity for bone formation^[52,53]. An additional challenge, particularly for the treatment of large and complex defects, is the poor shapeability of these materials. Large and complex geometry bone defects can hardly be treated with available forms of bone grafts, i.e. granules, cement pastes, or monoliths^[54,55].

Bioceramic-based material processing

The limited shapeability of bioceramics-based materials has encouraged the development of advanced manufacturing methods for the fabrication of bone substitutes with individual shapes and properties. The introduction of additive manufacturing (AM) technologies, or three-dimensional printing (3DP) in lay terms, which allow for a relatively fast, precise, controllable and potentially scalable fabrication process, has opened new opportunities for the generation of bioceramic scaffolds with controllable shapes and properties. The available AM approaches for bioceramic processing can be typically be divided in powder-based and slurry-based methods. In powdered-based techniques, such as selective laser sintering (SLS)^[56] and three-dimensional powder printing (3DPP)^[57], ceramic particles are spread over a printing bed and locally bond by laser or a binder; while in slurry-based techniques, such as stereolithography (SL)^[58] and direct ink writing (DIW)^[59], fine ceramic particles are dispersed in a liquid phase to form light-responsive bioresins or hydraulic setting pastes. A summary of AM methods for bioceramic processing is illustrated in Fig. 4.

In terms of materials, a wide range of bioceramics ranging from biphasic calcium phosphate (BCP)^[56,57], to bioglass^[61] and calcium phosphates^[62,63] have been used for either powdered-based printing and slurry-based techniques⁵². These processes show great promise, because they are applicable with a wide range of bioceramics, while they also allow high fabrication speed and accuracy. However, most of these processes, require sintering at high temperature (usually ³ 1000°C) of the printed structures, limiting the capability of incorporating biomolecules during the fabrication process. Even after sintering at high temperature, the bioceramics printed scaffolds are still brittle for press-fit implantation even with the perfect size

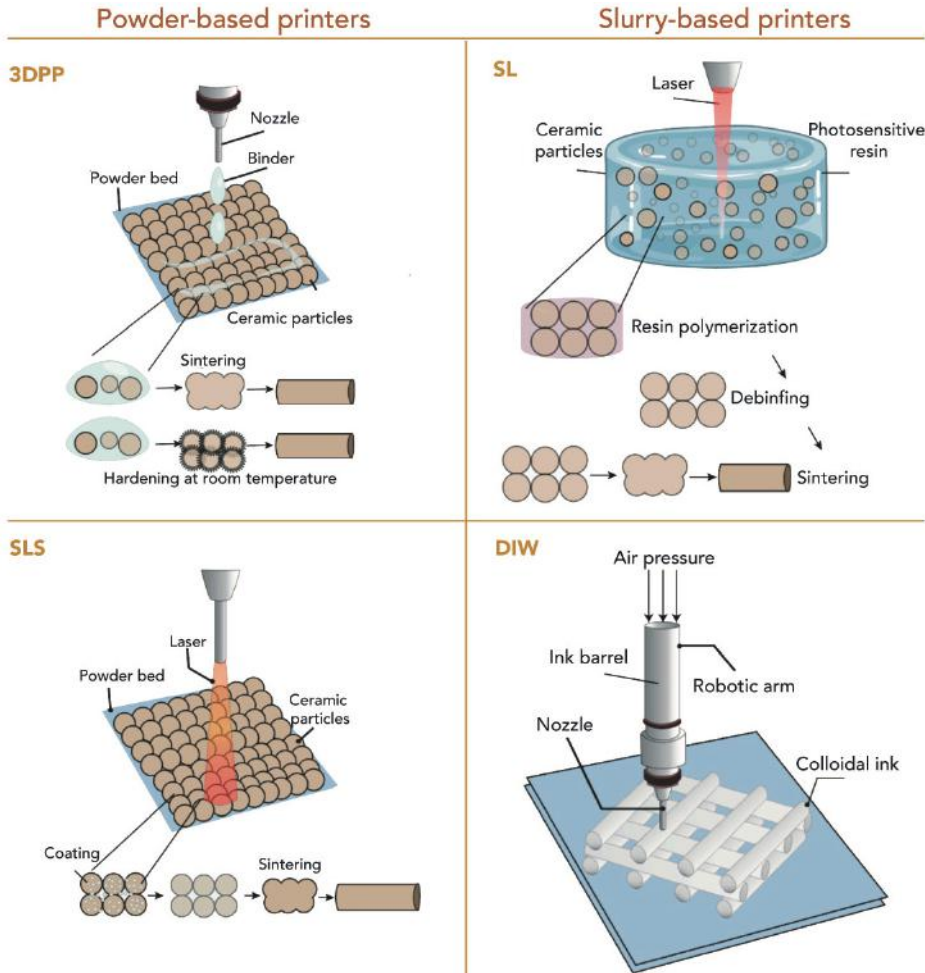


Figure 4. Schematic of common additive manufacturing techniques used for bioceramics scaffolds printing. These techniques include 3D powder printing (3DPP), selective laser sintering (SLS), stereolithography (SL), direct-ink writing (DIW) ^[60].

and shape of the implants in accordance with the defect site. To overcome these drawbacks, bone implants with a high concentration of HA (90wt.%) and PCL or PLGA (10wt.%) have been fabricated by 3D printed using a room temperature using solvent based, extrusion process, which did not require further post manufacturing sintering. In this process, the scaffold architecture is designed by computer aided design (CAD) file and subsequently fabricated in a layer-by-layer manner by applying pressure. The ink for the printing is prepared by dissolving the initial materials in the appropriate viscosity for extrusion-based printing. This process allowed the fabrication of large and geometrically complex scaffolds with desire porosity, mechanical properties,

and relevant geometry^[64]. Furthermore, more recently, extrusion-based printing of aligned HA (up to 50%) and poly(D,L-lactide) (PDLA⁵⁴) have even shown the ability to produce scaffolds that approximate to the native microstructural organization of natural bone, resulting in mechanical properties in the range of 25 MPa for strength and 700 MPa for elastic modulus^[65].

Outstanding challenges

Despite promising results outline above, there are still open challenges related to the fabrication of bone substitutes that can be used to regenerate complex-shaped bone non unions at load-bearing locations. These challenges are summarized below and illustrated in Figure 5.

- Existent osteopromotive ceramic-based bone substitutes still lack adequate mechanical properties to survive in load-bearing environments.
- Combination of osteopromotive scaffolds with polymers can lead to the generation of bone substitutes with mechanical properties compatible with implantation in load-bearing environments; however, such composite materials typical compromise osteopromotive properties provided by the ceramic phase.
- A better understanding of how resorbable implants perform in mechanically loaded locations is needed.
- Control of bone substitutes *in vivo* degradation rate to ensure continuous mechanical support throughout the entire bone healing process is still a major challenge.
- Finally, as natural bone is surrounded by various connective tissues, such as cartilage and ligament, we still lack knowledge on how to design resorbable bone substitutes that can not only promote bone regeneration but also facilitate integration with surrounding soft, connective tissues.

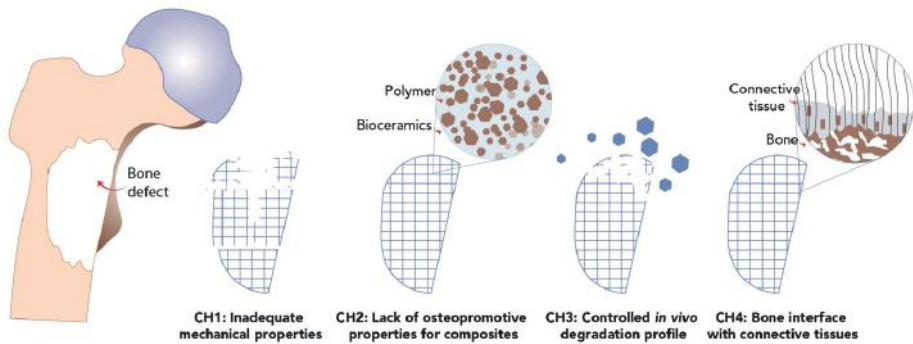


Figure 5. Open challenges related to the fabrication of resorbable bone grafts. From left to right, a representative bone defect in femur is shown. The challenges (CH) regarding the bone scaffolds are summarized to be listed as mechanical competent, osteopromotive, degradable and facilitate integration with surrounding tissue.

Main objectives and thesis outline

Therefore, the main objective of this thesis is to generate an individually shaped, mechanically competent, resorbable and osteopromotive bone substitute that can be used in load-bearing clinical applications. The main objective is further divided into three sub-objectives, in particular,

1. To develop a flexible, bone-inducing biomaterial ink for extrusion-based 3D printing of clinically relevant sized implants with personalized shape
2. To understand the biological and mechanical performance of the generated implants under (load-bearing) *in vitro* and *in vivo* conditions.
3. To further advance bone implants to facilitate integration with soft connective tissues, i.e. cartilage and ligament.

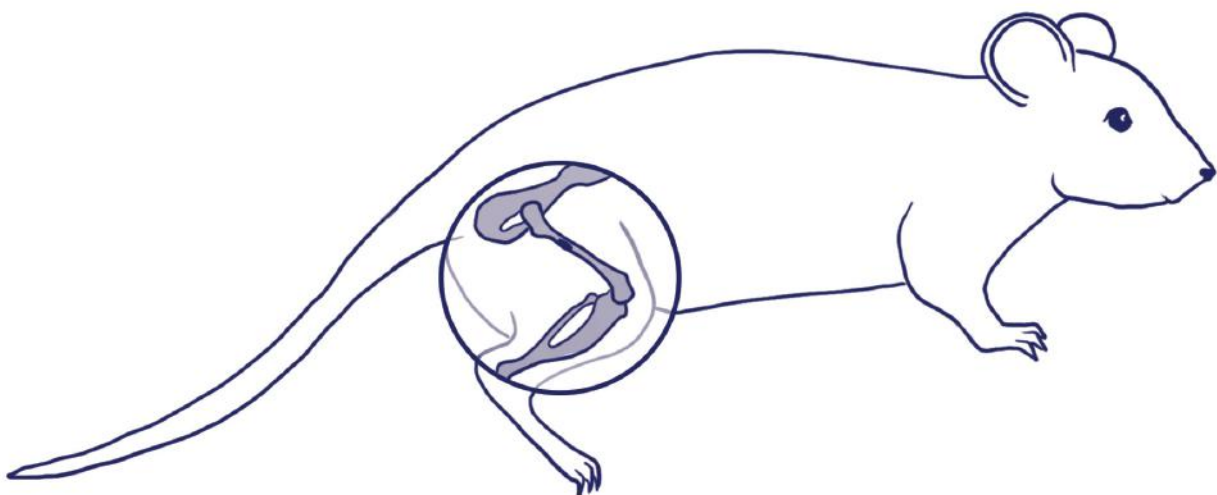
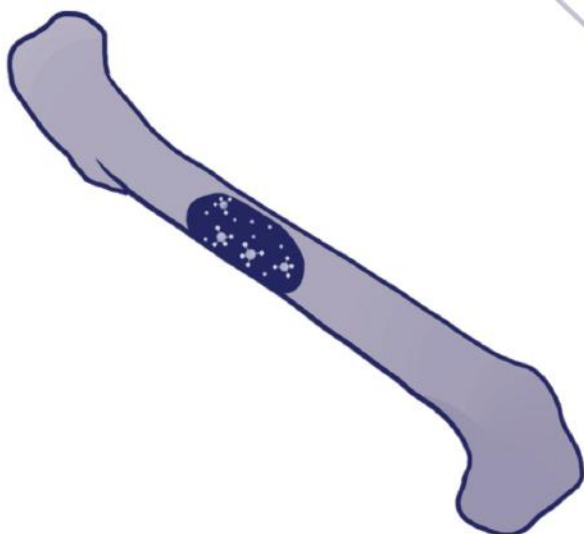
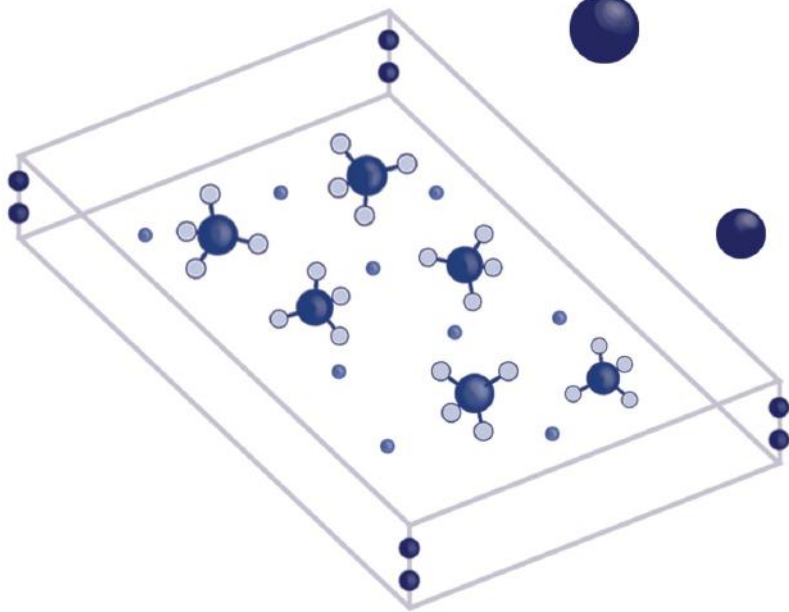
To address these objectives, **Chapter 2** first introduces a novel apatite structure (fluorapatite) material doped with Mg^{2+} and Sr^{2+} ions and evaluates its osteopromotive properties in rat model. **Chapter 3**, then describes the development of a MgP-based biomaterial ink modified with Sr^{2+} ions (MgPSr) and a medical-grade polycaprolactone (PCL) polymer phase for extrusion-based 3D printing of clinically relevant sized implants. The effect of PCL on MgP-based ink printability is investigated. In addition, the structural, mechanical, and biological performance

of printed implants is characterized *in vitro*, and in a proof-of-concept *in vivo* test in an equine tuber coxae defect model. **Chapter 4**, builds on these findings and explores the fabrication of MgP-based implants with non-regular geometrical shapes for stable restoration and treatment of hip dysplasia. The fabrication process, degradation and respective biomechanical properties of the hip implants are thoroughly examined. Furthermore, with an eye- on potential clinical translation, in **Chapter 5** the potential of the developed MgP-based biomaterial ink and extrusion-based printing method is investigated to fabricate a gap-filling wedge implant for unicompartmental osteoarthritis of the knee joint treatment and tested upon implantation into human cadaveric legs. To address the last objective of this thesis, **Chapter 6** and **Chapter 7** focus on advancing fabrication of bone substitutes that can interface with connective tissues. In **Chapter 6**, the fabrication of developed bone material to serve as a bone anchor of engineered cartilage implants is investigated. **Chapter 7** introduces the fabrication of highly resolution porous implant from previously developed biomaterial ink using a novel extrusion-based technique assisted by an electrical field. The potential of the developed bone scaffolds is investigated to guide regeneration of bone-dental ligament interface and tested *in vivo* in fenestration defect model in rats.

Finally, the discussion and conclusion of developed materials and manufacturing processes, with a focus on open challenges and future perspectives, is provided in **Chapter 8**.

Mg

Sr



CHAPTER 2

Combinatorial Fluorapatite bioceramic substituted with strontium, magnesium and silicon ions for mending bone defects

Nasim Golafshan

Morteza Alehosseini

Tahmineh Ahmadi

Ardeshir Talebi

Mohammadhossein Fathi

Mahshid Kharaziha

Gorka Orive

Miguel Castilho

Alireza Dolatshahi-Pirouz

Abstract

In bone tissue engineering, ionic doping using bone-related minerals such as magnesium (Mg) or strontium (Sr) is a promising strategy to make up for the inherent disadvantages (low solubility) of various apatite-based materials such as Fluorapatite (FAP) and Hydroxyapatite (HA). Therefore, number of studies in recent years have tried to address the lack-of-methodology to improve the properties of bioceramics in the field. Even though, the outcome of the studies has shown some promises, the influence of doped elements on the structures and properties of *in vitro* and *in vivo* mineralized FAP has not been investigated in detail so far, and thus, it is still an open question mark in the field. In this work, strontium modified fluorapatite (Sr-FAP), magnesium and silica modified fluorapatite (Mg-SiFAP) nanopowders were synthesized using a mechanical alloying methodology. Results showed that the doped elements could decrease the crystallinity of FAP (56%) to less than 45% and 39% for Sr-FAP and Mg-SiFAP, respectively. Moreover, *in vitro* studies revealed that Sr-FAP significantly enhanced osteogenic differentiation of hMSCs, after 21 days of culture, compared to Mg-SiFAP at both osteogenic and normal media. Then, *in vivo* bone formation in a defect of rat femur filled with a Sr-FAP and Mg-SiFAP compared to empty defect was investigated. Histological analysis revealed an increase in bone formation three weeks after implanting Sr-FAP compared to Mg-SiFAP and the empty defect. These results suggest that compared to magnesium and silica, strontium ion significantly promotes bone formation in fluorapatite making it appropriate for filling bone defects.

Keywords

Bone tissue engineering; Fluorapatite; Magnesium; Osteoinductive; Strontium

Introduction

Bone disease is still one of the big burdens for healthcare systems worldwide which particularly impacts older people. One of the treatments for the healing of bone defects caused by trauma involves the implantation of synthetic bioceramics that could support bone regeneration. Among various bioceramics, synthetic hydroxyapatite [HA, $\text{Ca}_{10}(\text{PO}_4)_6(\text{OH})_2$] mimicking the structure of natural bone has received significant attention in the field ^[66–68] and could promote bone growth and improve bone induction ^[69–71]. However, in order to control the dissolution rate of HA which is stable in vivo, Fluoride (F^-) ion substituted OH ions in the chemical structure of HA have shown great promise. Błaszczuk et al ^[72] showed that partially or total substitution of hydroxyl groups (OH^-) in HA with small doses of fluoride (F^-) can improve HA solubility in vivo and improve the treatment of osteoporosis and various vertebral body fractures ^[73].

To enhance the bioactivity and biocompatibility of FAp, various ions can be doped in its crystal structures ^[74,75]. These ions which exist in the bone such as strontium (Sr^{2+}), magnesium (Mg), silica (Si), zinc (Zn), and cobalt (Co) ^[76,77]. Even though the amount of these elements is low in natural bone, they do have a great impact on the physico-chemical properties and regeneration of bone ^[78]. For instance, Mg^{2+} deficiency restricts the growth of osteoblasts leading to a decrease in bone mass density. Thus, Mg^{2+} also plays a key role in mediating cell-extracellular matrix interaction ^[79]. In this respect, Cai et al. ^[80] demonstrated that the incorporation of Mg^{2+} ions to FAp bioceramics improved the ability to stimulate new bone formation. In addition, previous studies have demonstrated that Si ions could promote bone growth ^[81,82]. In fact, Si could promote the proliferation and differentiation of rat bone marrow stromal cells (rBMSCs) and improve the collagen synthesis process of osteoblasts ^[83]. In order to enhance the osteoinductivity of FAp, it has been reported that Strontium (Sr^{2+}) could act as an inhibitor of osteoclasts resorption as well as a stimulus to induce osteogenesis ^[84].

Due to the above-mentioned properties and valuable aspects of Sr^{2+} in bone formation, Sr-based bioceramics have gained extensive attention as a new class of bioceramic materials ^[85–87]. For instance, recently, it has been shown that Sr^{2+} ions doped into calcium phosphate ceramics. The osteoprogenitor cells proliferated and differentiated at the relevant doses of Sr^{2+} ions (2.21 at%) ^[84]. Accordingly, by incorporation of various ions, the proliferation and differentiation of the cells could be influenced. In a similar study, it was shown that doping the ions such as Mg, Zn, Sr, and Si in the hydroxyapatite structure, the chemical, physical, and biological properties are influenced ^[88].

Despite the wide interest towards using Sr in the field, the synergistic role of various ions on the ability to stimulate bone formation has not been fully investigated yet. For this reason, this study aimed to investigate the role Mg, Si and Sr ion substituted FAp. In this regard, two types of fluorapatite-based nano powders were synthesized: Sr doped fluorapatite and Mg-Si doped fluorapatite and their potential as bone substitutes were investigated both *in vitro* and *in vivo*.

Materials and methods

Materials

Calcium hydroxide (Ca(OH)_2), calcium fluoride (CaF_2), phosphorous pentoxide (P_2O_5), strontium carbonate (SrCO_3) and magnesium hydroxide (Mg(OH)_2) were purchased from Merck, Germany and silica oxide (SiO_2) was obtained from Sigma-Aldrich. For the *in vitro* cell culture experiments, human Mesenchymal stem cells were supplied by the Pasteur Institute in Iran (passage 5). Dulbecco's modified Eagle's medium (DMEM/F12), fetal bovine serum (FBS), penicillin/streptomycin and phosphate buffer saline (PBS) were bought from Bioidea, Iran. Dexamethasone, acetic acid, ascorbic acid, ammonium solution, b-glycerophosphate, Glutaraldehyde, MTT (3-(4,5-dimethylthiazol-2-Yl)-2,5-diphenyltetrazolium bromide), Resazurin, Alizarin red S, Glutaraldehyde, and dimethyl sulfoxide (DMSO) were obtained from Sigma-Aldrich.

Synthesize of fluorapatite based powders

Two kinds of ceramic powders consisting of Sr-doped FAp (SrFAp) and Mg and Si-doped FAp (Mg-SiFAp) were synthesized via the mechanical alloying process, according to the protocol described elsewhere [23]. In this regard, the precursors of the SrFAp and Mg-SiFAp powders were weighted and mechanochemical activation for both powders were performed in a planetary ball mill (Fretch Pulverisette 5) for 12 h with the ball to powder ratio of 25:1 and the speed of 250 rpm. The precursor types and amounts are presented in Table 1.

Physical and chemical Characterization

Phase characterization of synthesized powders was evaluated by X-ray diffractometer, XRD (X'Pert Pro X-ray diffractometer, Phillips, Netherlands) performed with $\text{CuK}\alpha$ radiation ($\lambda = 0.154 \text{ nm}$, 40 kV, 40 mA). Based on the XRD patterns, the crystallographic parameters, crystallite size, and crystallinity of each sample compared with FAp (24) as a reference value, were estimated. Fourier transform infrared spectroscopy (FTIR, Bruker tensor) was used to characterize the functional groups and chemical composition of the powder over a range of $650\text{--}2000 \text{ cm}^{-1}$ and resolution of 2 cm^{-1} .

The morphology of the synthesized powders was evaluated using a scanning electron microscope (SEM, Philips XL30) at an operating voltage of 20 kV and electrical current of 10 mA. The particle size of ceramic powders was studied using a Transmission Electron Microscope (TEM) (Zeiss 100 kV). Before imaging, following the dispersion of samples in acetone using ultrasonication for 15 min, the suspensions were put on the carbon-coated copper grid and the grids were dried at room temperature.

Table 1. The precures and the amount to synthesize Mg-SiFAp and SrFAp.

table	$\text{Ca}_{9.5}\text{Mg}0.5(\text{PO}_4)_{5.5}(\text{SiO}_4)0.5\text{F}_2$		$\text{Ca}_{9.5}\text{Sr}0.5(\text{PO}_4)_{5.5}\text{F}_2$	
	gr	Mol	gr	mol
$\text{Ca}(\text{OH})_2$	6.298	8.50	6.298	8.50
CaF_2	0.781	1.00	0.781	1.00
P_2O_5	3.904	2.75	4.259	3.00
SrCO_3	-	-	0.738	0.50
SiO_2	0.300	0.50	-	-
$\text{Mg}(\text{OH})_2$	0.292	0.50	-	-

Apatite-formation ability of the synthesized powders was evaluated by immersing the ceramic discs in simulated body fluid (SBF). The synthesized powders were uniaxially pressed (N=50 for 5 min) to fabricate ceramic disks with 12 mm in diameter (n=3). The obtained disks were then soaked in SBF (pH=7.4) at 37°C for 7 days (n=3), while the ratio of disc surface area to SBF solution volume was kept 0.1 cm²/ml. The concentration of released Calcium and phosphorous ions in SBF was quantified using inductively coupled plasma atomic emission spectroscopy (ICP-AES).

Cell culture

Human mesenchymal stem cells (hMSCs) obtained from healthy donors (according to the existing regional and national ethical guidelines) were cultured in DMEM/F12 supplemented with 10 % (v/v) fetal bovine serum (FBS), 1 % (v/v) penicillin-streptomycin (passage number = 3). Prior to cell seeding, the compacted discs (diameter= 5 mm, n=3) were fabricated and soaked in 70 % (v/v) ethanol (30 min), rinsed with PBS (3x) and UV-sterilized for 1 h each side. Human MSC cells were seeded on the disks at a density of 1×10^4 cells in a 96 well-plate. The disks were cultured in normal media for 7 days while the media was changed every 3 days. On day 7, a part of the ceramic discs was cultured in osteogenic media (normal media supplemented with 50 mg/ml ascorbic acid, 100 nM dexamethasone, and 10 mM β -glycerophosphate), while others have been cultured in normal media.

Proliferation and osteogenic differentiation of human MSCs

To evaluate the proliferation rate of MSCs on the discs, MTT colorimetric and Resazurin assays were performed. After 1, 5, 10 and 15 days of culture, the MTT and Resazurin assay were performed, according to the following. For MTT assay, the cell-discs samples (n = 3 per group) were incubated with 0.5 mg/ml MTT solution in PBS for 4 h. Finally, the absorbance of dissolved formazan using dimethyl sulfoxide (DMSO) was measured at 570 nm in a microplate reader (Bio-Rad, Model 680 Instruments). The relative viability at each time-point was described as below:

The values indicated the cell proliferation relative to the control groups (TCP).

The Resazurin assay is based on the reduction of Resazurin, so after discarding the culture medium from samples, Resazurin solution (10 µg/ml) was added to each sample and kept in an incubator until the color of the Resazurin solution was changed. Subsequently, the absorbance of the solution was read at 630 nm using a microplate reader.

The osteogenic differentiation of MSCs in normal media (days 7, 14, 21, and 28 of culture) and differentiation media (days 14, 21, and 28 of culture) was assessed using alizarin red S staining (n=3). At the specific time point, after fixation of the cell-discs in 10%(v/v) formalin solution, the Alizarin red solution (400 mM in PBS) was added to each sample on a shaker for 20 min. After washing with water, they were studied using a stereoscope and their images were captured by a digital camera (Moticam 480). For quantitation of alizarin staining, the samples were immersed in 10%(v/v) acetic acid for 30 min at room temperature and then shaken for 30 min. Subsequently, the samples were kept at 80°C for 10 min and immediately in an ice bath for 5 min. Afterthought, the tubes were centrifuged for 15 min at the speed of 4300 rpm and the supernatants transferred to 10%(v/v) ammonium solution. The absorbance of samples was read by a microplate reader at 405 nm. In order to investigate the role of various ions released from samples on hMSCs behavior, the concentration of Sr, Ca, Mg and P ions were collected from culture media at different time-points (14 and 21 days) by ICP-AES, quantified and displayed in figure.

Cell morphology in normal and osteogenic media (day 28) was evaluated using SEM observation (n=3). The samples were fixed with 2.5 %(v/v) Glutaraldehyde solution for 2 h. After rinsing with water, the samples were further dehydrated through gradient concentrations of ethanol for 5 min each solution. Finally, they were air-dried, gold-coated and evaluated by SEM. Additionally, to confirm the chemistry of the deposited matrix, SEM coupled with energy-dispersive spectroscopy (EDS) was performed after 28 days of culture in osteogenic medium.

***In vivo* studies**

The surgical procedures have been precisely accomplished according to the provisions of the protocol of the Ethics Committee at Isfahan University of Medical Sciences on the care and use of animals for scientific purposes (ethical grant number = 52268). All *in vivo* study were performed in rat femoral defects according to the previous studies^[89,90]. The ceramic powders (0.2 g) were compressed into discs and sterilized by gamma irradiation for 30 min before the surgery. Fifteen healthy Albino female rats with an average body weight of 300 gr were divided randomly into five groups and used in the animal experiment. The compressed bioceramics powder were implanted in both femurs of the same animal, and all animals were anesthetized after two and three weeks of implantation. Each animal was implanted with the same bioceramic combination using both femurs in the animal. Three of the animals were used as a control meaning that nothing was implanted in the femur defects (Empty defects; the control group). Before the experiment, buprenorphine (0.1 ml/kg) was injected into the rats for pain relief. Consequently, the animals were anesthetized with an intraperitoneal injection of 3% coupled with oxygen prior to the surgery. A drill hole defect with a diameter of 2 mm and a depth of 3 mm was made in the lateral Femoral Condyles, perpendicular to the long axis of the femur. The defects were washed by physiological saline from the remaining bone fragments. The ceramic powders including Sr-FAp and Mg-SiFAP were pressed into the defect, while the defects in the third group were remained empty. Then, the wounds were rubbed with 5% povidone-iodine disinfectant to prevent infections. Animals were sacrificed by deep anesthesia, 2 and 3 weeks after operations. Bone formation was evaluated by histology and immunohistochemistry. Samples were fixed in 4% paraformaldehyde before embedding in paraffin. The slides were stained with hematoxylin-eosin (H&E) and Masson's trichrome methods according to standard protocols^[91]. The slides were observed by a light microscope (HP cx21) and the amount of newly formed bone after 2 and 3 weeks were quantified using by ImageJ 1.52n based on the difference in the threshold of the histological images.

Statistical analysis

Results were expressed as Mean \pm Standard deviation. Prior to the ANOVA tests ($p_{\text{value}} < 0.05$), the data passed the normality test (D'Agostino-Pearson Test, $\alpha = 0.05$). The data were subsequently analyzed using Prism 6 software with a 5% significance level ($p < 0.05$).

Results and discussion

Characterization of ceramics powders

In order to evaluate the role of ion substitution on the structural properties of powder, XRD patterns of samples were investigated (Fig. 1a). The characteristic peaks $-(211), (300), (002)-$ were detected at both Sr-FAp and Mg-SiFAp powders were related to FAp phase, $\text{Ca}_5(\text{PO}_4)_3\text{F}$ [92]. However, the position of these characteristic peaks changed, depending on the sample type. For instance, the characteristic peaks of Mg-SiFAp shifted to higher angles compared to FAp, while they were shifted to lower angles for Sr-FAp. This can be explained by the differences in ionic radius between Mg^{2+} (0.065 nm) and Sr^{2+} (0.113 nm) with Ca^{2+} (0.099nm) and Si^{4+} (0.042 nm) with P^{5+} (0.035 nm) [91,93]. It could be concluded that the lattice parameters changed due to the substitution of Ca^{2+} with Mg^{2+} or Sr^{2+} ions and P^{5+} with Si^{4+} ions in the lattice of FAp. Both samples, Sr-FAp and Mg-SiFAp, revealed nanostructures (crystallite size 55 and 40 nm) with a crystallinity of about 45% and 39%, respectively (Fig. 1b). We speculate, that the lower crystallinity of Mg-SiFAp could be caused by the substitution of two elements in the structure of FAp instead of one. Indeed, a number of studies have demonstrated similar behavior in previous studies entailing combinatorial ion substitution in apatite-coatings. Moreover, the incorporation of Sr in FAp crystal resulted in the formation of a stronger bond between Sr-OH compared to that of Ca-OH, which resulted in a decrease in the lattice energy. In addition, substitution of Mg and Si in FAp lattice led to a broadening and decrease in the intensity of the XRD peaks (Fig. 1a) compared to that of FAp and Sr-FAp patterns, which may be attributed the increase in the lattice energy of FAp (showed by red arrows).

FT-IR spectra of Sr-FAp and Mg-SiFAp (Fig. 1c) confirmed that presence of a crystalline FAp. The major characteristic absorption peaks of the PO_4^{3-} group belonging to ν_3 vibration peak appeared in the $1000\text{-}1100\text{ cm}^{-1}$ region in spectrum of Mg-SiFAp [94], while it was detected as two separate absorption peaks at 1041 and 1092 cm^{-1} in the spectrum of Sr-FAp. Moreover, the ν_1 absorption peak observed as a shoulder at about 960 cm^{-1} in both samples regarding PO_4^{3-} . In addition, the absorption peaks at 1421 and 1459 cm^{-1} (ν_2) and a small absorption peak at 872 cm^{-1} (ν_3) of Mg-SiFAp spectrum revealed the presence of carbonated groups in phosphate sites in FAp structure. There was no evidence of these peaks in Sr-FAp samples. Moreover, according to Fig. 1c, the intensity of CO_3^{2-} and PO_4^{3-} absorption peaks were decreased by incorporation of Si, confirmed the incorporation of SiO_4^{4-} groups into the FAp lattice [95]. In addition, incorporation of Sr in FAp lattice created a broader P-O bonds than FA, as similarly reported previously [96].

To evaluate the morphology of ceramics powder, TEM image of Mg-SiFap and Sr-Fap are presented in Fig. 1d. In this respect, Mg-SiFap particles with spherical shape morphology with the size of 22 ± 13 nm was seen to become agglomerated together. On the other hand, Sr-Fap powder consisted of relatively uniform spherical particles with average size of 44 ± 15 nm. These results confirm that the incorporation of larger ions such as Sr^{2+} into the Fap crystals led to greater distance of Sr-hydroxyl than that of Ca-hydroxyl, which is in accordance to previous works [97].

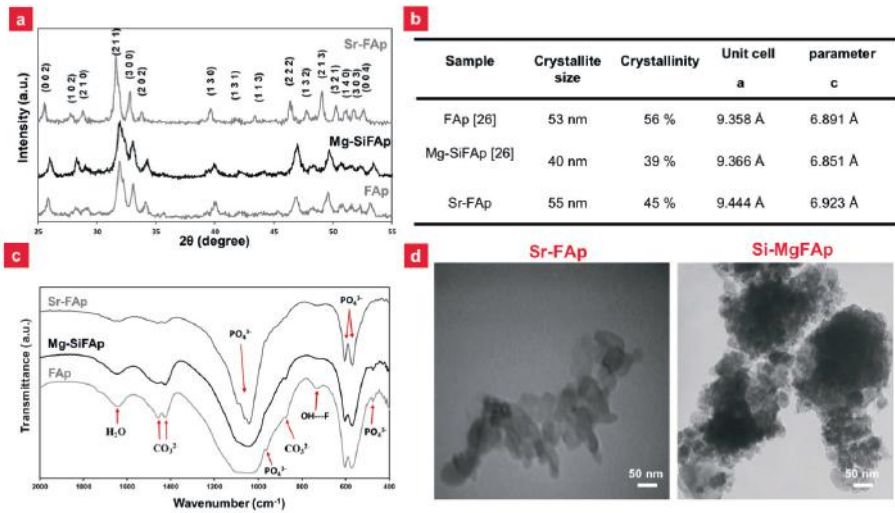


Figure 1. (a) XRD patterns and (b) The table showed the crystallite size, crystallinity degree and lattice parameters (a and c) of Sr-Fap and Mg-SiFap powders compared to Fap reference. (c) FT-IR spectra of Sr-Fap, Mg-SiFap and Fap powders. (d) TEM images of Sr-Fap and Mg-SiFap powder.

***In vitro* bioactivity evolution of bioceramics**

The bioceramics applied for bone regeneration should represent high reactivity in a native environment to fulfill their promise and enable optimal bone-regeneration. In this regard, to evaluate the ability of bone-bonding capacity of the powders, the capability of apatite formation on its surface evaluated in a simulated body fluid (SBF). According to the SEM analysis, a layer of Ca-P deposition was deposited on the surface of both Mg-SiFap and Sr-Fap disks after 7 days of immersion in SBF (Fig. 2a). The tiny particles scattered over the surface of Mg-SiFap and Sr-Fap corresponded to bone-like apatite. There were no morphological differences between apatite formed on the surface of the samples which could be due to the constant Ca/P molar ratio in all solutions. In addition, according to the results of ICP, the dissolution rate of Ca^{2+} ions from Mg-SiFap were higher than Sr-Fap at day 7 which is not statically significant (Fig.

2b). However, this might be due to the dissolution-precipitation reaction on Mg-SiFAP disks in SBF. As mentioned in some previous studies^[98,99], high doses of metallic ions such as magnesium and strontium have been associated with toxicity in the human body. Fortunately, our ion release results reveal that the ions concentration releasing in the media are too low to facilitate any toxic responses^[100,101].

Cell culture

The metabolic activity increased from day 1 to day 15, for both Sr-FAP and Mg-SiFAP (fig. 2c). Moreover, while the cells were active in both normal and osteogenic media, less cell proliferation capacity could be detected in osteogenic media compared to normal medium. For example, after 15 days of culture, the metabolic activity on the Mg-SiFAP significantly increased and reached to 123 ± 5 % (control) and 100 ± 13 % (control), in normal medium and osteogenic medium, respectively ($P < 0.05$). Moreover, the metabolic activity on the Sr-FAP sample was enhanced to 137 ± 16 % and 117 ± 10 %, in normal medium and osteogenic medium, respectively ($P < 0.05$). Moreover, the metabolic activity on the Sr-FAP sample was enhanced to 137 ± 16 % and 117 ± 10 %, in normal medium and osteogenic medium, respectively ($P < 0.05$). The proliferation of human MSCs on Sr-Fap and Mg-SiFAP samples was also evaluated by Resazurin assay in normal and osteogenic mediums (Fig. 2d). This assay confirmed that the proliferation of cells increased on various samples with increasing culture time in normal media ($P < 0.05$). Moreover, the proliferation rate of hMSCs on Sr-FAP was greater than those on Mg-SiFAP. For example, after 15 days of culture in normal medium, the fluorescent Resazurin measurement for Sr-FAP and Mg-SiFAP were 133 ± 8 and 119 ± 5 , respectively. Furthermore, the cell proliferation in osteogenic media was less than in normal media which was due to that fact that the cells in osteogenic media were differentiating toward osteoblasts^[102]. According to the data presented in Fig. 2, we can therefore confirm that various apatite substituted ions have different roles on the cell growth. Si is an initiator of mineralization and bound to glycosaminoglycan which plays a crucial role in forming cross-links between collagen and proteoglycan. In a similar vein, studies have shown that Si substitution into the HAP crystal lattice altered surface charge and enhanced cell proliferation and early cellular attachment of mesenchymal stem cells. Substitution of Si also effectively induced cell proliferation, adhesion, and differentiation as compared to pristine HAP – notably it was found that Si can accelerate bone healing^[103]. Moreover, researches have demonstrated that Sr^{2+} , like calcium, can act as an agonist on the calcium-sensing receptor and in turn promote cell replication, differentiation, and survival^[104]. Based on these results, despite the significant role of released ions on the cellular behavior, there was not significant difference between the results of cell proliferation. Therefore, these ions did not meaningfully change the significant characteristic property compared to each other.

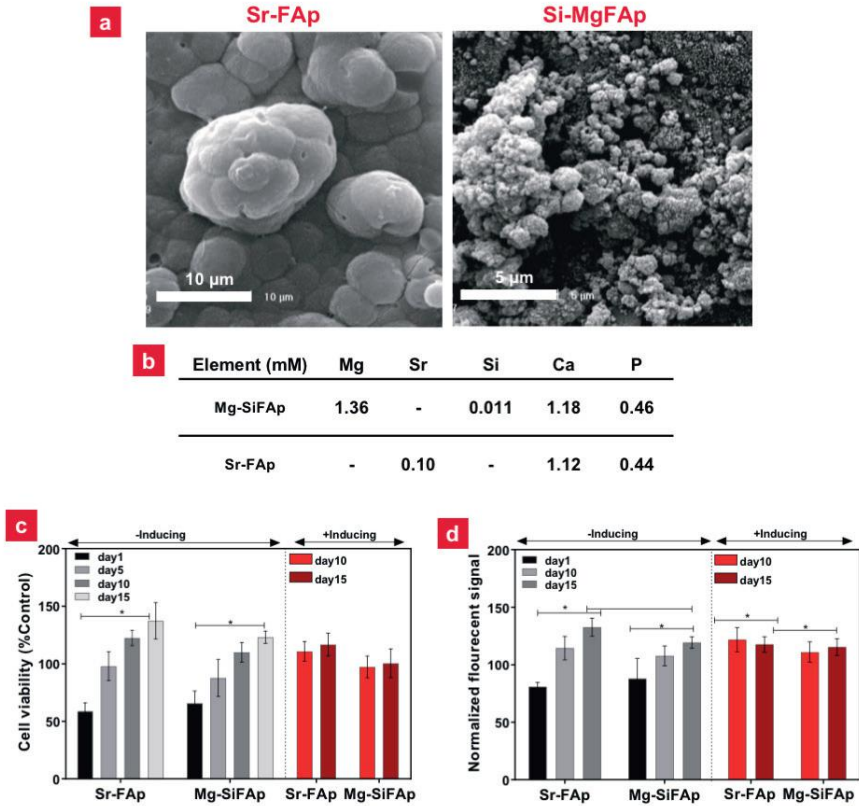


Figure 2. SEM images of (a)Sr-FAp and Mg-SiFAP powders after 7 days soaking in SBF. (b) Ca, P, Sr, Mg and Si concentration of Sr-FAp and Mg-SiFAP after 7 days immersion in SBF. (c, d) Proliferation of MSCs cells on Sr-FAp and Mg-SiFAP substrated cultured through (c) MTT and (d) Resazurin assays evaluated in normal (-inducing) and osteogenic (+inducing) mediums.

To confirm the differentiation of MSCs, alizarin red staining was performed. Fig.3a shows the digital images of the alizarin red stained samples after 21 and 28 days of culture. Intense red dots were observed on the samples corresponded to the calcium deposition. After culturing in normal and osteogenic medium for 28 days, Alizarin red staining indicated that the cells could produce mineralized extracellular matrices, an important precursor of bone formation *in vivo*. Furthermore, the degree of staining quantified with a colorimetric analysis (Fig. 3b) revealed that the differentiation of MSCs cultured on Sr-FAp was 1.4 and 1.1 times greater than that of cultured on Mg-SiFAP in normal and osteogenic culture medium, after 28 days of culture, respectively ($p < 0.05$). According to a previous study, it could be argued that the calcium ions produced during cermaics degradation enhanced mineralization, which generally occurred in the last stage of osteogenic differentiation^[105-109]. However, in addition

to Ca ions, the release of other metallic ions may provide a stimulating environment for bone growth, which would be beneficial for important signals involved in stem cell differentiation towards the osteogenic lineage ^[110].

In order to evaluate the role of ions released from samples, the concentration of ions in culture medium was investigated. Results (Fig. 3c) showed that the concentration of Ca in culture medium for Sr-FAp and Mg-SiFAp were decreased from 3.90 mM and 8.08 mM after two weeks and reached 2.75 mM and 6.23 mM by after three weeks. This gradual decrease in Ca^{2+} might be due to the consumption by the continuously forming apatite layer. Moreover, the release of Si and Mg ions reached to 2.11 mM and 3.31 mM, respectively, after 14 days of MSC culture with respect to Mg-SiFAp. This level was considered to be relatively non-toxic and within the doses stated to positively affect osteoblast-like cells *in vitro* (<10mM) ^[111]. Previous studies have also shown that such ions were able to impact on cell differentiation as well. For instant, the amount of Mg released from the Mg-SiFAp powder may also interact with integrins of osteoblasts, which are responsible for cell adhesion and stability, which could stimulate new bone formation ^[112]. The concentrations of Sr ions in culture medium increased from 2.66 mM in the second week to 3.17 mM in the third week of culture of SrFAp. Our results demonstrated that the concentration of Sr^{2+} ions released in the culture medium could promote the proliferation and osteogenic differentiation of MSCs, which is in accordance with previous works ^[84,113].

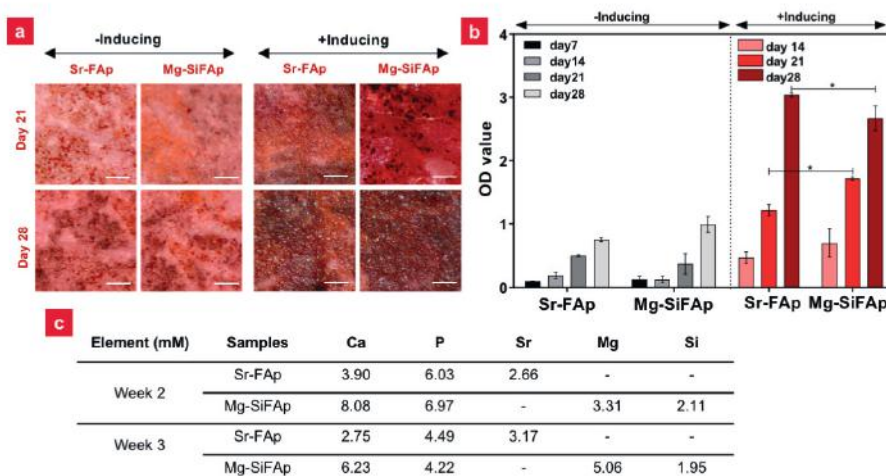


Figure 3. Effects of Sr-FAp and Mg-SiFAp powders on the differentiation of MSCs: (a) The mineralized matrix was stained with Alizarin Red S and (b) quantified after following days of incubation in normal and osteogenic mediums. (c) Ca, P, Sr, Mg and Si concentration changes of Sr-FAp and Mg-SiFAp after 2- and 3-weeks immersion in culture medium.

The role of released ions on the osteogenic differentiation of stem cells was further investigated via evaluation of cell morphology (Fig. 4). To be able to distinguish the calcified structures from the mineral deposits from hMSCs, the images of bioceramics in SBF were also included after 28 days (Fig. 4a). The EDS analysis of the samples has shown the precipitation of Ca and P on the bioceramics powder (Fig. 4b). In this direction, after 28 days of culture in osteogenic medium, higher magnification SEM images showed that analogous particles densely covered the surface of samples, which were qualitatively identified as consisting of calcium and phosphate by EDS analysis (Fig. 4c). In addition, results demonstrated that large accumulation of calcium and phosphorous were deposited on both samples, which effectually revealed the capacity of the samples to form a bone-like hydroxyapatite (Fig. 4d). From the EDX analysis, it is been concluded that the concentration of Ca and P after immersing in SBF and after osteogenic differentiation is less than those after immersing in SBF solution. Moreover, the Ca/P molar ratio (Fig. 4e) deposited on the cells (labeled by a yellow rectangle) was 1.51 and 1.54 for Sr-FAp and Mg-SiFAP samples, respectively, which was in the range of Ca/P ratio for bone-like apatite coatings (1.5–1.67) [114]. Overall, these results demonstrated the effective role of the substrates to support the differentiation of MSCs toward the osteogenic phenotype.

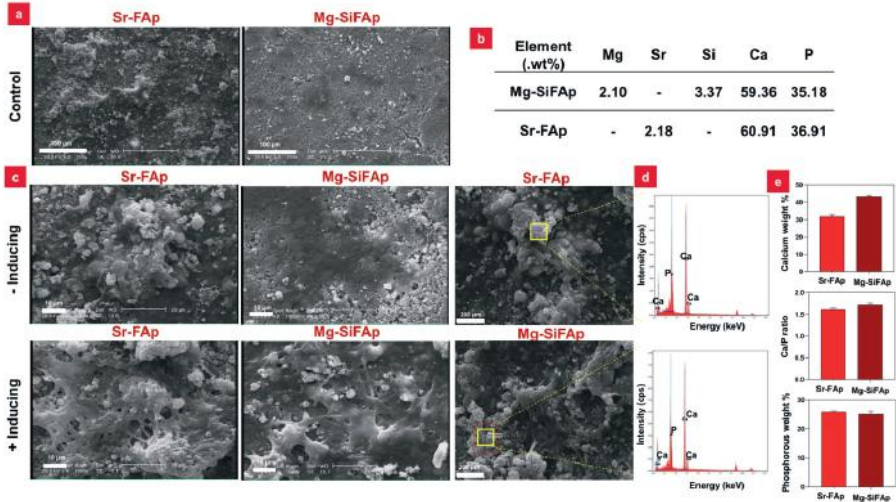


Figure 4. SEM images of MSCs on different bioceramics powder after 28th days of culture in SBF as a control (b) Energy dispersive X-ray spectrometer analysis of the bioceramics powder after 28 days immersing in SBF. (c) SEM images of the hMSCs after culturing on the bioceramics powder in normal and osteogenic medium. (d) Energy dispersive X-ray spectrometer analysis of calcified formation on scaffolds was showed in the right panel. (e) The amount of deposited Ca and P on the surface of the discs. The calculated ratio between the Ca and P also determine the purity of hydroxyapatite.

In vivo study

The local evolution of Sr-FAp and Mg-SiFAp after 2 and 3 weeks of in vivo implantation demonstrated significant differences in bone formation (Fig. 5 and 6). According to Fig. 5, two weeks after implantation, the formation of connective tissue was detected in the defect sites in the presence of Mg-SiFAp and Sr-FAp samples. For Mg-SiFAp samples, the proliferative connective tissues and fibrous tissues were observed (Fig. 5). Moreover, the formation of bone was observed in defect sites of Sr-FAp samples after 2 weeks. From the quantification of histology staining, it is concluded that the amount of mineralized tissue after three weeks increased significantly both for Sr-FAp and Mg-SiFAp ($p < 0.05$). In parallel, the amount of connective tissue after three weeks decreased for Sr-FAp. The mineralized tissue in both bioceramics powder is more than that in empty defects after 3 weeks implantation.

New bone tissue was detected after three weeks of implantation of Mg-SiFAp samples (Fig. 6). After three weeks of implantation, the formation of collagen fibers in immature trabecula of bone were observed by Masson's trichrome staining (Fig. 6). The bone formed in defect site could be shown in Masson's trichrome staining image. On the other hand, for control samples, almost no new bone formation was observed in the defect site after three weeks (Fig. 6), except in small areas surrounding the defect site. These results have quantified and it shows the significant differences among all the samples ($p < 0.05$).

These results were in accordance with previous literature where authors investigated the in vivo performance of a HA substituted with Si in a rabbit calvarial defect [115]. Along the same vein, another study demonstrated a faster new bone formation in Merwinite ($\text{Ca}_3\text{Mg}(\text{SiO}_4)_2$)-filled-bone-defect than in HA models which was due to its superior degradation rate, proper biocompatibility and the existence of Mg and Si ions [116]. Besides, bone remodeling improved and established a good bonding with living bone and sufficient density in the presence of Sr-FAp samples. Also, the integration of Sr-FAp powder could significantly promote the differentiation and proliferation of osteoblast cells due to the osteoinductive properties of metallic ions like Sr^{2+} doped in the FAp structure.

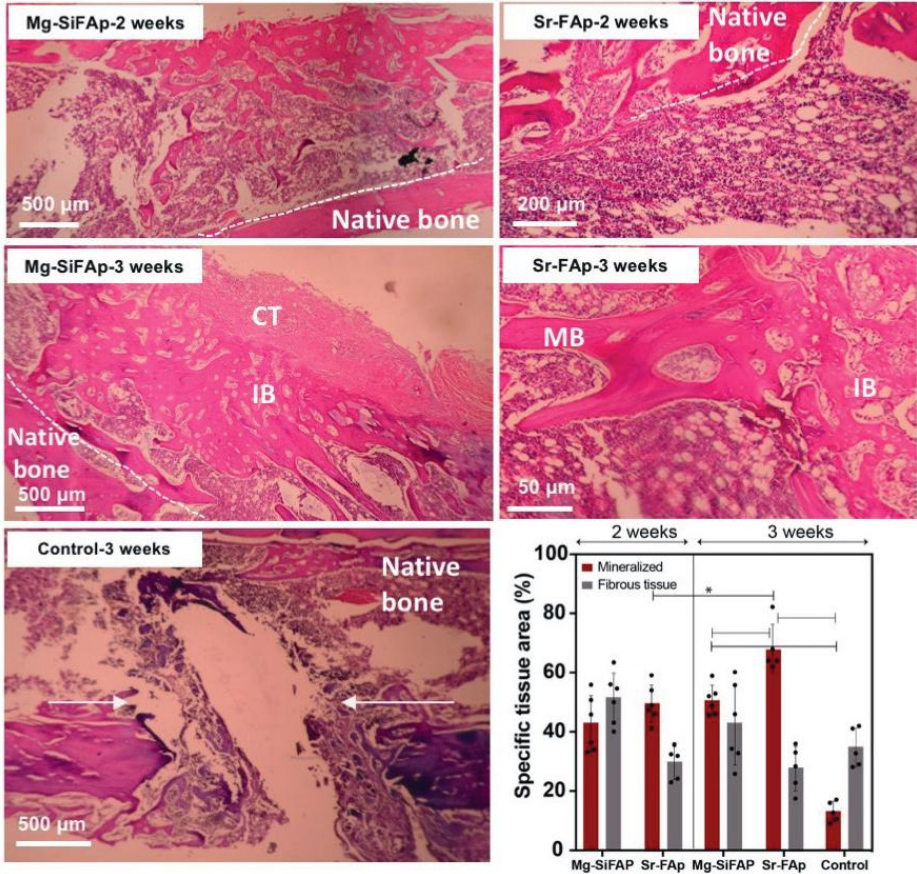


Figure 5. Bone injury repair in bioceramics powder discs were implanted animals after 2 and 3 weeks. After 2 weeks, invasion of connective tissue elements into the site of injury for repair, but at this time there is no sign of bone formation (CT shows the connective tissue). After 3 weeks, for Mg-SiFAP, immature Bone (IB) and connective tissue (CT) and for Sr-FAP, invasion of connective tissue elements (CT) and formation of bone islands (MB) can be distinguished. The quantification of mineralized and fibrous tissue for various bioceramics during 3 weeks.

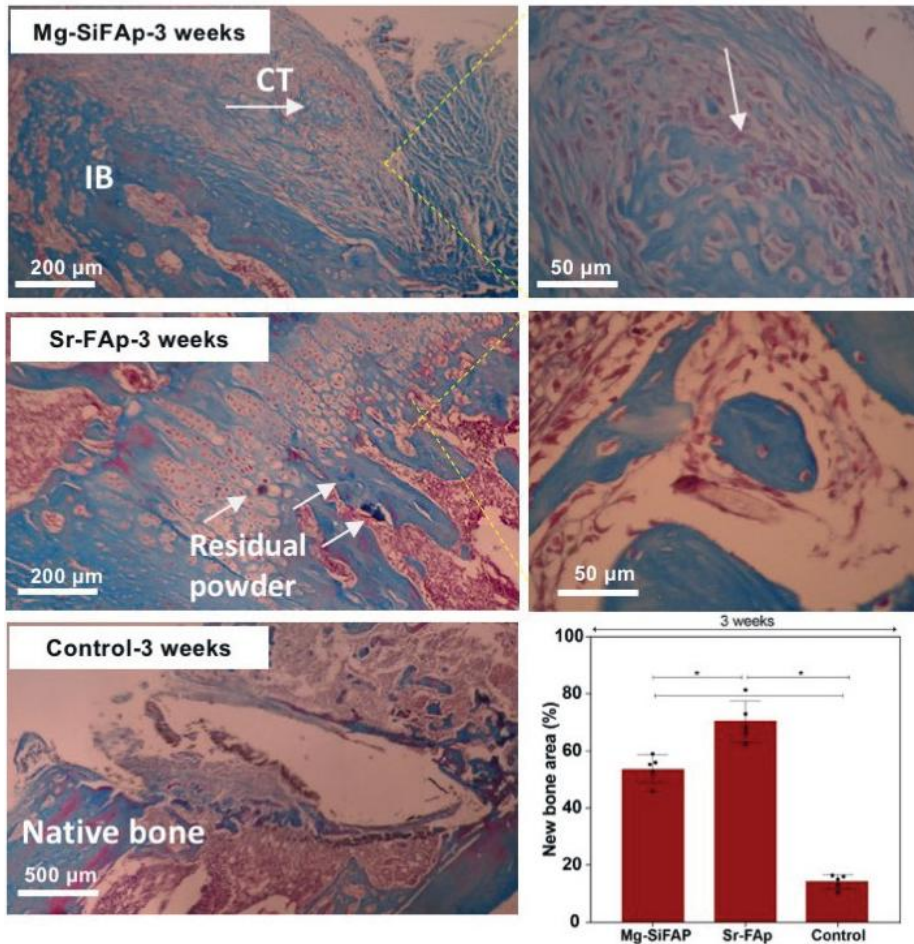
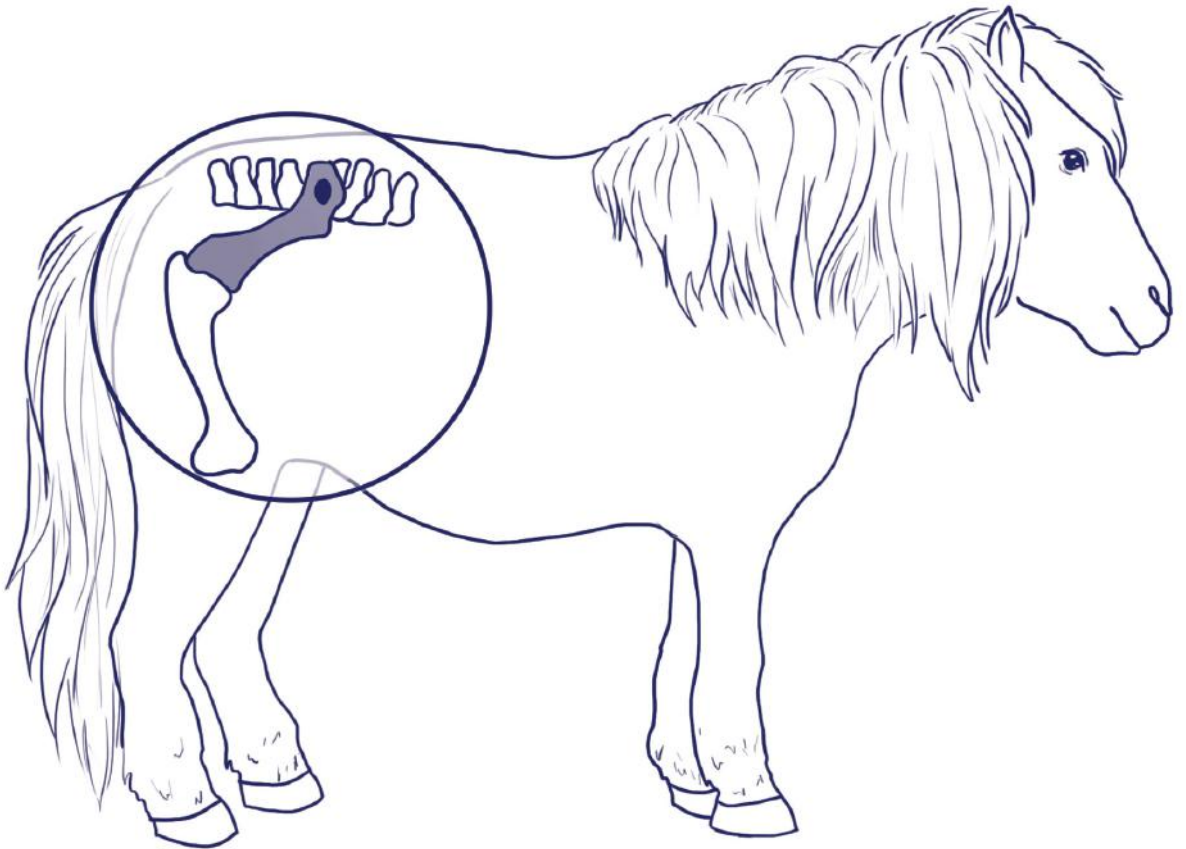


Figure 6. Photomicrographs showing Masson-trichrome staining of samples from rats after 3 weeks. Higher magnifications of the boxed regions at right as Masson-trichrome staining, which showed collagen fibers were stained blue (arrows marked active osteoblast cells). H&E and Masson-trichrome staining of samples showed the initial stages of bone formation in empty bone defects in control group after 3 weeks. Sharp tips of compact bone in defect sites are marked by white arrow and limited immature bone (IB) formed in the site of defects. The percentage of newly formed bone after 3 weeks of implantation.

In the present study, from histological analysis, larger regions of newly formed bone were identified in the Sr-Fap groups than Mg-SiFap and control groups after 3 weeks. This potentially indicates a faster bone remodeling for the Sr-Fap. The released Sr from Sr-Fap powder was most likely responsible for the higher new bone formation compared to Mg-SiFap powder.

Conclusion

In conclusion, we studied the role of various metallic ions Sr, Mg and Si, on the chemical, physical and biological properties of Fluorapatite (FAp) by comparing two powders compositions, Mg and Si doped FAp (Mg-SiFAp) and Sr doped FAp (Sr-FAp) produced through a procedure known as mechanical alloying. Results showed that both nanopowders enabled *in vitro* cellular proliferation and enhanced bone formation when compared to non-modified FAp. Both Mg-SiFAp and Sr-FAp revealed a significant enhancement of new bone formation compared to empty defects in a distal femur bone defect model in rats. Interestingly, Sr-FAp exhibited a significant higher new bone formation both at the biomaterial-bone interface and in the entire defect area compared to Mg-SiFAp. Taken together our study suggests that incorporation of Sr ions into FAp can result in improved bone growth, which has great potential as a new bone substitute or coating of metallic implants for bone replacement



CHAPTER 3

Tough magnesium phosphate-based 3D-printed implants induce bone regeneration in an equine defect model

Nasim Golafshan

Elke Vorndran

Stefan Zaharievski

Harold Brommer

Firoz Babu Kadumudi

Alireza Dolatshahi-Pirouz

Uwe Gbureck

René van Weeren

Miguel Castilho

Jos Malda

Published in **Biomaterials**

DOI: 10.1016/j.biomaterials.2020.120302

Abstract

One of the important challenges in bone tissue engineering is the development of biodegradable bone substitutes with appropriate mechanical and biological properties for the treatment of larger defects and those with complex shapes. Recently, magnesium phosphate (MgP) doped with biologically active ions like strontium (Sr^{2+}) have shown to significantly enhance bone formation when compared with the standard calcium phosphate-based ceramics. However, such materials can hardly be shaped into large and complex geometries and more importantly lack the adequate mechanical properties for the treatment of load-bearing bone defects. In this study, we have fabricated bone implants through extrusion assisted three-dimensional (3D) printing of MgP ceramics modified with Sr^{2+} ions (MgPSr) and a medical grade polycaprolactone (PCL) polymer phase. MgPSr with 30wt.% PCL (MgPSr-PCL30) allowed the printability of relevant size structures ($>780 \text{ mm}^3$) at room temperature with an interconnected macroporosity of approximately 40%. The printing resulted in implants with a compressive strength of 4.3MPa, which were able to support up to 50 cycles of loading without plastic deformation. Notably, MgPSr-PCL30 scaffolds were able to promote *in vitro* bone formation in medium without the supplementation with osteo-inducing components. In addition, long-term *in vivo* performance of the 3D printed scaffolds was investigated in an equine tuber coxae model over 6 months. The micro-CT and histological analysis showed that implantation of MgPSr-PCL30 induced bone regeneration, while no bone formation was observed in the empty defects. Overall, the novel polymer modified MgP ceramic material and extrusion-based 3D printing process presented here greatly improved the shape ability and load bearing properties of MgP-based ceramics with simultaneously induction of new bone formation.

Keywords

3D printing, bone tissue engineering, composites, magnesium phosphates, strontium, *in vivo*, osteoinduction

Introduction

Given the diversity of the treated clinical pictures (ranging from infantile craniofacial anomalies to trauma or cancer), medical progress, and population ageing, a 10% annual increase of bone grafting procedures is expected [117]. To satisfy the growing need for bone repair, the development of new biomaterials and fabrication methods has received great attention. Degradable scaffolds can be either ceramic (e.g. hydroxyapatite [66,118], tri-calcium phosphate [119], or bioglass [120]), polymer-based (e.g. polycaprolactone [121], polylactide-co-glycolide [28]) or composites of both classes of material [64]. These materials have been produced by different methods to use as bone scaffolds, ranging from porogen leaching [122], the polymeric sponge method [123], freeze-casting [124], gas foaming [125], and meltelectrowriting [126] to 3D printing [127]. Due to their poor shape ability and limited mechanical properties of these materials, one of the biggest challenges remains the generation of scaffolds for the treatment of larger and complex defects (typically above 10 mm) [128]. One promising approach to address the abovementioned limitations is through extrusion assisted three-dimensional (3D) printing of ceramics. 3D printing allows the generation of engineered bone scaffolds from a computer-aided design (CAD) model. Numerous 3D printing techniques have been developed to fabricate tailored bone scaffolds. The most investigated techniques for 3D printing of bioceramics involve 3D powder printing [129–132], low temperature [63,133] and high temperature [64,134] extrusion-based 3D printing. Previously, Adam *et al.* manufactured hyper-elastic scaffolds for bone repair composed of hydroxyapatite and polycaprolactone or poly(lactic-co-glycolic acid), using extrusion based 3D printing at room temperature, which is a versatile technology for pasty materials [64]. However, printed purely ceramic materials generally lack load-bearing properties. However, the polymer-ceramic composites may have improved mechanical properties, but feature limited osteoinductivity due to polymer masking and lower solubility of the ceramic phases, such as hydroxyapatite (HA), tri-calcium phosphate (TCP), calcium-deficient hydroxyapatite (CDHA), and biphasic calcium phosphates (BCPs). Recently, magnesium phosphate cement (MPC) or metal ions into calcium phosphate cement (CPC) were introduced, showing a great promise for stimulating bone formation [135,136]. Magnesium phosphate (MgP) has captured attention due to its high solubility and low tendency to transform into lower soluble phases *in vivo*. Magnesium (Mg^{2+}) ions suppress HA formation since they inhibit crystal growth by stabilizing gel-like amorphous calcium phosphate phases [137]. In addition, the incorporation of strontium (Sr^{2+}) ions into the MgP structure (MgPSr) has been shown to enhance new bone formation *in vitro* [84,129,138,139]. In accordance with abovementioned properties for bone compatible biomaterials, the addition of PCL makes the scaffolds mechanically robust by acting as a binder for MgPSr ceramic particles.

Here, we have developed individually shaped 3D printed magnesium phosphate scaffolds with controlled mechanical and biological properties. Control over mechanical and biological properties was obtained by incorporation of an elastic medical grade PCL phase and low dosages of biologically active Sr^{2+} ions, respectively. The effect of PCL and Sr^{2+} on MgP printability was evaluated by filament collapse and fusion testing. In addition, the structural and mechanical properties of the printed composite were investigated. The biological effect of PCL and Sr^{2+} on MgP ceramic bone forming potential, was evaluated *in vitro* over 28 days in both basal and osteogenic medium firstly and then followed by a long-term (6 months) *in vivo* experiment in an equine tuber coxae defect model.

Materials and methods

MgP based ceramics powders preparation

MgP based powders for 3D printing were synthesized as previously described ^[140]. Briefly, a homogenous mixture of reactants composed of magnesium hydrogen phosphate ($\text{MgHPO}_4 \cdot 3\text{H}_2\text{O}$, Sigma-Aldrich, Steinheim, Germany), magnesium hydroxide ($\text{Mg}(\text{OH})_2$, VWR International GmbH, Darmstadt, Germany), and strontium carbonate (SrCO_3 , Sigma-Aldrich, Steinheim, Germany) in appropriate molar ratios (Table 1) were homogeneously mixed in a planetary ball mill (PM400, Retsch GmbH, Haan, Germany) for 1 h at 200 U/min using 4 agate balls ($d_{\text{ball}} = 30$ mm). Thereafter, these powder mixtures were sintered at 1050 °C for 5 h. Afterwards, the sintered cakes were crushed with a pestle in a mortar followed by wet grinding in 100% ethanol for 2 h in the planetary ball mill (180 ml ethanol, 125 g cement, 250 U/min) using 200 agate balls ($d_{\text{ball}} = 10$ mm). In a final step the cement powders were decanted and dried at room temperature.

Table.1 Chemical composition ratio of the reactant to synthesize MgP based powders

	Reactant composition ratio in mole		
	$\text{MgHPO}_4 \cdot 3\text{H}_2\text{O}$	$\text{Mg}(\text{OH})_2$	SrCO_3
$\text{Mg}_3(\text{PO}_4)_2$	0.6	0.3	0
$\text{Mg}_{2.33}\text{Sr}_{0.67}(\text{PO}_4)_2$	0.6	0.1	0.2

Paste preparation and extrusion-based 3D printing

Extrusion pastes were prepared by combining prepared $\text{Mg}_{2.33}\text{Sr}_{0.67}(\text{PO}_4)_2$ powder (MgPSr) and commercial medical grade Poly (ϵ - caprolactone) (mPCL, Purasorb PC 12, Purac Biomaterials, Netherlands) in different weight ratios of MgPSr to PCL (70:30, 60:40, and 50:50 wt.%). The initial materials were dissolved in a mixture of high volatile solvents composed of dichloromethane (Sigma-Aldrich, Germany), 2-BU-1-(4- (diethylamino) anilino)-3-me-pyrido(1,2-a) benzimidazole - 4 - carbonitrile (Sigma-Aldrich, Germany), and dibutyl phthalate (Sigma-Aldrich, Germany) in a ratio of 10:2:1 wt.%. After the mixture of 90 wt.% powder with the solvent as described above, pastes were left homogenizing for 24h on a roller mixer at 37°C.

According to the amount of polymer (100, 50, 40, and 30 wt.%), different compositions were identified as PCL alone, MgPSr-PCL50, MgPSr-PCL40, and MgPSr-PCL30, respectively. This nomenclature will be used throughout the manuscript.

MgP based scaffolds were fabricated using an extrusion-based 3D printing system (3D Discovery, regenHu, Switzerland). Initially pastes were transferred to a 5 mL syringe (Nordson EFD, USA) and extruded through a 22G conical nozzle, 0.41mm (Nordson EFD, USA) (Fig. 1A). Continuous paste deposition was achieved by applying a dispensing pressure of 0.9 bar. Printability of the different pastes was first evaluated by a filament collapse and fusion test according to a protocol described elsewhere^[141]. Briefly, for the filament collapse test, a single paste filament was deposited onto a platform with pillars spaced by 1.0, 2.0, 4.0, 8.0, and 16.0 mm using extrusion parameters as mentioned before. Filament sagging was quantified by measuring the angle of deflection (θ) at the edge of the suspended filament using image J software (version 1.51k, NIH, USA), as illustrated in Fig. 1B at various gaps. For the filament fusion test, pastes were printed in meandering patterns composed of parallel strands at increasing spacings, from 0.1 mm to 2.5 mm, and increasing 0.2 mm for each subsequent line (Fig 1B). After taking pictures, the fused segment length (f_s) at each filament distance (f_d) were measured using ImageJ and normalized by dividing f_s by the average of filament thickness (f_t) to avoid the effect of filament thickness variation between different concentrations of PCL. All measurements were repeated 3 times and the images were recorded by a stereo microscope (Olympus SZ61, magnification 4.2x, resolution 2040 x1536 pixels) immediately after printing. Afterwards, cylindrical shape scaffolds with different sizes ($d = 10$ mm and $h = 10, 15$ mm), and rectangular (10mm, 10 mm, and 20 mm) with a defined pore size of 1 mm were fabricated to further analysis.

Physical and chemical characterization

The morphology of the synthesized ceramic powders and the microstructures of the 3D-printed constructs were analyzed using a Scanning Electron Microscope (XL30SFEG, FEI, USA) at an acceleration voltage of 10 kV. Prior to imaging, all samples were coated with gold with the thickness of 6 nm. In addition, the phase composition of both synthesized powders was determined by X-ray diffraction (Bruker AXS, Germany) using monochromatic Cu-K α radiation. Measurements were collected from $2\theta = 20\text{--}40^\circ$ with a step size of 0.02° . The phase composition of homemade powders was checked by JCPDS reference patterns (Mg₃(PO)₄, Farringtonite, PDF ref. 00-033-0876) and Magnesium Strontium Phosphate (Mg₂Sr(PO)₄)₂, PDF ref. 00-014-0206).

The porosity of the printed scaffolds was characterized by micro-CT analysis using a Quantum FX-Perkin Elmer (μ CT, Quantum FX, PerkinElmer, USA). Constructs were scanned at 90 kV tube voltage, 180 mA tube current, 30 μ m resolution and 3 minutes scan time. Volume calculation and the porosity of the printed scaffolds were determined by measuring trabecular parameters in a 3D μ CT images according to the suggested protocol^[142]. Briefly, slices scan of the scaffolds was opened and the local threshold was adjusted based on Bernsen and Niblack's thresholding method using ImageJ software. Finally, bone volume fraction (BV/TV) and porosity ($1 - (BV/TV)$) were measured with BoneJ plugin for the circular region of interest (ROI).

Mechanical characterization of printed constructs

Uniaxial compression tests were performed using a universal testing machine (Zwick Z010, Germany) equipped with a 1 kN load cell. Quasi-static tests were performed at a rate of 1 mm/min, in air at room temperature, according to a protocol described elsewhere^[131]. Tests were conducted on cylindrical samples ($d = 6$ mm, $h = 12$ mm, $n=5$) with a pore size of 1 mm. From the quasi-static measurements, the elastic modulus (defined as the slope of the linear region from 0.02 to 0.05 mm/mm), the yield stress (defined as the point where nonlinear deformation begins), and toughness (defined as the absorbed energy by the scaffolds up to yield stress) were determined. In addition, to access the elastic behavior of the printed constructs, dynamic compression tests were conducted on MgPSr-PCL30 samples ($n=3$). Tests were performed by applying a ramp force to a height of 2 mm (equivalent to a strain of 2%) followed by a sinus wave deformation at a frequency of 0.1 Hz. From the dynamic tests, the compression loading profiles of MgPSr-PCL30 scaffolds in the strain and time domain were determined. Uniaxial tensile testing was performed on rectangular shaped MgPSr-PCL30 based scaffolds ($l = 60$ mm, $w = 10$ mm, and $t = 1$ mm). Tests were conducted at a rate of 1 mm / min at room temperature. From the engineered stress-strain curves, elastic modulus, yield stress, and toughness were

determined. Tensile elastic modulus was determined as the slope of the linear part of the curve between 0.02 and 0.03 mm/mm, while yield stress and toughness were determined as stated above for the uniaxial compression tests."

Lipase accelerated degradation experiments

MgSrP-PCL30 printed implants were incubated in a 0.4 mg/ml lipase solution (from *Pseudomonas cepacian*, Sigma-Aldrich, Germany) and 1 mg/ml sodium azide (Sigma-Aldrich, Germany). Incubation was performed at 37°C for 15 days (with intermediate time points 1, 5, 10 and 15 days) and media were refreshed every 4 days. As a control, scaffolds were also incubated in PBS alone. At each time point, samples were monitored for weight loss (quantified as %) and compressive mechanical properties. Compression tests were performed according to section 2.4. Before mechanical testing, scaffolds were washed thoroughly with Mili-Q water and dried in a desiccator for 2 days.

Ion release study

The release profile of magnesium, phosphorous and strontium ions from the 3D-printed scaffolds were recorded by means of Inductively Coupled Plasma Mass Spectrometry (ICP-MS, Varian, Darmstadt, Germany) during 21 days. Samples (disc shape with a diameter of 10 mm and thickness of 3 mm) were immersed in 5 ml Mili-Q water and Tris-HCl at 37°C. To quantify the concentration of released ions, the solutions were 10X diluted in 1.3 v/v% HNO₃ (65% Suprapur, Merck, Schwalbach, Germany) and measured against standard solutions (Merck, Schwalbach, Germany, Ca²⁺: 0.5 ppm and 1 ppm, Mg²⁺: 1 ppm, 5 ppm, P: 100 ppm and 500 ppm, Sr²⁺: 10 ppm and 200 ppm). The ion concentrations at each timepoint were calculated relative to the amount of fresh medium and the cumulative concentration of released ions was reported over 21 days. To compare the ion release of MgPSr-PCL30, the MgP-PCL30 scaffolds were used as control.

***In vitro* cell culture**

To ensure effective removal of solvents all scaffolds used for *in vitro* cell experiments were washed for 6 h in 70 v/v% ethanol in water followed by 5 times washing with Mili-Q water for 24h. After washing, samples were sterilized for 2h under ultraviolet (UV) light and subsequently immersed in cell culture media supplemented with 1v/v% penicillin/streptomycin (Pen-Strep) (all Gibco, Thermo Fisher, USA) for 3 days to remove any remaining solvents from the printing process. Equine mesenchymal stem cells (eMSCs) were harvested from healthy bone marrow aspirates according to a protocol described elsewhere^[143]. EMSCs were then first expanded 7 days in α -MEM supplemented with 10% (v/v) fetal bovine serum (FBS), 0.2 mM L-ascorbic-

acid-2-phosphate (ASAP), and 1% (v/v) Pen-Strep at 37 °C in a humidified atmosphere containing 5% CO₂, and then seeded (passage number = 3) onto scaffolds (PCL, MgPSr-PCL30, and MgP-PCL30) at a density of 30,000 cells per cm². Cell-laden constructs were cultured in basal media for 7 days, then divided into two groups: samples cultured in 1) basal medium (α-MEM+10% FBS+0.2mM ASAP+1% Pen-Strep, Sigma Aldrich, Germany) and in 2) osteogenic medium (α-MEM+10% FBS+0.2 mM ASAP+1% Pen-Strep+ 10 nM Dexamethasone, +10 mM B-glycerophosphate, Sigma Aldrich, Germany). Medium was changed every 3 days and at least 3 scaffolds were tested per group.

Cytocompatibility and osteogenic potential evaluation

Cell viability of MgP based scaffolds was determined using a live-dead viability kit for mammalian cells (Invitrogen Life Technologies, USA), according to the manufacturer's instructions and a protocol described elsewhere ^[144]. Stained cell-laden constructs were imaged with a confocal microscope (Leica SP8X Laser Scanning, Germany) with 494 nm (green, Calcein) and 528 nm (red, EthD-1) excitation filters, and at least 3 samples were analyzed per group. Images of the whole scaffolds were merged using the mosaic function of the Leica LASX software. Moreover, the distribution of live and dead cells relative to the scaffold was quantified using Adobe Photoshop cc 2019. Cell metabolic activity was quantified by Alamar blue, following manufacturer's instruction, while DNA content was measured using a Quant-iT-Picogreen-dsDNA kit (Molecular Probes, Invitrogen, Carlsbad, USA).

The osteogenic differentiation of the cells was measured using alkaline phosphatase (ALP) and Alizarin Red staining (ARS) as early and late osteogenic markers, respectively. The alkaline phosphatase assay was performed after lysis of the cells in TE-buffer (Tris-EDTA buffer, 10 mM Tris-HCl, 1 mM EDTA, pH 8) after 1 and 7 days of culturing. The cell-laden constructs were thawed and frozen 3 times to lyse the cells in TE-buffer. The alkaline phosphatase activity was measured using conversion of the p-nitrophenyl phosphate liquid substrate System (pNPP, Sigma-Aldrich). The standard ALP measurements using serial dilutions of calf intestinal ALP (Sigma-Aldrich, Germany) in TE-buffer was used to normalize the measured ALP values. The samples were incubated on the shaker for 30 min and every 5 min, the absorbance was measured at 405 nm and corrected at 655 nm (Bio-rad, Hercules, CA, USA). Results were normalized to DNA content from the same cell lysate used to measure ALP, using a Quan-iT-Picogreen-dsDNA kit (Molecular Probes, Invitrogen, Carlsbad, USA) following the manufacturer's instructions.

Calcium deposition was determined by Alizarin red staining (ARS) (2% solution, pH 4.2, Sigma-Aldrich) staining at 21- and 30-day time points as described elsewhere^[108]. Prior to incubation of cell-laden constructs with ARS solution, the samples were fixed in 4% formaldehyde. Calcium deposits were visualized by stereo microscope (Olympus SZ61, magnification 1.5x). For quantification of calcium deposition, 35 mg/ml fresh cetylpyridinium chloride (CPC) solution in DI water (pH=7.4-7.8) was added to the stained samples under agitation for 30 min at 37°C. It was then read with a UV/vis plate reader at 405 nm. Absorbance of ARS concentration conversion was done using a pre-plotted standard curve. Moreover, to confirm the calcium deposition within the extracellular matrix, after 30 days of culturing, the cell-laden scaffolds were washed with deionized water and fixated in 2.5% Glutaraldehyde (Sigma-aldrich, Germany).

To analyze the chemical structure of the seeded scaffolds, Fourier-Transform Infrared spectra were obtained in the range of 4000 - 500 cm^{-1} at a resolution of 4 cm^{-1} using an FTIR spectrometer (PerkinElmer Spectrum 100, USA) fitted with a diamond crystal attenuated total reflectance (ATR). Spectrum signals were averaged over 16 scans and the obtained spectra were baseline-corrected and normalized using the Perkin Elmer Spectrum software. X-ray diffraction patterns of the seeded scaffolds after 30 days of culturing were recorded at room temperature using Cu K α 1 radiation ($\lambda = 1.54056 \text{ \AA}$) and Ge (111) monochromator operating at 40 kV and 40 mA (HUBER G670 Guinier imaging-plate detector powder diffractometer, Germany). XRD patterns were collected with 2θ ranging from 20° to 50° and a scan step size of 0.005°. The morphology of eMSCs on 3D printed scaffolds were observed using backscatter scanning electron microscope (voltage 10kV). To fix the cells, at specific timepoints, the scaffolds immersed in 2.5 vol% Glutaraldehyde (Sigma-aldrich, Germany) for 1 hour and then dehydrated in gradient ethanol solution (each step 10 minutes). Afterwards, the scaffolds were kept in desiccator prior to imaging.

After 14 and 21 days of *in vitro* experiment, all the samples kept in formalin (4%), embedded in Agarose (4w. %, Sigma-Aldrich, Germany) and cut through the top of the scaffolds. Osteonectin a major non-collagenous protein in bone (Osteonectin AB SPARC AON-1, DSHB; nuclei: blue, positive osteonectin: brown) and collagen type 1 (Anti-collagen I antibody EPR7785, Abcam; nuclei: blue, positive collagen type I: brown) were performed to reveal the activity of osteoblasts.

Animal experiments

In total, 8 adult female ponies (age 5-14 years, mean body weight 173±38 kg) were used for this study. Surgery was performed in a standing position, under local anesthesia and sedation (detomidin (Domosedan®, 10 mcg/kg) + morphine (0.1 mg/

kg) intravenously applied via a jugular catheter in combination with local infiltration with mepivacaine (Mepidor), 10 mL/site). A critical-sized defect was created in both tubera coxae of the ponies. In detail, a vertical incision was created through the skin, subcutis and periosteum onto the bone of the tuber coxae. Subsequently, the periosteum was dissected from the bone. A drill hole of 11 mm diameter and 10 mm deep was created using an orthopedic drill and drill sleeve. The cylindrical MgPSr-PCL30 scaffolds ($d = 10$ mm, $h = 10$ mm) were implanted at one side while the contralateral tuber coxae remained empty as control. The surgical wounds, including periosteum, the overlying fat, subcutis and skin were closed in 3 layers using synthetic resorbable suture material post-operatively, clinical parameters such as degree of lameness, discomfort, and temperature were monitored daily during 4 weeks while the animals were kept in boxes. NSAIDs were given for 5 days (meloxicam, Metacam®, per os, 0.6 mg/kg bwt). Subsequently, the animals received pasture exercise for 5 months. After six months, the ponies were sacrificed and the tubera coxae were harvested and fixed in formalin for processing and further analysis. The animal study was approved by the Instantie voor Dierenwelzijn Utrecht (IvD, Utrecht Animal Welfare Body) and was in compliance with international recommendations for care and use of laboratory animals (approval ethical number AVD108002015307).

Micro-computed tomography

To visualize the calcified tissue at the defect site, the harvested tissue underwent micro-CT analysis (Quantum FX-Perkin Elmer, USA). The scan parameters were 90 kV tube voltage, 180 mA tube current, 40 mm resolution and 3 min scan time. Bone ingrowth and degradation of the scaffolds were quantified using BoneJ plugin and ImageJ based on the thresholding method specified in point 2.3.

Histology and immunohistochemistry

The harvested constructs were cut into two parts; one half was embedded in polymethylmethacrylate (MMA, Sigma Aldrich, Germany) and the other half was slowly decalcified in formalin and ethylenediamine tetra-acetic acid (EDTA, Sigma-aldrich, Germany) for 3 months and subsequently embedded in paraffin. Samples embedded in MMA were sectioned in 300-400 μm slices using a Leica 4 SP1600 Saw Microtome system (Leica, Germany). After sectioning, the samples were stained with methylene blue/basic fuchsine and evaluated with light microscopy (Olympus BX51, Japan) ^[145]. Paraffin embedded samples were sectioned using a microtome ($n = 6$ for each sample) (Leica sawing microtome, Nusslochh, Germany) in 5 μm slices and stained with hematoxylin and eosin (H&E staining, thermo Fisher scientific, USA) for tissue overview analysis, and picro-sirius red staining (thermo Fisher scientific, USA) for collagen analysis. Collagen orientation was visualized with polarized light

(Olympus BX51, Japan). Backscatter images using a Secondary Electron Detector were analyzed by EDX with a scanning electron microscope (FEI XL30SFEG, USA). Before EDX analysis for newly formed bone and native bone, MMA sections were polished and sputtered with gold.

Statistical analysis

Data were represented as mean \pm standard deviation. The significance of differences between the groups for the different printability and mechanical parameters was assessed using a one-way Anova and post hoc Tukey's test (Graphpad prism V8). Differences were considered significant at a probability error (p) of $p < 0.05$.

Results

Extrusion printing of magnesium phosphate-based materials

MgP-based powders substituted with Sr^{2+} ions were thermally synthesized and then milled to achieve particle sizes suitable for extrusion-based printing, *i.e.* between 2-5 μm , (Fig. S1A and B). X-Ray diffraction confirmed the purity of MgP and successful incorporation of Sr^{2+} ions (Fig. S1C). The 3D printed scaffolds composed of MgPSr and PCL were successfully fabricated by extrusion-based printing at room temperature (Fig. 1A). The printability of the MgPSr powder modified with different amounts of PCL polymer was quantitatively assessed via filament collapse and stackability test. The filament sagging angle decreased with less polymer content, which revealed that the decrease of polymer content resulted in a more viscous paste, improving filament printability (Fig. 1B). Furthermore, the filament fusion tests show that a minimum inter-fiber spacing of 0.5-0.8 mm could be achieved for MgPSr-PCL30 (Fig.1B). For the other compositions such as MgSrP-PCL40 and MgSrP-PCL50, an increase in fd was observed for shorter fs distances. A non-linear inverse relation between fs and fd was observed, which is also clear from the meandering printed patterns (Fig. 1B). To further explore the printing flexibility and scalability of this composite material, MgPSr-PCL30 composition was printed in cylindrical and rectangular shapes constructs of different sizes as describe in part 2.2 (Fig. 1C).

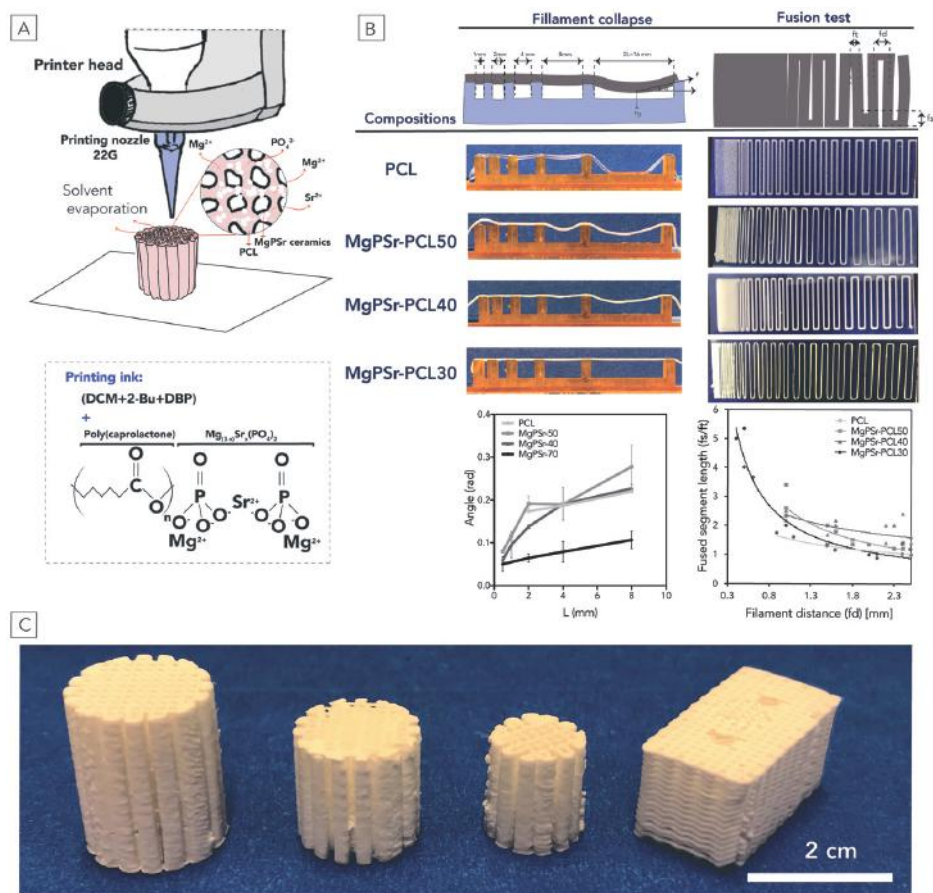


Figure 1. Preparation and printability characterization of the bioactive materials. A) Schematic illustration of the low temperature printing process and the composition of the ink. B) Printability evaluation. Filament test: different compositions extruded over a pillar support with different spacings. Effect of ceramics concentration on the angle of deflection θ , in radians, as a function of half the gap distance L , in mm ($n=3$ for each group). Fusion test: Pictures from stereo microscopy after deposition on the glass slides ($n=3$). The exponential fitting of the fused filament length is normalized by filament thickness as a function of the filament distance for the tested compositions. C) Designed and printed scaffolds with various shapes of MgPSr-PCL30.

Mechanical characterization of 3D printed magnesium-based scaffolds

Addition of a PCL phase overcame the brittleness of MgP ceramics modified with Sr²⁺ ions. All the ceramic-polymer composite scaffolds showed similar stress-strain behavior as the pure PCL scaffolds alone (Fig. 2A, B). The increase of polymer content resulted in a decrease in both elastic modulus and yield stress of the composites. For

instance, the elastic modulus and yield stress increased for MgPSr-PCL30 4.5 and 2.7 times, respectively, when compared to PCL scaffolds alone (Fig. 2C, D) reaching values of 36.8 ± 2.9 MPa and 4.3 ± 0.1 MPa, respectively. Moreover, the determined elastic modulus for MgPSr-PCL30 was 1.5 and 2.3 times higher than those observed for MgPSr-PCL40 and MgPSr-PCL50, respectively. After the addition of 40 and 30 PCL% to the MgPSr ceramic phase, composite scaffolds reached a compressive toughness of 375.5 ± 50.1 kJ/m³ and 324.8 ± 50.0 kJ/m³ respectively (Fig. 2E). Notably, MgP composite scaffolds allowed easy handling and shaping, which is crucial for orthopedic surgeons to allow optimal accommodation of implants to the defect (Fig. S2). This elastic behavior of the composite scaffolds was further evaluated by performing uniaxial tensile tests. MgPSr-PCL30, the composition that allowed a high printing resolution combined with high compressive toughness (324.8 ± 50.0 kJ/m³), was also able to deform up to 10% tensile strain without failure and showed values for tensile yield stress (1.5 ± 0.4 MPa) and toughness (24.8 ± 13.2 kJ/m³) in the range of pure PCL scaffolds^[146]. This elastic behavior was confirmed by evaluating permanent deformation under cyclic compression at 2% deformation. MgPSr-PCL30 composites could resist compressive forces of 0.14 kN over 50 cycles without signs of permanent deformation (hysteresis < 2%) (Fig. 3F, G).

Mechanical characterization of 3D printed magnesium-based scaffolds at rapid scaffold *in vitro* degradation

To assess the mechanical stability of the printed implants after degradation, uniaxial compression tests and morphology analysis were performed over 15 days on MgSrP-PCL30 immersed in PBS and lipase doped PBS (Fig. S3). MgSrP-PCL30 implants showed approximately 25% weight loss when immersed in enzymatic media for 15 days and no significant degradation when immersed in PBS (Fig. S3 A-C). Although a significant decrease in implants stiffness was observed after immersion in lipase doped PBS (Fig. S3 D), implants largely maintained their mechanical compliance (Fig. S3 E-F).

Ion release study

To investigate the effect of polymer masking on ceramic phase exposure, SEM analysis and release of Mg²⁺, PO₄³⁻ and Sr²⁺ ions from MgPSr-PCL30 and MgP-PCL30 scaffolds was investigated in Mili-Q water and Tris-HCl solutions. Both scaffold compositions presented a highly exposed ceramic surface area (Fig. S3A-B) and a sustained ion release over 21 days (Fig. S3C-D). Mg²⁺ and PO₄³⁻ ions released from the MgPSr-PCL30 scaffolds were, respectively, 0.8 and 0.42 times less than those released from the MgP-PCL30 scaffolds after 21 days immersion in Mili-Q water (Fig. S4 C). As expected, release of Mg²⁺ ions was significantly higher in Tris-HCl, a more

physiologically relevant fluid, than in Mili-Q (Fig. S4 C-D). In addition, release of Mg^{2+} ions from the MgPSr-PCL30 scaffolds was approximately 7 times less than from MgP-PCL30, after 21 days immersion in Tris-HCl. Interestingly, no significant difference was observed between the amount of Sr^{2+} and PO_4^{3-} ions released from MgPSr-PCL30 scaffolds in both Mili-Q water and Tris-HCl (Fig. S4 C-D).

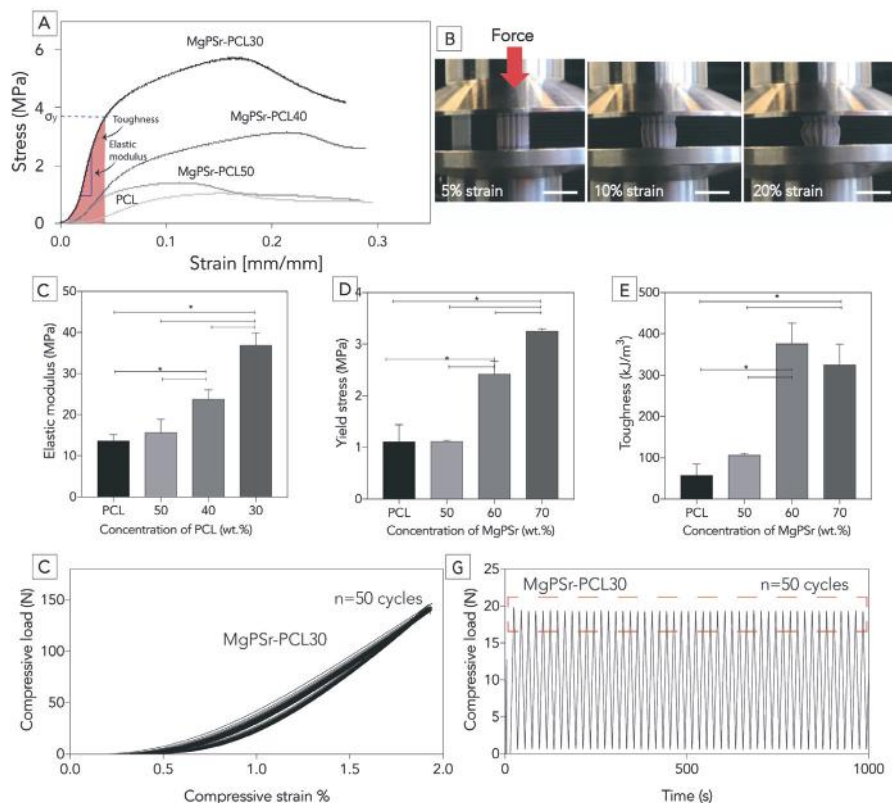


Figure 2. Evaluation of the static and dynamic mechanical properties. A) Longitudinal compression profile of 3D printed scaffolds with various ratios of PCL. B) Corresponding photographs showed the plastic deformation of the scaffolds begins at 10% strain and proceeds to buckle and barrel. Interpreted data (scale bar 10 mm) C) Elastic modulus, D) Yield stress, and E) Toughness from compressive loading profile for various concentrations of PCL. The compression and recovery profile of 3D printed scaffolds (50 cycles) in F) strain domain and G) time domain for MgPSr-PCL30 scaffolds. Additional information on mechanical properties can be found in the Supplementary Information.

Cytocompatibility and osteogenic potential of modified MgP constructs

eMSCs proliferated and grew faster in MgPSr-PCL30 scaffold structures, compared to those based on MgP-PCL30 or PCL alone, as revealed by live-dead staining (Fig. 3A). Quantitative live-dead staining showed that the ratio of live to dead cells after 14 days of *in vitro* culture was 99% for MgPSr-PCL30, which was 1.04 and 1.4 times higher than MgP-PCL30 and PCL alone, respectively (Fig. 3B). Cytocompatibility of the PCL, MgP-PCL30, MgPSr-PCL30 implants was confirmed by additional Alamar blue experiments. Seeded eMSCs remained active during the culture time of 14 days in both basal and osteogenic media (Fig. S5B-C). The morphology of eMSCs on various scaffolds was investigated by scanning electron microscope during 14 days. From SEM images, the spreading and proliferation of the eMCS were confirmed at various timepoints of culturing (Fig. S4A). Furthermore, the effect of Sr²⁺ substitution and polymer modification on MgP osteogenic potential was assessed. ALP activity of the eMSCs cells on PCL, MgP-PCL30 and MgPSr-PCL30 scaffolds was evaluated in osteogenic media (Fig. 3G). After 7 days of culture, the ALP activity for the MgPSr-PCL30 scaffolds was 1.2 and 1.8 times higher than MgP-PCL30 and PCL scaffolds. Also, to assess the osteogenic potential of MgSrP-PCL30 scaffolds, after 7 days of *in vitro* culture the alkaline phosphatase activity (ALP) increased up to 2.4 U.mg⁻¹ DNA for MgPSr-PCL30 in basal media which was substantially higher than for MgP-PCL30 (1.2 U.mg⁻¹ DNA) and PCL scaffolds alone (0.8 U.mg⁻¹ DNA) (Fig. 3C). Furthermore, the alp activity of MgSrP-PCL30 in basal media was 3.7 times more than in osteogenic media.

In the osteogenic media the amount of calcium deposited on the MgPSr-PCL30 scaffolds after 30 days of culturing in osteogenic media was 1.1 and 3.2 times higher than on MgP-PCL30 and PCL scaffolds (Fig. 3H). Alizarin red staining confirmed the osteogenic properties of the MgPSr-PCL30 scaffolds (cultured in basal medium) as the average calcium deposition on MgPSr-PCL30 (277.6 μM) was 1.4 and 11.5 times higher than on MgP-PCL30 and PCL scaffolds, respectively (Fig. 3D). the calcium deposition of the MgSrP-PCL30 in basal media was 1.4 times higher than osteogenic media.

To investigate the chemical composition of newly formed tissue after 30 days culturing MgPSr-PCL30 scaffolds, mineralization of the samples was analyzed using XRD and FTIR in both culture media (Fig. 3E, F, I, and J). XRD analysis showed two hydroxyapatite-related peaks in basal medium for MgPSr-PCL30 which could not be found in the diffraction pattern of MgP-PCL30 or PCL alone (compare to the precultured XRD results) (Fig 3E, D). The FTIR spectra were in line with this observation, as they confirmed the presence of phosphate groups on the mineralized

scaffolds of MgPSr-PCL30 in basal medium. Phosphate groups were also identified in the scaffolds doped with Sr²⁺ ions (Fig. 3F, G).

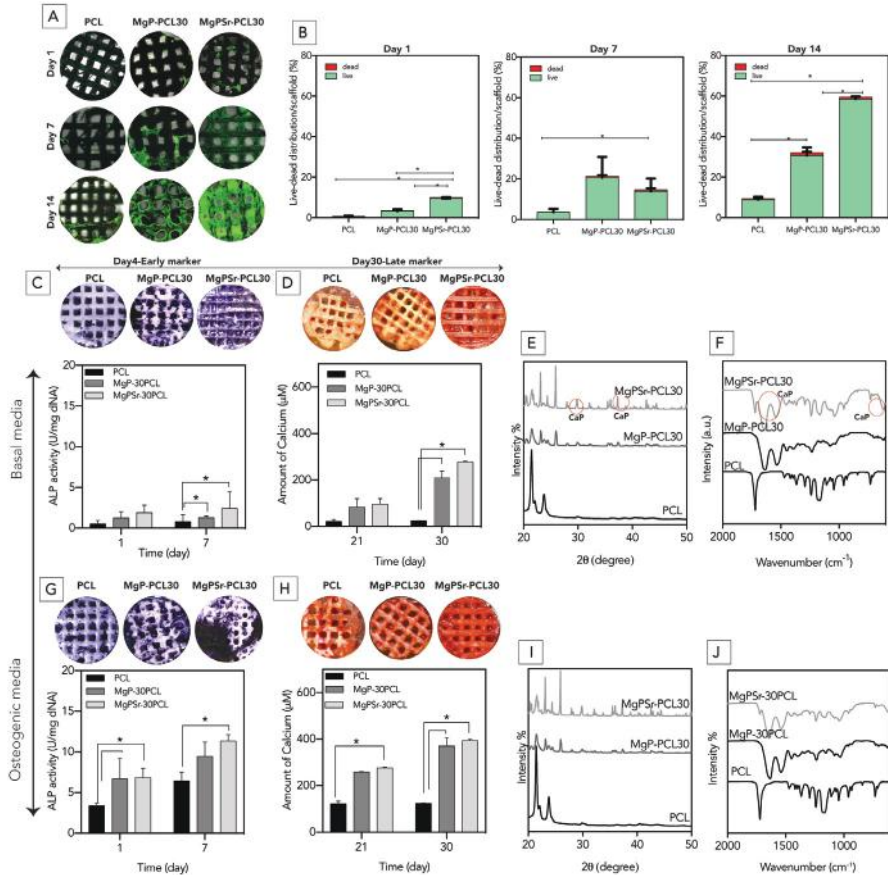


Figure 3. In vitro assessment of bioactivity of the printed scaffolds. A) confocal images from the live-dead staining assay during 14 days culturing of eMSCs in basal media. B) Quantified results of the distribution of live and dead cells per scaffold. C and G) alkaline phosphatase (ALP) images of the printed samples. ALP activity levels were normalized to DNA content. D and H) Formation of calcified matrix by eMSCs investigated using Alizarin Red S staining after 30 days of culture. Quantified amount of calcified matrix evaluated by Alizarin Red S content on the 3D printed scaffolds using a colorimetric assay. Scale bars represent 1 mm. E and I) XRD and F and J) FTIR analysis of the scaffolds after culturing of eMSCs. Peaks corresponding to hydroxyapatite are marked with red circles.

Immunostaining signal for osteonectin and collagen type I was detected in the cells adjacent to the scaffolds (Fig. S6). From the protein staining pictures, it has been clear that the signals of osteonectin proteins increased after 21 days of culturing.

Moreover, the collagen type I is also expressed during the *in vitro* experiment. Moreover, the expression of the proteins in presence of the Mg and Sr ions are significantly more than PCL alone.

***In vivo* behavior of the printed MgPSr composite scaffolds**

MgPSr-PCL30 scaffolds were successfully implanted in the tuber coxae of ponies (Fig. 4A, B, and C). Micro-CT analysis revealed that the defects filled with MgPSr-PCL30 scaffolds contained $12 \pm 2\%$ newly formed bone tissue, against only $2 \pm 1\%$ in empty defects. Bone growth was observed not only at the periphery of the scaffolds but also in its center (Fig. 4D). Measured volumes of the MgPSr-PCL30 scaffolds within the created bone defects showed that $15 \pm 2.7\%$ of the scaffolds were degraded after 6 months of implantation

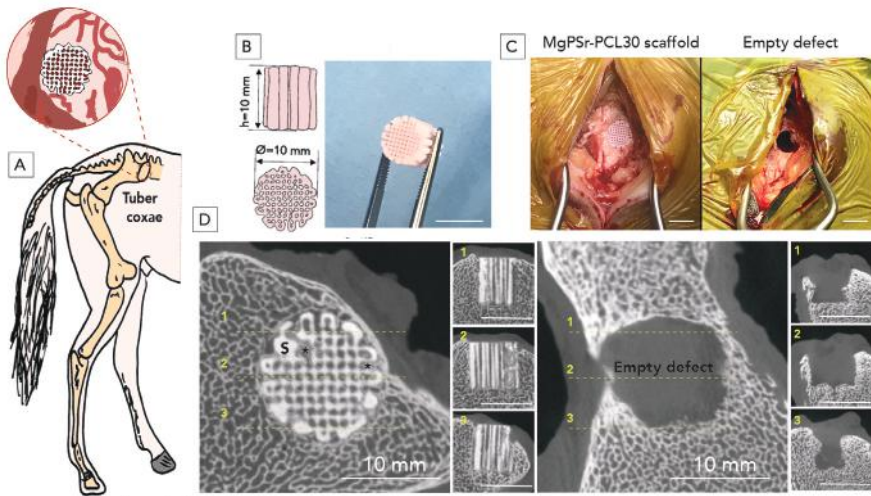


Figure 4. *In vivo* study preparation and implantation. A) Schematic representation of the implantation of cylindrical constructs in the equine tuber coxae. B) Drawing and photograph of the large-size printed implants (10 mm×10 mm). C) Intra operative views of the surgical procedure, showing empty defect and defect filled with construct. D) μ -CT analysis of new bone formation after 6 months. Representative reconstructed images of longitudinal and transverse cross-sections of defects implanted with the MgPSr-PCL30 and empty defect after 6 months *in vivo* (scale bar = 10mm).

Histological analysis by H&E staining confirmed that bone defects filled with MgPSr-PCL30 composites were able to promote new bone formation (Fig. 5A), while in empty defects no new bone growth was observed. Basic fuchsin/methylene blue-stained staining confirmed no signs of local tissue reaction or infections after 6 months of implantation (Fig 5A). Areas with positive staining for collagen type I were located homogenously throughout the scaffolds (Fig. 5A). Polarized light microscopy

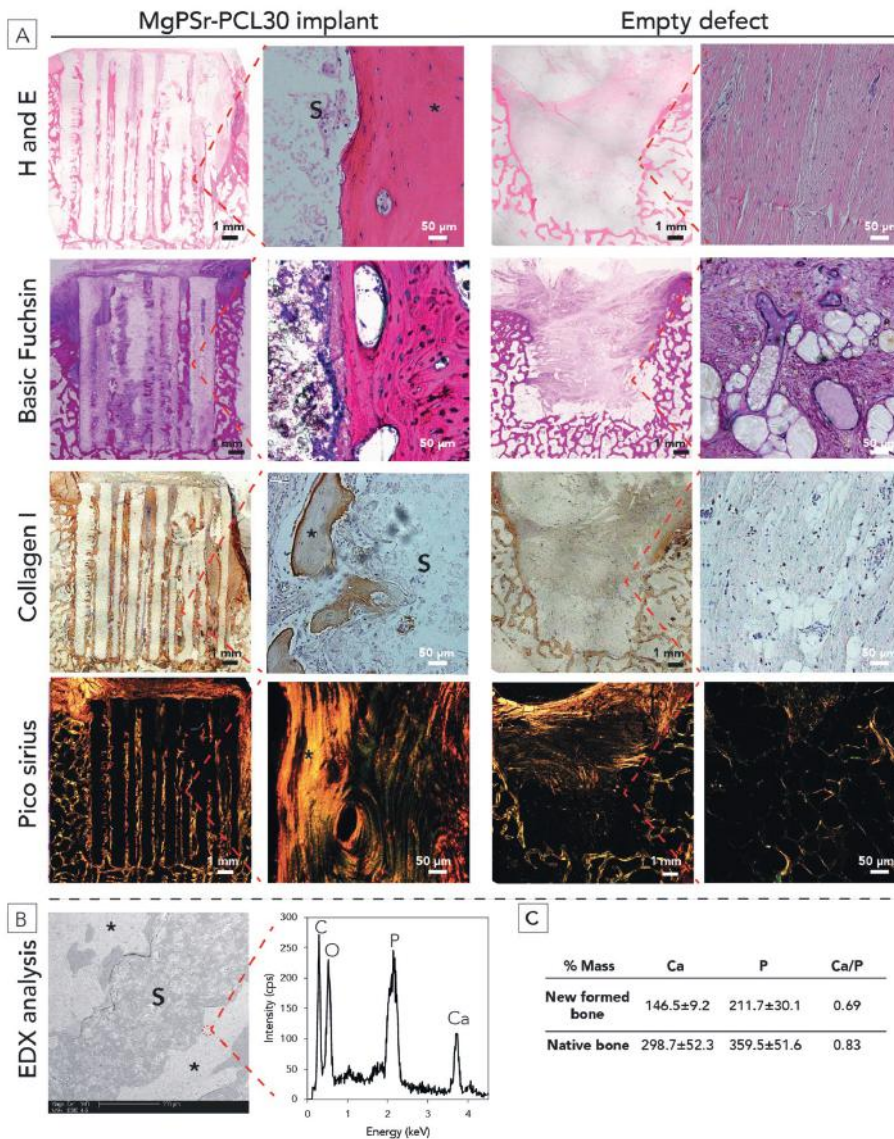


Figure 5. Histology assessment after 6-months *in vivo* study for equine model. A) Histological assessment of new bone (*) within the MgPSr-PCL30 scaffolds after 6 months. Representative hematoxylin and eosin, Basic fuchsin/methylene blue-stained MMA samples, immunohistochemical staining for collagen type I (brown region), and picrosirius red-stained tissue sections of defects filled by MgPSr-PCL30 scaffolds (S) and of empty defects. The scale bar is 50 μ m. B) EDX analysis of newly formed bone. Representative BSE image of newly formed bone adjacent to the scaffold strut. C) Calcium and Phosphorous analysis for newly formed bone and native one.

evaluation of picrosirius red-stained slides showed no significant difference between the collagen orientation in the newly formed bone and the native bone next to the scaffolds (data not shown). Mineralization of the new bone tissue was confirmed by EDX analysis (Fig. 5B). Calcium and phosphorous appeared to be homogeneously distributed (Fig. 5B) in newly formed bone as is the case in native bone (Fig. 5C). Moreover, the calcium to phosphorous ratio is 0.69 and 0.83 for newly formed bone and native bone, respectively.

Discussion

Currently, there is an urgent need to develop patient-tailored implants to repair large bone defects. To this end, solutions must be found that combine optimal bone repair while maintaining mechanical integrity. Herein, we have developed a novel tough and bioactive material, composed of MgPSr and PCL, that can be extruded 3D printed at room temperature. The resultant 3D printed composite implants significantly enhanced the osteogenic response of mesenchymal stem cells without any osteo-inducing factors in the *in vitro* culture media and were capable of effectively repairing a critical sized bone defect, while implanted in equine tuber coxae models for 6 months.

Notably, 3D-printed scaffolds with 30 % PCL content (high viscosity) were readily printable at room temperature. However, when the PCL content increased to 50 % (low viscosity) the 3D printing process became substantially compromised and it was difficult to achieve the needed architectural resolution for bone ingrowth which is in the range of 300 to 900 μm ^[147]. Specifically, with higher polymer content the deposition of extruded filaments was feasible, however, due to rapid solvent evaporation they dried out, thereby losing their shape integrity and bending inwards due to their high elasticity. This of course strongly limits the possibility to print large and complex shaped scaffolds for further down-stream clinical applications. For this reason, we decided to only use 30 % PCL to manufacture the 3D printed scaffolds.

Due to the successful incorporation of a thermoplastic PCL phase into the ceramic MgPSr phase, the resulting composite structures exhibited superior mechanical properties than pure printable ceramic materials (Table S1). The addition of 30 wt.% PCL prevented the occurrence of nucleation of cracks and premature failures during loading, which is an important advantage when using ceramic based materials at load-bearing sites. Importantly, the compressive mechanical properties of the MgPSr-PCL30 composites were in the range of native cancellous bone (Table S1) ^[148,149].

Moreover, since the solvent is still present during printing, the MgPSr-PCL30 struts could be fused at the junctions, which provides strong bonding between the struts. Similar findings have previously been reported for, e.g., PCL-HA printed scaffolds that can slightly merge at the junction of printed filaments resulting in strong bonds between the struts^[150]. To evaluate the elastic properties, accumulation of the defects, and possible permanent deformation of the proposed scaffolds, mechanical properties were tested for over 50 cycles up to 0.2% strain. From the hysteresis loops, it was evident that the accumulated deformation - the shift of the hysteresis loop after 50 cycles - is less than 5 % and no failure was observed. These results indicate that the 3D printed scaffolds are highly durable and thus usable as tough implants. These results are promising, since the physiological strains imposed on human bones during daily activities are less than 0.1% with frequencies ranging from 0.5 to 2 Hz^[151]. In addition, the tensile yield stress and toughness of MgPSr-PCL30 confirmed the compliance of MgPSr-PCL30 implants and their easy shapeability. Unlike the pure MgP ceramic scaffolds (Table S1)^[129,136], the strength, elastic modulus and toughness were significantly higher in both compression and tensile loading. Importantly, even after accelerated *in vitro* degradation, the MgPSr-PCL30 implants were able to maintain their unprecedented compliance and load bearing capacity.

The printability and superior mechanical properties of the MgPSr-PCL30 scaffolds is an important asset, but an often-observed challenge is the blending of osteogenic ceramics with polymers, since some studies have shown that this can result in decreased osteogenic properties of the end-material as the polymers may mask the ceramic phase and compromise the release of osteogenic ions^[152,153]. From the ion release studies, we confirmed that the addition of the polymer phase did not hamper the sustained release of osteogenic ions. In particular, for MgP-PCL30 scaffold, the quantity of the Mg²⁺ ions used during the synthesis was 1.3 times more than MgPSr-PCL30, resulting in a similar difference in release value. Interestingly, the presence of Sr²⁺ in MgP ceramics appears to play a role in stabilizing the MgP structures hindering the release of Mg²⁺ and phosphorous ions in both media. This could be due to Sr²⁺ substituting Mg²⁺ in MgP and thereby inhibiting the release of neighboring^[154-156]. Nevertheless, the eventual overall performance of the scaffolds *in vitro* and *in vivo* and the process of mineralization and repair of bone tissue is greatly influenced by the combined influence of bone minerals, such as Mg²⁺, Sr²⁺, and PO₄²⁻. From the metabolic activity and morphology of the eMSCs, it has been showing that the cells are active during the culturing on all the scaffolds. Moreover, SEM images have shown that the cells are spreading and adhering well on the surface of both MgP-containing scaffolds.

This was also clear from our *in vitro* cell assays as hydroxyapatite precipitation was detected after 21 days of culturing on the MgPSr-PCL30 scaffold, but there is no HA formation for MgP-PCL30. We speculate that the bioactive scaffolds resulted in the release of Mg^{2+} and Sr^{2+} ions due to dissolution of MgP ceramics – something which has been proven earlier to significantly affect cellular response and matrix and mineral deposition^[157,158]. For instance, Mg^{2+} is one of the intracellular divalent cations driving cells into the S-phase and thereby enabling them to proliferate^[135]. However, the clinical use of MgP ceramics is still limited due to the burst release of Mg^{2+} . Such a burst release is linked to an increase in pH value above 7.4, which can comprise the bone formation process^[135]. This can be counteracted by Sr^{2+} release, known to decrease pH and enhance the calcium deposition process^[159]. We hypothesized that cell expression of noncollagenous and collagenous matrix proteins such as osteonectin and collagen type I may be associated with the mineralization process caused by release of Mg^{2+} and Sr^{2+} ions.

We deliberately tested MgPSr-PCL30 scaffolds in a critical size equine model; as rodent and rabbit models are deemed not suited for this application and large animal models are seen as essential to test the feasibility of tissue engineering strategies for regenerating larger bone volumes^[160]. During the bone mineralization process, the organic bone matrix becomes filled with deficient calcium phosphate nanocrystals which the ratio of Ca to P is 0.83 for the native bone. From the EDX analysis, the new inorganic phase containing Ca and P were distinguished around the implants. It represented the osteogenic properties of the MgPSr-PCL30 which induced the formation of CaP phase. Our results suggested that the ratio of Ca/P of the newly formed phase which might be possible to use as a biomarker for the effective calcification criteria is in the same range as native bone. It is well accepted that intrinsic osteoinduction properties occurring in large animal models are closer to the human body compared to small animal models^[161]. Furthermore, since intrinsic osteoinduction is a long-term process, the *in vivo* study lasted 6 months to allow enough time for substantial bone formation. The scaffolds showed the ability to induce bridging of the critical-sized defects *in vivo* and μ -CT analysis indicated that the volume of mineralized tissue in the implanted group was significantly higher than in the empty defects. Additionally, the scaffolds appeared to possess both osteoconductive and osteoinductive properties, being not only able to support bone growth surrounding the implant, but also to bridge the bone defect. There was also a significant invasion of new bone through the scaffold pores from the edges toward the center of the defect.

Conclusion

In conclusion, we have successfully fabricated mechanical robust and osteoregenerative bone implants composed of strontium doped MgP- ceramics combined with medical grade polycaprolactone. We identified a MgPSr / PCL composition that resulted in tough scaffolds and facilitated the osteogenic differentiation of eMSCs. Importantly, the scaffolds demonstrated improved mechanical and biological properties in comparison to pristine PCL. The MgPSr-PCL30 scaffolds, releasing of Mg^{2+} and Sr^{2+} ions, enabled eMSCs to deposit a mature bone-like matrix consisting of differentiated cells and crystalline apatite without being exposed to any additional differentiation conditions. Notably, the printed composite implants facilitated surgical handling and induced the formation of new bone when implanted in equine tuber coxae model for 6 months, without eliciting any negative inflammatory reaction. Overall, our results showed that the addition of PCL and MgP doped with Sr^{2+} ceramics to 3D printed scaffolds could provide a tough scaffolds and viable mechanism to induce bioactivity for bone tissue engineering, respectively.

Supporting information

Table S1. Comparison of the structural and mechanical properties of magnesium phosphate-based scaffolds.

Composition (fabrication method)	Structural properties			Mechanical properties			Ref
	Pore size [μm]	Porosity [%]	Compressive modulus [MPa]	Compressive Strength [MPa]	Tensile modulus [MPa]	Tensile Strength [MPa]	
Magnesium phosphate (3D-printing)	300	-	43	19	-	-	[52]
Strontium modified magnesium phosphate (3D powder printing)	21	15	10	30	10	-	[16]
Magnesium phosphate (3D printing and leaching)	-	30	23.9	3	-	-	[24]
Magnesium-calcium phosphate (leaching)	-	52-78	-	8.6-3.1	-	-	[53]
Magnesium hydrogen phosphate (cement)	-	-	-	10	-	-	[54]
Magnesium phosphate - Calcium sulfate (cement)	-	-	-	12	-	-	[55]
Magnesium phosphate (Microwave assisted)	-	-	200	12	-	-	[56]
Current work	490	40	36.8	4.3	24.8	1.5	-
Trabecular bone	300-600	75-85	120-1100	0.1-16	-	10-20	[57-59]

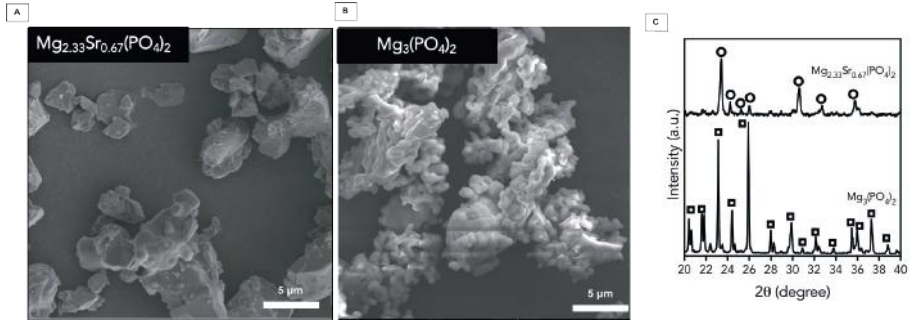


Figure S1. A, B) SEM image and C) X-ray diffraction pattern of MgPSr and MgP ceramics particles after annealing at 1050°C.

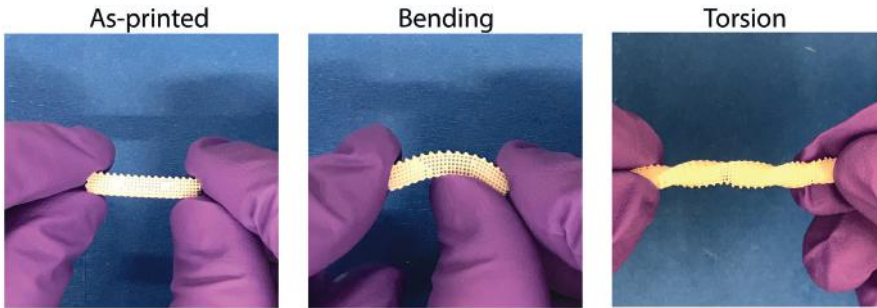


Figure S2. Photograph series of MgPSr-PCL30 scaffold under bending and torsion load.

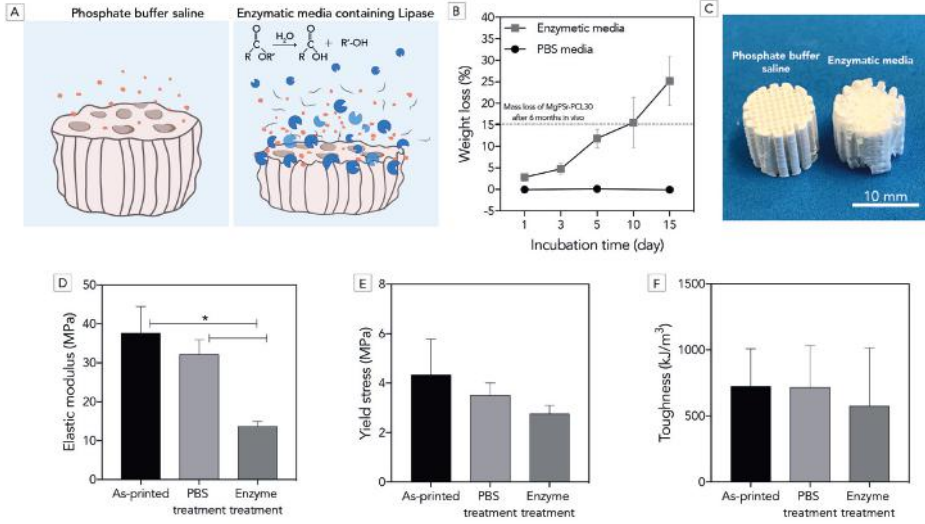


Figure S3. Effect of *in vitro* enzymatic degradation on MgPSr-PCL30 morphological and compressive mechanical properties. A) Schematic figure of MgPSr-PCL30 hydrolysis in PBS and in lipase doped PBS. B) Weight loss of MgPSr-PCL30 implants in PBS and in lipase doped PBS over 15 days. C) Representative images of MgPSr-PCL30 implants after 15 days incubation in lipase doped PBS incubation. Quantification of D) elastic modulus, E) yield stress, and F) toughness of the implants as printed and after 15 days incubation in PBS and in lipase doped PBS incubation.

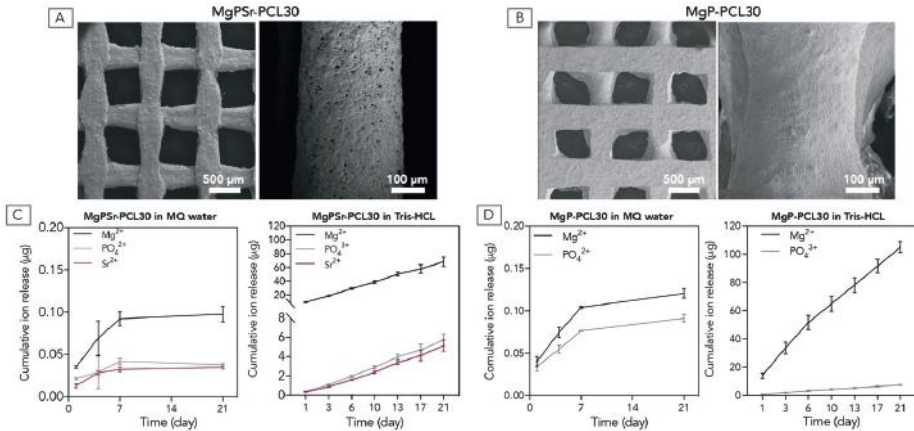


Figure S4. A and B) representative SEM images of MgPSr-PCL30 and MgP-PCL30, respectively. Ion release from 3D printed MgPSr-PCL30 and MgP-PCL30 scaffolds after immersion in C) Mili-Q water and D) Tris-HCL, respectively. Ion concentrations of Mg²⁺, PO₄³⁻ and Sr²⁺ were measured in supernatants by means of ICP-MS.

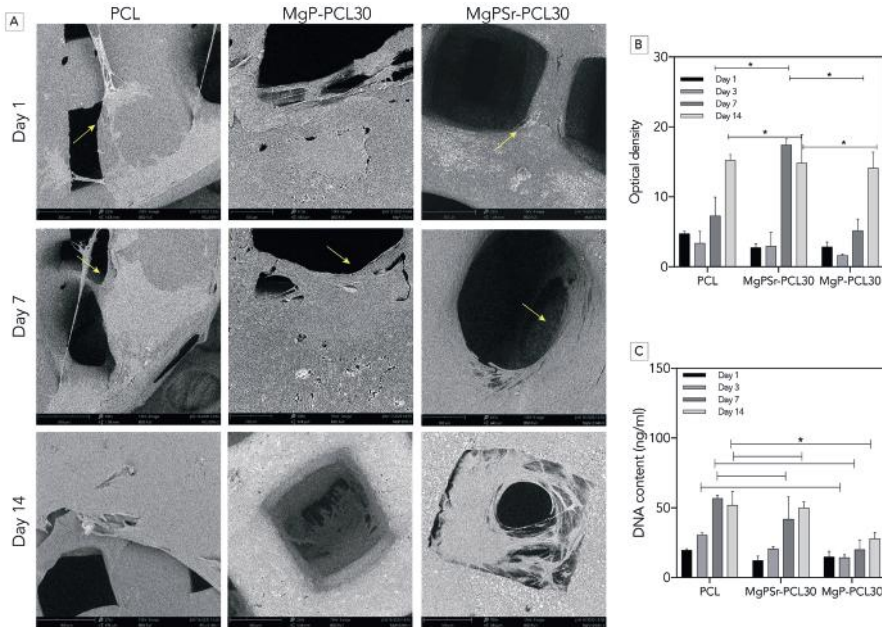


Figure S5. Cytocompatibility of 3D printed materials. A) Representative SEM images of cell attachment to 3DP implants when cultured in basal media. Metabolic activity normalized to DNA at day 1, 7 and 14 of 3D printed constructs cultured in B) basal medium and C) osteogenic.

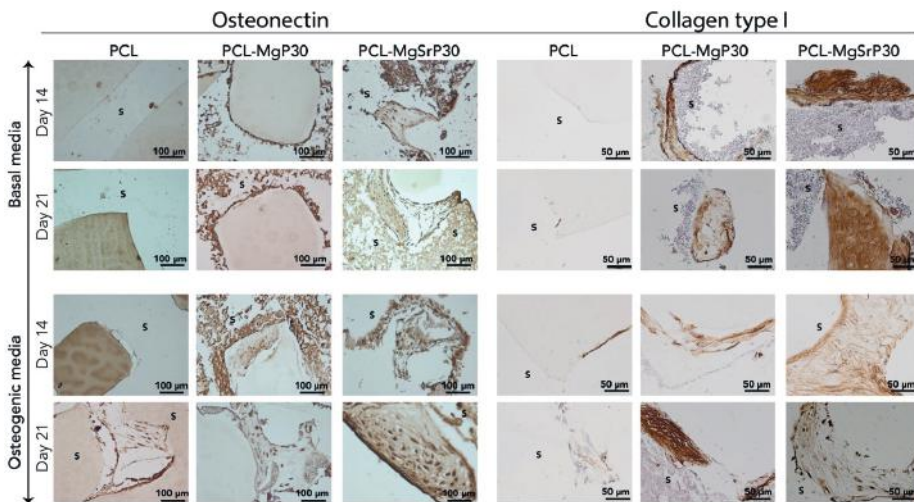
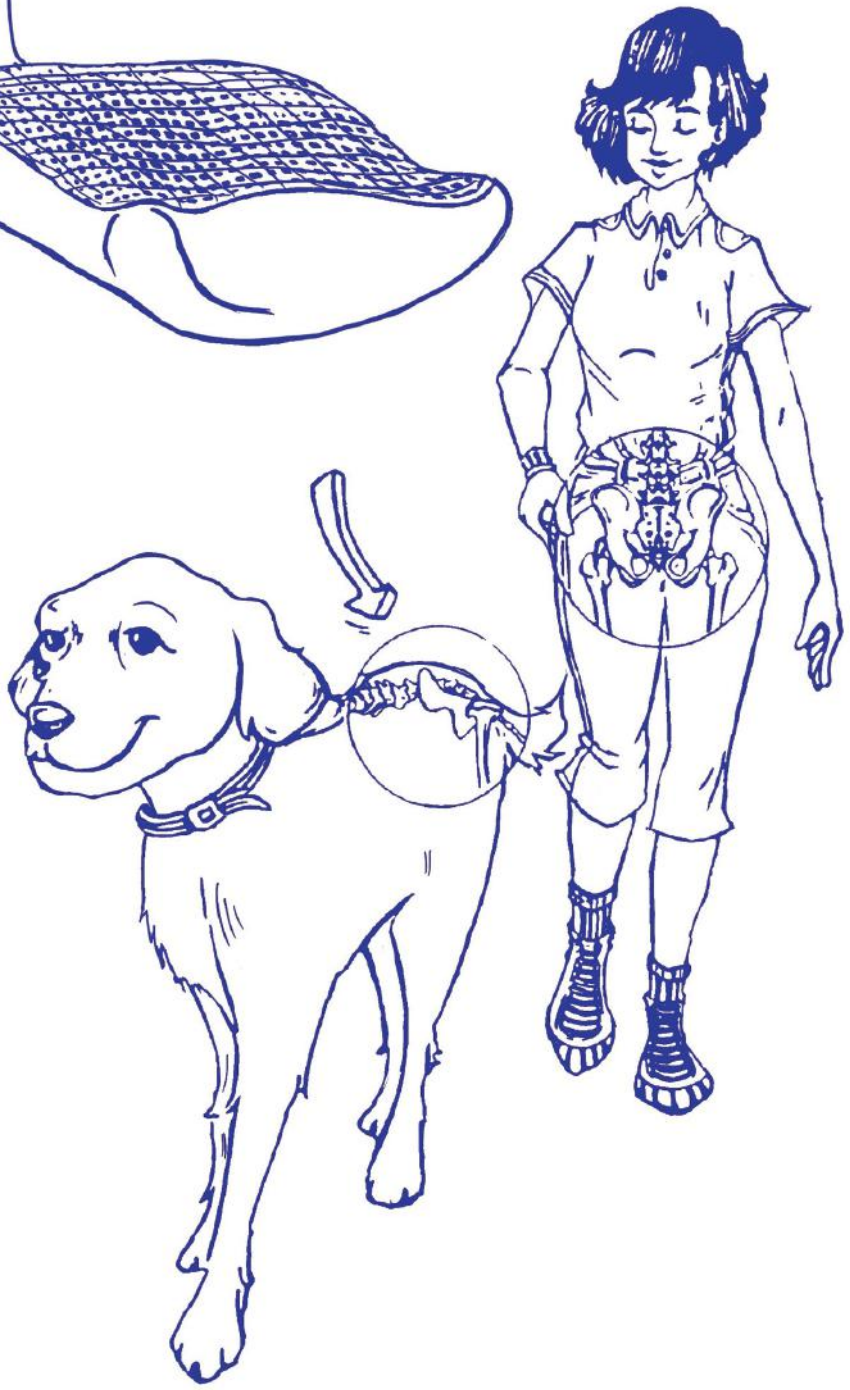
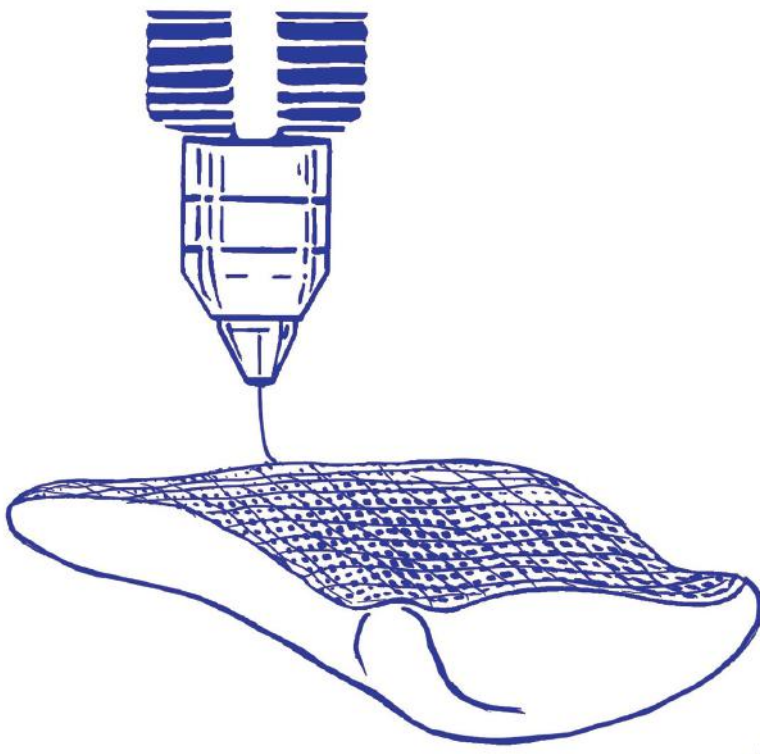


Figure S6. osteonectin, and collagen type I staining of decalcified sections of MgP-based scaffold after 14 and 21 days of *in vitro* experiment in basal and osteogenic medium (S represents the site of the scaffolds).



CHAPTER 4

3D-printed regenerative magnesium phosphate implant ensures stability and restoration of hip dysplasia

Nasim Golafshan

Koen Willemsen

Firoz Babu Kadumudi

Elke Vorndran

Alireza Dolatshahi-Pirouz

Harrie Weinans

Bart C.H. van der Wal

Jos Malda

Miguel Castilho

Published in **Advanced Healthcare Materials**

DOI: 10.1002/adhm.202101051

Awarded by Mimics Innovation program of 2022

Abstract

Osteoarthritis of the hip is a painful and debilitating condition commonly occurring in humans and dogs. One of the main causes that leads to hip osteoarthritis is hip dysplasia. Although the current surgical methods to correct dysplasia work satisfactorily in many circumstances, there are associated with serious complications, tissue resorption and degeneration. In this study, we report a one-step fabrication of a regenerative hip implant with a patient-specific design and load-bearing properties. The regenerative hip implant was fabricated based on patient imaging files and by an extrusion assisted three-dimensional printing process using a flexible, bone-inducing biomaterial. The novel implant could be fixed with metallic screws to host bone and loaded up to physiological loads without signs of critical permanent deformation or failure. Moreover, after exposing the hip implant to accelerated *in vitro* degradation, we confirmed it was still able to support physiological loads even after losing approximately 40% of its initial mass. In addition, we demonstrated the osteopromotive properties of the novel hip implant as shown by an increase expression of osteonectin and osteocalcin by cultured human mesenchymal stem cells after 21 days. Overall, the proposed hip implant provides an innovative regenerative and mechanically stable solution for hip dysplasia treatment.

Keywords

3D printing, bone implants, bone regeneration, hip dysplasia, load bearing, patient-specific implant

Introduction

Osteoarthritis (OA) of the hip is a painful and debilitating condition that affects over 40 million people just in Europe ^[170,171]. One of the main causes for hip OA is hip dysplasia (HD), which is an instability of the hip joint ^[172]. This instability is caused by incomplete coverage of the femoral hip by the acetabulum ^[9,173] and is commonly observed in humans, including children, as well as in veterinary patients, mainly dogs ^[174]. The incorrect alignment of the hip joint in HD results in overload of the joint edges with subsequent degenerative changes of the cartilage and the acetabular labrum at a young age, leading ultimately to the development of osteoarthritis. Most HDs resolves without treatment or after bracing at early childhood ^[175]. If HD remains during puberty, a very high risk of osteoarthritis results and often surgical treatment is required to correct the dysplasia by *e.g.*, re-alignment of the hip socket (osteotomy) or the insertion of a bone graft (shelf arthroplasty) to enlarge the acetabular rim ^[176]. Osteotomies are technically demanding and invasive surgical procedures with associated complications, typically related to risk of nerve damage, inappropriate orientation of the acetabulum and extensive rehabilitation periods ^[177,178]. On the other hand, shelf arthroplasty is a less complex surgical procedure, but requires the use of bone grafts typically harvested from the patient's iliac crest, which can result in donor site morbidity ^[179]. Moreover, the success rate of this procedure is relatively low, about 40 to 60%, due to the challenges in shaping and positioning of the bone graft to the defect size with associated accelerated graft resorption or impingement of the femoral head ^[180]. There is thus, an urgent need for less invasive treatments that can overcome the drawbacks of the state-of-the-art procedures and subsequently ensure a near-perfect fit, facilitating optimal integration and durable restoration of the hip socket.

Progress in Additive Manufacturing (AM) techniques has provided new possibilities for the fabrication of individually shaped orthopedic implants. In particular, fabrication of titanium-based implants using a direct metal printing process has shown to generate personalized implants to treat hip dysplasia with a perfect repair of the bony defect and fit to the bone. Such a procedure can overcome the need for an osteotomy or shelf arthroplasty procedure. However, the use of metallic implants cannot ensure complete integration with native bone due to their non-resorbable properties and the implants may be associated with infection or loosening. In addition, the use of non-resorbable implants is not preferred for the treatment of younger (pediatric) patients due to mismatch of the implant size after patient growth.

Here, we developed a regenerative, yet stable, patient-specific bone implant for the treatment of hip dysplasia. The external and internal architecture of the implant was rationally designed to increase femoral coverage and mechanical stability. To manufacture the implant, a flexible and bone-inducing biomaterial ink, based on a magnesium phosphate (MgP) composite material^[181], was extruded using an extrusion based three-dimensional printing (3D) process and sacrificial support material. After implant fabrication, the effect of the internal structure on mechanical stability and fixation to host bone was extensively investigated by three-point flexure and compression mechanical testing. To confirm the biocompatibility and osteopromotive properties of the biomaterial, printed constructs were *in vitro* cultured over 21 days using human mesenchymal stem cells. Finally, to anticipate the *in-vivo* mechanical performance of the resorbable implant, implants were loaded under physiological loading conditions using a custom-built bioreactor system and after exposed to accelerated *in vitro* enzymatic degradation.

Materials and methods

Preparation of the MgP biomaterial ink

Printable biomaterial ink was prepared by combining $\text{Mg}_{2.33}\text{Sr}_{0.67}(\text{PO}_4)_2$ powder and commercial medical grade poly (ϵ - caprolactone) (mPCL, Purasorb PC 12, Purac Biomaterials, Netherlands) in weight ratios of 70:30 wt.% of MgPSr to PCL, according to a procedure previously described^[181]. Briefly, the ceramic component was synthesized by sintering (1050°C, 5 hours) a mixture of 0.6 mol magnesium hydrogen phosphate ($\text{MgHPO}_4 \cdot 3\text{H}_2\text{O}$, Sigma-Aldrich, Steinheim, Germany), 0.1 mol magnesium hydroxide ($\text{Mg}(\text{OH})_2$, VWR International GmbH, Darmstadt, Germany), and 0.2 mol strontium carbonate (SrCO_3 , Sigma-Aldrich, Steinheim, Germany). The sintered cake was manually crushed with pestle and mortar followed by wet grinding for 2 hours in pure ethanol in a planetary ball mill (250 U/min) using 200 agate balls. Afterwards, the cement powder was dried at room temperature. Then the MgPSr powder and mPCL were dispersed in a mixture of high volatile solvents (dichloromethane (Sigma-Aldrich, Germany), 2-BU-1-(4- (diethylamino) anilino)-3-me-pyrido(1,2-a) benzimidazole - 4 - carbonitrile (Sigma-Aldrich, Germany), and dibutyl phthalate (Sigma-Aldrich, Germany) in a ratio of 10:2:1 wt.%, at the concentration of 90 wt.% of solid material in solvent. After dispersion, the composite paste was left homogenizing for approximately 4 days on a roller mixer at room temperature before printing.

Biomaterial ink printability was first accessed according to a protocol described elsewhere ^[181]. Briefly, a one-layer triangular shaped structure with a fill-in pattern of straight lines at increasing interfilament spacings, from 0.5 mm to 1 mm, was printed. Then, the length of fused filament (f_s), at each filament distance (f_d), was quantified. F_s was normalized by the average of filament thickness (f_t). Moreover, to evaluate effect of filament stacking on printing resolution, rectangular shaped scaffolds (10 mm x 20 mm x 4 mm) with three different interfibre spacings were printed. As a measure of scaffolds printing accuracy, open pore ratio was quantified by,

$$\text{Open pore ratio} = \frac{At - Aa}{At} \quad \text{Eq 1}$$

where, A_t and A_a are a theoretical and actual pore areas, respectively. Open ratio varies between 0 (open) and 1 (close). All measurements were performed with Image J.

Design and extrusion-based 3D printing of implants

To design the hip implants, three cadaveric dogs (6 hips) were CT scanned (Siemens SOMATOM Definition AS, Siemens, Healthcare) with the following standardized parameters, 120kV, 250mAs, and 0.6 mm slice thickness. The segmentation was done semi-automatically using standardized bone threshold values (HU 226 – upper boundary) using an imaging processing software, Mimics Medical 21.0 (Medical v21.0, Materialise, Leuven, Belgium). The implant's rim was designed in 3-Matic software (Medical v12.0, Materialise, Leuven, Belgium) to add 30 degrees of coverage to the dysplastic acetabular rim without interfering with the hip capsule or muscles (e.g. Rectus Femoris) when using the standard dorsolateral approach to the hip joint. Additionally, the external implant was designed to provide adequate scaffold material (average thickness, 4 mm) and surface area to fixate the implant to the pelvis with bone screws.

After assessment of the implant external geometry, BioCAM™ software was used to define the hip implant internal architecture and subsequently translate the design into a G-Code. The external region of the implant (shell) was kept closed while for the internal region (core) of the implant two inter-fibre spacings, 1 mm and 0.7 mm (abbreviated as IFS-1 and IFS-0.7, respectively) were considered (Figure S2). Designed implants were fabricated by a multi-material extrusion-based 3D-printing system (3D Discovery, regenHU, Switzerland) using the MgPSr-PCL biomaterial ink. The ink was transferred to a 10 mL syringe (Nordson EFD, USA) and extruded through a 22G conical nozzle, (diameter = 0.41 mm, Nordson EFD, USA) at pressure of 0.9 bar and collector speed of 6 mm/s. For the fabrication of the anatomically shaped hip implants, a supporting material, 40 wt.% of poloxamer (Pluronic® F-127,

Sigma-Aldrich, Germany) was used. Poloxamer ink was dissolved for 24 hours at 4°C transferred to 10 ml syringe and extruded printed through a 27G conical nozzle (diameter = 0.2 mm) at room temperature. After the printing process using the poloxamer and biomaterial ink, the scaffolds were immersed in cold water for 3 hours to remove the support material.

Physical and chemical characterization

Pore size and porosity was analyzed by micro-computed tomography (micro-CT) analysis was used. Micro-CT was performed using a Quantum FX-Perkin Elmer (μ CT, Quantum FX, PerkinElmer, USA). Hip implants were scanned at 90 kV tube voltage, 180 mA tube current, 30 μ m resolution and 3 minutes scan time. Volume fraction and respective porosity of IFS-1 and IFS-0.7 was determined by measuring trabecular parameters in 3D μ CT images according to a protocol described previously^[181]. Briefly, the 3D scans of the implants were adjusted based on Bernsen thresholding method using ImageJ software. Next, the volume fraction (BV/TV) was measured with BoneJ plugin for a specific region of interest (ROI) and porosity (Φ) was determined as

$$\Phi = 1 - \frac{BV}{TV} \quad \text{Eq 2}$$

Moreover, the printing deviation of the prepared implants was quantified as,

$$\text{Printing deviation} = \frac{V_p}{V_{cs}} \quad \text{Eq 3}$$

where V_p and V_{cs} represent volume of the printed implants (based on the micro-CT images) and CAD designed implants, respectively. The volumes were measured with Meshlab (v.2016). In addition, the phase composition of printed implants was analyzed by X-ray diffraction using monochromatic Cu-K α radiation was utilized. X-ray measurements were collected from $2\theta = 10^\circ - 40^\circ$ with a step size of 0.02° . The inorganic phase composition of MgPSr was checked by reference patterns of the ICDD database (magnesium strontium phosphate, $Mg_2Sr(PO_4)_2$, PDF ref. 00-014-0206, $Mg(H_2PO_4) \cdot 2H_2O$, PDF ref. 00-39-0132, and $Mg(H_2PO_4) \cdot 4H_2O$, PDF ref. 01-075-1445).

3D printed implant microstructure and elemental composition was analyzed by Scanning Electron Microscope (SEM; XL30SFEG, FEI, USA) and Energy-Dispersive X-ray (EDX; Bruker AXS, Germany), respectively. Prior to imaging, samples were coated with gold (thickness = 6 nm). Both SEM and EDX were performed at an acceleration voltage of 10 kV.

Rheological evaluation of MgPSr-PCL ink was performed on a rheometer (Discovery HR-2, TA instruments). Biomaterial ink was placed between parallel plates (20 mm in diameter) at a gap distance of 0.5 mm. Viscosity was recorded during an oscillatory shear rate sweep test (10 - 100 s⁻¹). Density of MgPSr-PCL ink was calculated based on the mass of a unit volume of the ink.

Three-point flexural tests

Three-point flexural tests were performed in a universal mechanical testing device (Instron, Model 5967, UK) with a 1kN load cell. For both designs (IFS-1 and IFS-0.7), rectangular bars (6'1' 0.5 cm) were printed with printing parameters described in section 2.2 and loaded at a cross head speed of 2 mm.min⁻¹, with support and loading span at 40 mm and 20 mm, respectively, according to a protocol previously described [182]. The flexural stress, strain, modulus and strain energy were calculated according to the classic beam theory considering a linear elastic material behavior. In particular, flexural stress was estimated as,

$$\sigma_f = \frac{3P_{max}L}{2bh^2} \quad \text{Eq 4}$$

where P_{max} is the maximum load on the beam, L is the length of the support span, and b and h are the width and thickness, respectively. Flexural strain (at P_{max}) was calculated as,

$$\varepsilon_f = \frac{6b\delta}{L^2} \quad \text{Eq 5}$$

where δ is the beam deflection under P_{max} at the midspan. The flexural elastic modulus was determined from the load-displacement curve as,

$$E_f = \frac{FL^3}{4b\delta h^3} \quad \text{Eq 6}$$

where F/δ the tangent of the initial straight-line (linear) portion of the load-displacement curve. Moreover, the strain energy (U) was determined by the area below the load-displacement curve until maximum peak load (P_{max}). At least five samples for each group were tested.

Implant fixation

To study the effect of initial implant fixation to the host bone, rectangular shaped implants (2'1' 0.4 cm) for both IFS-1 and IFS-0.7 internal architectures were fixed to rectangular shaped saw-bone blocks (2'1' 1 cm) using cortical screws (diameter = 3.5 mm) and loaded in shear with a customized loading device. A cross head speed

of 2 mm.min⁻¹ was applied until a maximum shear force of 100 N and 200 N was reached. At each maximum shear force, loading was repeated for 5 consecutive cycles to investigate the capacity of the material to recover. The applied load and deformation were monitored and the dissipated energy (U_d) after unloading at 1st and 5th cycle was quantified as

$$U_d = \int_0^{\delta u} F_t(\delta) d\delta - \int_{\delta 0}^{\delta u} F_e(\delta) d\delta \quad \text{Eq 7}$$

where $F_t(\delta)$ and $F_e(\delta)$ are the loading function and the unloading function, respectively. δu is the total strain at the unloading point, and $\delta 0$ is the permanent strain after unloading. To further investigate permanent deformation of the tested samples the area of the screw fixation holes, before and after loading, was quantified by micro-CT analysis. Shape of the fixation holes before loading was approximated as a circle of unit radius, and after loading as an ellipsoid. The deformed shape of ellipse (R) was quantified as,

$$R = (1 + \epsilon_1) / (1 + \epsilon_3) \quad \text{Eq 8}$$

where ϵ_1 and ϵ_3 represents deformation along X and Y axes (minor and major axis of the ellipse). At least, five samples for each group were tested.

***In vitro* degradation experiments**

The effect of enzymatically induced degradation of the implant material was evaluated *in vitro* over 15 days, with intermediate time points 1, 5, 10 and 15 days, following a protocol described elsewhere^[181]. Rectangular shaped samples (4'1'0.5 cm) were incubated in a 0.4 mg/ml lipase solution (from *Pseudomonas cepacian*, Sigma-Aldrich, Germany) and 1 mg/ml sodium azide (Sigma-Aldrich, Germany) at 37°C. Incubation medium was refreshed every 4 days. At each intermediate time point samples were washed generously with mili-Q water and kept in the desiccator until 48 hours prior mechanical testing and weight assessment. Subsequently, the effect of *in vitro* degradation on material mechanical performance was evaluated by flexural properties under three-point flexural testing, following the protocol described previously in section 2.4. In addition, weight loss of the implants and pH of the incubation solution were monitored at each intermediate time. Finally, the cumulative ion release profile of magnesium and strontium ions was recorded utilizing Inductively Coupled Plasma Mass Spectrometry (ICP-MS, Varian, Darmstadt, Germany) at each incubation time point.

***In vitro* cell culture**

To confirm the cytotoxicity and osteogenic potential of the bone-inducing implants, MgPSr-PCL and plain PCL cylindrical samples (diameter = 5 mm and height = 1 mm) with an internal architecture of IFS-0.7 were prepared and cultured *in vitro* with human mesenchymal stem cells (hMSCs, passage number 3) for 21 days. Samples were sterilized in 70 v/v% ethanol for 2 hours followed by 30 min under ultraviolet (UV) light. hMSCs were first expanded for 7 days in α -MEM supplemented with 10% (v/v) fetal bovine serum (FBS), 0.2 mM L-ascorbic-acid-2-phosphate (ASAP), and 1% (v/v) penicillin-streptomycin at 37 °C in a humidified atmosphere containing 5% CO₂, and then seeded (passage number 4) onto implants at a density of 150,000 cells per cm². After seeding hMSCs onto implants, constructs were cultured in basal media.

hMSCs viability was determined using a live-dead viability kit for mammalian cells (Invitrogen Life Technologies, USA), prepared according to the manufacturer's instructions. Stained cell-laden constructs were imaged using a confocal microscope (Leica SP8X Laser Scanning, Germany) with 494 nm (green, Calcein) and 528 nm (red, EthD-1) excitation filters. In addition, cell metabolic activity was quantified by Alamar blue, following manufacturer's instruction. Moreover, hMSCs osteogenic differentiation was measured using alkaline phosphatase (ALP) analysis performed at day 1 and 7 of *in vitro* culture, following a protocol described elsewhere^[181]. Briefly, ALP activity was measured using conversion of the p-nitrophenyl phosphate liquid substrate system (pNPP, Sigma-Aldrich) and a serial dilution of calf intestinal ALP (Sigma-Aldrich, Germany) in TE-buffer. ALP results were normalized to DNA content from the same cell lysate used to measure ALP, using a Quan-iT-Picogreen-dsDNA kit (Molecular Probes, Invitrogen, Carlsbad, USA) following the manufacturer's instructions. In addition, ALP staining of hMSCs was assessed by utilizing a BCIP/NBT (5-Bromo-4-chloro-3-indolyl phosphate/Nitro blue tetrazolium, ThermoScientific, USA) solution. At least 3 samples were analyzed per group, i.e. MgPSr-PCL and plain PCL cylindrical samples.

The implants and attached hMSCs were fixed 30 min in formalin to prepare for osteonectin and osteocalcin immunocytochemistry. Then the cell-laden implants constructs were incubated for 10 min in 0.2% (v/v) Triton X-100 in PBS, and thereafter blocked for 30 min with 5% (v/v) bovine serum albumin/PBS. The samples were incubated overnight at 4°C with 10 mg/mL rabbit monoclonal anti-SPARC antibody (osteonectin, ab225716) and mouse monoclonal antibody recognizing human osteocalcin (clone OCG4; Enzo Life Sciences), respectively. This was followed by incubation with 10 mg/mL goat-anti-mouse polyclonal antibody conjugated to Alexa Fluor 488 (Invitrogen). All cell-laden implants were also stained for F-actin (TRITC) and

DAPI (FAK100 Kit; Merck Millipore), according to the manufacturer's protocol. All other fluorescence images were taken with a Leica SP8X Laser Scanning Confocal Microscope using a white light laser (470–670 nm) and Leica LASX acquisition software.

Ex vivo biomechano-reactor studies

To investigate the mechanical performance of hip implants under representative physiological loading conditions, hip implants (IFS-0.7 group) were mounted on an *ex-vivo* macerated dog pelvis before and after accelerated *in vitro* degradation (15 days). The pelvis was embedded in epoxy resin (poly-pox THV 500, Poly-Service B.V. Amsterdam, the Netherlands) to facilitate implant loading. The implants are placed in their correct surgical position to repair the acetabular defect and mechanically loaded in Y direction to mimick normal gait of the canine.

using a universal mechanical testing device (Instron, Model 5967, UK) equipped with a 1kN load cell. Implants were loaded at a compressive speed of 5 mm/min until implant (or pelvis) failure was reached. From the load-displacement curves different mechanical parameters were determined, in particular the load at failure (defined as the maximum load before implant failure), the strain energy (determined as detailed in section 2.5) and the stiffness (as the slope of the load-displacement curves between 2 mm to 3 mm deformation). A minimum batch of 3 samples before and after 15 days of *in vitro* degradation was tested.

Statistical analysis

A one- or two-way ANOVA with post-hoc Tukey's test was performed to compare the means of the different groups. Only for the pore size and porosity, normality and homogeneity were first checked with Kolmogorov-Smirnov test and then means of the groups were compared with an independent t-test. Differences were considered significant at a probability error (p) of $p < 0.05$. Data was represented as mean \pm standard deviation (SD) and at least 3 samples were evaluated for each test. All statistical analysis was performed using GraphPad prism V6.

Results

Extrusion 3D printing of anatomically shaped hip implants

Based on imaging data, the external implant design was adapted to provide adequate attachment to the pelvis and to provide the largest acetabular extension without impairing the range of motion of the femur (Figure 1A-C). Before being finalized for 3D printing, the anatomically designed hip implant was confirmed to not

induce femoroacetabular impingement and to ensure a perfect fit to the hip socket. Further, to allow for the fabrication of the implant's complex anatomical shape, we combined extrusion printing of a poloxamer hydrogel as a support material with extrusion of a MgPSr-PCL biomaterial ink in a single printing process using a printer set-up equipped with two printheads (Figure 1D). Both viscosity and density of the biomaterial ink were evaluated to ensure ink extrusion reproducibility. MgPSr-PCL showed a viscosity of approximately 27.5 Pa.s (Figure S1) and a density of 1.7 gr/ml.

Moreover, the implant's structure encompassed different architectures at the external and internal region of the implant (Figure 1E). The external region is made of a fully dense layer and the internal region is made of a porous region with an inter-fibre spacing of 1 mm and 0.7 mm (IFS-0.7 and IFS-1) (Figure 1F, G). These two inter-fibre spacings were investigated for optimal mechanical stability and have been selected based on best compromise between biomaterial ink printing accuracy and porosity (Figure S2). We observed that independent of the internal architecture considered, the printed external architecture resembled well the CAD designed counterpart (Figure 2 H, I). In addition, a final pore size of $606 \pm 108 \mu\text{m}$ and $319 \pm 57 \mu\text{m}$ was observed for IFS-1 and IFS-0.7 hip implants (Figure 1J), respectively. This resulted in a residual printing deviation from the CAD design for both internal architectures. Moreover, the final porosities of the IFS-1 and IFS-0.7 hip implants were observed to be $54.7 \pm 2.6 \%$ and $46.1 \pm 1.2 \%$, respectively (Figure 1K).

Subsequently, X-ray diffraction analysis confirmed the presence of an MgPSr inorganic phase and PCL organic phase on the printed implants (Figure 1L). Notably, SEM analysis on the implant microstructure showed that the ceramic phase was highly exposed and not masked by the PCL phase (Figure 1M, Figure S3A). This was also confirmed by elemental analysis, which revealed the presence of Mg, P, and Sr ions at the surface of the 3D-printed hip implants (Figure 1N, Figure S3B).

Effect of internal architecture on implant three-point flexural properties

In order to evaluate the internal porosity on the mechanical performance of the generated implants, three-point bending tests were performed. Both IFS-1 and IFS-0.7 implant structures presented similar load-displacement behavior. Load-displacement curves started with a steep slope in the elastic region, followed by an inflexion point after the yield until maximum force was reached. Afterwards, the force decreased substantially and plateau after failure (Figure 2A). As expected, implant fractures were observed to occur in the regions that experienced high tensile stresses (Figure 2B, red arrow), and interestingly were observed to initiate at similar displacements for both

implant porosities. The maximum flexural stress and flexural elastic modulus of the IFS-0.7 implant were approximately 1.6 and 2.2 times higher than for the IFS-1 implant (Figure 2C-D), respectively. However, no significant differences were observed in flexure strain between both internal architectures (Figure 2E). In addition, the strain energy was 1.4 times higher for IFS-0.7 implants than for IFS-1 implants (Figure 2F).

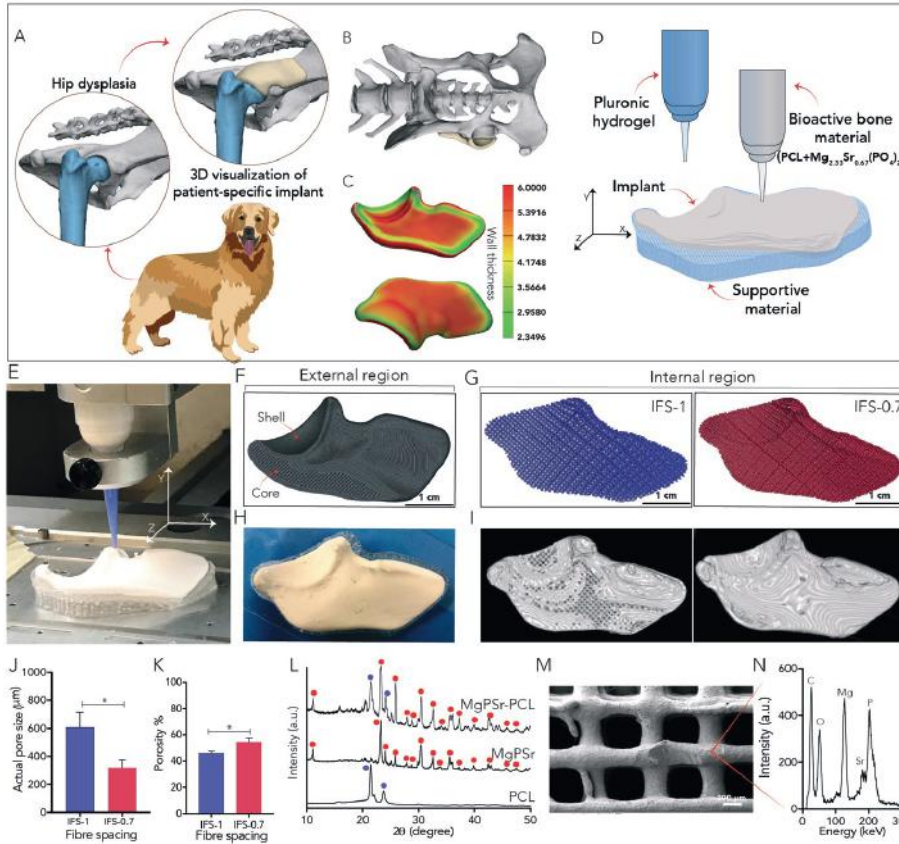


Figure 1. Design, fabrication and respective printing accuracy and compositional analysis of the developed hip implants. A) Schematic illustration of the hip dysplasia in a canine model. B) CAD design of anatomically shaped implant based of patient image data. C) The wall thickness of the designed hip implants. D) Schematic illustration of extrusion 3D printing using a bone-inducing biomaterial ink and support material. E) Room-temperature extrusion-based printing process showing support material (transparent) and hip implant (white). F) Hip implant external and internal architecture, where G) internal architecture encompassed two inter-fibre spacings: 1 mm (IFS-1) and 0.7 mm (IFS-0.7). H) Representative image printed hip implant shell region. I) 3D reconstructed micro-CT images of hip implants with IFS-1 and IFS-0.7 core region. J) Printed pore size for IFS-1 and IFS-0.7 and respective K) porosity (significant differences were analyzed by t-test, n=3 and *p<0.05). L) X-ray diffraction pattern of printed hip implants, with PCL identified with blue dots and MgPSr with red dots. Plain PCL and MgPSr were analyzed as controls. M) Representative SEM image of the hip implant with IFS-0.7 microstructure and respective N) EDX elemental analysis.

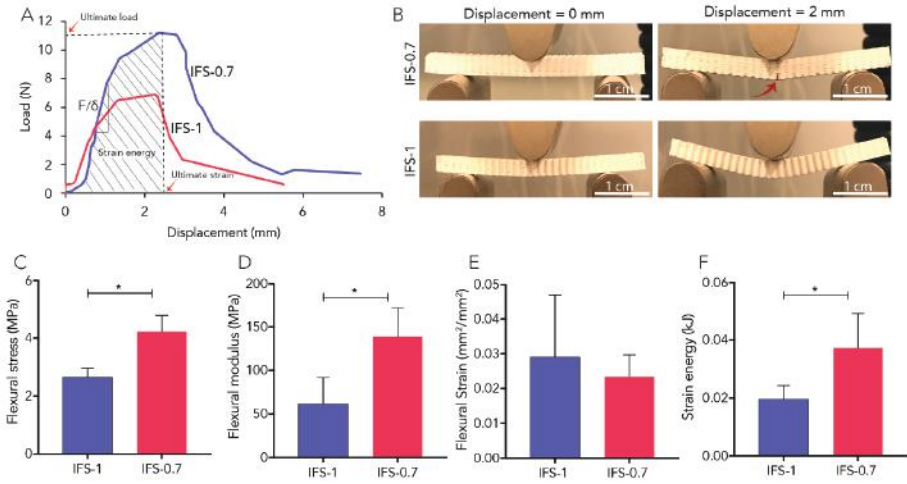


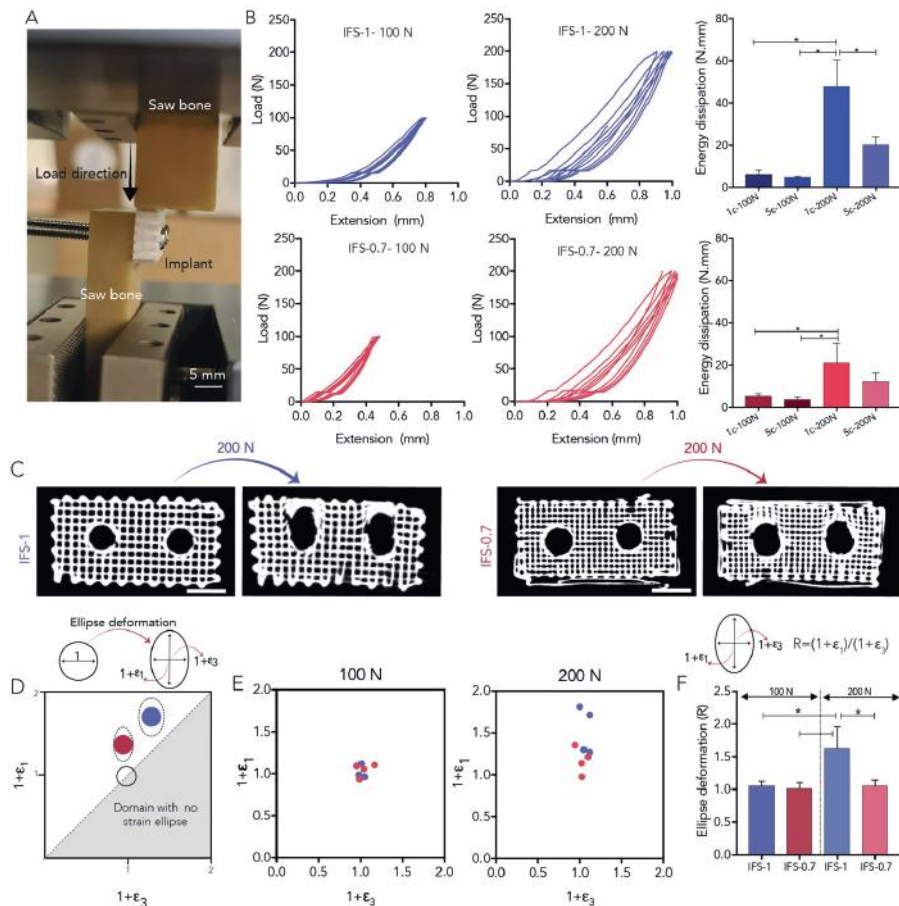
Figure 2. Flexure response under three-point loading of rectangular shaped implant structures with different internal porosities. A) Representative load–displacement curves and B) corresponding photographs showing implants deformation before loading (Displacement = 0 mm) and after loading (displacement = 2 mm). Determined C) flexural stress, D) flexural elastic modulus, E) flexural strain, and F) strain energy (significant differences were analyzed by one-way ANOVA, $n=3$ and $*p<0.05$). $n=3$ and $*p<0.05$).

Flexible biomaterial ink allows stable implant fixation

The successful fixation of hip implants to the saw-bones using metallic screws was demonstrated (Figure 3A). The effect of implant porosity on fixation and stability upon cyclic shear loading was investigated by quantifying dissipated energy after cyclic shear loading at 100 N and 200 N (Figure 3B) and respective implant permanent deformation. Important to mention that a maximum shear load of 200 N was selected, as it would corresponds to a force exerted on one of the hip quadrants of a dog with an average dog body weight of a 30 kg.

After the first loading cycle at 100 N, the energy dissipation is approximately 1.2 times higher for the IFS-1 than IFS-0.7. Same trend was observed for samples loaded until 200 N, but with a significant higher dissipated energy, approximately 2.3 times, for IFS-1 than for IFS-0.7 (Fig 3B). Furthermore, micro-CT analysis confirmed a higher permanent deformation of IFS-1 implants than of IFS-0.7 implants after cyclic loading (Figure 3C). The deformed shape of the fixation holes was approximated by an ellipsoid geometry and the deformation ratio quantified by $1+\varepsilon_1$ (long axis) and $1+\varepsilon_3$ (short axis) (Figure 3D-E). Permanent deformation was only statistically different between IFS-1 and IFS 0.7 implants at 200 N (Figure 3F). It should be noted, that

independently of the deformation observed, both internal architectures maintained their overall structural integrity through cyclic loading without failing even at higher applied forces than 200 N. Nevertheless, based on these fixation results and the results from three-point flexural characterization, we selected the IFS-0.7 implants for further evaluation since they presented negligible accumulated deformation and improved flexural properties.



Monitoring implant mechanical integrity upon degradation

We examined the microscopic features, as well as the mechanical performance of the implant internal structure upon accelerated *in vitro* enzymatic degradation. After 15 days of accelerated *in vitro* degradation, we observed that $38.5 \pm 1.1\%$ of the implant was degraded (Figure 4A). It is important to note that the lipase-enzyme medium solution used for the degradation tests, catalyzes the implant degradation through hydrolysis, which is the major degradation mechanism in polymer-based scaffolds. Therefore, this allows us to resemble long term *in vivo* degradation in a relatively short *in vitro* experiment. In addition, the observed degradation was accompanied by a sustained release of Sr^{2+} and Mg^{2+} (Figure 4B) without MgPSr major ceramic phase transformation, as confirmed by XRD analysis (Figure 4C). However, it is important to note, that the presence of $\text{Mg}(\text{H}_2\text{PO}_4)_2 \cdot 2\text{H}_2\text{O}$ and $\text{Mg}(\text{H}_2\text{PO}_4)_2 \cdot 4\text{H}_2\text{O}$ were also detected in the degraded implants which might be attributed to the hydration product of MgPSr. Furthermore, from the analysis of the flexural properties during *in vitro* degradation, we observed a significant decrease in maximal flexural stress and flexural modulus over the 15 days from 4.2 ± 0.6 MPa and 138.8 ± 33.2 MPa to 0.9 ± 0.5 MPa and 14.1 ± 4.7 MPa, respectively (Figure 4D-I). Interestingly, an increase in flexural strain was observed at days 10 and 15. This might be attributed to the hydrolysis of the PCL bulk structure that resulted in high mobility of polymer chains and consequent increase in flexibility.

Cytocompatibility and osteogenic potential of implants

In further analysis, we checked whether the biomaterial ink and 3D printing manufacturing strategy used resulted in toxicity of the produced implant or changes in their osteogenic potential. To investigate this, we benchmarked implants produced with biomaterial ink against PCL only implants. The hMSCs proliferated faster on MgPSr-PCL implants than on PCL implants (Figure 5A). In addition, the metabolic activity analysis over 14 days also confirmed that the solvent-based printing approach did not affect cell activity and that cells, cultured on the MgPSr-PCL, were approximately 1.4 times more active than when culture on pristine PCL implants after 14 days (Figure 5B). Furthermore, the ALP activity, as a measure of the osteogenic potential of the MgPSr-PCL implants, was 3 times higher than on PCL implants after 7 days of culture (Figure 5C-D). An upregulation of osteonectin (Figure 5E) and osteocalcin (Figure 5F), both markers of osteogenic differentiation, was also observed for cells cultured on the MgPSr-PCL scaffolds after 14 and 21 days of culture, confirming the osteoinductive potential of the hip implant biomaterial composition.

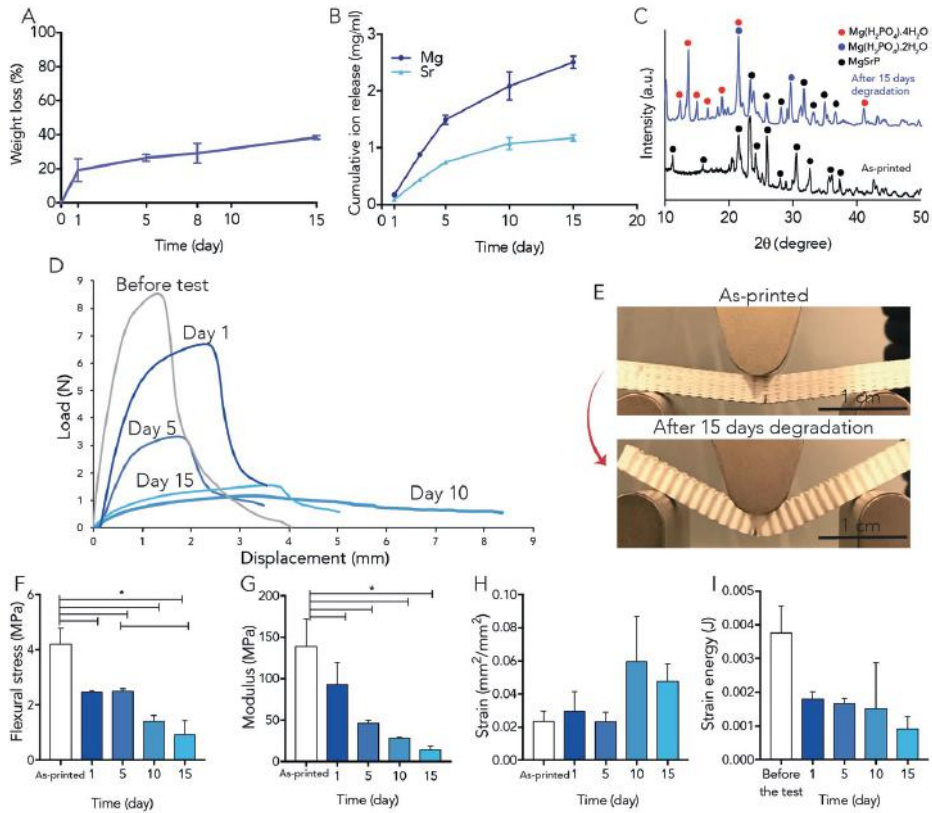


Figure 4. IFS-0.7 implant mechanical integrity and material composition stability upon *in vitro* enzymatic degradation. A) Implant weight loss, B) cumulative ion release and C) XRD composition and D) Representative flexural load-displacement curves of IFS-0.7 implants at different time points of *in vitro* degradation and E) representative snapshots of as-printed and 15 days degraded implants after the flexural test failing. Determined F) flexural stress, G) flexural elastic modulus, H) flexural strain and I) strain energy (significant differences were analyzed by one-way ANOVA, n=5 and *p<0.05).

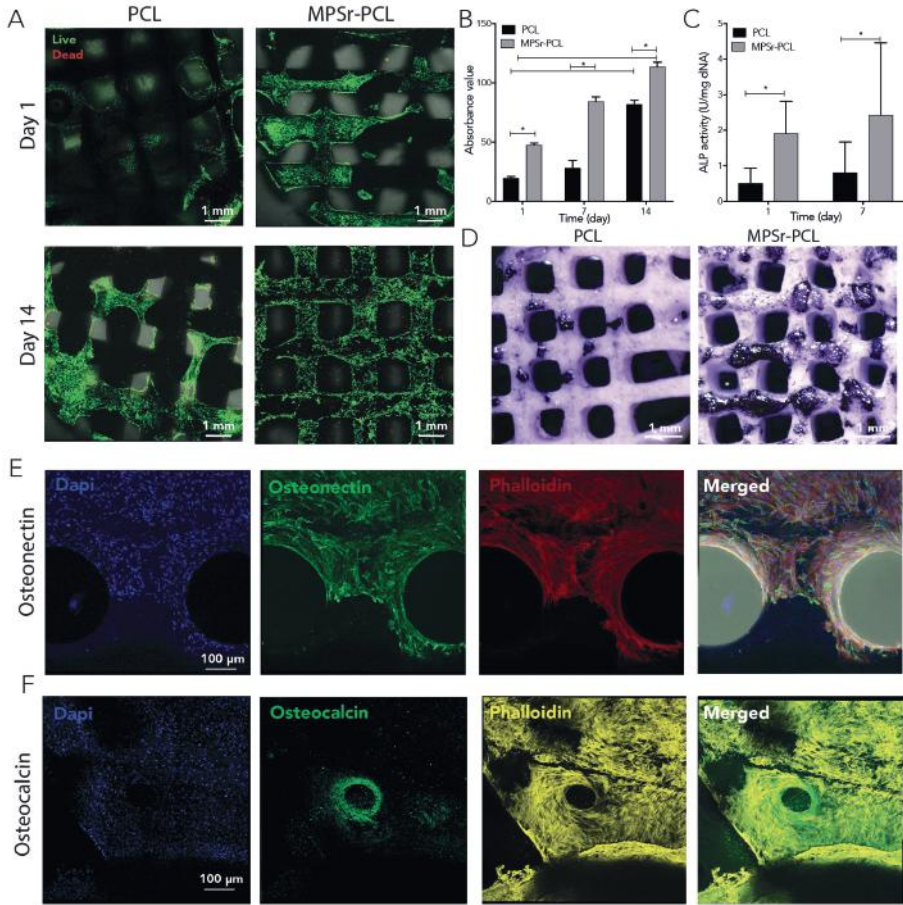


Figure 5. *In vitro* assessment of cytocompatibility and osteogenic potential of IFS-0.7 hip implants. A) confocal images from the live-dead staining assay during 14 days culturing of hMSCs in basal media. B) metabolic activity of hMSCs during 14 days culturing. C and D) alkaline phosphatase (ALP) images of the printed samples. ALP activity levels were normalized to DNA content. E and F) Confocal images of osteonectin and osteocalcin expression in basal media after 14 and 21 days, respectively (significant differences were analyzed by two-way ANOVA, $n=3$ and $*p<0.05$).

Ex-vivo biomechanical evaluation under physiological loading

To confirm the mechanical integrity of the hip implants under physiological loading, implants were tested in a custom-made biomechanical set-up before and after accelerated *in vitro* degradation (Figure S5). After 15 days in enzymatic media, implants did not exhibit a significant deterioration of their internal and external architecture, although the presence of material voids and alternation of surface smoothness could be observed (Figure 6A). This material degradation, resulted in a

decrease in the overall mechanical performance of the implants when loaded under punctual compressive load (Figure 6A-E). In particular, after 15 days of degradation provided a material loss of 38.5 % bringing the pore size from $(319 \pm 57) \mu\text{m}$ to $(524 \pm 21) \mu\text{m}$. At the same time the maximum load decreased from $(91.9 \pm 7.2) \text{ N}$ to $(18.7 \pm 2.9) \text{ N}$ ($p < 0.05$), while the overall implants stiffness dropped from $(36.8 \pm 6.9) \text{ N/mm}$ to $(13.4 \pm 1.2) \text{ N/mm}$. Moreover, a significant decrease in implants strain energy uptake from $(252.1 \pm 60.3) \text{ N/mm}$ to $(134.6 \pm 7.9) \text{ N.mm}$ was also observed. Local microscopic analysis of implants failure, revealed that failure was initiated close to the fixation screws (white arrows).

Although a significant decrease in mechanical properties was observed after 15 days of accelerated degradation, it was notable to observe that hip implant even after a loss in weight of material of approximately 38 % did not lose completely its mechanical integrity.

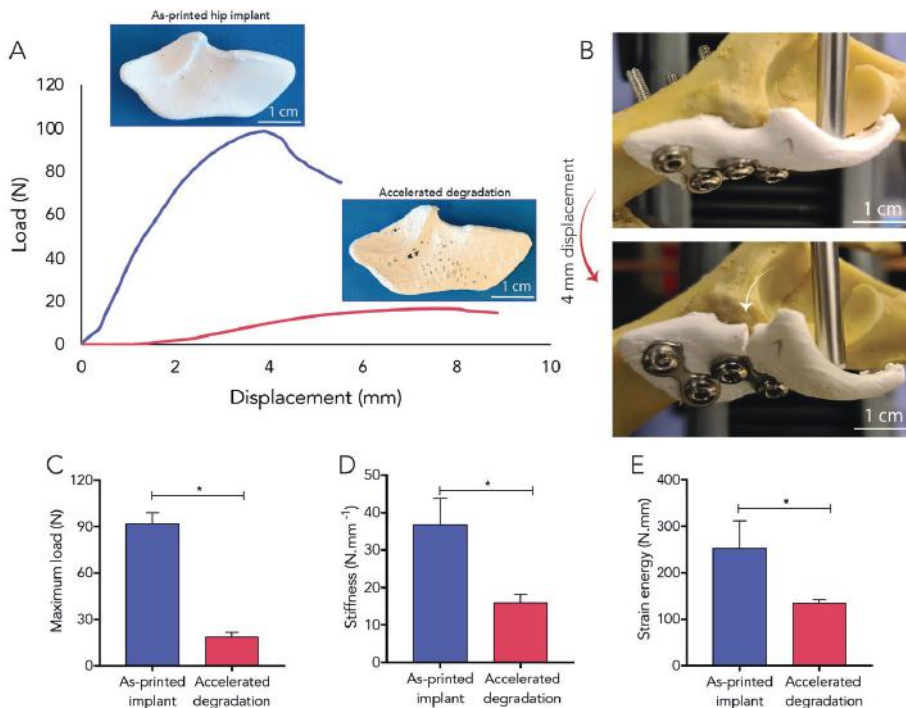


Figure 6. Mechanical performance of hip implants under physiological loading conditions for IFS-0.7. A) Load-displacement curves of as-printed implants and after 15 days immersing in enzymatic solution (accelerated degradation) and corresponding images of the hip implants. B) The snapshots of the as-printed and 15 days degraded implants after the failure. Determined C) maximum load, D) stiffness and E) strain energy (significant differences were analyzed by one-way ANOVA, $n=3$ and $*p<0.05$).

Discussion

Currently, there is a great need for regenerative implants that could provide optimal integration and restoration of the hip socket as a regenerative and stable treatment for hip dysplasia. Here, we described the development of such implant by using extrusion 3D printing of a flexible, bone-inducing biomaterial ink and subsequently rigorously investigate its mechanical and (*in vitro*) biological performance.

The implant was designed based on CT scans of a dog hip joint. In an internal ongoing study, we have recently shown that a metallic hip implant with a similar design was able to provide an extension of the acetabular rim to keep the femoral head in its correct position, while still retained maximal range of motion of the hip joint. In the current work, local modifications on the implant thickness were specifically included to accommodate for its resorbable properties, without compromising its mechanical stability. Moreover, we observed, that the one-step extrusion-based printing strategy and the bone-inducing material here combined, could yield a hip implant that uniquely matched the anatomical designed counterpart, with minimal geometrical deviation from CAD design. Important to mentioned that fabrication of such anatomically-shaped and size relevant ceramic-based implants is typically a limiting factor for the conventional extrusion-based printing processes when comparing to other technologies like 3D powder printing ^[130,183] or stereolithography ^[184,185]. The use of a sacrificial support material, together with the ceramic-based material ink that rapidly solidified due to presence of high volatile solvents, allowed to overcome this limitation.

In addition, through a rigorous mechanical evaluation we confirmed that both the biomaterial ink and anatomically shaped implant with a highly porous and interconnected porosity can provide sufficient strength and resilience to support physiological loads. In particular, we first tested the effect of hip implant's internal structure under 3-point flexure. This allowed us to characterize both material and internal structure behavior, under simultaneous compression and tension loading, that the hip implants are known to be subjected to *in-vivo* ^[186]. As expected, we observed that internal porosity plays a significant role in the final implants mechanical performance, and that the low porosity implants (IFS-0.7) resulted in higher strength and flexural modulus. The flexural strength was largely dictated by the size of pores; therefore, the mechanical properties of IFS-1 was inferior than the IFS-0.7. Moreover, the obtained flexural strength of the hip implant internal architecture was approximately one order of magnitude higher than other previously reported ceramic-based bone implants ^[187]. For example, calcium phosphate-based

scaffolds obtained by casting of the cement paste were reported to present flexural strengths ranging from 3.1 MPa to 4 MPa for a macroporosity between 40 % - 50 %. Low flexural and tensile strength has so far restricted the application of ceramic based materials to non-load bearing areas. Thus, our novel magnesium-based biomaterial demonstrates the potential to be not only shaped in complex geometry implants, but importantly to be used in load-bearing applications.

It is also important to notice that the flexible nature of the biomaterial ink allowed a stable fixation with metallic screws, which is not possible for most of the pure ceramic-based implants due to their brittle nature ^[187,188]. Although a significant permanent deformation was observed upon loading on the IFS-1, which was mostly attributed to its highly porous internal architecture, the IFS-0.7 only showed only a residual permanent deformation at the implant fixation interface upon cyclic loading at 200 N (approximate maximum load exerted on one of the hip quadrants of a dog with an average bodyweight of 30 kg ^[189,190]). Therefore, only hip implants with the internal porosity of IFS-0.7 were selected for *in vitro* biological evaluation and bioreactor study.

Through cytocompatibility and osteogenic differentiation studies, without the addition of osteogenic factors, we confirmed that the biomaterial ink (and printing strategy adopted) is not cytotoxic and can stimulate osteogenic differentiation of clinically relevant hMSCs. The cytocompatibility of the implants was attributed to the high volatility of the solvent combination used, which did not leave any toxic residues within the printed implant independent of its large volume and geometrical complex shape. This is particular important for future clinical translation of the hip implants. Furthermore, we were able to confirm the osteopromotive potential of the hip implants. The osteogenic differentiation of hMSCs was attributed to the high exposure of the MgPSr ceramic phase on the implant structure and to the consequent release of Mg²⁺ and Sr²⁺ ions, that are both known to significantly promote bone formation ^[191,192]. Importantly, the degradable characteristics and osteopromotive properties of the biomaterial ink combined with its high porous internal architecture, is expect to maximize bone ingrowth and consequent hip implant stability and fast integration with host bone. This will finally offer a viable alternative to the existent metallic hip implants, with particular impact for pediatric patients ^[193,194].

Moreover, despite the regenerative and osteopromotive properties of the hip implant, it is also fundamental that the mechanical integrity of the implants is preserved during the degradation process and properly balanced with bone ingrowth speed ^[181]. We opted to study the *in vitro* acceleration degradation in the presence of lipase since

it is known to hydrolyze PCL, which comes closer to the *in-vivo* condition (as the degradation starts from the surface) than other conventionally used enzymes, such as Cutinase ^[195]. Interestingly, the implants weigh loss here observed is in line with our previous findings in an *in-vivo* study using an equine tuber coxae model ^[181]. Importantly, the decrease in mechanical properties followed by *in vitro* degradation is in line with other reports on ceramic-based implants ^[196].

Our results also demonstrated that the developed hip implant can support a load exerted on the acetabulum of a dog with an approximate body weight of 30 kg, even after a material degradation of approximately 38 wt% was observed. Important to mention, that the implant stability is expected to further improve after implantation due to resorbable nature and porous structure of the implant which will result in bone ingrowth into the porous structure, which typically occurs within 4-12 weeks post implantation^[197]. Therefore, it is likely that any initiation of failure observed in our study, as a result of degradation of the implant, will be compensated by the additional stability provided by bone ingrowth.

Conclusion

In conclusion, we have designed, fabricated and fully characterized a patient-specific hip implant for hip dysplasia treatment. The patient-specific design was precisely fabricated from a flexible bone-inducing biomaterial using printed (sacrificial) supporting structures. Moreover, the implant was strong and resilient enough to bear physiological loads, is cytocompatible, can stimulate *in vitro* bone growth, and has the ability to resorb *in-vivo*. This new regenerative implant opens a new perspective for the treatment of hip dysplasia of both veterinary (and potentially) human patients.

Supplementary Information

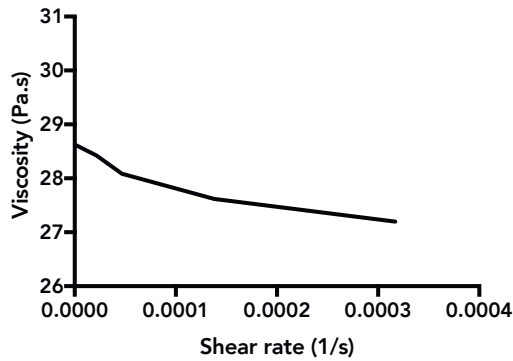


Figure S1. Viscosity evaluation of MgPSr-PCL ink.

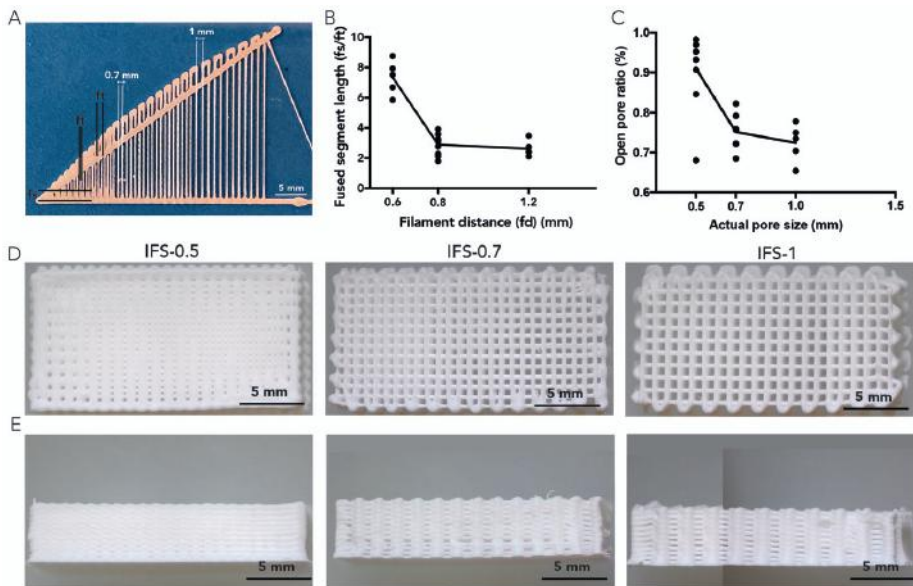


Figure S2. A) Representative stereo microscopic images of one-layer printability test. B) Plot of fused filament length (fs) normalized by filament thickness (ft) as a function of the filament distance (fd). C) Open pore ratio for 4mm thickness scaffolds. D) Top and side E) representative stereo microscopic images of 20 layers implants with different inter-fibre spacing, 0.5, 0.7, and 1 mm. At least 3 samples were tested for each condition.

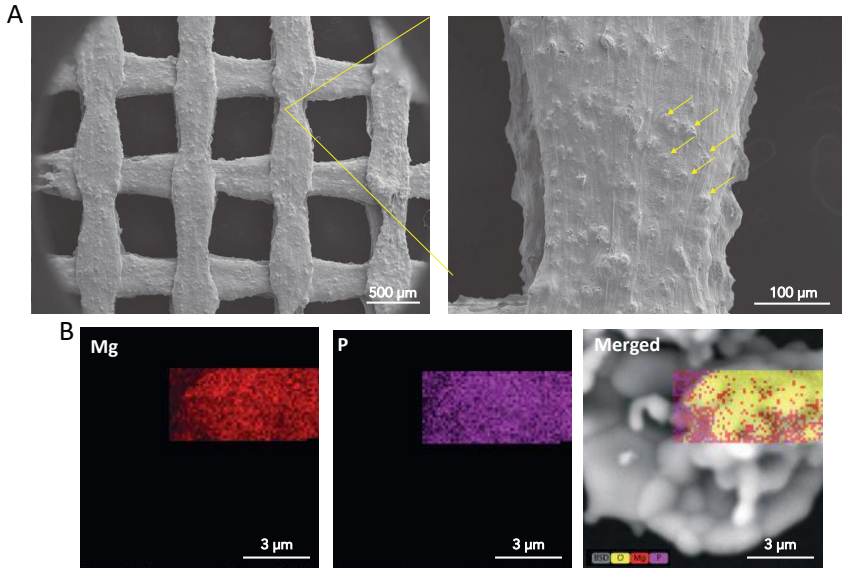


Figure S3. A) SEM image of as-printed IFS-1 implant. Ceramic particles are identified with yellow arrows. B) EDX map of IFS-1 implant surface confirming presence of Mg and P elements.

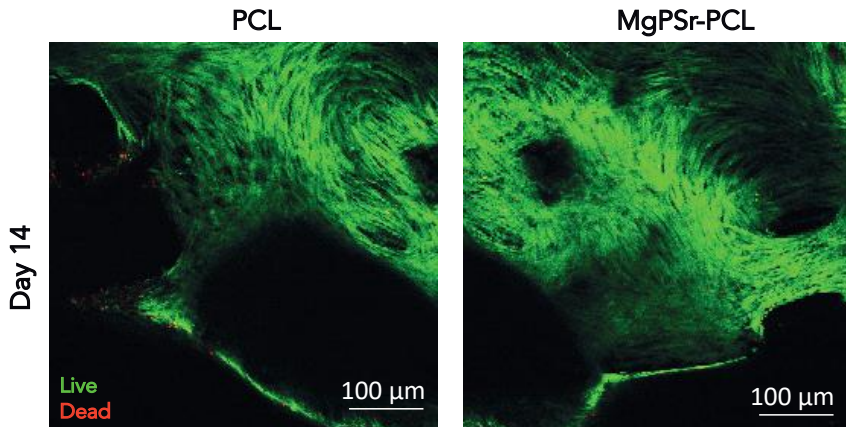


Figure S4. Representative higher magnification images of cell viability and distribution in PCL and MgPSr-PCL implants at day 14 of *in vitro* culture in basal medium.

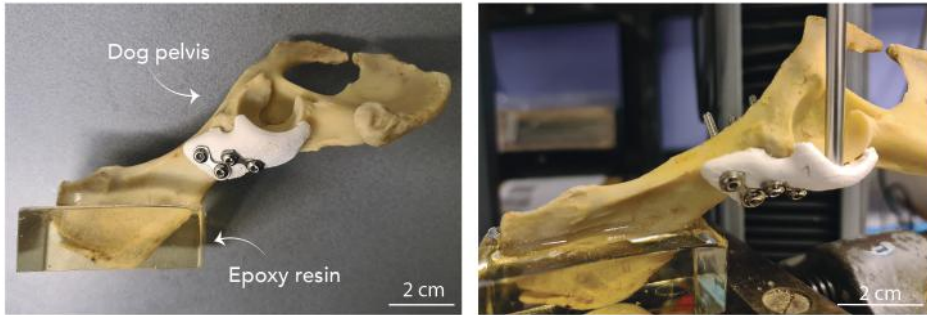
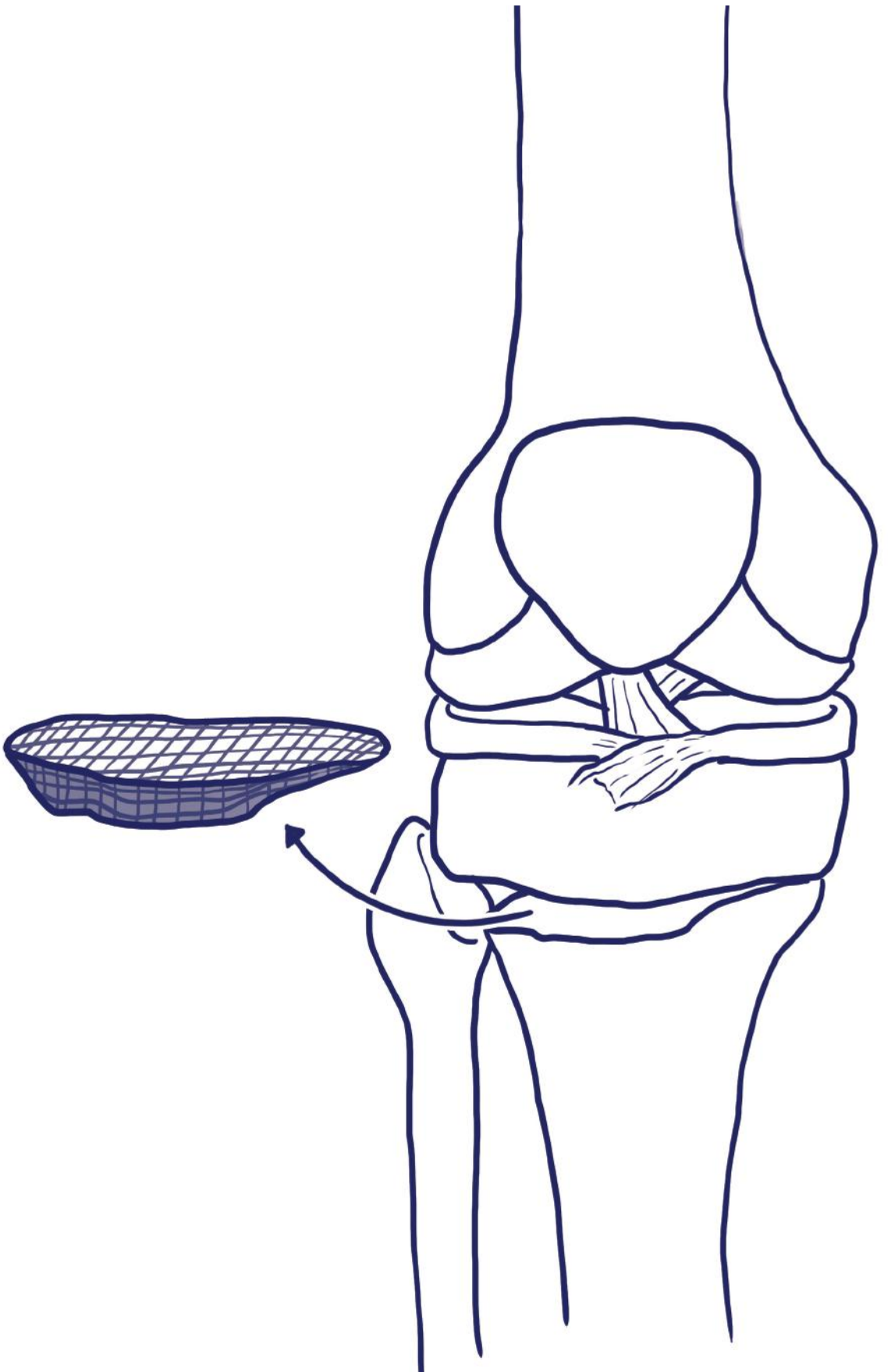


Figure S5. Snapshots pictures of the 3D-printed hip implants fixation strategy. To ensure a proper fixation to the *ex-vivo* biomechanical tester, epoxy resin was used to embed a dog pelvis bone.



CHAPTER 5

A gap-filling, regenerative implant for open-wedge osteotomy

Margot Rijkers

Nasim Golafshan

H Chien Nguyen

Mylène de Ruijter

Riccardo Levato

Lucienne A Von

Nienke van Egmond

Miguel Castilho

Roel JH Custers

Jos Malda

Abstract

Purpose

In patients suffering from unilateral osteoarthritis in the knee, an osteotomy can provide symptomatic relief and postpone the need for replacement of the joint. Nevertheless, open-wedge osteotomies (OWO) around the knee joint face several challenges like postoperative pain and bone non-union. In this study, the aim was to design, fabricate, and evaluate a gap-filling implant for OWO using an osteoinductive and degradable biomaterial.

Methods

Design of porous wedge-shaped implants was based on computed tomography (CT) scans of cadaveric legs. Implants were 3D printed using a magnesium strontium phosphate-polycaprolactone (MgPSr-PCL) biomaterial ink. Standardized scaffolds with different inter-fibre spacing (IFS) were mechanically characterized and osteoinductive properties of the biomaterial were assessed *in vitro*. Finally, human-sized implants with different heights (5 mm, 10 mm, 15 mm) were designed and fabricated for *ex vivo* implantation during three OWO procedures in human cadaveric legs.

Results

Implants printed with an interior of IFS-1.0 resulted in scaffolds that maintained top and bottom porosity, while the interior of the implant exhibited significant mechanical stability. Bone marrow concentrate and culture expanded mesenchymal stromal cells attached to the MgPSr-PCL material and proliferated over 21 days in culture. The production of osteogenic markers alkaline phosphatase activity, calcium, and osteocalcin was promoted in all culture conditions, independent of osteogenic induction medium. Finally, three OWO procedures were planned and fabricated wedges were implanted *ex vivo* during the procedures. A small fraction of one side of the wedges was resected to assure fit into the proximal biplanar osteotomy gap. Pre-planned wedge heights were maintained after implantation as measured by micro-CT.

Conclusion

To conclude, personalized implants for implantation in open-wedge osteotomies were successfully designed and manufactured. The implant material supported osteogenesis of MSCs and BMC *in vitro* and full-size implants were successfully implemented into the surgical procedure, without compromising pre-planned wedge height.

Keywords

Osteotomy; open wedge; implant; 3D printing; osteoinductive; magnesium phosphate

Introduction

Unicompartmental knee osteoarthritis (OA) is often associated with lower limb malalignment. Especially for younger patients (age < 65 years) with unicompartmental OA and a malalignment, a correctional osteotomy can be a surgical solution, aiming to unload the affected compartment^[198–200].

While open-wedge osteotomies (OWO) and closing-wedge osteotomies (CWO) have shown comparable clinical outcome^[201,202], OWOs have gained popularity over CWOs in the tibia, mainly due to practical considerations. When performing a CWO in the tibia, an osteotomy of the fibula is necessary and future conversion to a partial or total knee arthroplasty is complicated^[203]. But not without importance, medial high tibial OWO remains associated with pain in the early postoperative stage and has a higher risk for delayed or non-union^[204,205]. Postoperative pain is believed to be (at least in part) caused by bone marrow leakage from the osteotomy site, causing swelling, resulting in impaired early weight-bearing, ambulation, and rehabilitation^[206].

In some cases, the opened osteotomy wedge is filled with an autologous bone graft from the iliac crest^[207]. However, this procedure is aimed at accelerating union rather than closing the gap and it is associated with donor site morbidity^[208]. Filling the osteotomy gap with an allogeneic bone graft could be a viable solution as gap filler, and has demonstrated improved pain levels after the procedure compared to baseline in a case series of 103 patients^[205]. Almost all of the patients (99%) were able to walk > 500 meters without any support three months after surgery. However, the use of allogeneic bone grafts is hampered by the limited availability of the grafts. Moreover, frozen allografts were shown to have a higher failure rate (defined as construct failure or non-union) compared to living autologous grafts^[209]. Alternatively, synthetic bone substitutes made of hydroxyapatite and/or beta-tricalcium phosphate^[204,210–212] aid in bone union without donor site morbidity. Nevertheless, most bone substitute wedges are not designed to imitate the structure of trabecular bone with a dense cortical border. To improve bone union, postoperative pain, and eliminate the need for an allo- or autograft in OWO procedures, a firm, gap-filling 3D-printed scaffold with osteoconductive properties and mechanical stability provides a solution.

Among the bioactive ceramic materials that have been used for bone tissue engineering, magnesium strontium phosphate (MgPSr) has gained particular interest due to the good solubility of magnesium phosphate phases under physiological conditions, and the presence of Sr²⁺ ions have been demonstrated to promote osteogenic differentiation of mesenchymal stromal cells (MSCs)^[213–218]. However,

pure ceramic scaffolds are usually brittle and prone to fracture which hampers their application in large, load-bearing defects^[219]. A previous study has investigated a ceramic-polymer composite of MgPSr and polycaprolactone (PCL), which is a versatile biomaterial ink that can be processed through extrusion-based 3D printing at room temperature. The biomaterial can be manufactured into different complex geometries to improve bone filling of a defect without compromising mechanical stability^[220]. The porous nature of a printed osteotomy wedge scaffold allows bone marrow to populate the wedge upon implantation. Alternatively, pre-surgical seeding of the implant with a bioactive product accelerating osteogenesis, such as bone marrow concentrate (BMC), could further accelerate bone union.

This study aimed to design and manufacture a scaffold as gap filler in OWO around the knee joint. The mechanical stability of the wedge scaffold, as well as the *in vitro* osteoinductive properties of the material on MSCs and BMC were investigated. Additionally, preservation of the pre-designed implant structure and height were assessed upon implantation into human cadaveric legs.

Materials and Methods

Study outline

To completely fill the opening wedge gap after an OWO, 3D printed scaffolds were manufactured using patient computed tomography (CT) data and computer-aided design. The printed scaffold structures were mechanically characterized and *in vitro* potency of the MgPSr-PCL material was evaluated to induce osteogenesis when seeded with bone marrow-derived MSCs, as well as BMC. Finally, a proof-of-concept surgical implantation in a cadaver model was performed for implementation of the implants into the current osteotomy procedure.

Computer-aided design of osteotomy wedge

For initial design of a wedge scaffold for mechanical characterization and *in vitro* experiments, an anonymized CT scan and surgical planning for an 8 mm medial opening-wedge distal femur osteotomy was acquired from a clinical case (University Medical Center Utrecht) (Figure 1Ai). The computer-aided design (CAD) of the wedge scaffold was developed in SolidWorks software (Dassault Systèmes, Waltham, MA, USA), using the CT scan images. After assessment of the wedge scaffold, BioCAM™ software was used to define the wedge scaffold internal architecture and subsequently translate the design into a G-Code. The external wall of the osteotomy scaffold was kept closed with two outer layers, while for the internal region of the

osteotomy scaffolds, three different inter-fibre spacings (IFS), 1.3 mm, 1.0 mm, and 0.7 mm (abbreviated as IFS-1.3, IFS-1.0, and IFS-0.7, respectively) were considered.

Material preparation and extrusion-based 3D-bioprinting

The biomaterial ink was prepared by combining in-house synthesized $\text{Mg}_{2.33}\text{Sr}_{0.67}(\text{PO}_4)_2$ powder and commercial medical grade poly(ϵ -caprolactone) (mPCL, Purasorb PC 12, Purac Biomaterials, Netherlands) in a weight ratio of 70:30 wt.% of MgPSr to PCL, according to a procedure previously described^[220]. Designed scaffolds were fabricated by an extrusion-based 3D-printing system (3D Discovery, regenHU, Switzerland) using the MgPSr-PCL biomaterial ink. The ink was transferred to a 10 mL syringe (Nordson EFD, USA) and extruded through a 22G conical nozzle (inner diameter = 0.41 mm, Nordson EFD, USA) at a pressure of 0.9 bar and collected at collector speed of 6 mm/s.

Mechanical characterization of printed wedge scaffolds

Uniaxial compression tests were performed using a universal testing machine (Zwick Z010, Germany) equipped with a 1 kN load cell. Tests were performed on cylindrical samples ($d = 6$ mm, $h = 12$ mm, $n = 5$) for all three groups (IFS-1.3, IFS-1.0 and IFS-0.7, without closed outer edges), at a rate of 1 mm/min (at room temperature). From the engineered stress-strain curves, the elastic modulus (defined as the slope of the linear region at the interval 0.02 - 0.05 mm/mm strain), the yield stress (defined as the point where nonlinear deformation begins), and toughness (defined as the absorbed energy by the scaffolds up to yield stress) were determined.

In vitro accelerated degradation of printed wedge scaffolds

The degradation of the materials was studied under controlled conditions which accelerated biomaterial degradation *in vitro*^[219]. Wedge scaffolds were incubated in a 0.4 mg/ml lipase solution (from *Pseudomonas cepacia*, Sigma-Aldrich) and 1 mg/ml sodium azide (Sigma-Aldrich) at 37°C for 15 days. At each time point (1, 5, 10, and 15 days), the enzymatic solution was refreshed, and samples were monitored for weight loss, quantified as follows:

$$\text{Weight loss} = \frac{W_{D15} - D_0}{D_0} \quad \text{Eq. 1}$$

In vitro osteogenesis of scaffolds

Donors and cell isolation

Human bone marrow-derived mesenchymal stromal cells (BM-MSCs) were derived from healthy donor bone marrow aspirates ($n = 3$, age range 2 – 12) as approved by the Dutch central Committee on Research Involving Human Subjects (CCMO,

Bio-banking bone marrow for MSC expansion, NL41015.041.12). The parent or legal guardian of the donor signed the informed consent approved by the CCMO. In brief, the mononuclear fraction was separated using a density gradient (Lymphoprep, Axis Shield). MSCs were isolated by plastic adherence and expanded for three passages in Minimum Essential Media (α MEM, Macopharma) with 5% platelet lysate and 3.3 IU/mL heparin and cryopreserved. Subsequently, MSCs were expanded for two additional passages in MSC expansion medium (α MEM [Gibco], 10% (v/v) fetal bovine serum [FBS; Biowest], 1% penicillin/streptomycin [pen/strep; 100 U/mL, 100 μ g/mL], 200 μ M l-ascorbic acid 2-phosphate [ASAP; Sigma-Aldrich], and 1 ng/mL basic fibroblast growth factor [bFGF; PeproTech]). BMC was obtained from donors undergoing an OWO or total knee arthroplasty surgery ($n = 2$, age range 39 - 49) after their informed consent (protocol approved by the local medical ethical committee). Bone marrow was concentrated to one tenth of its original volume using Ficoll paque (GE Healthcare) density separation.

***In vitro* culture of scaffolds**

Standardized 5 mm diameter cylindrical scaffolds (ISF-1.0) were printed as described before^[220] and sterilized by washing in 70% ethanol and Milli-Q, followed by exposure to ultraviolet light for 1 hour. Scaffolds were cut in half with a sterile scalpel and seeded with either 15,000 MSCs / scaffold in fibrin gel (25 μ L fibrinogen [1:15 in PBS] crosslinked with 25 μ L thrombin (1:50 in PBS); Tisseel, Baxter) or 25 μ L BMC (crosslinked with 16.6 μ L thrombin and 16.6 μ L CaCl_2 [500 mM in 0.9% NaCl]). Cell-seeded scaffolds were pre-cultured in MSC expansion medium for two days, followed by 21 days of osteogenic induction with osteogenic differentiation medium (α MEM supplemented with 10% FBS, 1% pen/strep, 200 μ M ASAP, 10 mM β -glycerophosphate [Sigma-Aldrich], and 10 nM dexamethasone [Sigma-Aldrich]). Control cell-seeded scaffolds were treated with MSC expansion medium without bFGF.

Alkaline phosphatase, calcium, and DNA quantification

Osteogenic differentiation of the cells was measured by the activity of the early osteogenic marker alkaline phosphatase (ALP) after 5, 7, and 11 days and by quantification of calcium produced after 21 days. To determine activity of ALP, cells were lysed in Tris-EDTA buffer (10 mM Tris-HCl, 1 mM EDTA, pH 8) by three freeze-thaw cycles. ALP activity was measured using the conversion of p-nitrophenyl phosphate liquid substrate (pNPP, Sigma-Aldrich). Absorbance was measured every minute for 30 minutes at 405 nm and corrected for absorbance at 655 nm. Calf intestinal ALP (Sigma-Aldrich) was used as a standard. Calcium concentration in the samples was quantified after 21 days using a colorimetric calcium assay kit (Abcam) according to the manufacturer's instructions. ALP activity and calcium levels were corrected

for DNA. DNA content was determined using the Quant-iT PicoGreen dsDNA assay (Invitrogen) according to the manufacturer's instructions.

Osteocalcin immunocytochemistry

To visualise the osteogenic marker osteocalcin, scaffolds were fixed in formalin for 30 minutes for the osteocalcin immunocytochemistry after 21 days of differentiation. Samples were permeabilized with 0.2% (v/v) Triton X-100 in phosphate-buffered saline (PBS), followed by blocking with 5% (v/v) bovine serum albumin (BSA) in PBS. Next, samples were incubated overnight at 4°C with 10 µg/mL mouse-anti-human primary antibody against osteocalcin (clone OCG4; Enzo Life Sciences). Samples were then incubated with 10 µg/mL goat-anti-mouse antibody conjugated to Alex Fluor 488 (Invitrogen) for one hour at room temperature. All samples were also stained for F-actin (1:200; phalloidin-TRITC; Sigma-Aldrich) and 4',6-diamidino-2-phenylindole (100 ng/mL; DAPI; Sigma-Aldrich). Images were acquired with a Leica SP8X Laser Scanning Confocal Microscope and Leica LASX acquisition software.

***Ex vivo* surgical implantation of the printed wedges**

Three fresh-frozen human cadaveric legs were obtained (all left legs, one male and two female) in accordance with the guidelines of the local medical ethical committee. CT-scans were obtained of the three included legs (Philips Healthcare, Best, The Netherlands; 100 kV and 130mAs), with 0.8 mm slice thickness. Single plane OWOs were pre-operatively planned in 3-Matic (Materialise, Leuven, Belgium), with for each leg a specific wedge height (5, 10, and 15 mm). This resulted in post-surgical 3D-models of the cadavers with left open osteotomy gaps, which functioned as surrogate for the 3D printing of the wedges. A proximal biplanar medial high tibial OWO was performed following a standard surgery protocol. During this procedure, the osteotomy gap was kept open using a lamina spreader and the 3D-printed scaffold wedge was inserted into the gap. The tips of the wedge scaffolds were resected to fit the biplanar osteotomy gap, without altering the outside rim of the wedge. The osteotomies were then fixated with angular stable plates (Activmotion, Newclip Technics, Haute-Goulaine, France). The same plates are used for patients in the clinic and have a smaller footprint compared to other commercially used plates. Following implantation of the scaffold wedges, additional CT scans were obtained of the operated cadaver legs, subsequently the wedges were explanted for further analysis.

Micro-computed tomography

The pre- and post-surgical wedge scaffolds underwent micro-CT (Quantum FX-Perkin Elmer, USA) for height analyses. Scan parameters were 90 kV tube voltage, 180 µA tube current, 60 or 73 µm resolution, and 2 min scan time. Scaffold heights pre-

and post-implantation were quantified using computer vision software Fiji (software version 2.1.0/1.53c, National Institutes of Health, Bethesda, USA). Scaffold height was measured at the highest point. The micro-CT images of a single scaffold pre- and post-implantation were superimposed to ensure the scaffolds were measured at the same location at both timepoints.

Statistical analysis

Statistical analyses were performed using GraphPad Prism 8.3 (GraphPad Software, Inc., La Jolla, CA, USA). All data were presented as mean \pm standard deviation (SD). To test for differences in mechanical evaluations and calcium content, a one-way analysis of variance (ANOVA) with Tukey's post hoc test was used. To test for differences in DNA and ALP quantifications, a two-way ANOVA with Tukey's post hoc was used. For scaffold wedge height, a two-tailed t-test was used. Normality was confirmed with a Shapiro-Wilk test ($p > 0.05$). P values below 0.05 were considered significant.

Results

Personalized implant design and fabrication

Wedge implants were designed for both open-wedge lateral distal femur (for *in vitro* analyses; Figure 1A) and medial tibial osteotomies (for implantation in cadavers; Figure 1B) from CT scan 3D reconstructions (Panels i). Wedges had closed outer edges, aimed at limiting leakage from the osteotomy site into the soft tissues surrounding the bone, while the interior was porous (Panels ii and iii).

Mechanical profile of printed porous material

Incorporation of the thermoplastic PCL into the ceramic MgPSr phase improved handling of the implants, overcoming downsides of brittle ceramic materials^[219]. The stress-strain curves of the standardized printed discs with different IFS showed comparable profiles (Figure 2A). The decrease in IFS resulted in an increase in mechanical stability, elastic modulus increased significantly from 105.3 ± 10.26 MPa (IFS-1.3) to 151.5 ± 12.61 MPa (IFS-0.7) (Figure 2C). Yield stress, defined as the point of maximum elastic deformation, increased from 4.2 ± 1.27 MPa (IFS-1.3) to 6.0 ± 1.90 MPa and 11.4 ± 1.86 MPa for IFS-1.0 and IFS-0.7, respectively (Figure 2D). In line, strain energy increased from 0.077 ± 0.0208 J for IFS-1.3 to 0.196 ± 0.0957 J for IFS-0.7 (Figure 2E). While a disc with an IFS of 0.7 mm presented the highest elastic modulus, printing of a complete wedge scaffold with this IFS resulted in a construct that was not completely porous from top to bottom, which is essential to flow of bone marrow through the scaffold *in vivo* (Figure 2B). Scaffolds with a planned

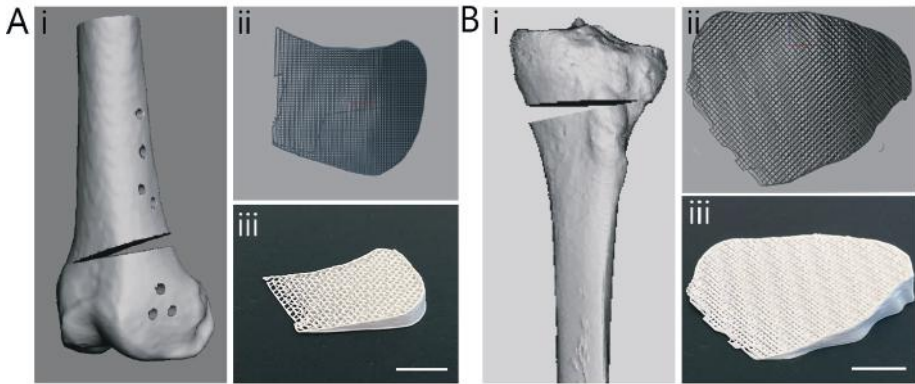


Figure 1. Surgical planning and extrusion-based printing. Wedge design for open-wedge osteotomies in (A) distal femur and (B) proximal tibia. (Panels i) Surgical planning of open-wedge osteotomies derived from computed tomography (CT) scans. (Panels ii) Top views of printing paths of computer-aided designs (CAD) of personalized wedge implants. (Panels iii) The finalized personalized wedges in magnesium strontium phosphate-polycaprolactone (MgPSr-PCL) biomaterial. Scale bar = 10 mm.

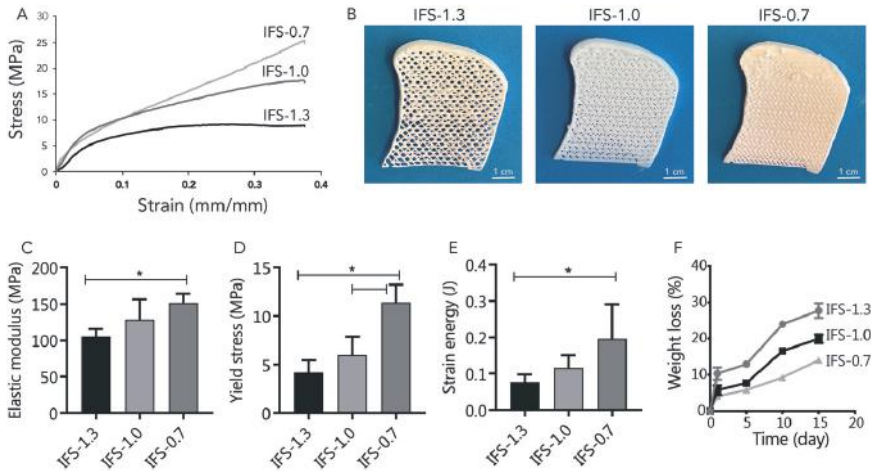


Figure 2. Evaluation of mechanical properties of the printed magnesium strontium phosphate-polycaprolactone (MgPSr-PCL) wedges. A) Longitudinal compression profile of 3D printed MgPSr-PCL wedge scaffolds for inter-fibre spacing (IFS) -1.3, IFS-1.0, and IFS-0.7. B) Corresponding photographs showed the different scaffolds after the printing. Open pores in wedges IFS-1.3 and IFS-1.0 can be appreciated, while IFS-0.7 wedges were not porous. C) Elastic modulus, D) Yield stress, and E) strain energy from compressive loading profile for IFS-1.3, IFS-1.0, and IFS-0.7. F) Weight loss of wedge scaffolds during accelerated in vitro degradation in enzymatic solution over 15 days. * $p < 0.05$

IFS of 1.0 mm resulted in completely porous wedges and only a slight difference in elastic modulus and strain energy compared to scaffolds with a planned IFS of 0.7 mm, which did not reach statistical significance. While the degradation rate of IFS-1.3 samples (as evaluated under accelerated degradation conditions) was 30% faster compared to IFS-1.0 samples (Figure 2F), the combination of tested characteristics led to the selection of IFS-1.0 for further analyses as the best compromise between open porosity, mechanical stability, and degradation properties.

***In vitro* osteogenic properties of the scaffold material**

Human BM-MSCs embedded in fibrin (MSC-fibrin) were seeded in the biomaterial scaffolds to evaluate osteogenic potential. Additionally, to simulate the *in vivo* situation, a second group of scaffolds was seeded with BMC. The culture-expanded human MSCs attached to the MgPSr-PCL material and proliferated over time. Cells in BMC also proliferated on the scaffolds (Figure 4A and Supplemental Figure 1). Activity of the early osteogenic marker ALP was similar in MSC-fibrin and BMC groups when scaffolds were cultured in control medium, yet were increased in MSC-fibrin when cultured in osteogenic medium (Figure 4B). BMC performed similar to MSC-fibrin in terms of calcium production at 21 days of culture (Figure 4C). Of note, both experimental groups had a higher ALP activity and increased calcium production compared to MSCs that were cultured in monolayers, indicating osteoconductive effects of the scaffold material and 3D environment. Production of osteocalcin, an exclusive marker for osteoblasts, was observed in cultures under all conditions irrespective of culture medium used (Figure 3D).

***Ex vivo* surgical implantation**

Three fresh-frozen human cadaveric legs underwent CT scanning in order to plan three OWOs with different heights; 5, 10, and 15 mm (Figure 4A, 4B, 4C). 3D models of the tibias were used to plan single plane osteotomy gap (Panels i) and design the wedge scaffolds (Panels ii). Wedges were implanted during a standard proximal biplanar OWO procedure and fixated with an angular stable plate (Panels iii).

Post-surgical X rays (Panels iv) and CT scans (Panels v) illustrate the scaffold positioning and fit. Micro-CT analyses of the wedges pre- and post-implantation indicated good analogy of the scaffolds (Figure 5A, pre-operative in red, post-operative in grey). Due to the biplanar approach of the osteotomy procedure^[221], the scaffolds were adjusted at one side using an automatic saw, not altering the rest of the scaffold shape and outer rim (Figure 5B, arrows indicating trimmed edge). Quantification of wedge heights from micro-CT images revealed that the wedge heights were not affected by the applied surgical procedure, during which they bear

loading for a brief moment when the laminar spreader is removed to allow sufficient space for the plate to be fixated (Figure 5C).

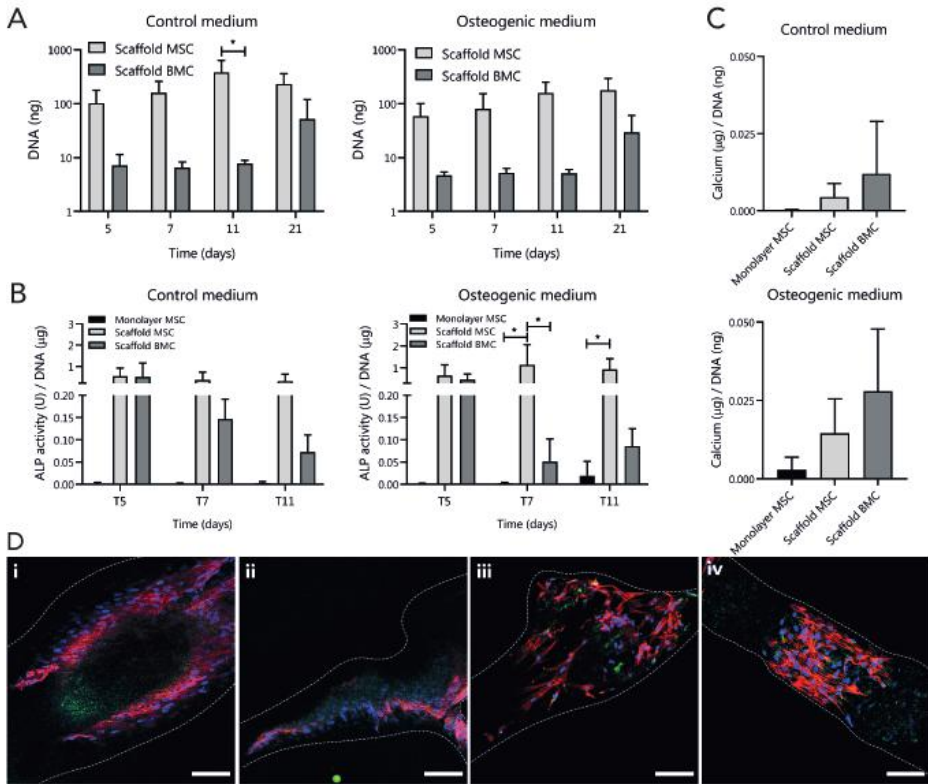


Figure 3. In vitro osteogenic performance of the magnesium strontium phosphate-polycaprolactone (MgPSr-PCL) biomaterial. A) Quantification of DNA in the MgPSr-PCL scaffolds at 5, 7, 11, and 21 days in culture with control (left panel) and osteogenic medium (right panel). B) Early osteogenic marker alkaline phosphatase (ALP) activity relative to the amount of DNA at 5, 7, and 11 days. C) Calcium content of the cultured constructs at day 21 in control medium (top panel) and osteogenic medium (bottom panel). D) Immunocytochemical osteocalcin staining on 21-day cultured standardized cylindrical MgPSr-PCL scaffolds (ISF-1.0) using: (i) culture expanded mesenchymal stromal cells (MSC) in control medium, (ii) MSC in osteogenic medium, (iii) bone marrow concentrate (BMC) in control medium, and (iv) BMC in osteogenic medium. Nuclei are shown in blue (DAPI), osteocalcin expression in green, and F-actin in red. Dashed lines indicate the location of three-dimensional scaffold material. Scale bar = 100 μm . * $p < 0.05$

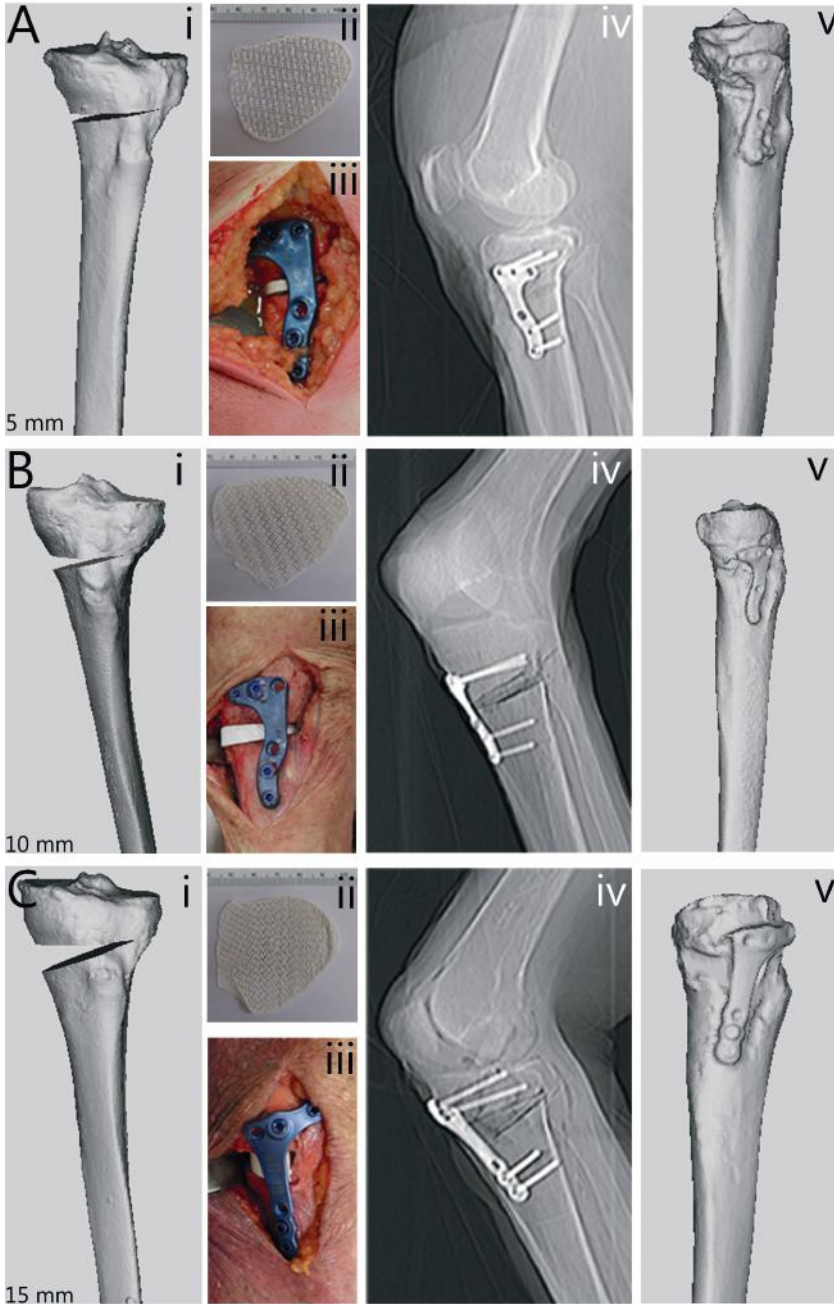


Figure 4. Surgical implantation of personalized scaffold wedges. Planned osteotomy heights of A) 5 mm, B) 10 mm, and C) 15 mm from computed tomography (CT) scans of human cadaveric legs (Panels i). (Panels ii) 3D printed wedge scaffolds in magnesium strontium phosphate-polycaprolactone (MgPSr-PCL). (Panels iii) Scaffolds implanted in the cadaveric legs. (Panels iv) X-ray of the legs after implantation. (Panels v) 3D reconstruction from CT scans after implantation of the wedge scaffolds.

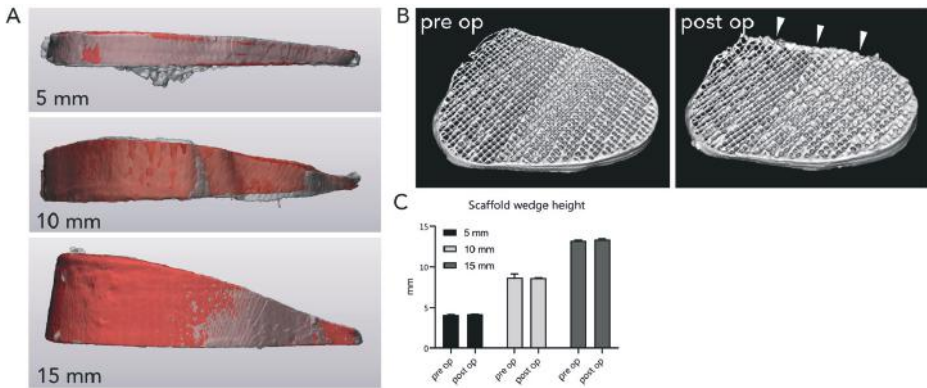


Figure 5. Micro-computed tomography (CT) analysis of printed wedge scaffolds. A) 3D reconstructions of the wedges from micro-CT images of the printed wedges pre- and post-implantation. Pre-implanted scaffolds in red, post-implanted scaffolds in grey. B) Micro-CT reconstruction of the 5 mm wedge. Note the small portion that was adjusted during the procedure (indicated by the white arrows). C) Quantification of scaffold wedge height before and after implantation into the cadaveric legs revealed no loss of scaffold height.

Discussion

This study demonstrated a proof of concept to manufacture implants for bone gap filling in femoral or tibial OWOs, by 3D printing a biodegradable and osteoinductive scaffold material. The printed material promoted osteogenesis of MSCs and BMC *in vitro* and scaffolds were implanted *ex vivo* without compromising pre-operatively planned wedge height. The aim was to design implants that fitted the planned osteotomy gap and height, fabricate these, and evaluate their implementation in the established surgical procedure.

Post-surgical pain poses a challenge in OWO care. One of the hypotheses for the cause of pain is bleeding from the osteotomy site. It has been shown that fitting an allogeneic graft, which closes the gap completely, enables early postoperative weight-bearing and improve clinical outcomes after three months^[205]. A variety of scaffold materials and growth factors is being investigated to accelerate osteogenesis in OWO. Most studies investigating a scaffold material make use of wedges composed of hydroxyapatite or beta-tricalcium phosphate^[204,211,222], whereas some focus on injection of biologics, like platelet-rich plasma and MSCs^[223], or use a single growth factor, like bone morphogenetic protein (BMP) 6^[224].

While a great deal of effort is put into accelerating bone healing, the current study investigates a combined approach of osteoinduction and filling of the osteotomy gap. The presented methods offer the possibility of personalizing an osteoinductive wedge implant and incorporating this into the existing 3D workflow. Yet, the manufactured implants were designed to match opening-wedge height and the anatomy of the bone. Adjustment of the scaffold edge enabled proper fit into the osteotomy plane, while still filling the gap. Precisely sealing of the whole gap was proven to be challenging in the current setup. The approach used in the current study led to a relatively symmetrical wedge, as opposed to a trapezoid-shaped wedge. To move towards clinical implementation and complete sealing of an osteotomy gap, a more precise, biplanar surgical planning should be performed. Most likely, this would also require using 3D printed patient-specific instruments (PSI), with pre-operatively determined saw cuts resulting in a predefined gap morphology, for which a fitting implant can subsequently be fabricated. In some cases of malalignment correction, PSI are preferred by orthopaedic surgeons, in the form of saw and drill guides pre-operatively. Further research can offer the possibility of adding a personalized wedge implant into this workflow. With predetermined bone cuts and gap morphology, our wedge scaffold can be 3D printed pre-operatively to fit. However, this initial study focussed primarily on the feasibility of implanting a 3D printed MgPSr-PCL wedge scaffold, without compromising the pre-operatively planned wedge height.

While most of the load on the osteotomy gap is absorbed by the angular stable plate and screws, the implant should remain stable during the brief period before the plate is fixed on the bone. The elastic modulus of the implants demonstrated similarities to human trabecular bone^[225]. Scaffolds with a planned fibre spacing of 1.0 mm maintained open pores, through which bone marrow would be allowed to flow and osteogenesis might be accelerated. While implant height was maintained post-implantation in the cadaveric legs, future *in vivo* and clinical studies are necessary to confirm maintenance of pre-planned wedge height during a longer period of implantation, as well as speed of bone union.

The full-size implants degraded over time in an accelerated *in vitro* setup using an enzymatic solution. Prior research in an equine model has shown that degradation of the MgPSr-PCL (pore size 1.0 mm) in the enzymatic solution for ten days corresponded to degradation over six months during *in vivo* implantation^[220]. Increasing inter-fibre spacing accelerated degradation by 30% in mass loss, indicating that *in vivo* mass loss might also be accelerated. However, the exact degradation and speed of bone formation of the osteotomy-specific MgPSr-PCL implants in this specific anatomical location should be evaluated in a large animal model.

The printed MgPSr-PCL material facilitated osteogenesis *in vitro*, confirming previous findings^[220]. For large defects, pre-seeding of the scaffold with a regenerative compound, like MSCs, might be beneficial to accelerate bone healing. Here, seeding of the material with both culture-expanded MSCs and BMC resulted in production of osteoblast-specific markers, indicating that infiltrated bone marrow in the scaffold material after implantation may be sufficient by itself to stimulate osteogenesis. This is most likely induced by its growth factor-rich nature and the presence of progenitor cells^[226]. While fabrication of personalized 3D implants from patient imaging data was demonstrated before for orthopaedic applications^[227,228], this study is the first to report on a personalized biodegradable implant for OWO.

The current study was mainly limited by the imbalance between preoperative osteotomy planning (single plane) and the intra-operative surgical biplanar osteotomy, leading to a slight mismatch between gap and fabricated implant. By implementing 3D printed PSI in the workflow, an optimal fit of the designed implant can be achieved. Because the purpose of this study was to design and manufacture a gap-filling wedge implant in an osteoinductive material and to evaluate this in an *ex vivo* model, achieving a perfect fit was beyond the scope of this investigation.

Conclusions

To conclude, a gap-filling implant for open-wedge osteotomies was designed and manufactured. This implant was 3D manufactured in an osteoinductive and biodegradable material that supported cell attachment, growth, and production of early and late osteogenic markers *in vitro*. Finally, an *ex vivo* proof-of-concept of the surgical procedure was successfully performed, implementing the designed wedge scaffolds into the standard osteotomy procedure, while maintaining implant integrity and pre-planned wedge height.

Supplementary information

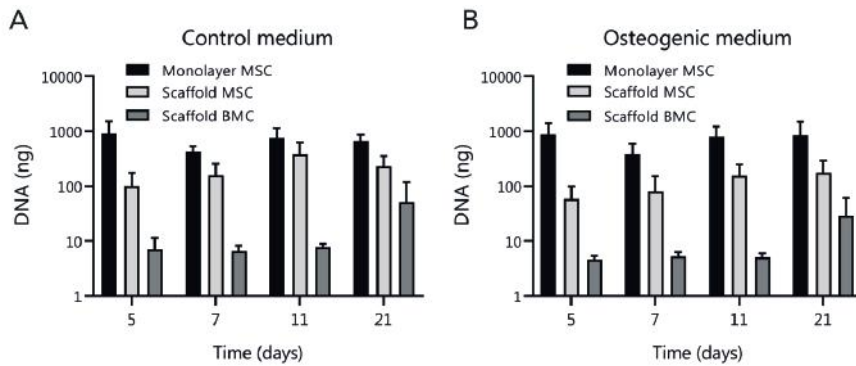
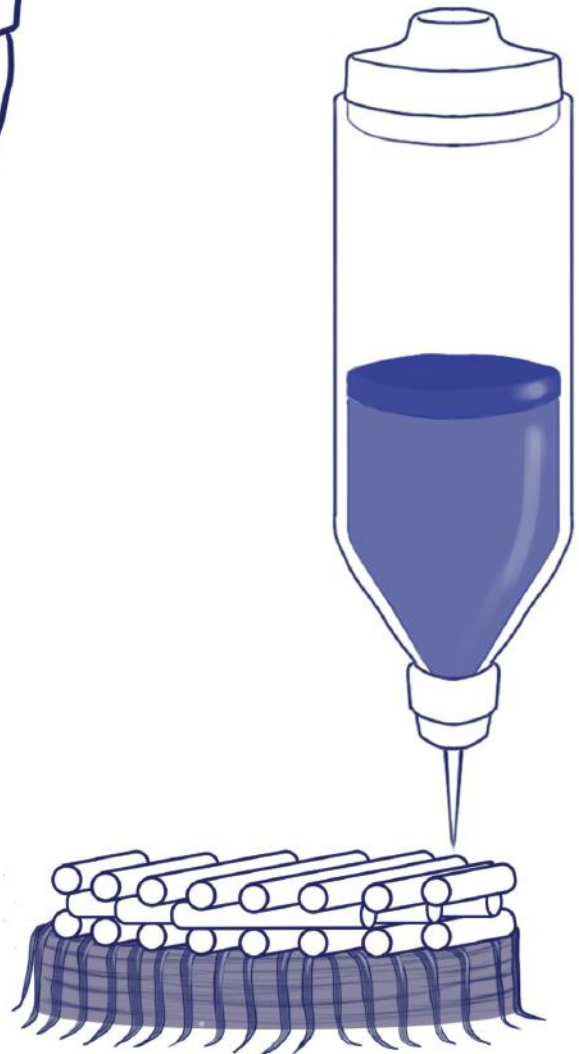


Figure S1. DNA quantification. Quantification of DNA in scaffolds seeded with bone marrow-derived mesenchymal stromal cells (MSC) and bone marrow concentrate (BMC) compared to MSCs cultured in monolayers as controls.



CHAPTER 6

Influence of osmotic swelling restriction on load bearing properties and neo-cartilage matrix formation on osteochondral implant

Nasim Golafshan

Miguel Castilho

Marcela Jiménez

Iris Pennings

Mike Chen

Alicia Damen

Keita Ito

Tina Vermonden

Jos Malda

Abstract

Melt-Electrospinning Writing (MEW) technique can generate micro-fibre scaffolds to further mimic the microstructure and mechanical properties of native articular cartilage (AC) in an effort to develop regenerative treatments for joint damage. The load bearing function of AC is provided by AC's unique extracellular matrix (ECM) structure. In particular, the high water and glycosaminoglycan (GAG) content, together with an organized fibre collagen (type II) structure, creates a swollen tissue able to resist exudation of water under compressive dynamic loads. In this study, a fully degradable osteochondral scaffolds was fabricated by MEW for chondral and extrusion-based printing for bone anchor. A polysaccharide-based hydrogel was used to encapsulate the chondrogenic progenitor cells while the osmotic swelling of the hydrogels was restricted by MEW fibre scaffolds. The fabricated scaffolds did not show any signs of delamination. Furthermore, the restriction of the swelling of the hydrogels improved the performance of the scaffolds under the dynamic mechanical properties. After 28 days of culture, production of sulphated glycosaminoglycans and collagen II was observed within the progenitor cells-inoculated scaffolds. This confirmed the capability of the scaffolds to support neo-cartilage formation. To conclude, these results are a step towards the design and manufacture of biomechanically competent osteochondral implants for cartilage regeneration.

Keywords

3D printing, Osteochondral implants, Bone regeneration, Cartilage regeneration

Introduction

The increasing burden of musculoskeletal disorders, in particular joint disease, is a major challenge for our healthcare systems ^[229]. Originating from an acute injury or micro trauma, joint damage initiates a cycle of degenerative processes that ultimately lead to osteoarthritis (OA), a disabling disease that results in loss and degradation of the articular cartilage (AC) ^[230]. OA affects already 40 million Europeans, and these numbers are expected to rise further as aging and obesity of the population increase, in particular in Western countries ^[231]. Current clinical choices to treat joint tissue defects provide mostly pain relief, but are of limited longevity ^[232,233] as they fail to produce a repair tissue that possess similar mechanical characteristics as the original tissue ^[234].

AC is known to carry joint loads higher than body weight, while providing low friction lubricated surfaces in synovial joints. The ability to provide a load bearing function is the result of the AC's unique extracellular matrix (ECM) structure and composition within the AC. In particular, the high water and glycosaminoglycan (GAG) content, together with an organized fibre collagen (type II) structure, creates a swollen tissue able to resist exudation of water under compressive dynamic loads ^[235,236]. On top of this, the ECM components are distributed heterogeneously throughout the AC's thickness to ensure resistance against both compressive and shear forces. Further, the tissue has a low density of specialized cells, the chondrocytes, that maintain the function of the AC in a high metabolite, low nutrient and mechanically challenging environment.

So far, the proposed regenerative strategies to repair joint tissue have failed to produce a long-term functional solution ^[237,238]. Cell-based therapies are mostly based on the autologous chondrocytes' implantation (ACI), but can only be applied in rather small cartilage defects (< 2cm²) ^[239]. Also, this procedure come with high costs and burden to the patients due to a two-stage surgical procedure that involves first harvesting of cells and then re-implantation ^[240]. Biodegradable biomaterial implants on the other side, fail to provide immediate load-bearing functionality while supporting AC regeneration ^[241,242]. One of the reasons for this failure is the inability of existent biodegradable implants to replicate the swelling behavior of the ECM, while simultaneously providing the restrictive nature of the collagen structure of native AC. Where ultimately this should be combined with attracting trophic factors from progenitor cells that can guide deposition of tissue-specific ECM components appropriately.

To reach for replicating the cartilaginous swelling properties in regenerative implants, GAG-based biomaterials based on chondroitin sulfate (CS), heparin sulfate or hyaluronic acid (HA) have been explored ^[243,244]. These highly negatively-charged

polysaccharides rich in carboxyl and sulfonate groups, are known to attract water in their hydrogel form and retain growth factors that potentially allow for cell infiltration and differentiation. Unfortunately, standalone GAG-based hydrogels, are rather soft and cannot survive load-bearing conditions in synovial joints. Reinforcement with melt electrowriting (MEW) printed fibres offers a promising alternative to achieve mechanically more stable gels by recapitulating the collagen fibre structure. Over the last years, it has been shown that already a small percentage (~7%) of thin, highly organized fibres can result in significant improvements in compressive properties of different soft based hydrogels composed of alginate ^[245], methacryloyl-modified gelatin (GelMA) ^[246,247] or norbornene-modified hyaluronic acid ^[248]. This concept has been explored for reinforcement with degradable polymers, such as poly (ϵ -caprolactone) and with different structural organizations ^[247]. Although promising, this fibre reinforcement strategy does not recapitulate the confinement of the swelling pressure, the biomechanical characteristics of native AC. Moreover, after implantation in the joint, implants are exposed to a combination of high compression and shear loading ^[247], which requires their proper fixation to native surrounding tissue to ensure a stable, long-term performance ^[249,250].

In this study, we hypothesize that (1) the load-bearing functionality can be obtained by engineering a confining fibre reinforced construct that can restrict expansion of a cell conductive swelling hydrogel; and that (2) fixation to the native joint can be provided by anchoring the fibre reinforced swelling hydrogel into a flexible ceramic-based cell free porous structure. To test this hypothesis, we first studied MEW printing parameters to develop a confining fibre reinforced structure that could restrict a swelling hydrogel and simultaneously maintain a high porous internal structure to support new cartilaginous tissue formation. Next, the integration of the bone anchor with a MEW scaffold was studied by exploring direct extrusion of bone anchor material based on calcium phosphate (hydroxyapatite) and PCL, without compromising the integrity of non-anchored MEW fibres. After the MEW scaffold and the bone anchor were integrated, the incorporation process of a hydrogel based on methacryloyl-modified chondroitin sulfate (CSMA) and hyaluronic acid (HAMA) inside of the MEW scaffold was optimized and characterized to ensure the generation of a void-free hydrogel-fibre scaffold. In addition, a rigorous mechanical evaluation was performed to assess load-bearing and frictional properties of the developed implant. And finally, a preliminary study was performed where the swelling hydrogel was seeded with chondrogenic progenitor cells and cultured *in vitro* for up to 28 days in chondrogenic medium. The effect of hydrogel composition and confinement on supporting and promoting neo-cartilage matrix formation was evaluated. All results were bench marked against a non-swelling, well characterized and chondrogenesis

supportive, methacryloyl-modified gelatin hydrogel (GelMA) [251]. Collectively, this study demonstrated that the combination of swelling pressure with well-organized reinforced fibres anchored in an osteo-promotive bone anchor, result in a biomechanically competent AC implant that indicate signs of chondrogenic differentiation in the chondral compartment.

Materials and method

Materials

Sodium hyaluronate was purchased from Lifecore Biomedical (82 kDa, Chaska, MN), and granular medical grade poly-(ϵ -caprolactone) was purchased from Corbion (Purasorb PC 12, The Netherlands). All the other reagents, nanohydroxyapatite (nHA_n) and gelatin (porcine skin, gelatin Type A) were obtained from Sigma-Aldrich (Zwijndrecht, The Netherlands). Organic solvents were purchased from either TCI Europe N.V. or Sigma-Aldrich (Zwijndrecht, The Netherlands). Chondroitin 4-sulfate sodium salt (bovine trachea, lyophilized powder, 19.9 kDa) was synthesized according to a previous protocol [252].

Macromer synthesis and characterization

CSMA, HAMA and GelMA were synthesized by reaction of chondroitin 4-sulfate sodium salt (CS), sodium hyaluronate (HA) and gelatin (Gel) with methacrylic anhydride (MA) following protocols described elsewhere [253]. Briefly, HA (11.9 mmol, 4.8 g) was dissolved in milliQ at a concentration of 2 wt.% (w/v). Next, DMF was added to bring the concentration at 1 wt.% (w/v) and the reaction mixture was placed in an ice bath. Methacrylic anhydride (36.9mmol, 5.5 mL) was then added very slowly, drop-wise over 4 h and pH was adjusted constantly to 8-9 using NaOH 0.5M. Next, the reaction mixture was supplemented with NaCl (final concentration of 0.5M), precipitated in cold ethanol and filtered. Finally, dialysis (cutoff 14 kDa) against water for 3 days, followed by lyophilization yielded HAMA as a white fluffy solid. CSMA was prepared in two steps; first sodium salt of CS was converted in tetrabutyl ammonium salt (CS-TBA) to allow solubility in organic solvents. Then, CS-TBA (31.1 mmol, 24.5g) was dissolved in anhydrous DMSO at a concentration of 2.5 wt.% (w/v) and the mixture was heated at 50°C under N₂. Next, 4-dimethylaminopyridine (36.8mmol, 4.5g) was added, followed by glycidyl methacrylate (37.3mmol, 5.1 mL) and the reaction mixture was stirred for 2.5 days. Finally, the mixture was diluted with milliQ water (DMSO:water ratio 1:1), the pH was adjusted to 5.5 using 0.2M HCl and it was dialyzed (cutoff 14 kDa) against water and lyophilized to yield CSMA as a white fluffy solid. After macromer synthesis, final products were analyzed by Nuclear

Magnetic Resonance ($^1\text{H-NMR}$) in D_2O , using an Agilent 400-MR NMR spectrometer (Agilent Technologies, Santa Clara, CA, USA). Chemical shifts were referred to the residual solvent peak ($\delta = 4.79$ ppm). Data analysis was performed using MestReNova Software and the degree of methacrylation determined as described previously ^[254].

Reinforcing microfibre fabrication

A reinforcing microfibre mesh ($\varnothing = 7$ mm and height = 2 mm), consisting of three different regions, top, middle and bottom, was fabricated with meltelectrowriting. The top and bottom regions consisted of MEW fibres (inter fibre distance = 50 μm) that were deposited in laydown pattern $0^\circ\text{-}45^\circ\text{-}90^\circ\text{-}135^\circ$ alternately to induce a higher density of tangentially aligned fibres. The middle region consisted of box-like MEW fibres in a laydown pattern $0^\circ\text{-}90^\circ\text{-}0^\circ\text{-}90^\circ$ (inter-fibre distance = 400 μm). The thickness of the top and bottom regions was 10%, while the middle region was 80%, of the construct final thickness. The fabrication was performed in a 3D Discovery Evolution meltelectrowriting system (regenHU, Switzerland) using medical-grade polycaprolactone. PCL pellets were loaded in metal cartridge and melted at 80°C . To access the effect of the number of stacked layers in the thickness and open porosity of the middle region, the measured interfibre distance between MEW fibres was compared with the designed one, while varying the number of deposited layers between 200 and 350 and using the following fabrication parameters, acceleration voltage (U) 5–6.5 kV, air pressure (P) 1.30 bar, collector velocity (V) 10 mm/s and collector distances (CD) of 5 mm. To optimize the integration between the top and middle region, both the deflection angle between middle and top layer was measure and the fibre length in the top region, while varying collector speed between 10-40mm/s for a U of 5–6.5 kV, P of 1.30 bar and CD of 5 mm.

Osteochondral implant fabrication

The bone anchor was composed of a flexible bone-inducing material ink composed of 70 wt. % of commercial nHA powder and 30 wt. % PCL and prepared as previously described ^[181,255]. Briefly, nHA-PCL was dissolved in the mixture of dichloromethane, 2-BU-1-(4- (diethylamino) anilino)-3-me-pyrido(1,2-a) benzimidazole - 4 - carbonitrile and dibutyl phthalate (Sigma-Aldrich, Germany) in a ratio of 10:2:1 wt%. Bone ink was left to homogenize for one week at room temperature and then printed by using a pneumatic extrusion-based 3D printing system (3D Discovery, regenHu, Switzerland). nHA-PCL ink was printed on top of three-layered reinforcing microfibre mesh ($\varnothing = 7$ mm and total height ~ 2 mm) placed inside of a custom-made teflon mold. nHA-PCL scaffolds consisted of 2-3 non-porous layers, followed by 10 macroporous layers in a laydown pattern $0^\circ\text{-}0^\circ\text{-}90^\circ\text{-}90^\circ$ (inter-fibre distance = 700 μm) deposited in a rectangular shape ($l = 20$ mm, $w = 10$ mm). nHA-PCL ink extrusion

was performed at room temperature ($\sim 20^\circ\text{C}$) with a 22G conical nozzle, 0.41 mm (Nordson EFD, USA) and using an extrusion pressure of 0.2 MPa and a translational speed of 2 mm/s. The printed bone ink was allowed to rest overnight to allow proper anchoring to the microfibre mesh, and then plugs were punched out of the printed nHA-PCL scaffold using the 7 mm biopsy punch (Acuderm, USA). Subsequently, the microfibre mesh was infused with a 10 wt% CSMA-HAMA (CSMA:HAMA ratio 6.5:1) polymer solution in PBS, supplemented with photoinitiator (lithium phenyl-2,4,6-trimethylbenzoylphosphinate -LAP at 0.2 wt.%) at 4°C overnight. Osteochondral samples were then crosslinked by exposure to UV light at 365 nm for 15 min (UV Handleuchte lamp A. Germany). Control osteochondral implants based on 10 wt.% GelMA were prepared following the same methodology as described above for CSMA-HAMA osteochondral implants.

Sol fraction and volumetric swelling

The effect of the microfibre reinforcing meshes cross-linking efficiency of the hydrogels was assessed through sol fraction analysis, following a method previously described [256]. Briefly, cylindrical reinforced chondral hydrogel structures ($\varnothing = 7$ mm \times height = 2 mm) were prepared in custom-made Teflon molds and cross-linked as described above. Weight of the samples was recorded prior ($m_{\text{in } t=0}$) and after (overnight) lyophilization ($m_{\text{dry } t=0}$). The remaining samples were incubated in PBS at 37°C for 24 h, and dry weight (m_{dry}) was determined after lyophilisation. The sol fraction was then calculated as, sol fraction = $((m_{\text{in } t=0} - m_{\text{dry}})/m_{\text{in } t=0})$. Bulk swelling of hydrogel materials was evaluated by first immersing samples in PBS over 14 days, following by measuring diameter and height of the samples before and after $d = 1, 3, 7$ and 14 days. Swelling was determined as follows, volumetric swelling ratio = $(V_{t=d}/V_0)$, where V_0 and V_t is the volume of the samples before and after PBS incubation, respectively. Both volumetric swelling and sol fraction analysis was performed on microfibre reinforced CSMA-HAMA and GelMA (confined), as well as on non-reinforced CSMA-HAMA and GelMA (as control, unconfined).

Imaging

Light microscopy (Olympus BX51, Olympus Nederland B.V., The Netherlands) was used to assess printed reinforced fibre scaffold quality. Scanning electron microscopy (SEM) (Phenom Pro Desktop SEM, USA) was performed at an accelerating voltage of 10 kV to image both fibre scaffolds alone and after integration with bone anchor. Prior to imaging, all samples were coated with 2 nm of gold. All measurements on printing quality were performed with ImageJ (version 2.0.0). Additionally, high-resolution micro-CT (μCT 100, Scanco Medical AG, Switzerland) analysis was performed on full osteochondral implant to access implant porosity and uniform

hydrogel integration. μ CT was performed at a voltage of 45 kVp, an intensity of 88 mA, and an integration time of 411 ms (Gauss filter applied, sigma = 0.8, support = 1 voxel). A water-based contrast agent solution (Ioversol, Optiray 300 TM) was used to facilitate hydrogel visualization during μ CT analysis. Osteochondral implants porosity was determined by measuring trabecular parameters in acquired 3D μ CT images according to a protocol previously described^[257]. Briefly, after thresholding μ CT images, the volume fraction (BV/TV) and porosity ($1 - (BV/TV)$) were measured with Scanco Medical AG software at different regions of interest (ROI, chondral, transition and bone). ROI were defined manually.

Mechanical testing

Unconfined compression tests were performed on cylindrical shaped osteochondral samples ($\varnothing = 7$ mm and $h = 7$ mm), following similar methodology as previously described^[247]. Briefly, samples were placed in a PBS bath at room temperature and compressed using a flat-ended platen ($\varnothing = 10$ mm) in a universal testing machine (MTS Criterion Model 42, US) equipped with a 50N load cell. A combined stress relaxation and dynamic test was performed. A pre-loaded of 0.05N was first applied to ensure contact between samples and platen and then samples were strained to 15% at a rate of 0.01 mm/s, followed by 900s relaxation. After relaxation, twenty compressive cycles at 2% strain and 1 Hz frequency were then superimposed. Engineered stress-strain curves were calculated from registered force-displacement data. Stress was defined as the applied force divided by the sample's unloaded cross-sectional area, while strain was determined as the ratio between the original sample thickness and displacement. The apparent peak and equilibrium modulus were determined during the ramp phase from the slope of the stress-strain curve near the maximum value of stress (considering the last ten seconds from the peak). The equilibrium modulus was determined by dividing the stress at the final recorded time by 15% strain. The dynamic test was performed directly after the stress-relaxation test. For this, an amplitude of 2% strain at a frequency of 1Hz was used for 20 cycles without the relaxation phase; therefore, deforming the sample between 14% and 16% strain. The dynamic stress was determined by dividing the average change in force by the cross-sectional area of the unloaded sample. The dynamic modulus was determined by dividing the dynamic stress by the 2% strain. At least 5 samples of reinforced CSMA-HAMA and GelMA (confined), as well as non-reinforced CSMA-HAMA and GelMA (as control, unconfined) implants were tested.

Effect of implants on wear of the opposing cartilage was investigated following the same methodology and in-house built apparatus as described in detail elsewhere^[258]. Briefly, osteochondral plugs (OC plugs, $\varnothing = 10$ mm, $h = 8$ mm) and cartilage strips

(l = 22 mm, w = 15 mm, h = 2 mm) were extracted from bovine patellae (n = 13, age 3 – 6 years old) obtained from a local slaughterhouse (Fig S3).

A cylindrical OC defect ($\varnothing = 6$ mm, h = 7 mm) was drilled at the center of OC plugs where implants were manually press-fitted. The cartilage strip was placed in a metal holder with an oval window and screwed to remain in position; while the OC plug, with the press-fitted implant, was fixed to a dead weight placed perpendicularly to the caudal-to-cranial (ca-cr) direction of the cartilage strips (supplementary Fig 3). For the better measurements of the wear properties, PBS was used as the lubricant instead of synovial fluid. Cartilage wear was characterized by applying an axial compression stress of the OC plug on the cartilage strip of 3.18 MPa and 0.33 MPa, when the indenter was sliding in the ca-cr direction and cr-ca direction, respectively. Indenter sliding was applied for 450 or 900 cycles for a 6 mm pathway and at a constant velocity of 2.5 mm/s in the ca-cr and of 3.75 mm/s in the cr-ca direction to approximate to the human gait cycle (stance phase 60% and swing phase 40% of the gait cycle). Cartilage strips were stained with Indian ink ((Royal Talens, Apeldoorn, the Netherlands) for 30 s and imaged before and after testing with an optical microscope (VHX-500F, Keyence Corporations, Osaka, Japan). Wear was quantified by measuring the area of ink retained in the damaged cartilage within a constant region of interest defined manually (oval-shaped area). Measurements were performed with ImageJ (version 2.0.0) and at least 5 samples of reinforced CSMA-HAMA and GelMA (confined) implants were tested.

Cell isolation and culture

Equine chondrogenic progenitor cells (ACPCs) from one donor were isolated and characterized as previously described in detail elsewhere^[249,259]. ACPCs were stored in liquid nitrogen until encapsulation in hydrogels. Before encapsulation, cells were expanded in standard culture flasks at a density of ~ 2300 cell/mm² in medium consisting of high glucose Dulbecco's Modified Eagle Medium (DMEM, Gibco, 31966), supplemented with 10% heat inactivated Fetal Bovine Serum (FBS, biowest, #S181H), 100 u/mL-100 μ g/mL Penicillin-Streptomycin (Gibco, 15140-122), 0.2 mM L-ascorbic acid 2-phosphate in PBS0 (ASAP, Sigma, #A5960), 1% Minimum Essential Medium Non-Essential Amino Acids (NEAA, Gibco, #11140050-035) and 5 ng/mL basic fibroblast growth factor (rh-FGF-2; R&D Systems, #233-FB). ACPCs were used for hydrogel encapsulation at passage 4.

Cell-laden implants fabrication and *in vitro* culture

A pilot assessment (1 donor, n=3 scaffolds per time-point) was first performed to evaluate neocartilage formation in reinforced CSMA-HAMA and GelMA constructs

in vitro. ACPCs were encapsulated in the hydrogel solution, loaded in the MEW structure and cultured up to 28 days after which biochemical and histological evaluations were performed. To assess for the influence of confinement of the swelling CSMA-HAMA polymers, the confined construct was compared to the 'open box' confinement (*i.e.*, with the middle, box-like region reinforcing mesh only) and to free swelling hydrogels (no reinforcing MEW construct, unconfined) after 28 days. First, the MEW reinforcing scaffolds ($\varnothing = 7$, $h = 2$ mm) produced as described above, were sterilized in 70% EtOH, washed in PBS and incubated overnight in expansion medium containing FBS and Pen/Strep at 37°C. Reinforcing scaffolds were dried and placed in sterilized custom-made PDMS molds ($\varnothing = 7 \times h = 2$ mm), with both sides eventually closed off with glass slides. ACPCs (20×10^6 /mL) were dissolved in either CSMA-HAMA or GelMA polymer solution to 10 wt.% (corrected for volume of the cell pellet/solution) and supplemented with the photoinitiator lithium phenyl-2,4,6-trimethylbenzoylphosphinate LAP (0.2 wt. %). The hydrogel precursor solution was then injected into the reinforcing MEW scaffolds with a 25G needle (BD Microlance[®] 3, #300400) and exposed to UV light for 7.5 minutes on both sides (365 nm, intensity 1.2 mW/cm²). After polymerization, the constructs were cultured in chondrogenic differentiation medium, consisting of DMEM (Gibco, Life Technologies, #31966), supplemented with 1% v/v ITS + premix (BD biosciences, #354352), 0.2 mM ASAP (Sigma Aldrich, #A5960), 0.1 μ M dexamethasone (Sigma Aldrich, #D8893), 1% v/v HEPES (Gibco, #15630-080), 100 u/mL-100 μ g/mL Penicillin-Streptomycin (Gibco, 15140-122), and 10 ng/ml of recombinant human transforming growth factor- β 1 (TGF- β 1, Peprotech, #100-21). Over the time of culture, the viability, cell metabolic activity and differentiation status were characterized.

Biochemical assays and histological examination of neocartilage formation

Metabolic activity was evaluated over time by means of the Alamar blue assay (Resazurin sodium salt, Alfa Aesar, R7017) according to manufacturer's protocol with an incubation time of 4 hours. The Resazurin solution was diluted in chondrogenic differentiation medium and was left on the constructs after the measurement until the next medium change. On day 1, 7 and 28, reinforced CSMA-HAMA and GelMA (confined), as well as on non-reinforced CSMA-HAMA and GelMA (as control, unconfined) implants were harvested ($n=4$) and box structure samples ($n=5$) were harvested after 28 days, ($n=3$ per time-point). The biochemical content of the constructs (1/2 sample) was determined and the other half underwent histological analysis. Both parts were weighed after cutting to eventually correct the biochemical contents for the complete scaffold.

For biochemical evaluation, the harvested samples were digested in hyaluronidase (1 mg/mL in MilliQ, Sigma H3884) overnight at 37°C. The digestion solution was spun down at 8000 x *g* for 15 minutes and the supernatant was collected and stored at -20°C. The pellet was further digested with proteinase K (0.5 mg/mL in PBS) overnight at 60 °C. Once more, the digestion solution was spun down at 8000 x *g* for 15 minutes and the supernatant was collected and combined with the hyaluronidase fraction. The DNA contents and Sulphated glycosaminoglycan of the constructs were quantified by means of the Quan-iTPicogreen-dsDNA-kit assay (Molecular Probes, Invitrogen, Carlsbad, USA, P7589) and dimethylmethylene blue (DMMB, Sigma-Aldrich, The Netherlands, #341088) colorimetric assay. To correct for background signal, 'cell free' hydrogels were taken along in the culture experiment, with corresponding culture times to the experimental groups.

Sample pieces designated for (immuno)histochemistry were fixated in 4% buffered formalin for 3 hours at room temperature. Dehydration was performed through a graded ethanol series, followed by clearing in xylene, embedding in paraffin-wax and sectioning into 5 µm-thick slices on a microtome. Slides were deparaffinized with xylene and gradually rehydrated through an ethanol series (100- 70 %) to demi water before starting the immunohistochemistry (IHC) staining. Type II collagen staining (primary antibody Col2A1 II-II6B3, 72 ug/ml, DSHB) was performed to visualize neocartilage formation. Endogenous peroxidase blocking (10 min in 0.3 % H₂O₂) was performed before antigen retrieval (1mg/mL pronase and 10 mg/mL hyaluronidase blocking, 30 minutes each at 37 °C). After protein blocking (30 min, BSA, 5% w/v in PBS) the primary antibody was incubated overnight at 4 °C. Mouse IgG (concentration matched to primary antibody, Dako, X0931) was used as a negative control. Sections were washed 3x for 5 min with PBS-Tween, and incubated with an anti-mouse horseradish peroxidase (HRP)-labelled antibody (Dako, P0447) for 60 minutes at room temperature (RT). The addition of 3,3'-diaminobenzidine (DAB) substrate solution (Dako, #K3468) to the HRP antibodies resulted in a brown staining. Nuclei were counterstained in blue with Mayer's hematoxylin (Merck). Finally, the sections were dehydrated and mounted with EUKITT xylene based embedding medium. Slides were also stained with safranin-O and Fast Green to visualize GAGs. After deparaffinization and rehydration, the sections were incubated with 0.4% aqueous Fast Green for 4 minutes. After washing with acidic alcohol, the slides were stained with 0.125% aqueous Safranin-O (5 minutes). Lastly, the sections were dehydrated and mounted. Histological slides were imaged using a light microscope (Olympus BX51, Olympus Nederland B.V.) equipped with a digital camera (Olympus DP73, Olympus Nederland B.V.).

Statistical analysis

All data were represented as mean \pm standard deviation. The significance of differences between the groups was assessed using a one-way ANOVA and post hoc Tukey's test (Graphpad prism V9). Differences were considered significant at a probability error (p) of $p < 0.05$.

Results

Effect of MEW process on confining microfibre scaffold fabrication

Melt electrowritten fibre scaffolds with dense crossing microfibres at the top and bottom zones and a box structure at the middle/deep zone were successfully produced (Fig 1A). Notably, the multi-layered scaffolds were fabricated with a single MEW printhead and in a single-step printing process. As the precise and reproducible placement of the MEW fibres across the total thickness range of human cartilage (*i.e.*, $\sim 2\text{mm}$ [260]) is challenging [261], the effect of fibre stacking on the construct architecture and porosity was first investigated (Fig 1 B-D). Fibre constructs with thicknesses of approximately 2 mm were obtained with 250 layers without compromising the open and interconnected porosity of approximately 40%. Thicknesses beyond 2 mm could be obtained, but did impact on the open porosity, which typically decreased to less than 15%. Subsequently, we observed that amongst key instrument parameters of MEW process, the collecting speed displayed strong correlation particularly with the fibre deposition at the top zone. By increasing the collecting speed from 10 to 40 mm/s, continuous fibre filaments could be generated, which did not break or rupture during and after printing process (Fig 1E-F). However, one limitation of working at higher collecting speeds was the apparent low thermal adhesion between the top layer and middle box structure (Fig 1G). Fibres at top layer were observed to create a "tenting" phenomenon over the middle zone, resulting in a deflection angle of approximately 30° (Fig 1H-I). This phenomenon can potentially compromise the interfacial mechanical properties between top and middle layers and consequently restrict the hydrogel swelling efficiency. Therefore, a collecting speed of 20 mm/s was used to fabricate confining fibre scaffolds for subsequent evaluation (Fig 1J, Supplemental Fig 1A-B).

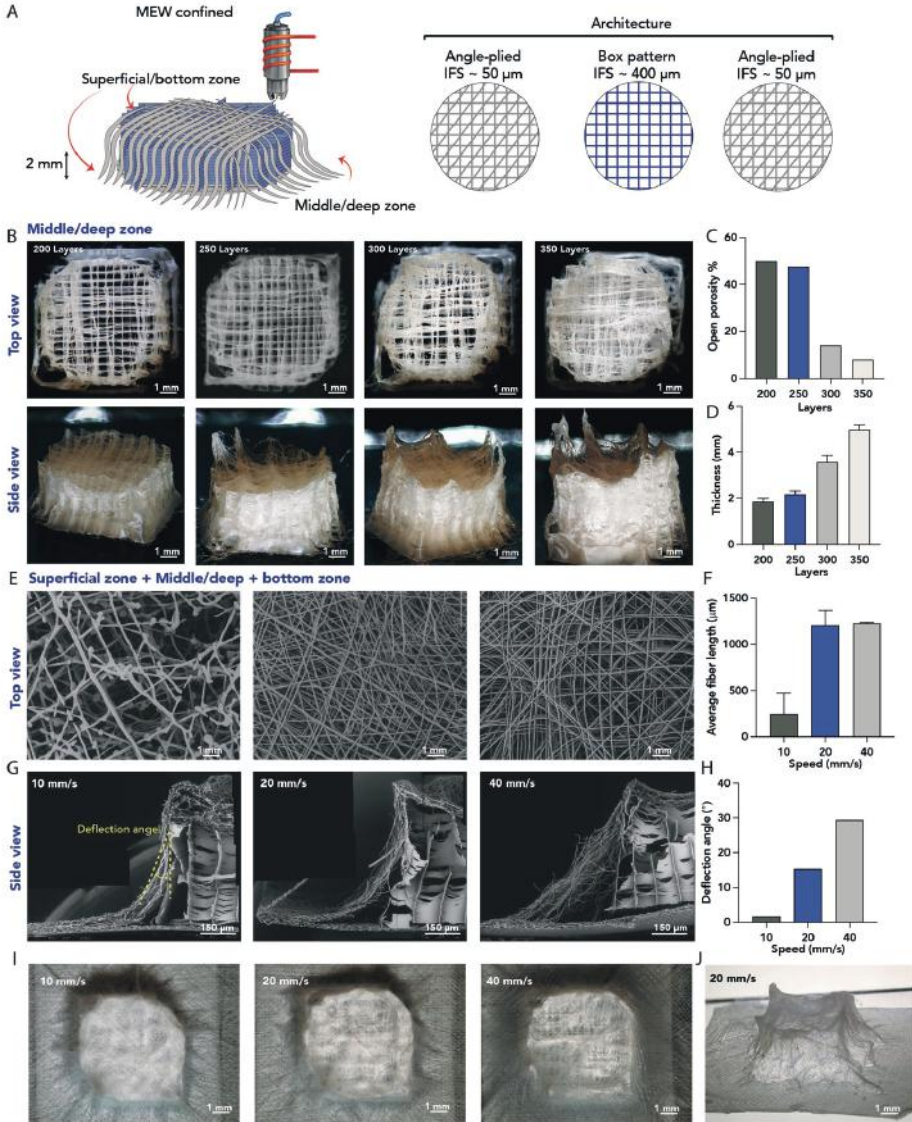


Figure 1. Microfibre reinforcing scaffolds fabrication process. A) Schematic of the reinforcing scaffold design with detail on fibre laydown patterns per region (IFS = interfibre space). B - C) printed middle/deep architecture scaffold with an increasing number of layers. The panel B) shows representative stereoscopic images of printed scaffolds (top and side view) while panel C) and D) present the determined open porosity and thickness, respectively. E - J) confined scaffolds (i.e., with all three regions) printed with superficial layer deposited at increased collector speeds. H) shows representative SEM images of superficial layer and F) the determined average fibre length. Each panel in G) presents a stitched SEM images showing a cross-section of printed scaffolds. Top left black panels were added to fill out empty space. H) presents determined deflection angle between superficial layer and middle/deep regions. I) presents stereoscopic images from confined scaffolds top at and J) side view of confined scaffold used for subsequent test.

Generation of the osteochondral implants

A 3D printable composite paste composed of nHA and PCL was used to serve as the bone anchor as describe elsewhere ^[181,255]. MEW reinforcing scaffolds were anchored in the bony anchor and protruded to the MEW reinforcing scaffold region, acting both as fixation device and reinforcement (Fig 2A-C). The measured porosities of the interface and bone compartment were, 9.6% and 38.3%, respectively; while the porosity of MEW scaffold porosities was, 17.3%, and 48.6% for the superficial and middle/deep zones respectively (Fig 2D). This confirms the printing accuracy of bony paste and the successful integration between MEW scaffold and the bony anchor. Then it was investigated whether the hydrogel material could be effectively incorporated into the multi-layered fibre construct, since this is a critical aspect for the success of the proposed fibre reinforced hydrogel system. To do this, a mass loss and swelling study were first performed to evaluate the cross-linking efficiency of CSMA-HAMA hydrogel alone (unconfined) and CSMA-HAMA within the multi-layered construct (confined) (Fig 2 E-G). The sol-fraction, which is defined as the amount of non-crosslinked polymer after polymerization, increased for the confined CSMA-HAMA from 4.1 ± 3.3 % to 8.5 ± 2.9 % compared to the CSMA-HAMA alone (Fig 2E). Although we estimated that top fibrous layer may hampered UV light penetration and consequently the hydrogel cross-linking, but the sol fraction of confined and unconfined CSMA-HAMA is not significantly different. The sol fraction for GelMA hydrogels indicated that the confined GelMA is significantly decreased for the confined GelMA (Fig 2E). It was also observed that the fibrous scaffold architecture was able to restrict swelling of the GelMA hydrogels and there were no signs of separation between the superficial layer and the middle-deep region of the MEW scaffold for both hydrogel compositions (Fig 2F-G). Lastly, μ CT analysis was performed to investigate hydrogel distribution within the MEW fibre scaffolds. Homogenous hydrogel distribution was observed for both CSMA-HAMA and GelMA groups (Fig 2H). Despite the fact that the multilayered scaffolds being hydrophilic (contact angle close to zero after NaOH treatment, Supplemental Table 2), the high viscosity combined with low sol fraction of CSMA-HAMA hydrogel might have prevented complete filling of the fibre networks pores compare to GelMA hydrogel.

Mechanical properties of engineered constructs

The mechanical properties of scaffolds were evaluated under a combined stress-relaxation and dynamic unconfined compression testing regime (Fig 3 A-F). The peak and equilibrium compressive modulus of the multi-layered reinforced hydrogel scaffolds (confined) increased significantly when compared to non-reinforced scaffolds (unconfined) (Fig 3D-F). The peak modulus of CSMA-HAMA scaffolds was 0.66 ± 0.10 MPa and 0.20 ± 0.01 MPa for confined and unconfined conditions,

respectively, which represents an approximate 3-fold increase compared to hydrogel alone. In the case of the GelMA based implants, the peak modulus was 0.39 ± 0.08 MPa and 0.04 ± 0.01 MPa for confined and unconfined conditions, respectively, which represents a 10-fold increase compared to hydrogel alone. This higher increase observed for the GelMA hydrogels (unconfined to confined) might be related to the big difference in sol fraction.

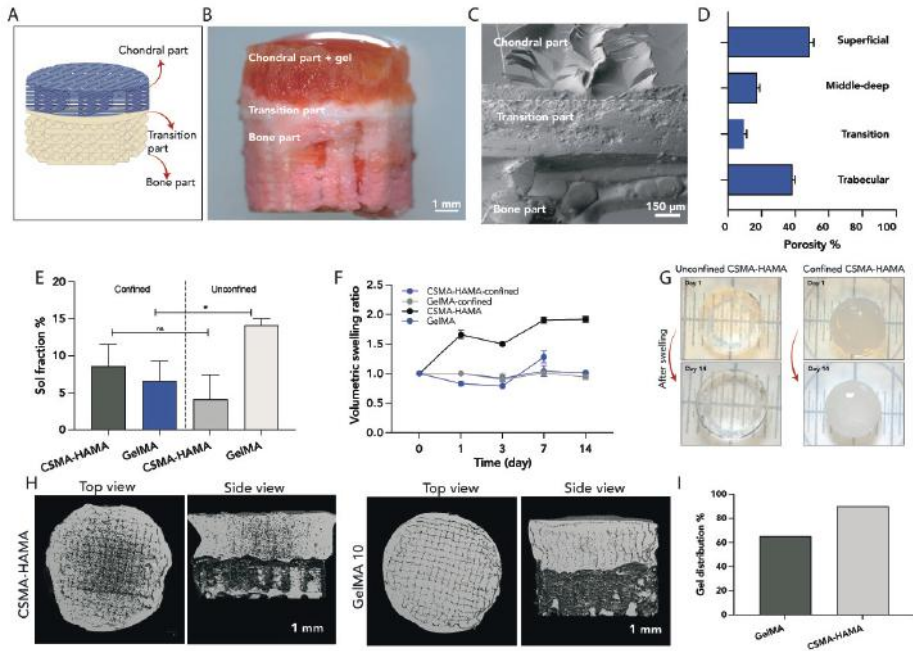


Figure 2. Integrating hydrogel and bone anchor with microfibre reinforcing scaffold for engineering osteochondral implants. A) Schematic of osteochondral (OC) implant design. B) Representative stereoscopic image of an OC unit with C) SEM images detailing the microstructure at different regions and D) the respective determined porosities. Chondral part only refers to reinforcing microfibre scaffold. E) Sol fraction and F) volumetric swelling of confined and unconfined hydrogel scaffolds without bone anchor. G) Representative stereoscopic images of confined and unconfined hydrogel after 14 days swelling. H) representative μ CT reconstruction images of OC units infused with either CSMA-HAMA or GelMA 10 hydrogel. Black regions within chondral implant represent absence of hydrogel. I) Percentage of hydrogel filling within the chondral region determined from μ CT reconstruction images of OC units. * Indicates a significant difference, $p = 0.05$.

In addition, the equilibrium and dynamic modulus were characterized as these are two important mechanical parameters to assess the mechanical function of engineered cartilage replacements. The equilibrium modulus is a measure of the compressive stiffness of the solid matrix; while dynamic modulus is related to

permeability of the solid matrix and represents the capacity of the construct to generate fluid pressurization and thus load support. No significant differences were observed between equilibrium modulus of CSMA-HAMA confined 0.21 ± 0.12 MPa and unconfined 0.18 ± 0.01 MPa; while in the case of the GelMA based scaffolds, the equilibrium modulus was 0.27 ± 0.01 and 0.02 ± 0.01 MPa for confined and unconfined conditions, respectively, which represents a significant increase of almost 14 times (Fig 3E). Interestingly, the obtained compressive peak and equilibrium modulus of the confined CSMA-HAMA constructs are in same order of magnitude of native (human) articular cartilage, although at the lower end of the previously reported values (60-80 kPa for compressive peak and 0.8-1.2 MPa for equilibrium modulus) ^[262]. In addition, the dynamic modulus of the confined CSMA-HAMA (0.73 ± 0.22 MPa) constructs showed an increase of approximately 3 times when compared to the unconfined gels (0.27 ± 0.01 MPa) (Fig 3F). In the contrast, there was no difference between the dynamic modulus of confined (0.06 ± 0.02 MPa) and unconfined GelMA constructs (0.05 ± 0.01 MPa). This is possible related with the higher capacity of CSMA-HAMA constructs to generate fluid pressurization.

In addition to being mechanically competent to bear compressive load, the frictional properties of cartilage implants should be sufficient in order for them to articulate and not damage the opposing native cartilage. Therefore, the lubrication of confined implant surfaces was investigated by assessing wear of the opposing cartilage using an in-house built set up (Fig 3G-I, Supplemental Figure 3). As expected, no significant differences in Indian ink retention were observed between CSMA-HAMA and GelMA confined implants at both 450 and 900 loading cycles, indicating the hydrogel composition has not affected the opposing cartilage (Fig 3I). However, an increase in wear of cartilage was observed from 450 to 900 sliding-indenting cycles. This is probably attributed to the partial removal of the hydrogel top layer and subsequent exposure of PCL reinforcing fibres (Fig 3J).

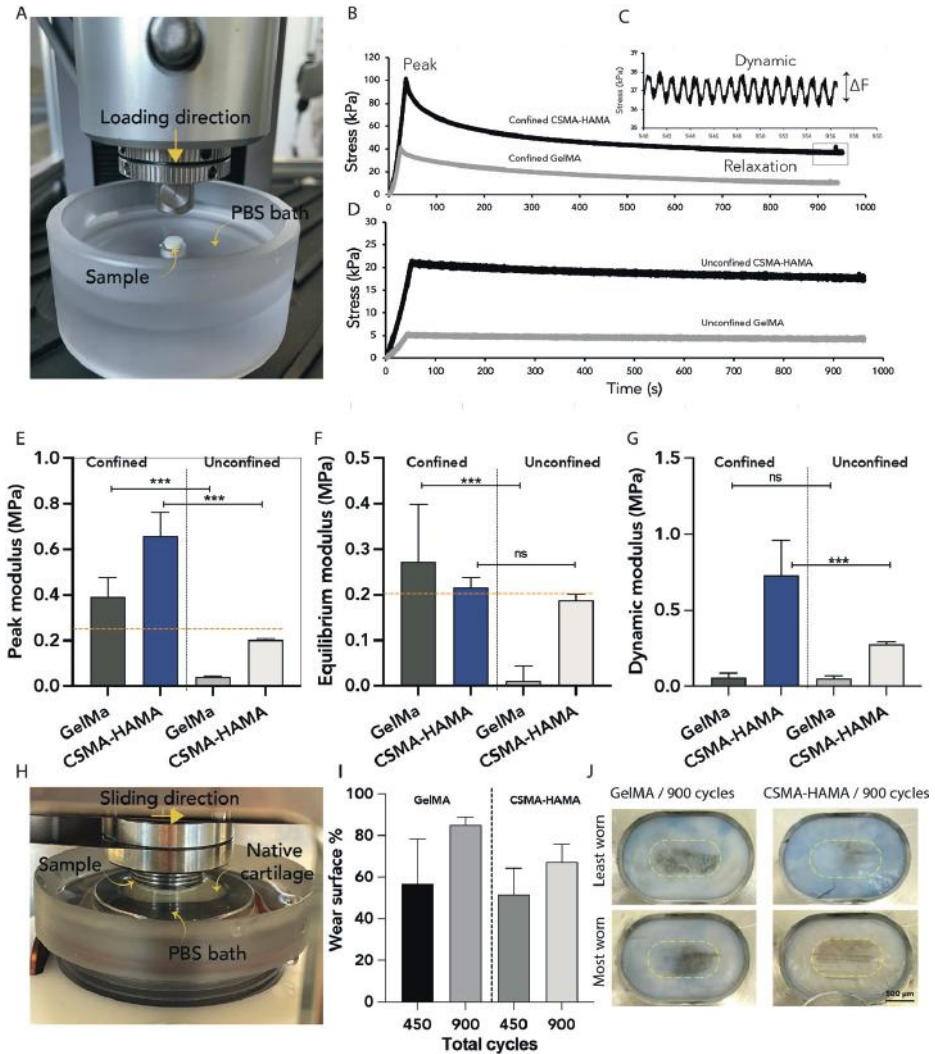


Figure 3. Mechanical characteristics of engineered OC implants. A) Set-up used for unconfined compression tests. B) Representative stress relaxation curves of confined and unconfined CSMA-HAMA (black line) and GelMA (grey line) implants. C) Detail of stress-time curve obtained from dynamic loading testing procedure. D) Compressive peak modulus, E) equilibrium modulus, and F) dynamic modulus in unconfined compression of confined and unconfined CSMA-HAMA and GelMA engineered OC implants. Dotted yellow lines indicate the minimal value recorded for articular cartilage in literature [263]. G) Set-up used to evaluate articular cartilage wear under loading with different OC implants. H) determined cartilage wear surface changes, and respective I) representative stereoscopic images of wear patterns of cartilage, after loading with confined CSMA-HAMA and GelMA engineered OC implants. Black regions indicate damaged regions. Yellow line represents region of interest used to calculate wear surface. *** indicate statistically significant differences (** $p < 0.001$), whereas “ns” denotes no significance (one-way ANOVA).

***In vitro* cartilage matrix formation**

In vitro investigation for ACPCs encapsulated in hydrogels are presented in Fig 4, Supplemental Fig 4 and Supplemental Fig 5. Histological staining for coll II indicates that chondrocytes in unconfined samples seem to differentiate better and deposit more coll II than confined constructs specially at the edges of the scaffolds (Fig S5B, qualitative observations). Although no clear differences in terms of coll II deposition were observed between CSMA-HAMA or GelMA unconfined samples, the coll II localization was different. The GelMA scaffolds showed localization of a very intense col II staining in their direct surrounding and some matrix in between these cell aggregates if they were located closely to each other. While for the CSMA-HAMA scaffolds, the matrix was stained more uniformly. Interestingly, the unconfined areas in MEW reinforced constructs (*i.e.* top part at the box construct - the 'free swelling' area) and top and bottom part of the MEW constructs and unconfined showed signs of better differentiation than in the core, as demonstrated by higher amounts of coll II deposition. This is both observed for the CSMA-HAMA and GelMA samples.

Furthermore, histological staining for GAG deposition on both CSMA-HAMA and GelMA samples confirmed differentiation of the ACPCs (Fig 4C). The GelMA scaffolds showed an increase in aggregation of the ACPCs over time (not yet observed after 7 days, as white arrowheads in Supplemental Fig 5), which was not observed in the CSMA-HAMA scaffolds. Interestingly, ACPC cultured in the confined CSMA-HAMA scaffolds had a more round morphology, while in the unconfined CSMA-HAMA scaffolds, cells presented in general a more elongated morphology (Fig 4 C, Supplemental Fig 5). For the GelMA scaffolds this is generally not the case, all cells show a round morphology at both day 7 and day 28. To confirm ACPC differentiation and cartilage matrix deposition, deposited GAGs were quantified (Fig 4D). In general, a higher deposition of GAGs was observed for CSMA-HAMA scaffolds when compared to GelMA scaffolds. Interestingly, this difference was higher in the confined groups when compared to the unconfined ones. This might be attributed to the fact that CSMA-HAMA gel is already providing GAGs to the cells (supplemental Fig 4) and the MEW fibres prevent the GAGs from leaching into the culture medium. In the cell free situation these GAGs could easily diffuse out of the samples (supplemental Fig 4).

Basically, the confined CSMA-HAMA groups show a synergistic effect between ACPC produced GAGs and that already available in CSMA-HAMA bulk material. Lastly, we confirmed that ACPCs showed a stable metabolically active over the culture period, independent of hydrogel type and reinforcement (Fig 4E).

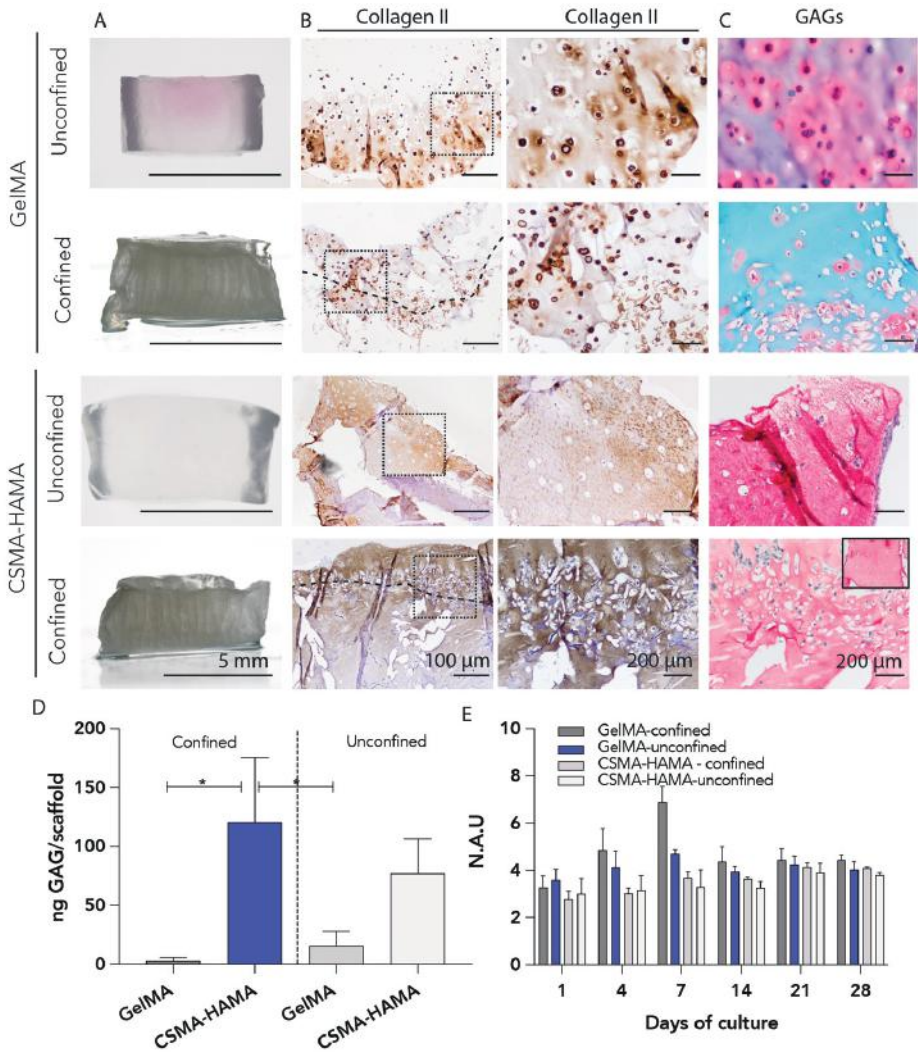


Figure 4. Chondrocyte performance in the hydrogel/ microfibre microenvironment. A) Macroscopic images and B – C) histological and immunohistochemistry analysis of confined and unconfined CSMA-HAMA and GelMA engineered implants without bone anchor. Parallel tissue sections stained for B) collagen type II and C) GAGs after 28 days of *in vitro* culture in chondrogenic medium. D) Quantitative analysis of the GAGs in the engineered constructs normalized to cell free hydrogels. E) Chondrocytes metabolic activity over 28 days of *in vitro* culture.

Discussion

The first motivation of this study was to develop a scaffold that better recapitulates the mechanical properties of native AC as well as the supporting for AC regeneration. In an attempt to mimic the collagen fibres in native AC, we have fabricated a MEW fibre scaffolds with dense crossing fibres at the top and bottom zones (superficial zone) and a box structure at the middle/deep zone. As normal AC contains interwoven collagen bundles near the articular surface, the MEW fibre scaffolds were printed with the same structure on the superficial zone to provide more strength to scaffolds. The middle/deep zone structure was printed in a box-like structure of multiple stacked fibres. The fabrication of MEW fibrous scaffolds has been done using a single step with one printhead to build the thickness of native AC. We have shown that by observing the collecting speed, the dense top layer could achieve without delamination at 20 mm/s. This is because of the sufficient time that the fibres can be stacked and bond with the previous zone without quilling of the fibres.

To fabricate fully degradable osteochondral scaffolds, the tough bone anchor, and the transition of bone to cartilage has been done after the printing of MEW fibre scaffolds using nHA-PCL. This overcomes the brittleness of the ceramics-based bone anchors reported in previously study ^[249]. It is shown in the current research that to fabricate a 3D osteochondral implant by utilizing different printing techniques, all the compartments of the osteochondral scaffolds have bonded perfectly. This is due to the flow of polymeric phase of bone compartment to MEW fibre scaffolds.

We used a polysaccharide-based hydrogels (CSMA-HAMA), mimicking the native cartilage ECM, as a carrier of the chondrogenic progenitor cells. However, as the hydrogel swells, the mechanical stiffness decreases. Therefore, the swelling of hydrogels was restricted by the MEW fibre scaffolds. We observed that the viscosity of the hydrogels plays an important deterrent of the ability of the gel to penetrate MEW fibre scaffolds. Even if the CSMA-HAMA was not distributed homogenously, the mechanical properties of confined MEW fibre scaffolds improved significantly. The reinforcement and the increase in the dynamic modulus of the scaffolds containing CSMA-HAMA than GelMA, are likely to be due to the synergy between the interaction with the MEW fibers and the osmotic stiffening that takes place when the MEW fibers restrain the swelling generated by this hydrogel. This suggests that the mechanical properties of these scaffolds could further improve once cells are incorporated due to the increased proteoglycan content as a result of the deposition by the embedded cells. Previous work has demonstrated the

reinforcement of hydrogels using MEW scaffolds due to resistance provided by the fiber cross-section interconnections and the tension exerted over the fibers by lateral expansion ^[247].

The effect of sliding the scaffolds in an *ex vivo* set up of the physiologically environment ^[264] showed that native cartilage can resist the wear exerted by the scaffolds. Despite that the cartilage strips showed a difference in the ink uptake in the indented region compared to the surrounding cartilage, macroscopically none of them suffered severe damage. But this may be an issue for the long run test which needs more evaluations.

Hydrogel stiffness has been shown to play an important role in modulating cell-based cartilage formation in 3D ^[265]. Generally, confined CSMA-HAMA have been shown to support greater neocartilage deposition by encapsulated cells *in vitro*. That might be due to the restriction of swelled hydrogels over time which keep the modulus of hydrogels almost the same over time and prevent the migration of the cells in 3D environment of hydrogels ^[266].

Conclusions

In conclusion, we have demonstrated that it is possible to fabricate an osteochondral scaffold that can further approximate the functional properties of both the chondral and bone compartments. The microstructure of chondral compartment including superficial and middle-deep zones improved the mechanical properties. The MEW fibre scaffolds restrict the osmotic swelling of hydrogel, which results in the improvement in mechanical properties. By encapsulating progenitor cells into polysaccharide-based hydrogel, ECM formation may improve the toughness of the implants. Our results also demonstrate that the new composite construct is able to support neo-cartilage formation after 28 days culturing. However, further work is needed to investigate the effect of ECM production on dynamic mechanical properties. Taken together, this research helps to take the next steps to develop fully degradable and mechanical competent osteochondral scaffolds for cartilage regeneration.

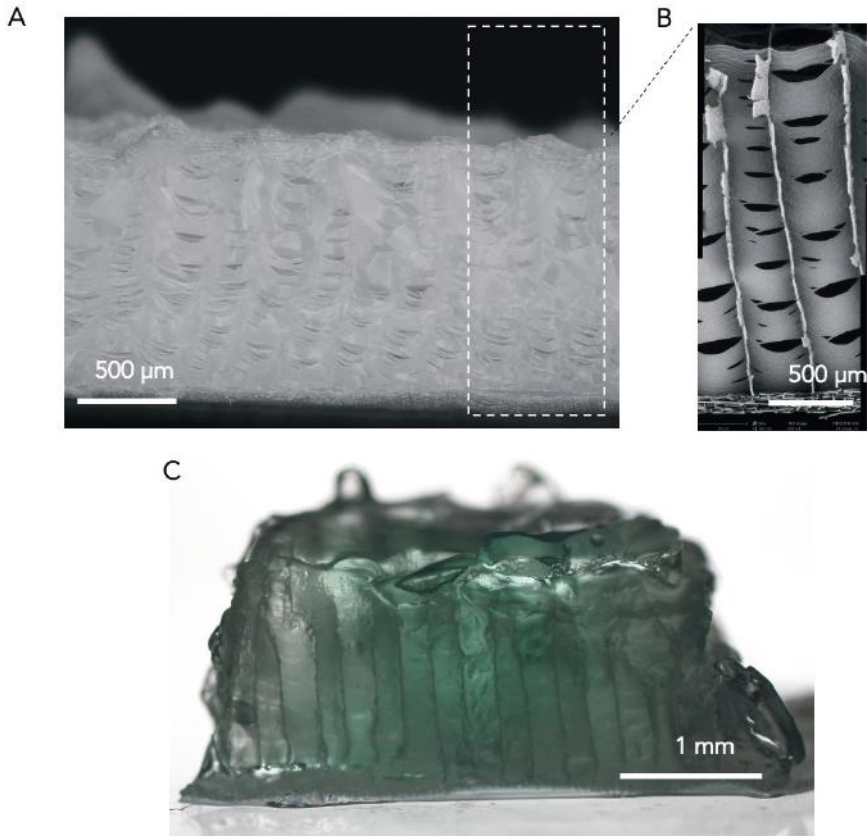
Supplementary Information

Supplemental Table 1. Degree of metacrylation of polymers used in the present work determined by Proton nuclear magnetic resonance ($^1\text{H-NMR}$)

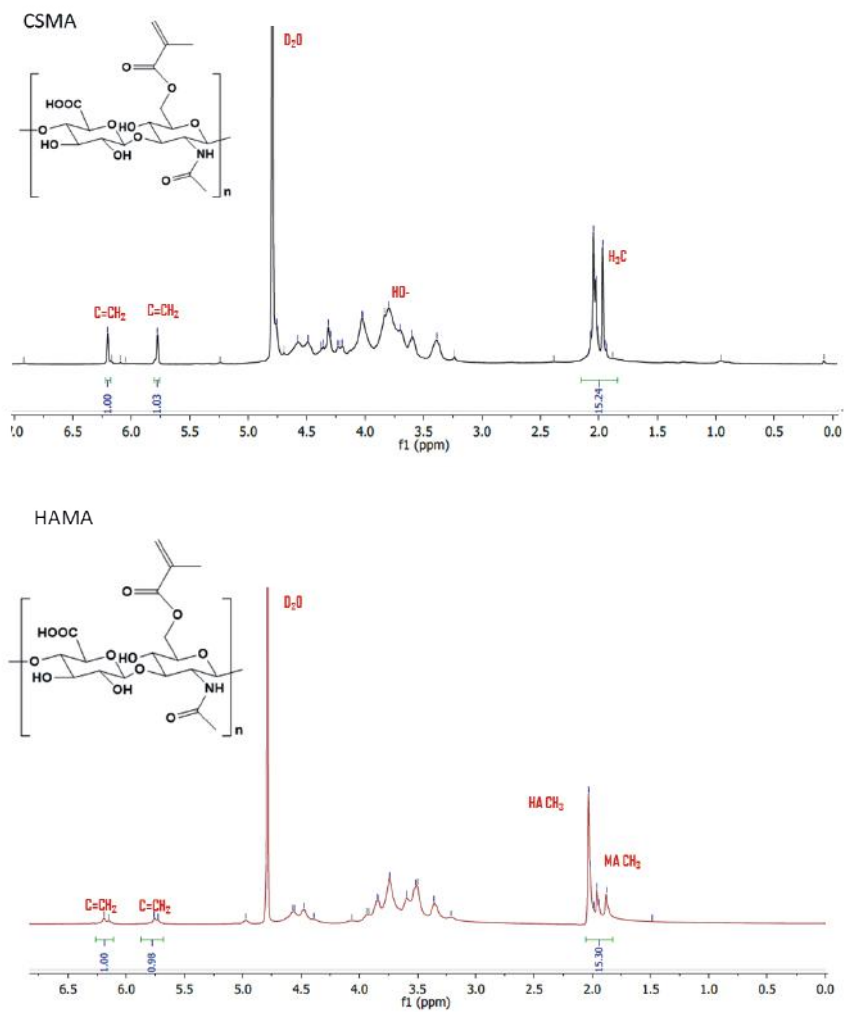
Polymer	CSMA	HAMA	GelMA
$^1\text{H-NMR}$	23 %	39 %	78 %

Supplemental Table 2. Effect of post printing sodium hydroxide (NaOH) treatment on fibre scaffold wettability.

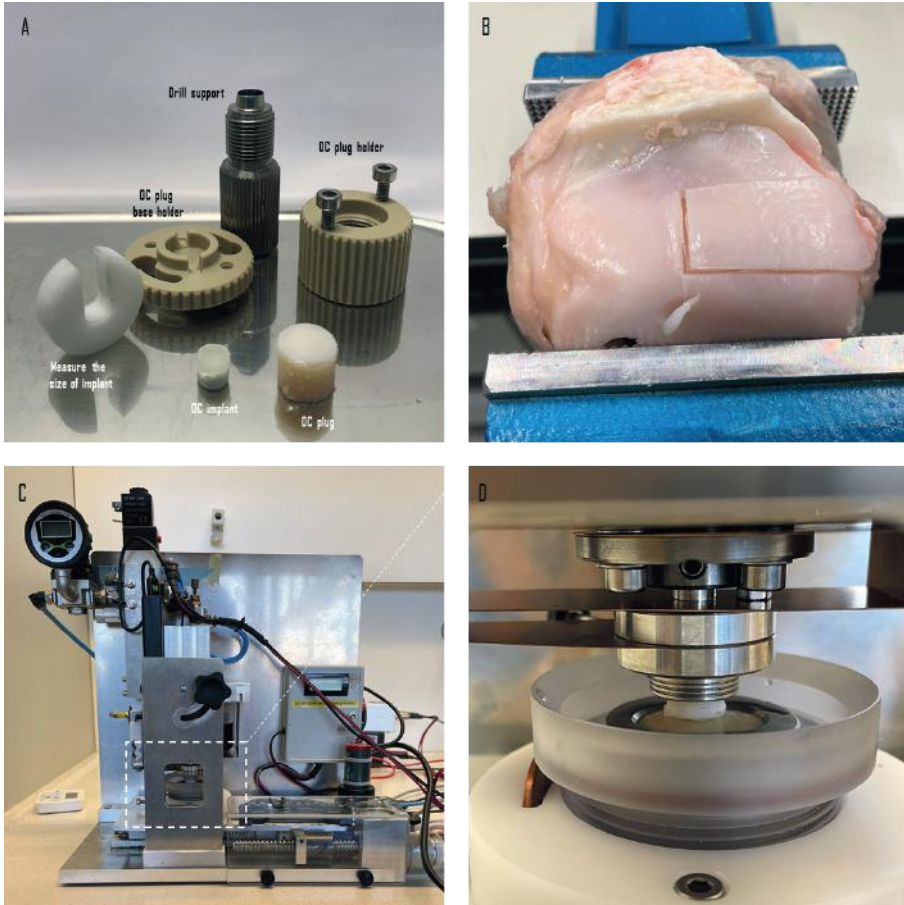
NaOH etching time (min)	Selected images of the wettability measurements	Determined contact angle ($^\circ$)
0		119.8 ± 1.3
5		116 ± 0.5
15		72.6 ± 6.2
30		0



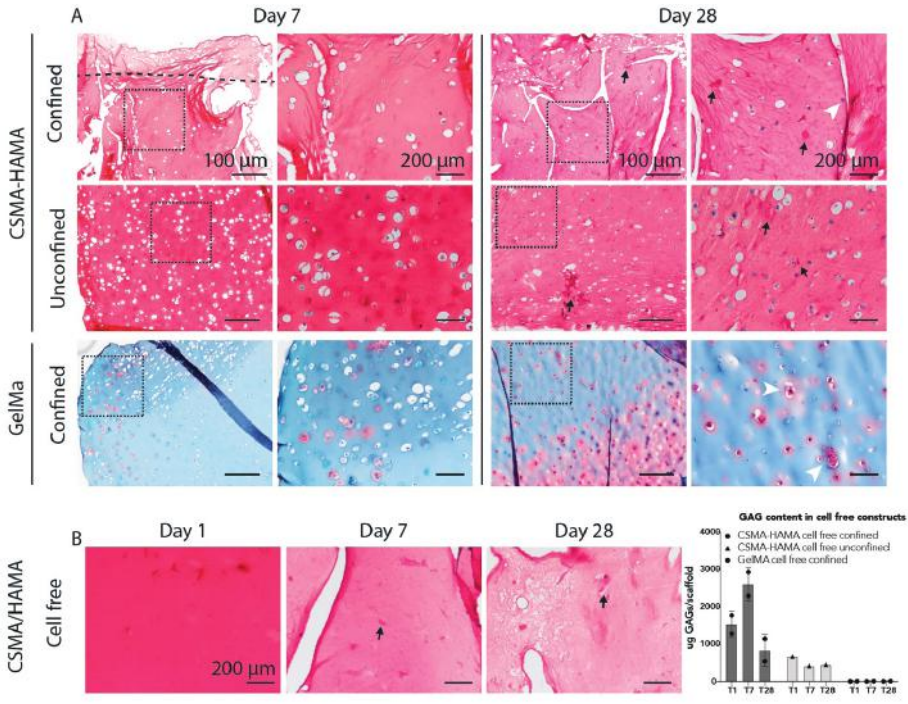
Supplemental Figure 1. Microfibre reinforcing scaffold. A) Macroscopic image of printed scaffold without superficial layer, and B) SEM of scaffold cross section highlighting well organized fibre stacking.



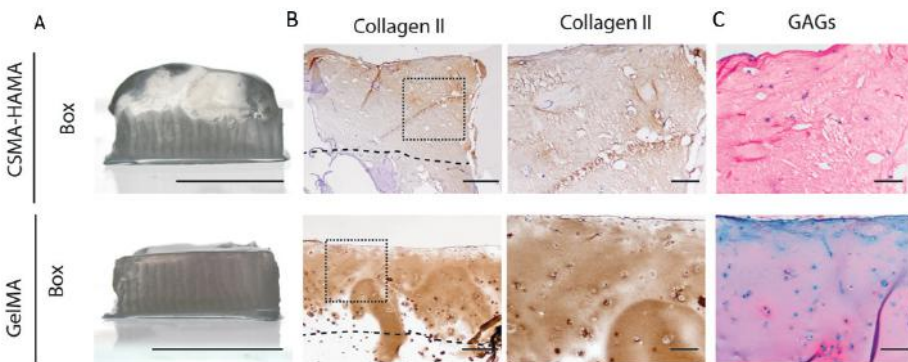
Supplemental Figure 2. NMR spectrum showing successful metacrylation of CS and HA polymers. Characteristic peaks are identified in red.



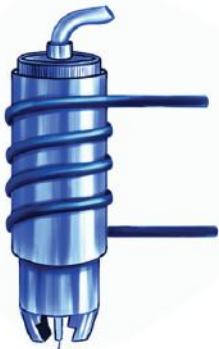
Supplemental Figure 3. A) Wear set-up tools and prepared osteochondral (OC) implants. B) Bovine patella with OC strip represented. C) In-house built wear set-up testing and D) detail of OC sample holder.



Supplemental Figure 4. GAGs deposition in confined and unconfined CSMA-HAMA and GelMA engineered implants without bone anchor. A) Parallel tissue sections stained with Safranin-O (GAG). B) Cell free CSMA-HAMA gel stained with Safranin-O used as control group. C) Quantitative evaluation of GAG content in different cell free tested groups.



Supplemental Figure 5. Chondrocyte performance in the hydrogel/ microfibre microenvironment. A) Macroscopic images and B – C) histological and immunohistochemistry analysis of CSMA-HAMA and GelMA hydrogels reinforced with only middle/deep region reinforced scaffolds (box-shaped) and without bone anchor. Analysis performed after over 28 days of *in vitro* culture.



CHAPTER 7

Composite graded melt electrowritten scaffolds for regeneration of the periodontal ligament-to-bone interface

Nasim Golafshan

Miguel Castilho

Arwa Daghery

Morteza Alehosseini

Firoz Babu Kadumudi

Tom van de Kemp

Mylene de Ruijter

Konstantinos Krikonis

Renan Dal-Fabbro

Alireza Dolatshahi-Pirouz

Marco C. Bottino

Jos Malda

Abstract

Periodontitis is a ubiquitous chronic inflammatory, bacteria-triggered oral disease affecting the adult population. If left untreated, periodontitis can lead to severe tissue destruction, eventually resulting in tooth loss. Despite previous efforts in clinically managing the disease, therapeutic strategies are still lacking. Herein, melt electrowriting (MEW) is utilized to develop a compositionally and structurally tailored graded scaffold for regeneration of the periodontal ligament-to-bone interface. The composite scaffolds, consisting of fibers of polycaprolactone (PCL) and fibers of PCL-containing magnesium phosphate (MgP) were fabricated using MEW. To maximize the bond between bone (MgP) and ligament (PCL) regions, we evaluated two different fiber architectures in the interface area. These were a crosshatch pattern at a 0/90° angle and a random pattern. MgP fibrous scaffolds were able to promote *in vitro* bone formation even in culture media devoid of osteogenic supplements. Mechanical properties after MgP incorporation resulted in an increase of the elastic modulus and yield stress of the scaffolds and fiber orientation in the interfacial zone affected the interfacial toughness. Composite graded MEW scaffolds enhanced bone fill when implanted in an *in vivo* periodontal fenestration defect model in rats. The presence of an interfacial zone allows coordinated regeneration of multi-tissues as indicated by higher expression of bone, ligament, and cementoblastic markers compared to empty defects. Collectively, MEW-fabricated scaffolds having compositionally, and structurally tailored zones exhibit a good mimicry of the periodontal complex, with excellent regenerative capacity and great potential as a defect-specific treatment strategy.

Keywords

Periodontitis, melt electrowriting, bone regeneration, periodontal ligament, interface.

Introduction

The interfaces between bone and connective tissues, *e.g.*, cartilage, ligament and tendon, are characterized by spatial changes in cell phenotype and matrix composition and organization^[267]. These changes result in graded biomechanical properties that allow the transmission of load without creating stress concentrations^[268]. In some interface regions, such as the bone-cartilage or bone-ligament interfaces, differences in mechanical properties (*e.g.*, stiffness), can reach three to four orders of magnitude within a very short distance^[269]. Undoubtedly, this highlights the clinical challenge of regenerating these structurally and functionally complex tissue interfaces^[270]. One of the interfaces that is particularly difficult to regenerate is the periodontal ligament-to-bone (PDL-bone) interface. The PDL is situated between the roots of the teeth and the alveolar bone sockets^[271]. Collagen fibers, known as Sharpey's fibers, form a firm connection between the tooth cementum and alveolar bone. These fibers are partially mineralized and inserted in the alveolar bone/cementum at an oblique angle, which ensures transmission of the occlusal force from the tooth to the alveolar bone^[271].

In the event of periodontitis, a widespread chronic inflammatory disease, the PDL-bone interface gets impaired, leading to tooth mobility, which without proper treatment can ultimately result in tooth loss^[272]. In Europe alone, periodontitis affects approximately 40% of older people^[273]. This results in significant loss of quality of life and increased healthcare costs^[274]. Conventional treatment methods, including but not limited to scaling and root planning, often result in disorganized tissue formation with inferior properties compared to their native counterpart^[275–277]. This ultimately leads to poor long-term outcomes and high failure rates, extenuating the need for the development of therapeutic strategies for regeneration of the PDL-bone interface^[278,279].

Current regenerative efforts are typically directed toward the development of composite^[247,280], stratified scaffolds^[281], with graded structures and physico-chemical compositions. There are many conventional techniques to produce 3D structures with characteristics to enhance tissue regeneration. Additive manufacturing (AM) allows for the fabrication of defect- and tissue-specific scaffolds with the ability to mimic native tissue morphology and biomechanics through various 3D printing technologies. A number of these techniques have been successfully used to engineer multi-layered fiber support structures to capture some of the complexity of native tissues, such as the interface between bone and ligaments; however, none of them could fully replicate the structural organization and long-term functional properties of native interface tissues. More recently, melt electrowriting techniques

have been introduced as a 3D printing technology to obtain organized microfiber scaffolds. This 3D printing technology is distinct from others in that the high fiber resolution (2-20 μm) is accompanied by the ability to 3D print structures with controlled microgeometries. This differs from other 3D printing technologies that have resolution limits of around 20 μm or are challenged in fabricating controlled microgeometries. In fact, this ability to create defined scaffolds' microgeometries is the reason why electrowriting ensued fiber scaffolds significant advantages to the regeneration of native tissue interfaces^[282].

Early attempts, including, scaffolds with PDL- and bone-specific regions using polymer fibers^[270] have shown encouraging results. Notably, bilayered scaffolds with aligned fibers for the PDL zone^[270], and graded polycaprolactone (PCL) scaffolds with distinct fiber alignments for bone and ligament zones^[283], have led to positive prospects in the quest to regenerate the periodontal ligament-to-bone interface. One of the particularly difficult interfaces to regenerate is the periodontal ligament-to-bone (PDL-bone) interface. Previous research has used MEW to create scaffolds tailored to bone and PDL regions^[283,19]. However, these studies did not produce a graded scaffold that mimics the native periodontal complex mechanical function. In this study, we not only focused on creating zonal-specific scaffolds for bone and PDL but also investigated the use of an interfacial zone to enhance the bond between the bone (MgP) and ligament (PCL) regions, with the goal of improving the overall mechanical performance and tissue-specific regenerative outcome. For instance, tissue-specific bilayered PCL scaffolds were fabricated by melt electrowriting (MEW). The resulting scaffolds encompassing two distinct zones, with specific fiber architecture and composition, were able to promote differentiation of human-derived periodontal ligament stem cells (hPDLSCs) toward ligament and bone lineage dependent on the fiber configuration and composition^[284,285].

Therefore, the control of fiber configuration and composition is necessary for the PDL-bone interface regeneration. However, existing scaffolds lack the appropriate fiber configuration and composition to enable the regeneration of such complex interfaces. The fiber organization can promote ligamentogenesis and drive PDL-like tissue formation^[285], while the chemical composition with osteoconductive properties can promote bone regeneration. Among the osteoconductive materials, magnesium phosphate (MgP) bioceramics have shown great ability to promote bone and degrade *in vivo*^[181,255]. Thus, we hypothesize that an osteoconductive scaffold with a graded blend of MgP bioceramics and polycaprolactone (PCL) with tissue-specific, stable interfacial zone and structural properties can facilitate long-term bone-to-ligament interface regeneration. Furthermore, the one-step fabrication

strategy to develop compositionally and structurally tailored graded scaffolds using MEW can achieve this challenging requirement. The effect of MgP content on the MEW processing was investigated in order to obtain reproducible and mechanically stable fibrous scaffolds with micrometer sizes and osteoconductive ability. Scaffolds' mechanical stability was investigated under uniaxial tensile loading while osteogenic properties were addressed *in vitro* over 21 days in both expansion and osteogenic medium. Further, the interfacial adhesion properties of graded scaffolds were evaluated *ex vivo*. Finally, the ability of as-fabricated graded scaffolds to promote synchronized regeneration of bone and PDL ligament was determined in an *in vivo* orthotopic periodontal rat model over 6 weeks.

Experimental Section

Biomaterial MgP-based bioceramic ink preparation

MgP-based inks were prepared by incorporating commercial magnesium phosphate ($\text{Mg}_3(\text{PO}_4)_2$ (Sigma Aldrich, Germany) at 10 and 20 wt.% concentration into PCL (PURASORB® PC 12, Corbion Inc., Netherlands), here abbreviated as 10MgP and 20MgP, respectively. Incorporation of MgP was performed by first dissolving PCL in dichloromethane (DCM, Honeywell™, USA) for 6 h with the subsequent addition of MgP under constant stirring. Blend homogenization was obtained by overnight stirring. Finally, the MgP-based ink was precipitated into pure ethanol (Sigma Aldrich, Germany), and the precipitate was dried in air at room temperature overnight.

Particle size and thermogravimetric analyses

MgP particle morphology and size were analyzed using Scanning Electron Microscopy (SEM, FEI Quanta 200 ESEM FEG, USA). Prior to the imaging, MgP particles were sputter-coated with gold for a thickness of 6 nm (Q150T S/E/ES, UK). SEM images were then analyzed to quantify MgP particle distribution with the help of ImageJ software (Version 7.0, National Institutes of Health, USA). Differential Scanning Calorimetry was performed (DSC Q200, TA Instruments, USA). In brief, PCL pellets, MgP particles, and 20MgP pellets were placed in T zero aluminum pans (Mettler-Toledo AG, Greifensee, Switzerland) and sealed. The measurements were performed between 25°C and 300°C with ramp rate of 10°C/min, under a nitrogen flow of 50 ml/min. The heat flow change was measured as a function of temperature with reference to an empty pan ^[286].

Melt electrowriting of MgP-based bioceramic ink

Prior to melt electrowriting, MgP-based inks of different compositions (10 and 20 wt.% MgP) were thermally treated at 140°C for 6 h. Next, inks were transferred to a 5 mL metallic cartridge. Ink processing compatibility was systematically evaluated according to key MEW parameters, namely applied voltage (6-9 kV), collection speed (5-40 mm/sec), temperature (100°C) and pressure (80 kPa) to evaluate the stable jet formation, (Figure S1), fiber diameter and morphology. The temperature and pressure were chosen based on the properties of the raw materials and kept constant during the experiment.

Fibrous scaffolds (20 mm ´ 20 mm, n = 3) with varying squared-shaped fiber strand spacing (500, 750, and 1000 µm), and number of stacked layers (1, 5, and 10) were fabricated for each composition at a melting temperature of 100°C, pressure of 80 kPa, and voltage between 6-9 kV. All scaffolds were prepared with a 23G nozzle using a 3DDiscovery Evolution MEW machine (RegenHU, Switzerland). All scaffolds were designed using BioCAD software (RegenHU).

Printed MgP-based scaffolds accuracy

Fiber morphology and diameter were evaluated by SEM. In addition, scaffolds were imaged with an upright microscope (Olympus BX43, Japan) and acquired images were processed with ImageJ software. Printing accuracy was quantified using a quality number, $Q_{alignment}$, determined as,

$$Q_{alignment} = \frac{A_{measured}}{A_{expected}} \leq 1 \quad \text{Eq. 1}$$

where, $A_{measured}$ and $A_{expected}$ indicate the experimental and theoretical areas, respectively. $A_{expected}$ was estimated as,

$$A_{expected} = n_{squares} \times (Fibre\ spacing - \phi_{fibre\ diameter})^2 \quad \text{Eq. 2}$$

At least 3 samples from each composition were measured.

Melt electrowriting of graded scaffolds

MEW graded scaffolds were fabricated using a 3D Discovery Evolution MEW machine (RegenHU, Switzerland). The crosshatch 0/90 architecture with 500 µm fiber spacing was designed for the bone zone using 20MgP, and an aligned fiber architecture was designed for the PDL zone using PCL.

The proposed graded scaffolds were designed to have three distinct zones composed of a bone zone (20MgP, fiber spacing 500 μm), an interfacial zone and a PDL zone (highly aligned PCL fibers, fiber spacing 50 μm). The bone zone represented 70% of the total height of the scaffold, while the interfacial and PDL zones represented 10 and 20% of the total height, respectively.

Two distinct architectures were designed for the interfacial zone:

1. A graded scaffold was composed of a square crosshatch architecture, henceforth referred to as 20MgP-crsht, with intersecting sets of parallel lines with strand spacing of 250 μm ^[284].
2. A graded scaffold was composed of randomly oriented fibers, henceforth referred to as 20MgP-rnd.

The 20MgP composite formulation and pure PCL were loaded into cartridges with 23G and 27G nozzles, respectively. Prior to printing, the metallic cartridges were heated up to 100°C and 80°C for 20MgP and PCL, for 45 min, and subsequently dispensed at 0.08 and 0.1 MPa system's pressure, respectively. A summary of the printed conditions is provided in Table 1.

Table 1. The MEW parameters for printing the graded scaffolds

Zones	Collection speed (mm/sec)	Collection distance (mm)	Applied voltage (kV)
20MgP / Bone zone	5	3.5	7
PDL / Ligament zone	40	4	6
Rnd / Interfacial zone	5	4	6.8
Crsht / Interfacial zone	13	4	6.8

Physical and chemical properties

The chemical structure of the developed scaffolds was analyzed via Fourier Transform Infrared Spectroscopy (FTIR) using an attenuated total reflectance spectrometer (Perkin Elmer Spectrum 100, USA). FTIR spectra were obtained with a 4 cm^{-1} resolution within the 400-3500 cm^{-1} range. Scanning electron microscopy was performed to evaluate the morphology of the scaffolds as mentioned above. Energy Dispersive X-ray spectroscopy (EDS, USA) analysis was conducted to assess the inorganic phase after the printing of the scaffolds. Prior to the imaging, the scaffolds were coated

with 8 nm gold layer. Based on SEM images, fiber diameter, porosity and fiber spacing of printed scaffolds (20MgP-crsht, 20MgP-rnd, 20MgP, crsht, rnd, and PDL) were measured by using ImageJ, V7.

Ions release

Melt electrowritten 20MgP scaffolds (20 mm × 20 mm length) with 500 μm fiber spacing were immersed in 0.1M Tris-HCl (Tris(hydroxymethyl)aminomethane, Sigma-Aldrich, Germany) at 37°C. The cumulative ion release profile of magnesium and phosphorous ions was recorded utilizing inductively coupled plasma mass spectrometry (ICP-MS, Varian, Darmstadt, Germany) at different incubation periods (1, 3, 5, 10, and 21 days). To quantify the concentration of released ions, the solutions were diluted 10X in 1.3 v/v% HNO₃ (65% Suprapur, Merck, Schwalbach, Germany) and measured against standard solutions of magnesium and phosphorous (Merck, Schwalbach, Germany).

Mechanical properties

Tensile mechanical properties of PCL, 10MgP, and 20 MgP were evaluated under uniaxial tensile loading using a Dynamic Mechanical Analyzer (DMAQ800, TA Instruments, USA) equipped with a 50 N load cell. 20MgP-na referred to the samples without interfacial zone, used as control. Rectangular samples (1 cm width × 30 mm length × 1mm thickness) were loaded at a deformation rate of 2 mm/min at room temperature until failure. The tensile modulus, tensile yield strain and tensile toughness were determined from engineered stress-strain curves. Tensile modulus was determined using a least square fit of the initial slope of the stress-strain elastic region (0.1-0.5 mm/mm); tensile yield point was defined as point where nonlinear deformation begins; and tensile toughness was obtained as the area under the stress-strain curve until yield point. Subsequently, to determine the interfacial mechanical properties between bone (20MgP composition, crosshatch structure, 500 μm fiber spacing) and PDL region (PCL, highly aligned fibers, 50 μm fiber spacing) of the graded scaffolds with two interface architectures (crsht and rnd), a delamination test was performed. Rectangular samples (10 mm width × 20 mm length × 1 mm thickness) with an interface contact area of 200 mm² were mounted on a dynamic mechanical tester loaded at a rate of 2 mm/min. the interfacial modulus, interfacial yield strain and interfacial toughness were obtained as previously described above.

***In vitro* cell culture**

To confirm the *in vitro* cell compatibility and osteogenic potential of the developed MgP-based MEW scaffolds, cylindrical samples (5 mm diameter x 1 mm height) of PCL, 10MgP and 20MgP were cultured *in vitro* with bone marrow derived human

mesenchymal stem cells (hMSCs, harvested according to the protocol describing elsewhere^[287], passage 4) for 21 days in expansion media α -MEM (Gibco, USA), supplemented with 10% fetal bovine serum (FBS, Gibco, USA), 0.2 mM L-ascorbic-acid-2-phosphate (ASAP, Sigma-Aldrich, Germany) and 1% penicillin-streptomycin (Pen-Strep, Sigma-Aldrich, Germany). Prior to cell seeding, scaffolds were sterilized in 70 v/v% ethanol for 1h followed by 30 min under ultraviolet (UV) light. hMSCs were first expanded for 10 days in expansion media at 37°C in a humidified atmosphere containing 5% CO₂, and then seeded onto scaffolds at a density of 50,000 cells/well in 48 well plates. As a positive control for determining the osteogenic potential of the scaffolds, samples were also cultured in media supplemented with osteogenic components (α -MEM+10% FBS+0.2 mM ASAP+1% Pen-Strep+10 nM Dexamethasone+10 mM B-glycerophosphate, Sigma-Aldrich, Germany). At least three samples were tested for each group (*i.e.*, expansion medium and osteogenic medium).

Cell viability and morphology analyses

Metabolic activity of hMSCs was quantified by Alamar blue assay (ThermoFisher, USA), following the manufacturer's instructions^[288]. In order to visualize the cell morphology, scaffolds were first fixed in formalin for 30 min after 1, 7, and 14 days of culturing in expansion media. Samples were permeabilized with 0.2% (v/v) Triton X-100 in phosphate-buffered saline (PBS), followed by incubation with F-actin (1:400; phalloidin-TRITC; Sigma-Aldrich) and 4',6-diamidino-2-phenylindole (100 ng/mL; DAPI; Sigma-Aldrich). Stained samples were imaged with a confocal laser scanning microscope (Leica SP8X, Germany) and dedicated acquisition software (Leica LASX, Germany).

Osteogenic potential evaluation

Osteogenic differentiation of hMSCs was measured using alkaline phosphatase (ALP) at day 7 and day 14 of *in vitro* culture, following a protocol described elsewhere^[255]. Briefly, ALP activity was measured using conversion of the p-nitrophenyl phosphate liquid substrate system (pNPP, Sigma-Aldrich, Germany) and a serial dilution of calf intestinal ALP for the standard curve (Sigma-Aldrich, Germany) in TE-buffer (Tris EDTA buffer). In addition, calcium concentration was quantified after 21 days using a colorimetric calcium assay kit (Abcam, UK) according to the manufacturer's instructions. ALP and calcium levels were corrected for DNA content from the same cell lysate used to measure ALP, using a Quan-iT-Picogreen-dsDNA kit (Molecular Probes, Invitrogen, Carlsbad, USA). To determine the calcium concentration after 21 days of culturing, Calcium Assay Kit (Colorimetric, Abcam ab102505, USA) was used according to the manufacturer protocol^[289].

Animal experiments, histology and immunohistochemistry

The University of Michigan Institutional Animal Care and Use Committee (IACUC, protocol #PRO00008502) approved all animal procedures. In total, 12 male rats (6-week-old male Fischer 344 rats, body weight 300–320 gr) were used for the experiments. The previously established defect dimensions are 3 mm in length × 2 mm in width × 1 mm in height, and the exact dimension of the printed scaffold was press-fitted inside the defect, protected by the defect borders, and then covered by muscles sutured in place. All surgical procedures were carried out under general anesthesia, which was induced with isoflurane (4–5%) inhalation (Piramal Critical Care Inc.) and maintained with isoflurane at 1–3%. After anesthesia, periodontal fenestration defects (3 mm length (X) × 2 mm width (X) × 1 mm height) were surgically generated bilaterally in the rat jaw. The alveolar bone, cementum, and other soft tissue structures were all removed in this procedure. The scaffolds (n = 3/group) were placed inside the defects and tested for their ability to regenerate the periodontium. The animals were humanely euthanatized 6-weeks post-scaffold implantation and the surgical sites fixed in 4 v/v% paraformaldehyde solution before microcomputed tomography (μCT) and histo- and immunological analyses. To simplify, the groups were named empty, 20MgP-na, 20MgP-crsht, and 20MgP-rnd according to the architecture of the graded scaffolds.

Micro-Computed Tomography (μCT)

Scanco CT 100 (Scanco Medical AG, Brüttisellen, Switzerland) equipment was used to examine the newly formed bone at the surgical sites. The following scan parameters were used 70 kV, 114 μA monochromatic X-rays, and 25 μm voxel sizes were used to create a 360° rotation. The exposure period was kept to an average of 500 ms per frame on average. For 3D image reconstruction, the Scanco Medical System software was employed. The 3D image was then utilized to trace the original defects circumferentially, which was named the region of interest afterward (ROI). Each sample's ROI was examined for bone volume (BV, mm³), bone fill (BF %, BV/TV), and tissue mineral density (TMD, mgHA/cm³)^[284].

Histological analysis and Immunofluorescence

The harvested samples were decalcified in 10% EDTA for 3 weeks. Following that, the samples were dehydrated in an ascending gradient of ethanol. Afterward, samples were embedded in paraffin. Histological sections of 4-μm were stained with hematoxylin and eosin (HE) and Masson's trichrome (MT). To examine soft and mineralized tissue neoformation, the slides were imaged using a light microscope equipped with a digital camera (Nikon E800, Nikon Corporation).

For immunostaining, the harvested samples were embedded in paraffin, and then cut into 4 μm -thick sections using a microtome. Sections were dewaxed at 60°C for 15 min, followed by rehydrating using well-established ethanol gradients. Sections were incubated for 20 min in 3% at RT to decrease the activity of endogenous peroxidase. Sections were incubated (10 min) in 3% bovine serum albumin (BSA) at room temperature to block unspecific binding. They were incubated with anti-periostin (rabbit polyclonal, ab14041, Abcam, Cambridge, MA, USA) (dilution 1:500), anti-Osteopontin (mouse monoclonal, ab69498, Abcam) (dilution 1:500), and anti-CEMP1 (Rabbit polyclonal, b254947, Abcam) (dilution 1:200), overnight at 4°C. Subsequently, the sections were incubated with Goat anti-mouse IgG H&L (ab6785, FITC) and Goat anti-rabbit IgG H&L (ab6719, Texas Red, Abcam) at (dilution 1:200) for 1 h at room temperature. Cell nuclei were stained with DAPI using vectashield antifade mounting media. The images were acquired with a microscope (Nikon E800, Nikon Corporation) at 100 \times magnification.

Statistical analysis

All data were represented as mean \pm standard deviation (SD) and at least three samples were evaluated for each test. Normality of distribution and equality in variance among groups were evaluated. Statistical analyses were performed using GraphPad prism V9. Assuming equal sample size of compared groups, a One- or Two-way ANOVA with post-hoc Tukey's test was performed to compare the means of the different groups. Differences were considered significant at a probability error (p) of *p < 0.05 for the printability, mechanical tests and **p < 0.01 for animal test.

Results

Melt electrowriting of magnesium phosphate-based biomaterial inks

The ability to melt electrowrite MgP-based biomaterial inks is mainly dependent on particle size and thermal properties of the compounded polymer. To prevent nozzle clogging, MgP powders were prepared with a monomodal particle distribution with an average particle size of approximately 1 μm (Figure 1A).

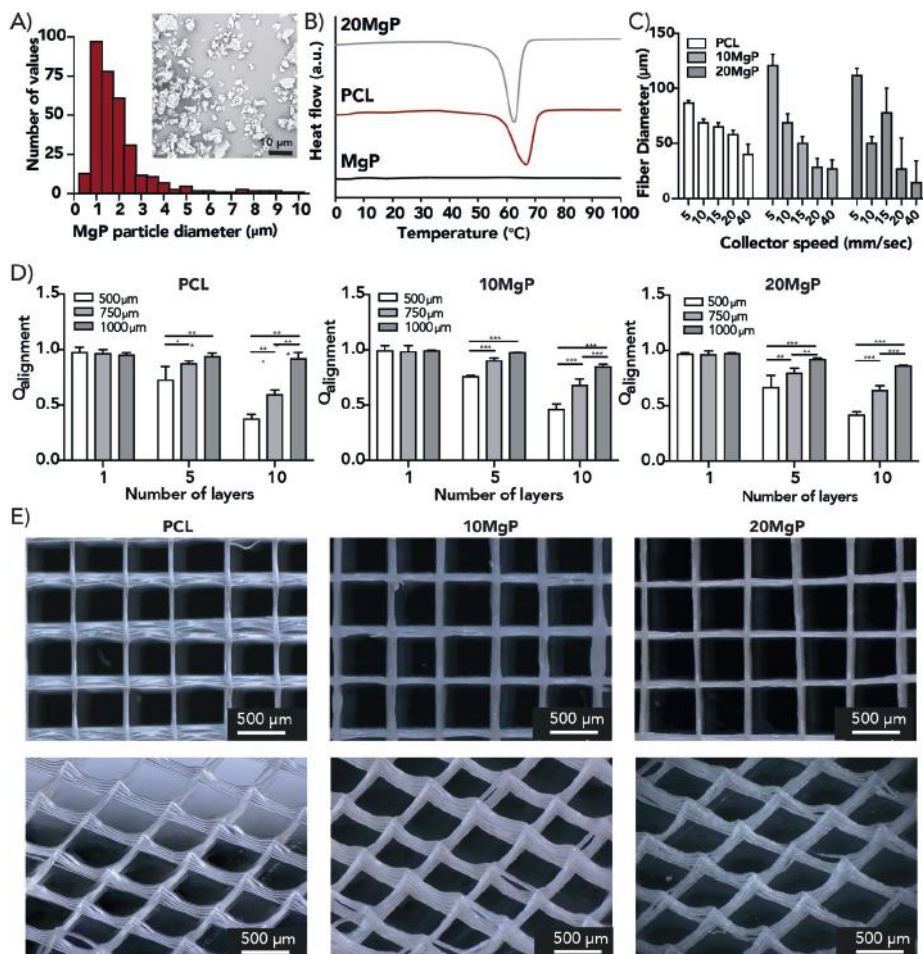


Figure 1. A) Particle size distribution and morphology analysis of the MgP ceramic powder. B) Thermal properties of PCL, 10MgP and 20MgP. C) The effect of MEW collector speed on fiber diameter. D) The effect of fiber stacking and fiber spacing on printing accuracy. E) Representative stereoscopic images of PCL, 10MgP, and 20MgP composite scaffolds with 500 μm fiber spacing and 10 stacked layers.

In addition, DSC analysis revealed that melting temperatures ranged from 70 to 80 °C and, more importantly, that the addition of MgP did not significantly alter the melting temperature of PCL (80 °C) (Figure 1B). It was found that although, according to DSC results, the melting point of 20MgP composite is close to PCL, we could not observe a jet formation below 100 °C. Furthermore, preliminary tests on the influence of key MEW processing parameters (*i.e.*, applied voltage, dispensing pressure, temperature, and collector speed) on stable jet formation (Figure S1A) and fiber collector speed revealed that temperature and collector speed were the most critical parameters. In

general, it was observed that, fiber diameters decreased by increasing the collector speed from 5 to 40 mm/sec. [290]. Additionally, collector speeds of 20 mm/min and 40 mm/min resulted in fiber diameters of 15 μm and 40 μm for PCL and MgP-based composite materials, respectively (Figure 1C). These speeds were selected for further studies on the effect of fiber stacking (Figure 1D). Independent of the MgP content, a decrease in $Q_{\text{alignment}}$ was observed with the increasing number of stacked layers (from 1 to 10), and decreasing fiber spacing, (from 1000 μm to 500 μm). Notably, a minimum fiber spacing of 500 μm could be obtained for an MgP content of 20 wt.% (Figure 1E and Table S1), without compromising the fiber stacking.

Osteogenic properties of MgP-based composite scaffolds

To determine the osteoconductive properties of MgP-based scaffolds, the osteogenic differentiation of seeded human MSCs onto the scaffolds was investigated. First, we confirmed that hMSCs were metabolically active during 21 days of *in vitro* culture (Figure 2A). Then, the ALP activity of the hMSCs cells on PCL and MgP-based scaffolds (10MgP and 20MgP) was evaluated in expansion media as a measure of early osteogenic potential (Figure 2B). After 7 days of *in vitro* culture, the ALP activity for 20MgP was almost 20-times higher than for MgP-free (*i.e.*, PCL) composition. We also observed that the ALP activity of hMSCs cultured on 20MgP increased from 306.93 U/mg to 460.27 U/mg DNA between 7 to 14 days (increase 150%), while the ALP activity of hMSCs cultured on PCL was 97.57 U/mg DNA after 14 days. Furthermore, the amount of calcium deposition on prepared scaffolds was assessed. Calcium deposited on 20 MgP was 1.3 and 3.6 times higher than on 10MgP and PCL, respectively (Figure 2C). Moreover, no significant differences in calcium deposition of MgP-based scaffolds cultured in expansion and osteogenic medium were observed (Figure 2C), which confirms the osteoconductive properties of MgP-based scaffolds. Although these findings corroborate our previous findings on the osteopromotive properties of extruded printed MgP based scaffolds [181], these results are particularly impressive since the content of MgP used here was only 20 wt.% while in previous efforts, the content was 70 wt.%.

Furthermore, an improved cell attachment and a more homogeneous distribution were noted when comparing MgP-based scaffolds with their neat PCL counterparts (Figure 2D). Higher magnification confocal images suggested a potentially higher level of cell-secreted matrix components on the 20MgP-based scaffolds than on PCL scaffolds (Figure 2E). To further understand the osteoconductive properties of the MgP-based scaffolds, the presence, distribution and release of ions (Mg^{2+} and PO_4^{3-}) from PCL fibers were analysed. SEM (Figure 2F) and EDX (Figure S1) analyses revealed that MgP ceramic particles were successfully incorporated into the PCL

matrix. FTIR analyses performed on printed MgP-based fibers (Figure 2G) confirmed the incorporation of ceramic particles. The peaks corresponding to Mg^{2+} and PO_4^{3-} were detected in the spectrum of 20MgP fibers. Lastly, a burst release of Mg^{2+} and PO_4^{3-} ions was noted during the first 5 days in an aqueous solution, followed by a gradual and sustained release of these ions up to 21 days (Figure 2H).

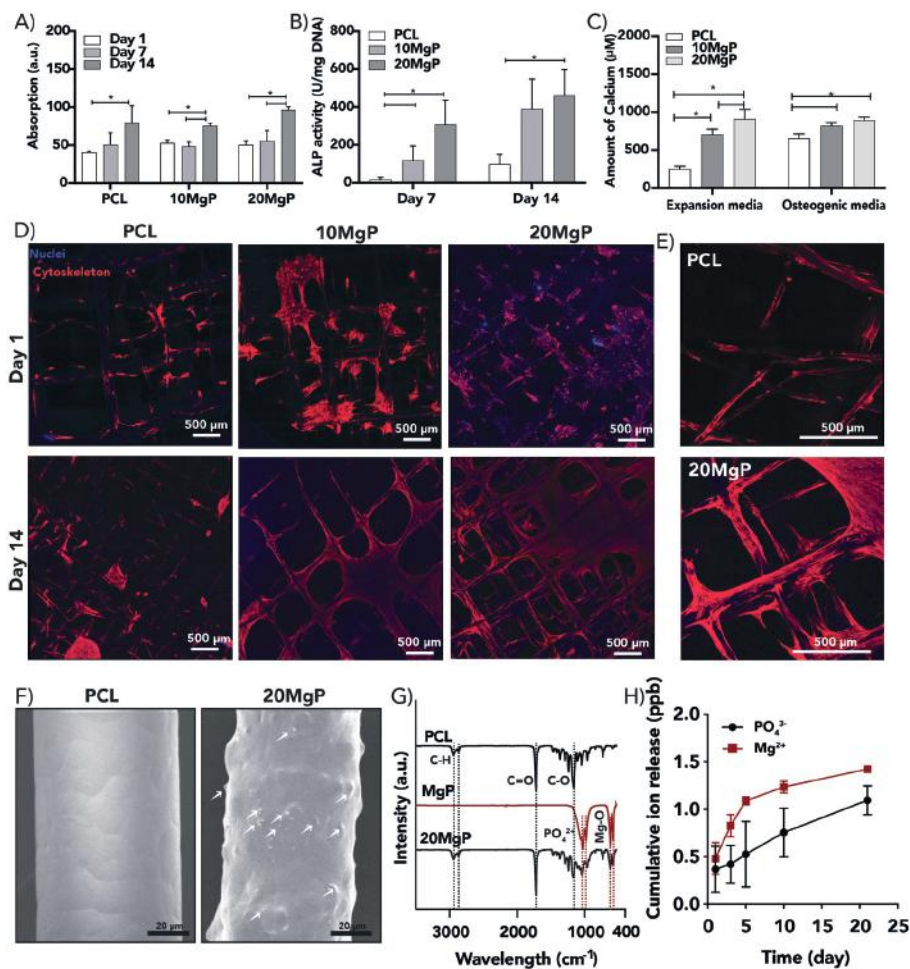


Figure 2. A) Metabolic activity of hMSCs during 14 days of *in vitro* culture. B) Alkaline phosphatase (ALP) activity of cells in MEW scaffolds cultured in expansion media. ALP activity levels were normalized to DNA content. C) Calcium deposition in scaffolds after 21 days of culture in expansion and osteogenic medium. D) Cytoskeleton and nuclei staining of hMSCs in expansion media. E) Higher magnification of stained hMSCs on PCL and 20MgP scaffolds after 14 days. F) SEM images of a single fiber of PCL and 20MgP (MgP particles identified with white arrows). G) FTIR analysis of as-printed 20MgP composite scaffolds. H) Cumulative ion release from 20MgP composite scaffolds upon incubation in Tris-HCl media over 21 days.

Melt electrowriting of graded scaffolds

MEW graded scaffolds were designed to recreate the spatial changes in matrix composition and organization observed in native PDL-bone interface (Figure 3A-B). In particular, a three-zoned scaffold with different porous boxed-shaped architectures and material compositions was successfully fabricated by melt electrowriting (Figure 3).

To maximize the adhesion between the bone zone (20MgP composite) and PDL scaffold zone (PCL), two different interfacial architectures, crosshatch 0/90 (crsht, Figure 3C) and random (rnd, Figure 3C) were investigated. The representative SEM images of PDL and bone zones are shown in Figure 3D-E. SEM analysis confirmed that independent of the interface architecture explored, the as-fabricated scaffolds showed consistent and reproducible printability (Figure 3F). The fiber diameter of bone zone is 45.3 μm for 20MgP, and of PDL zone is 8.2 μm for PCL (Figure 3G). As such, the fiber diameter of interfacial zone is 9.9 and 29.6 μm for rnd and crsht, respectively. The difference in the fiber diameter is due to various fabrication (MEW) parameters. The fiber spacing of 20MgP deviated to 369.21 μm from the design of 500 μm , while the fiber spacing of PDL deviated to 39.48 μm for 50 μm scaffold (Figure 3H). This resulted in porosity values for all three regions above 50% (Figure 3I). In particular, the porosity of the bone and PDL zones was 65.6% and 52.8%, respectively.

Mechanical characterization of melt electrowritten scaffolds

We next investigated whether the incorporation of MgP particles or interface architecture could improve tensile properties of the developed graded scaffolds (Figure 4A). All investigated scaffolds showed similar stress-strain behavior (Figure 4B). The increase in MgP content from 10 wt.% to 20 wt.% resulted in an increase in both the tensile modulus and tensile yield stress. For instance, the tensile modulus and tensile yield stress of 20MgP increased approximately 3.5 and 3.1 times when compared to PCL scaffold, respectively (Figures 4C-D). Incorporation of MgP into the PCL matrix, resulted in an increase of approximately 2 times in tensile toughness, however, no significant differences were noticed between 10MgP and 20MgP scaffolds (Figure 4E).

Furthermore, the interfacial tensile test between the different zones of the scaffolds (*i.e.*, bone and PDL zones) revealed the strong bond between two different phases of the scaffold, as compared to the delamination of the scaffolds with a single zone (Figure 4F). Interestingly, the interfacial modulus of 20MgP-crsht was almost 2.5 times higher than and the 20MgP-na (Figure 4H); while the interfacial yield strength for 20MgP-crsht was 3 times greater than 20MgP-na (Figure 4I). Moreover, the interfacial

toughness of 20MgP-crsht and 20MgP-rnd were $0.06 \pm 0.01 \text{ kJ.m}^{-3}$ and $0.02 \pm 0.01 \text{ kJ.m}^{-3}$, respectively (Figure 4J).

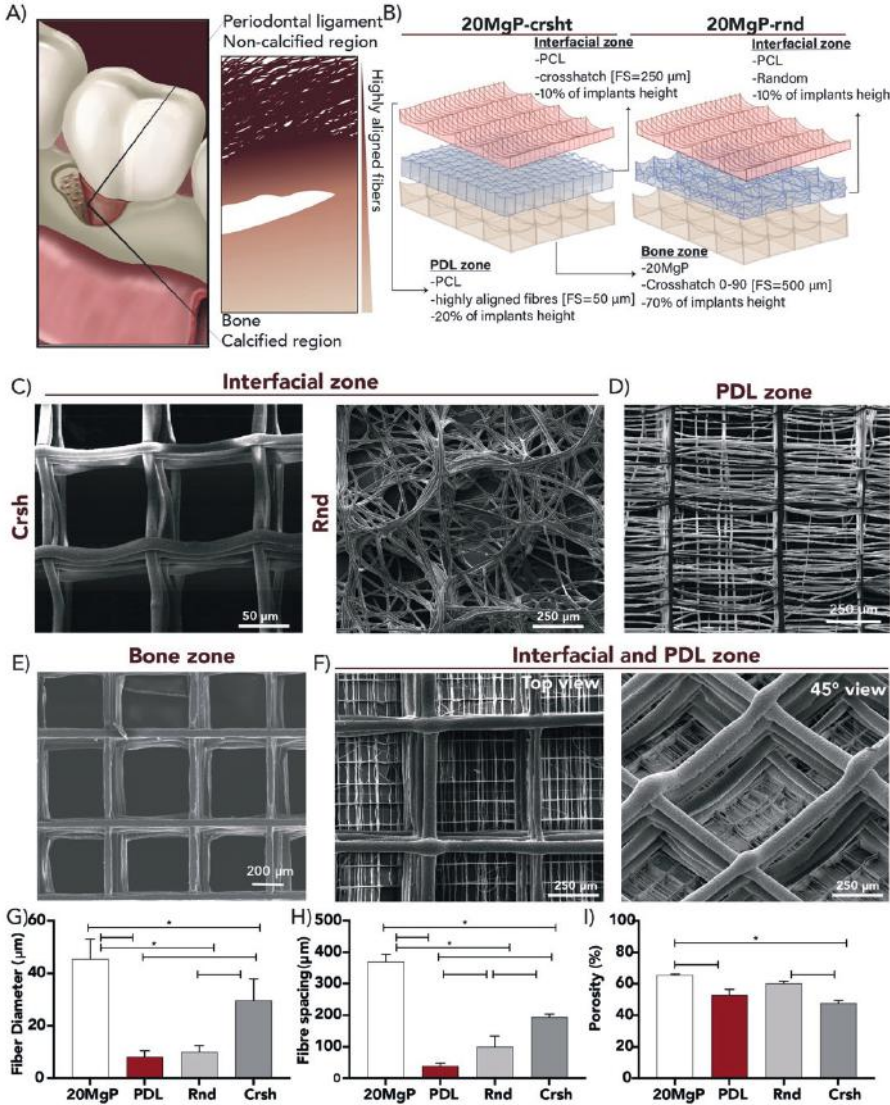


Figure 3. A) The illustration of periodontal site and the structure of bone to PDL interface. B) Design approach and sequential melt electrowriting strategy of the graded scaffolds (FS = fiber space). Representative SEM images of the C) crosshatch random structure of electrowritten PCL, D) highly aligned PCL fibers for PCL zone, E) 20MgP fibers as bone zone, and F) interfacial crosshatch and PDL zones from top and side views. G) fiber diameter, H) fiber spacing and I) porosity at the different zones of the printed graded scaffolds.

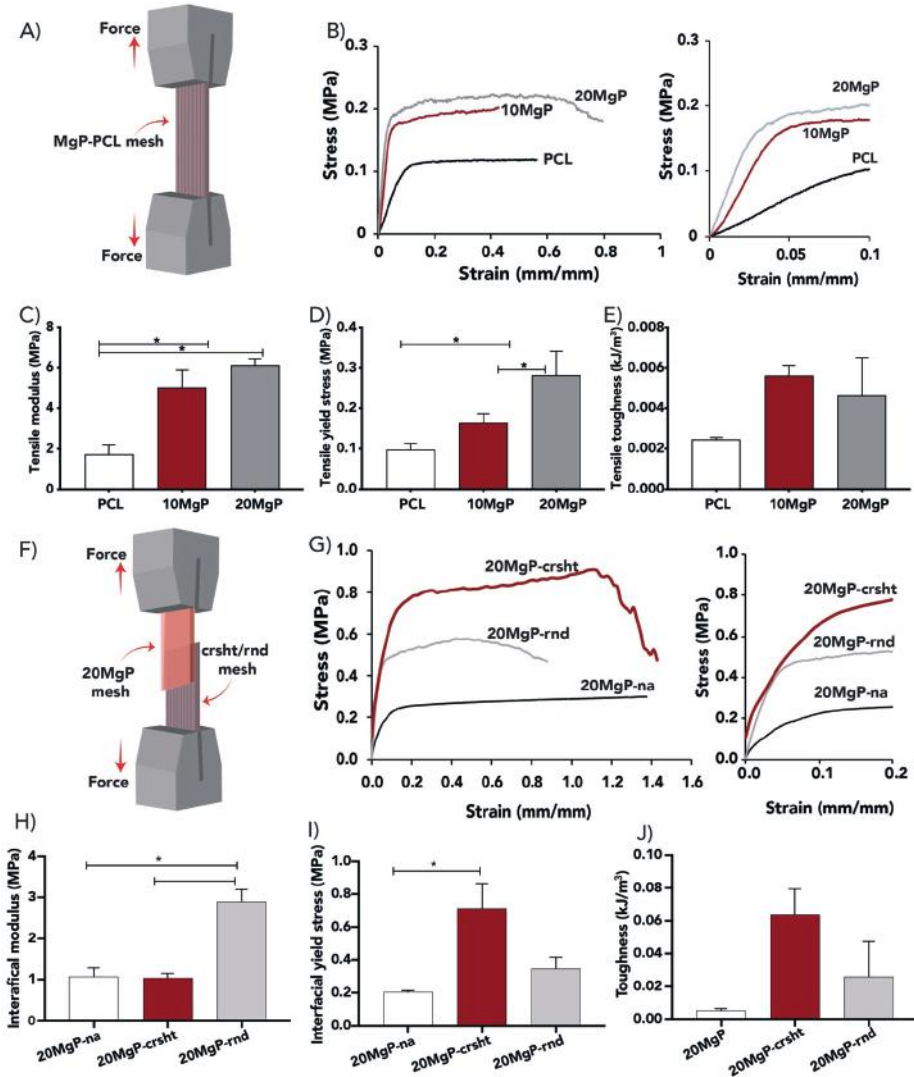


Figure 4. A) Schematic of testing set up. B) Representative stress-strain curves of melt electrowritten scaffolds with different MgP concentrations. Determined C) Tensile modulus, D) Tensile yield stress, and E) Tensile toughness of scaffolds with various MgP concentrations. F) Schematic of tensile set up used for interfacial tests. G) Representative stress-strain curves of the graded scaffolds with different interfacial architecture, and determined H) interfacial modulus, I) interfacial yield stress, and J) interfacial toughness.

Micro-computed tomographic (μ CT) analysis of regenerated tissue

The ability of the designed scaffolds to support the growth of new tissues *in vivo* was tested using a well-established periodontal fenestration defect model in rat mandible ^[285] (Figure 5A).

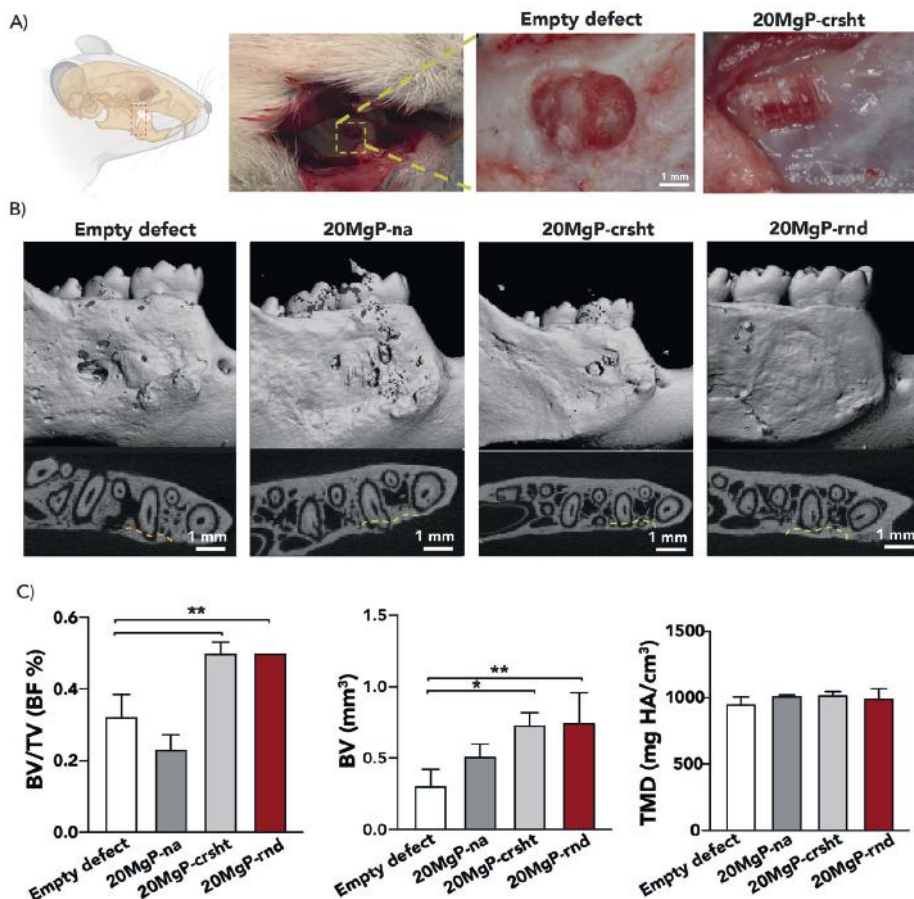


Figure 5. A) The illustration of the rat mandibular periodontal fenestration model. Photographs of a rat mandible after the incision, flap elevation, creation of the defect, and exposing the distal root of the mandibular first molar. B) Representative μ CT images of the fenestration defect exposing the distal root of the second molar at 6 weeks. Transverse views in yellow color highlight the visual differences between the area and density of bone regenerated within the defect. (Scale bar = 1 mm. C) μ CT assessments of bone fill, and tissue mineral density (TMD) 6 weeks after surgery, within the different groups (** $p < 0.01$).

Based on μ CT examination, the graded scaffolds group exhibited considerable improvement in alveolar bone healing following surgery (Figure 5B). Quantitative μ CT measurements showed that bone volume and bone fill in groups with interfacial layers were approximately 42% greater than control (sham) and 25% than those with no interfacial layer (Figure 5C and S2). The group with interfacial layers achieved nearly full bone repair compared to partial bone repair in the control sham and the group with no interfacial layer by 6 weeks, leaving a visible remaining bone defect on the buccal surface and uncovered distal root (Figure 5B). Compared to these groups, the 20MgP-rnd group had a higher rate of complete bone fill, which bridged the entire lesion region, indicating active osteogenesis. The newly formed bone in the interfacial group displayed more significant bone fill and was less distinct from the adjacent native bone, suggesting a higher bone bridging than the other groups.

The histological findings underscore the multi tissue regeneration via both structural and compositional guidance of graded scaffolds towards periodontium regeneration (Figure 6).

HE and MT staining after 6-week of *in vivo* implantation have shown distinctive yet integrated bone and ligament tissues that form in the graded scaffolds with a random interface architecture. The presence of the interfacial zone in 20MgP-rnd group was sufficient to maintain PDL zone and restrict the fibrous tissue formation confined toward the intended PDL zone mimicking the natural PDL area. Interestingly, the randomly interfacial layer compared to crosshatch pattern formed a better integrated transition from the bony to PDL-like tissue. This difference can be attributed to the smaller fiber spacing of random interface layer (20MgP-rnd) compared to 20MgP-crsht group. Moreover, the PDL-like tissue was formed into the mineralized bone. It is worth mentioning that the scaffold with no interfacial layer showed more soft tissue formation between the PDL-bone interface.

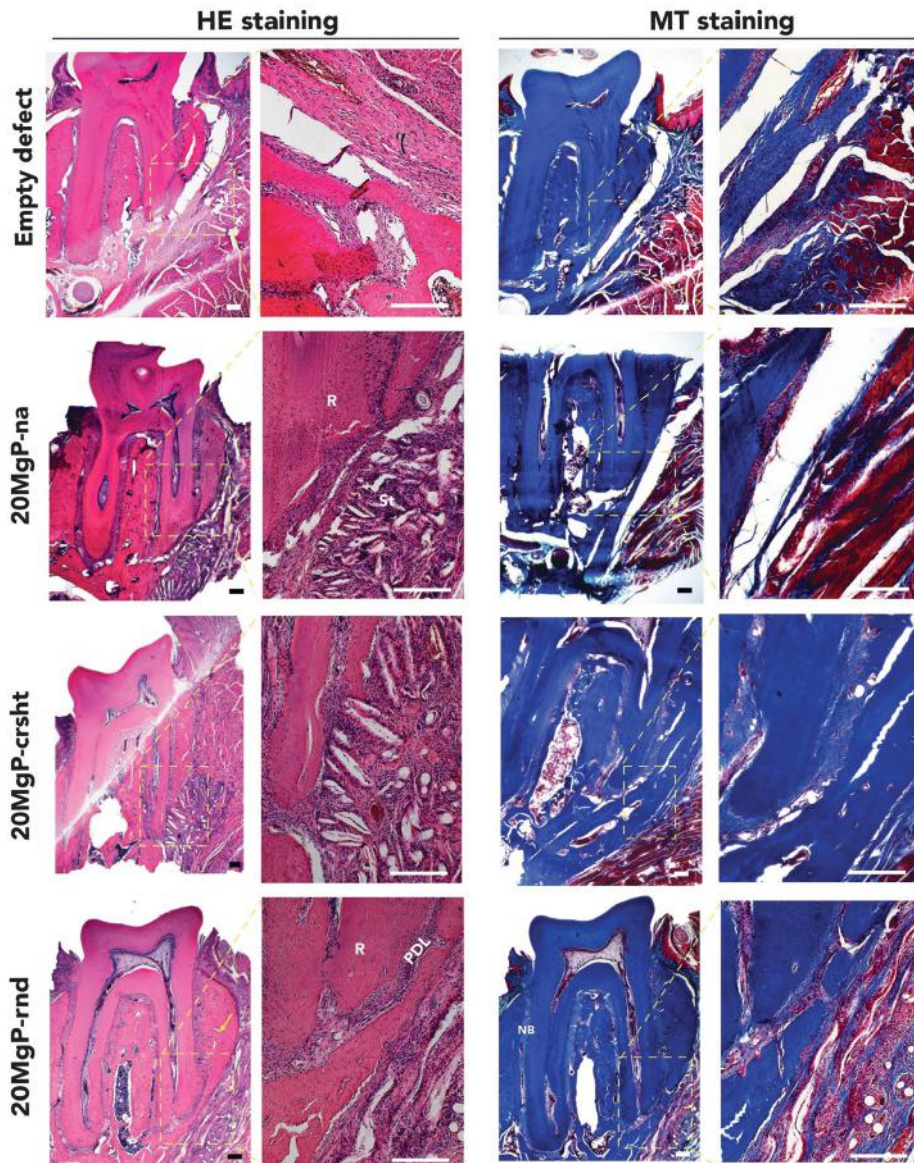


Figure 6. Histological analyses of Hematoxylin and Eosin (HE) staining and Masson's Trichrome (MT) staining of periodontal defects treated with the distinct graded scaffolds and evaluated after 6 weeks post-implantation (scale bar = 100 μ m), NB: new bone, R: Root surface; St: Soft tissue.

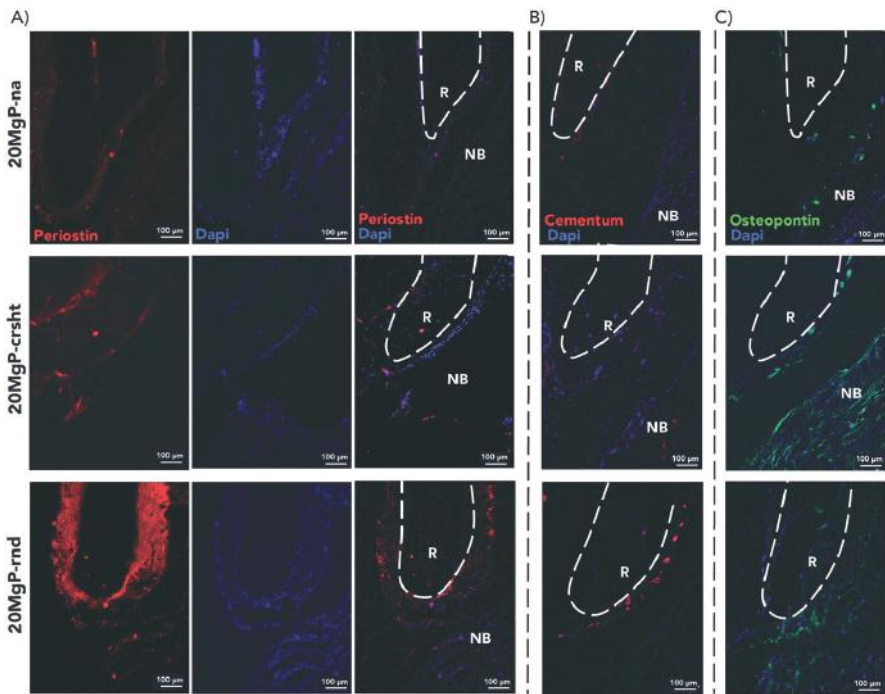


Figure 7. A) Immunofluorescence staining for the expression of periostin at the PDL zone. Representative mesiodistal cross-section at the first lower molar region. Texas Red[®] showing positive periostin immunolabeling and DAPI for cell nuclei staining. Merged colors on the right side with post-processing background reduction. 100x magnification; scale bars: 100 µm; NB: new bone; R: Root surface. Immunofluorescence staining for the expression of B) cementum and C) osteopontin at the PDL zone. Representative mesiodistal cross-section at the first lower molar region. Texas Red[®] and Fluorescein (FTIC) showed positive cementum and osteopontin immunolabeling, respectively. The two markers were merged with DAPI images for cell nuclei staining. 100x magnification; scale bars: 100 µm; NB: new bone; R: Root surface.

Immunofluorescence staining for the expression of periostin, osteopontin, and cementum at the PDL zone

The graded scaffolds 20MgP-crsht and 20MgP-rnd appear to have shown a better periodontal ligament regeneration and new-formed bone support in the employed defect model with superior potential in 20MgP-rnd group compared to 20MgP-na. The expression of CEMP1, Osteopontin, and Periostin were immunolabeled. The early marker for periodontal regeneration is expressed by periostin protein which is distinguished for 20MgP-rnd. Also, 20MgP-rnd exhibited a higher Cementum protein 1 (CEMP1) expression along with enhanced immunolabeling for osteopontin and periostin compared to 20MgP-na and 20MgP-crsht (Figure 7 and Figure S2). The osteopontin also expressed for all the tested groups but for 20MgP-rnd, osteopontin is expressed around the root of the tooth.

Discussion

In this investigation, we described the development of a graded melt electrowritten scaffold, which was composed of an osteoconductive ceramic-based biomaterial for the bone zone, and highly aligned polymer fibers for PDL zone. The embedded MgP bioceramics were able to promote bone regeneration and simultaneous degradation of the scaffolds *in vivo*. Similar scaffolds, based on MEW processing, previously showed potential for application in periodontal repair procedures and the inclusion of low concentrations of bioceramics, *i.e.*, hydroxyapatite or fluorapatite, was demonstrated to enhance bone regeneration^[291–293]. While this application of MEW enabled the generation of thin ceramic-coated PCL fibers with diameters ranging from 20 to 50 μm ^[293,294], it did result in a burst release of osteogenic ions from the PCL fibers^[285]. In order to overcome this, the polymer was compounded with bioceramics. This strategy showed promising results, although only composites with a bioceramic content lower than 10 wt.% could be successfully generated, which resulted in limited osteoinductivity properties due to masking of the bioceramics by polymer^[295].

In this study, processing of a MgP biomaterial ink with 20 wt.% of ceramic content (20MgP) was successfully achieved at 100°C, however only after thermal exposure of 6 h at 140°C. This is probably related to the pre-processing of PCL, which affects its crystallinity and will, in turn, facilitate the extrusion of 20MgP. Further, it was confirmed that the composition was not cytotoxic and promotes better osteogenic differentiation of mesenchymal stem cells compared to bare PCL or the composite containing 10 wt.% ceramics. The increased osteogenic potential is very likely related to the higher ceramic content and the consequent higher release of osteogenic ions (Mg^{2+} and PO_4^{3-}) from the MgP ceramic phase^[163,296–298]. In a previous study, we showed abundant calcium (200 μM) deposition on the extrusion-based printed PCL scaffolds with 70 wt.% of MgP after 21 days *in vitro* culture^[181]. The calcium deposited on the 20MgP MEW scaffolds is, however, 5 times higher than in the previous study. This underscores the synergistic effect between the osteoinductive ions and the high surface area provided by the small fiber diameters of the MEW scaffolds. Moreover, the network of small fiber diameters fibers does also better resemble the extracellular matrix microstructure of the native bone^[299–301]. This underscores the synergistic effect between the osteoinductive ions, and the high surface area provided by the small polymeric fiber diameters of the MEW scaffolds. Moreover, the network of small fiber diameters better resembles the extracellular matrix (ECM) microstructure of the native bone^[283],¹⁹. Furthermore, according to our findings, a more homogenous distribution of the MgP particles can be achieved by extruding the formulated composite paste at high temperature prior to actual printing of the scaffolds.

In addition, the tensile mechanical properties of the 20MgP scaffolds have the highest elastic modulus and strength among the tested groups. This is probably explained by the fact that the addition of 20 wt.% of MgP allows for a more uniform dispersion and interaction with the PCL matrix, without the introduction of defects^[302]. The tensile yield stress of 70 wt.% MgP based scaffold generated by extrusion was 1.5 MPa^[181] while the melt electrowritten 20MgP scaffolds have a tensile yield stress of 3 MPa. After establishing the MEW processing of the 20MgP for the bone region, graded scaffolds were generated with two different interfacial zone architectures and highly aligned fibers for PDL region. Evaluation of the interfacial tensile properties revealed that randomly oriented fibers (20MgP-rnd) provided better mechanical integration between the two regions than 20MgP-crsht. This is likely due to the fact that the randomly oriented fibers have more contact points with the PDL scaffold than those in the graded scaffolds.

Recently, our group reported on a graded scaffold whereby the bone region was comprised of fluorinated calcium phosphate (F/CaP)-coated MEW fibers, while the PDL region featured highly aligned fibers. Positive effects of aligned PCL fibers on the formation of PDL tissue have been previously reported^[303–305]. Remarkably, *in vivo* findings in the current study revealed that these tissue-specific scaffolds led to formation of PDL fibers perpendicularly oriented to the root surface and which integrated to newly formed bone surface^[284]. Despite the promising outcomes, the necessity for post-processing in order to obtain the bioceramic (F/CaP) coating to enhance the bioactivity of the scaffolds can pose drawbacks for clinical translation. This study overcomes the need for an additional step, as we hypothesize that an osteoconductive scaffold with a graded blend of MgP bioceramics and polycaprolactone (PCL) with tissue-specific, stable interfacial zone and structural properties can facilitate a long-term bone-to-ligament regeneration. In line with the present findings, Staples *et al.* evaluated a biphasic scaffold generated with MEW and comprised of two integrated compartments for bone and PDL^[306]. The PDL compartment consisted of parallel fiber organization creating 100 μm spaced channels, while the bone compartment was constituted of a gradient of pore size ranging between 200 to 1200 μm . Although the scaffold resembled the tooth-ligament interface, the lack of osteoinductive factors might explain the limited new bone formation observed in that study.

In this study, the composite scaffolds were evaluated in an *in vivo* periodontal fenestration defect model. This well-established *in vivo* defect model allows to determine the ability of the scaffold to support the coordinated neotissue formation of soft and hard periodontal tissues^[284]. Notably, our scaffolds showed the ability to induce simultaneous regeneration of bone and PDL. The enhanced repair in groups

treated with composite scaffold compared to other groups is apparent due to increased immunolabeling for CEMP1 expression, osteopontin and periostin. Of note, CEMP1 is a cementum component limited to cementoblasts and their progenitors. The apparently equal expression between the tested groups, as indicated by the immunolabeling, demonstrates that the proposed scaffolds do not impair the ability of neotissue formation, since the overexpression of CEMP1 downregulates periodontal ligament cell marker ^[307]. Meanwhile, osteopontin, also known as bone sialoprotein I, regulates mineralization *in vitro* and *in vivo* and is a crucial factor in the extracellular matrix of both cementum and alveolar bone ^[308]. Lastly, Periostin, in turn, has successfully been used as a periodontal regeneration marker since it is a secreted adhesion molecule highly expressed in the periosteum and periodontal ligament, playing a vital role in the regeneration of periodontal ligament and alveolar bone ^[309].

Collectively, our findings demonstrate the benefit of a multilayered, composite scaffold for enhanced bone formation, while also reflecting the natural process of PDL formation. The beneficial effect can be attributed to the compositional gradients and the structural organization of the scaffolds. The presence of an interfacial layer with a lower porosity confines the tissue-specific regenerative environment and subsequently supports simultaneous regeneration of both the bone and PDL tissues. The combined osteopromotive and ligament-regenerative properties of the developed scaffolds can also support stable mechanical integration. Collectively, MEW-fabricated scaffolds having compositionally and structurally tailored zones exhibit a good mimicry of the periodontal complex, with excellent regenerative capacity and great potential as a defect-specific treatment strategy.

Conclusions

In summary, the as-developed graded composite melt electrowritten scaffolds showed great potential to regenerate the PDL-bone interface. Structurally and compositionally graded scaffolds were successfully fabricated by MEW in a one-step printing procedure and by combining two biomaterial inks, a flexible, osteoconductive biomaterial ink based on MgP, and a PCL ink (20MgP). The addition of MgP increased the tensile properties of PCL. The tensile modulus of 20MgP increased 3 times compare to PCL alone. Additionally, the relatively high content (20 wt.%) of MgP bioceramics incorporated into PCL matrix supported *in vitro* mesenchymal stem cells differentiation towards the osteoblastic lineage and *in vivo* bone regeneration; while, the highly aligned PCL fibers induced PDL regeneration. To ensure the mechanical stability, PCL fibers with random architecture were printed

as interfacial zones. The *in vivo* results confirmed that graded scaffolds with the randomly architecture interfacial zone allowed for coordinated bone and periodontal tissue regeneration within their respective zones.

Supplementary Information

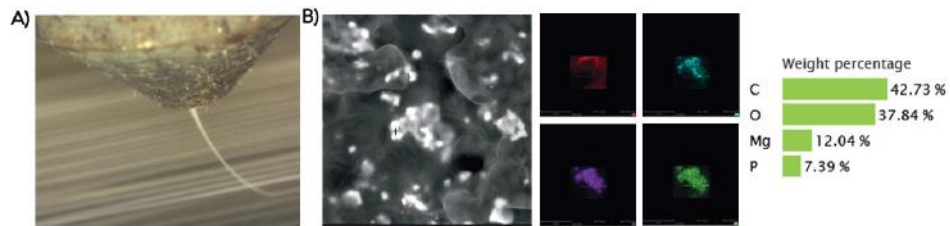


Figure S1. A) Snapshots of jet formation for 20MgP biomaterial ink, B) EDX mapping and elemental analysis results of 20MgP MEW scaffolds.

Table S1. Structural properties

Groups	Spacing (μm)	Fiber spacing (μm)
PCL	500	268 \pm 15
	750	530 \pm 18
	1000	899 \pm 26
10MgP	500	281 \pm 9
	750	546 \pm 19
	1000	867 \pm 2
20MgP	500	297 \pm 16
	750	566 \pm 23
	1000	862 \pm 11

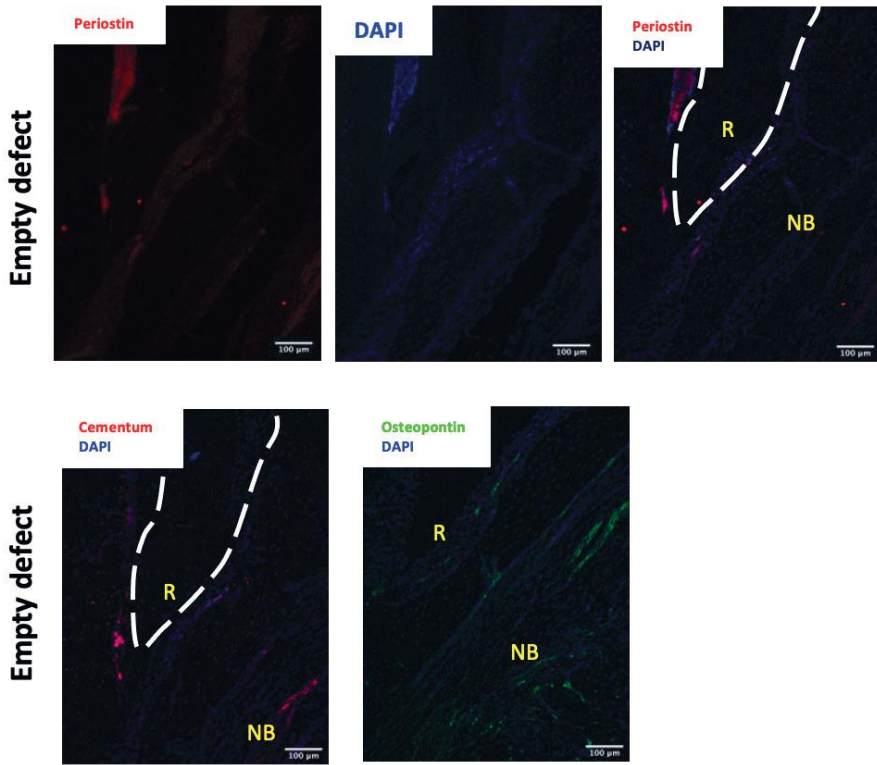
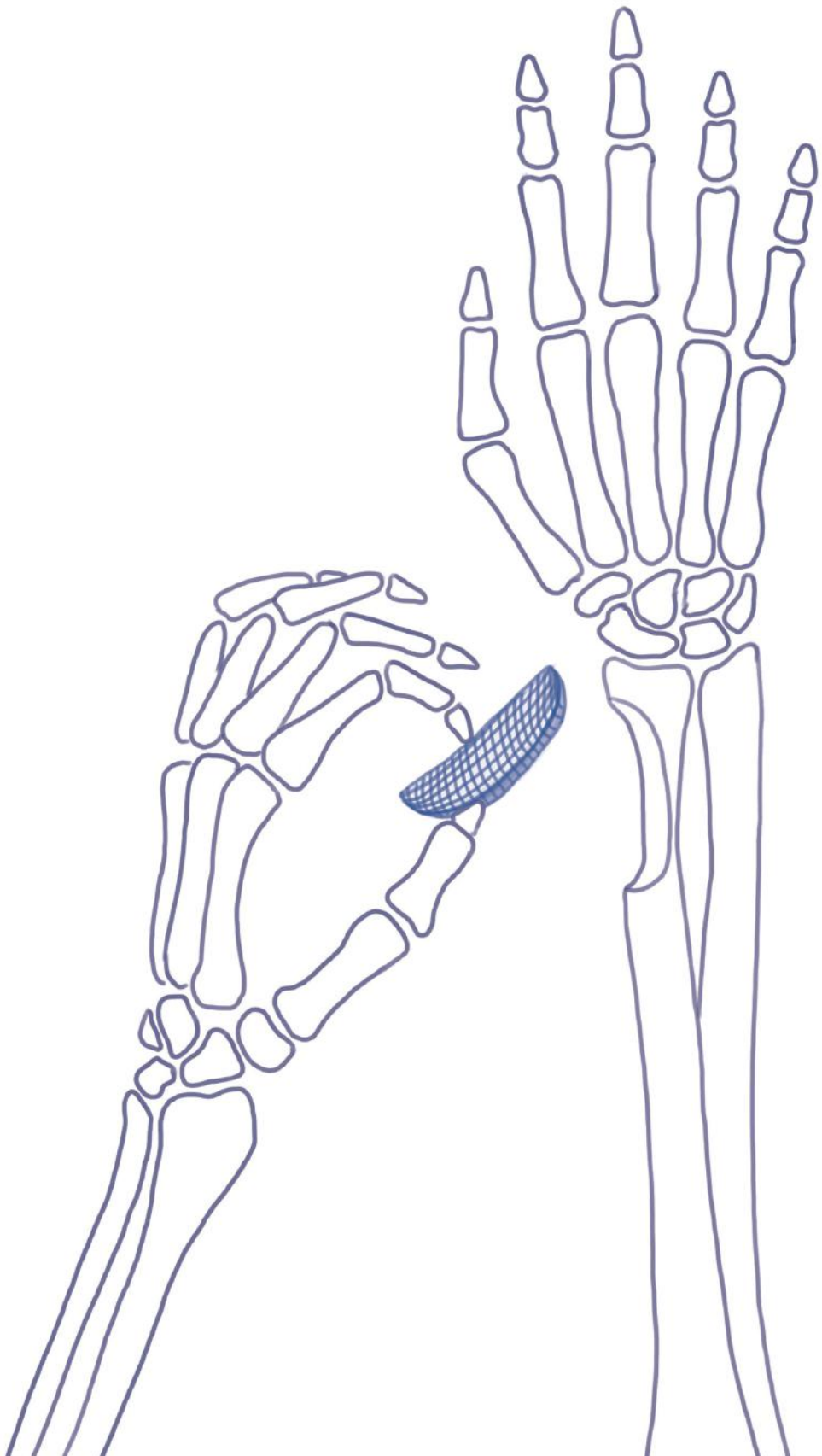


Figure S2. Immunofluorescence staining for the expression of periostin at the PDL zone for the empty defects.



CHAPTER 8

General discussion

Despite over 20 years of research, the development of bone graft substitutes that are both osteoinductive and load-bearing remains a major challenge. This thesis presents an effort to solve this challenge by developing an innovative MgP-based implant with tuned solubility and load-bearing properties. Throughout the thesis, a thorough characterization of the biological and mechanical performance of the developed MgP-based composite implants under both *in vitro* and *in vivo* conditions is provided. The potential of the developed composite implants was investigated for the restoration of bone defects and for interfacing with ligament and cartilage tissues.

Improving osteoinductive properties of MgP-ceramic materials

Recent studies have reported that metallic ions can have a great impact on the osteoinductive properties of degradable bone implants ^[310–312]. The working mechanism is based on the fact that metallic ions, such as Mg^{2+} , Si^+ , Zn^{2+} , and Sr^{2+} , bind to cellular DNA. This leads to an upregulation of important osteogenic genes related to cellular proliferation and differentiation. ^[191,313] For example, Sr^{2+} ions enhance the osteogenic differentiation of mesenchymal stem cells (MSCs) by participating in signaling pathways that can inhibit osteoclastic activity. Signaling pathways refer to the ability of a cell to receive, process, and transmit signals from its environment ^[42]. Other intriguing studies have shown that chickens deprived of silica through dietary restrictions were more prone to developing osteoporosis ^[314]. This has sparked interest in the scientific community about the importance of metallic ions in the process of bone healing, leading to several advancements in the field of bioceramics research. For instance, in a study by Lin *et al.* ^[315], it was demonstrated that apatite formation *in vitro* can occur by using calcium silicate scaffolds doped with Mg^{2+} and Sr^{2+} ions after four weeks. In a related *in vivo* study, the authors confirmed the importance of Mg^{2+} and Sr^{2+} in promoting bone regeneration by implanting calcium silicate scaffolds in a femoral rat defect ^[315]. For these reasons, **Chapter 2** was devoted to examining the potential of Mg^{2+} , Sr^{2+} , and Si^+ ions to mitigate the lower solubility (and osteopromotive properties) of established CaP ceramic materials like fluorapatite. In particular, Mg^{2+} , Sr^{2+} , and Si^+ ions were doped into the fluorapatite (FAp) structure using a mechanical alloying process. Both *in vitro* and *in vivo* experiments confirmed that Mg^{2+} and Sr^{2+} ions were able to decrease the crystallinity of FAp and enhance its osteoinductive properties. Interestingly, Mg^{2+} and Sr^{2+} doped FAp showed even faster bone healing than widely used HA and TCP ceramics ^[316,317]. This is most likely related to the upregulation of COL10A1 and VEGF expression in hBMSCs, as demonstrated in this study using Mg^{2+} ^[318]. In addition, Sr^{2+} ions are also known to be involved in a dual

mechanism of coupling the stimulation of bone formation with the inhibition of bone resorption^[319]. By upregulating the expression of extracellular matrix (ECM)-related genes such as type I collagen (COL1), bone sialoprotein (BSP), and osteocalcin (OCN), Sr²⁺ ions can influence mesenchymal stem cells^[319]. However, optimizing the balance between implant resorption and bone formation remains a challenge^[320,321]. In prior works, the degradation time of CaP-based bioceramics like HA has been slow for critical size bone defects, thereby delaying the bone healing process. For the FAp bioceramics presented in this thesis, this issue also prevailed. It was observed that although the crystallinity of FAp could be decreased by the addition of dopant ions, the developed implants were only partially degraded after three weeks when implanted in a rat femur defect. We speculated that this was due to the small size of the defects and that the FAp was not degradable during the time of the study. During the three weeks, the osteoclasts were unable to dissolve FAp, even with the decreased crystallinity^[40,322-324]. We hypothesized that this aspect could potentially be addressed by developing bioceramics based on MgP chemistry^[67,69]. One of the aims of this thesis was to address the solubility challenges associated with CaP bioceramics by replacing them with MgP-based bioceramics while maintaining a high capacity for bone regeneration. The results showed that the solubility of MgP-based implants is better than that of CaP ones, leading to superior osteopromotive properties. Previous studies have examined the effect of various concentrations of Sr²⁺ ions substituted into Mg^[255], which could be used to fine-tune implant degradation and facilitate even better bone regeneration. **Chapter 3** of this thesis focused on developing a MgP-based biomaterial with superior osteopromotive properties by incorporating Sr²⁺ ions.

Overcoming brittleness of MgP-ceramic materials

Despite the successful developments, bone graft substitutes are considered a good alternative to natural bone grafts only in non-load bearing defects (and healthy patients), as MgP (and CaP) ceramics are intrinsically brittle. In **Chapter 3**, a composite biomaterial ink was developed to overcome the brittleness of pure MgP-based bone grafts, without comprising their unique osteopromotive properties. The biomaterial ink was based on an inorganic phase of MgPSr, compounded with various concentrations of a synthetic polymer, PCL. A weight ratio of 30wt.% PCL was selected as it allowed adequate mechanical properties and prevented physical encapsulation of the MgP phase. Furthermore, *in vitro* cell assays confirmed that osteogenic potential of composite material was not hampered by polymer masking, as observed in a study using PLA and nano HA^[325]. Finally, the 6-month *in vivo* study in an equine model proved the osteopromotive potential and easy surgical

handling of the novel 3D-printed MgP-based scaffolds. It is important to note that the assessment of developed biomaterial ink in a large animal model is an important step towards clinical translation, as this model comes closer to the human situation [54,320]. In comparison with the previous work by Adam *et al.* which employed HA as an inorganic phase [64], the MgP-PCL implant developed in this thesis showed improved osteopromotive properties. This is related to the more soluble nature of MgP-based materials compared to HA in combination with the presence of osteoinductive properties of the Sr^{2+} metallic ions. Although we have found an exciting results by employing MgP-based ceramics, but there are still some aspects to be improved. In future studies the structural properties can be further improved by orienting the bioceramics particles in the composite. This could potentially facilitate alignment of hMSCs and secretion of an anisotropic collagen 3D fiber matrix in accordance with other studies. This can be done by changing the morphology of the bioceramics particles into more rod-shaped particles [65], or by modifying the MgP particles to make them magnetic and subsequently using a magnetic field to align them in the same manner as seen in native bone structure.

After confirming the osteopromotive properties of the developed MgP-based composite scaffolds in a non-load bearing skeletal location, we then investigated its performance in a challenging mechanical environment. To do so, a canine model for hip dysplasia as a pre-clinical animal model for human hip dysplasia was chosen to treat by patient specific 3D printing method. The implants were printed with the bone-inducing biomaterial were tested in a load-bearing mechanical environment simulated *in vitro* using an *ex vivo* system (**Chapter 4**). We demonstrated that the implants can bear various loads due to their bulk materials composition. It is also shown that the permanent deformation is less for the lower porosity implants. In particular, the implants were able to support loads up to 100 MPa, which corresponds to a canine with weight of 20-30 kgs. One of the advantages of MgP-PCL implants is that even after degradation in the physiological environment, the implants can be fixed and support the body weight by the newly bone.

Although these results confirm the potential of MgP-based implants to perform in load environments, further work is needed to evaluate the bone regeneration and the biomechanical properties of the implants in load bearing locations. A potential strategy to address the challenges during the fabrication process, is to gain further control over deposition of printed filaments on the mechanical properties of the scaffolds. This reads as the printing direction has an influence on the mechanical properties of the implants. This is due to the reason that the molecular bonds forming the ink is stronger than the filaments laid down on top of each other. Therefore, for

further investigation, the mechanical properties can be evaluated for the different printing directions. Thus, the mechanical properties increase even more by looking more in-depth into this phenomenon.

Scaling up towards clinically relevant geometries and sizes

The fabrication strategy here proposed was based on extrusion printing of a single biomaterial ink at room temperature. This led to deposited ink filaments subjected to deformations, such as collapse of overhanging filaments, which compromises the ability to stack several layers, as well as merging them between adjacent filaments. This limits full control over the implant structure including pore size, distribution and interconnectivity. We addressed this limitation by using a supportive ink based on a sacrificial hydrogel that was printed simultaneously to the MgP-based biomaterial ink using a dual head extrusion system. This supportive ink was stable enough to support weight of large scaffolds ($\approx 15 \text{ cm}^3$) without compromising their shape.

Another challenge in scaling up bone implants, is the lack of nutrient and oxygen supply within them, which in turn severely limits regeneration of large bone defects. A potential way to overcome this challenge is to print a vasculature network within the implant structure, or even doping pores with angiogenic factors. A potential strategy to ensure sufficient vascularization is to dope implant pore structure with angiogenic metallic ions such as, copper (Cu^{2+}). In previous reports, 3D-printed $\text{SrCuSi}_4\text{O}_{10}$ nanosheets and polycaprolactone (SC/PCL) composite scaffolds were prepared as a bifunctional therapeutic implant for bone tumor photothermal eradication and vascularized bone regeneration^[310]. This allowed to stimulate of factors involved in vessel formation and maturation, such as vascular endothelial growth factor (VEGF), which is mainly responsible for its angiogenesis effect. Furthermore, according to a recent study, gradient PCL scaffolds improved the osteogenic differentiation of human mesenchymal stem cells (hMSCs) *in vitro* by increasing the calcium content and ALP activity because of better supply of oxygen and nutrients in larger pores^[326]. In such an implant, the large pores enhance permeability, cell migration to generate more bone mass and vascularization, while the small pores promote cells growth by providing higher surface area.

Another concern related to scaling up implant sizes using current manufacturing approach is linked to the cytotoxicity of biomaterial ink due to the use of toxic solvents. To further investigate this, we performed additional research to study effect of implant sterilization process on potential trapped solvent inside implant

structure (results presented in **Annex II**). Proton nuclear magnetic resonance (hNMR) analysis, revealed that no specific peaks related to the solvent composition used in the implant preparation was detected after implant washing steps with ethanol and water. The next step forward in use of the implant in first in-human application has reported in **Chapter 5** as osteotomy wedge implants. In this chapter, we showed that degradation of the implants can be control by changing the design and specifically the porosity of osteotomy wedge implants. It has been shown that the implants can be improve their bioactive properties even more by using human bone marrow to regenerate bone. However, more experiments are needed to confirm the potential of the bone marrow coated scaffold for bone regeneration for the relevant size implants.

Osteochondral implants are fabricated to treat articular cartilage by recreating the bone and chondral architecture in biochemical and structural compositions. The large clinically-relevant and patient-specific implants was developed using MgP-based materials as bone anchor and MEW PCL as chondral anchor (**Annex I**). Partial failure of the brittle pure ceramics material upon implantation potentially leads to an imperfect fit and (micro-) movement along bone tissue, which subsequently results in osteolysis ^[327]. Therefore, Annex I suggest that there is a good interconnection between extrusion-based 3D printed MgP-based material and MEW PCL fibres, the strength of the cartilage-to-bone interface needs to be quantified.

Integration with connective tissues

Bone is surrounded by connective tissues such as ligament and cartilage. Bone is thus a substrate for the connective tissues which plays a support role in cartilage and ligament anchoring. Any stress applied to bone could also potentially be transferred from bone to connective tissues and thereby damaging them. This has a great impact on the success or the failure of the implants. Therefore, the application of MgP-based bone implants developing in this thesis can be a great impact on the quality of the newly formed bone and the other tissues in contact with bone. Notably, the physical, mechanical and biological properties of the adjacent tissues are dissimilar and can create some challenges. This can be solved by defining an interface that can transfer load between bone, cartilage and ligament. The transition in mechanical properties from bone to other connective tissues reduce stress concentrations at the interface and preventing failure ^[328]. For such a degradable bone scaffold, the interface between the scaffold surface and the surrounding tissue migrates over time. It is therefore possible to make inferences, morphologically, about the direction of bone and cartilage/ligament formation by the structure of the scaffolds.

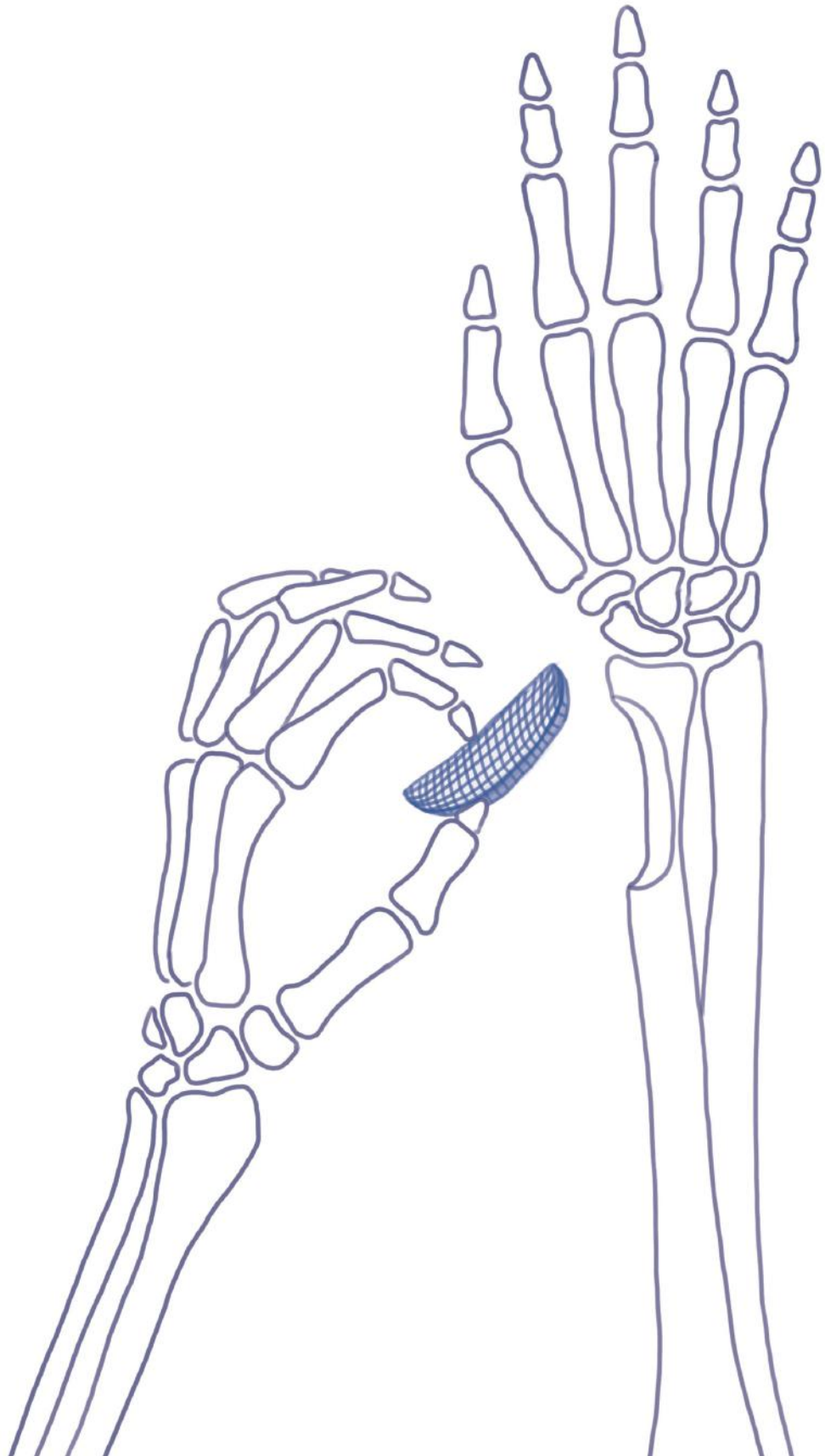
In **Chapter 6**, the fabrication of osteochondral implants was investigated by the developed bone scaffolds and MEW fibre scaffold for cartilage regeneration. The bone component of the osteochondral scaffolds functioned as an anchor for the chondral region of the scaffold. The main finding is that it is feasible to fabricate osteochondral implants using extrusion-based and melt electrowriting printers with a strong interface between the bone and chondral part as shown by stress relaxation tests. One of the limitations of this study is that the interface of the bone to chondral component can be defined as more porous structure with less amount of MgP bioceramics to mimic the structure of the interface of bone to cartilage tissues. For further investigation of the success printing of the relevant sized of the scaffolds, the bonding between the bone and chondral anchors should be quantified using the mechanical properties investigations. Furthermore, the extended *in vivo* study of the osteochondral plug can reveal the collagen fibers extend from the subchondral zone to cartilage through a wavy tidemark.

In **Chapter 7**, graded implants were printed using high content of MgP-PCL and aligned PCL fibres to regenerate the bone to ligament tissues in a one-step strategy. High concentration of MgP particles were incorporated into the PCL polymers to print with an extrusion-based printer assisted by an electrical field (MEW). In previous literature, the composition of PCL and bioceramics were investigated, however the encapsulation of the particles is also yet a challenge due to the low concentration of bioceramics (0.5 – 10 wt.%) [126,295]. To support the mechanical properties between two different materials (MgP-PCL and PCL), the implants were designed with different structures of the interface zone (random and cross-hatch structure). The tensile mechanical properties confirmed that the different zones of the implants bond perfectly after the fabrication. The results have shown that the degraded implants with randomly structure at the interface zone improve the bone and ligament tissues significantly after 6 weeks *in vivo* in fenestration defects. For further investigation, the formation of Sharpy's fibre can be evaluated after the *implantation*. The other limitation regarding the fabrication of degraded implants is that due to the high content of bioceramics, the stackability of the fibres for the height more than 10 mm is a great challenge with MEW technique. By increasing the conductivity of the biomaterial ink, the resolution of the implant can be improved. The conductive materials prevent the blockage of electrical field of the printer and forming the Taylor cone [329].

Conclusion and avenues for future research

The present thesis describes the development and fabrication of tough and osteopromotive MgP-based implants using extrusion-based printing processes. The combination of a composite biomaterial ink, composed of a ceramic phase of MgP and a polymer phase of PCL with extrusion printing at room temperature, allowed the generation of osteoinductive implants with mechanical properties compatible with implantation in relatively load-bearing environments. The osteopromotive properties and easy surgical handling were confirmed in a 6-month *in vivo* study in an equine model; while the load bearing properties and potential translation to veterinary and human healthcare were demonstrated by the fabrication of hip and osteotomy wedge implants. Additionally, the fabrication of high resolution (fiber) MgP-based implants was demonstrated using a paste extrusion-based printing process assisted by an electrical field. The high-resolution scaffolds showed great potential to better resemble bone microenvironments and guide bone. The findings in this thesis confirms the success fabrication of tough and osteoconductive bone implants for large defect size.

Despite promising results present in this thesis, future research is needed to understand mechanical performance of constructs under load bearing *in vivo* environments, as well as to incorporate angiogenic agents to facilitate vascularization in large bone non unions.



Appendices

Annex I

Scaling up from osteochondral plug to patient-specific condyle resurfacing: fabrication, *in vitro* characterization, and mechanical characterization under physiological conditions of clinically relevant osteochondral implants

Mylène de Ruijter

Nasim Golafshan

Inge Dokter

Ioanna Gkoni

Roderick Verberne

Joao Garcia

Laura Creemers

P. René van Weeren

Pieter. A.J. Brama

Daniel J Kelly

Keita Ito

Paige Little

Peter Pivonka

Jos Malda

Miguel Castilho

A

Abstract

Articular cartilage defects are common and current surgical treatments provide sub-optimal tissue repair. Multiple biofabrication approaches have tried to recreate the chondral architecture in biochemical and structural composition and this has frequently been combined with an osteal anchor in the form of an osteochondral plug. In this study, the translation from this relatively small plug to larger clinically-relevant and patient-specific implants is explored. Osteochondral patient-specific large (surface area = 469 mm²) implants consisted of a porous bone component, close cartilage-to-bone interface, and a microfibre reinforced cell-laden gelatin methacryloyl (gelMA) cartilage component. The effect of implant size (bone component only) on stress-strain distribution and cartilage-like tissue formation is studied by means of axial compression and compression under 50° and 60° flexion angles using a robotic arm system. The implant stiffness decreased with increased implant size. An increase in size of the cartilage component (from 6 mm diameter discs to 24 mm diameter discs) did not hamper cartilage-like tissue formation *in vitro*. As the larger implants include a patient-specific complex shaped geometry, a software tool has been developed and validated to automatically generate a numerical control programming language (*i.e.*, g-code) that resurfaces a bone structure with melt electrowritten (MEW) microfibres based on a 3D-standard tessellation language (.STL) file. As a proof of principle, a large complex shaped implant was fabricated and cultured *in vitro* to assess 3D matrix distribution. This study shows the first steps in translating from osteochondral plugs to larger patient-specific implants.

Introduction

Articular cartilage (AC) defects generally result in progressive deterioration of the joint, causing pain and reducing mobility, significantly affecting the quality of life of patients.^[330,331] The problem is intensified by the fact that AC has limited regenerative capacity^[332,333] and current surgical approaches to repair focal defects show sub-optimal long-term outcomes due to the formation of fibrous tissue with inferior mechanical properties. Although allograft transplantation may result in the retainment of qualitatively better tissue, this application is restricted due to logistical constraints and difficulty in achieving a patient-specific fit.^[334]

Biofabrication^[335] seems a promising approach to fulfil the need to improve treatment of AC damage by fabrication of patient-specific implants. This field aims to restore tissue function by combining the regenerative capacity of the patient's own cells with biomaterials and/or bioactive cues using additive manufacturing techniques that allow spatial control over the deposition of such components. Implants generated with biofabrication strategies are very versatile as they can be tailored to the individual patient's specific AC defect(s), based on the translation of patient data retrieved from medical imaging techniques to machine-specific instructions. Up to now, evaluated implants for the restoration of AC defects are shaped as osteochondral plugs, where the osteal component acts as an anchor for the cartilage part upon implantation.^[336,337] Integration with the host tissue of the biodegradable osteal component is generally based on the recruitment and stimulation of endogenous cells from the bone marrow. PCL-magnesium-based 3D printable paste is a promising composite material explored for this osteal components due to its biodegradability and load-bearing properties.^[338] Further, biofabrication approaches for the restoration of the chondral part have mainly focused on recreating the native zonal cartilage tissue architecture^[339,340] in terms of biochemical and structural components, including the distinct type II collagen "Benninghoff arcades"^[341] architecture that are imperative for AC's mechanical function.^[342] To achieve 3D cartilage-like matrix deposition *in vitro*, chondrocytes^[343], mesenchymal stromal cells (MSCs)^[344], or articular cartilage resident chondroprogenitor Cells (ACPCs)^[345] are embedded in mechanically soft hydrogels. However, these soft hydrogels are not able to withstand the challenging mechanical environment of the joint and thus, fibre reinforcing technologies have been explored to achieve mechanical competent cell-laden biodegradable constructs.^[346–349] Melt electrowriting (MEW)^[350,351] is considered a promising fibre reinforcing technology for hydrogel-based cartilage implants as it uses only a small fraction of (sub)micro-fibres, yet still allows for a significant increase in the mechanical properties of these hydrogel-thermoplastic

constructs due to the tight control over the network architecture.^[352–355] Recently, MEW has been combined with the extrusion-based 3D printing of bioinks in a single-step fabrication approach^[356], which allowed for accurate deposition of both the fibrous and non-fibrous components and also created a mechanically secure interconnection between the cartilage-to-bone interface.^[357] Osteochondral plugs that were fabricated with this converged printing approach showed to be mechanically stable enough to withstand the challenging *in vivo* environment in the stifle joint in the equine model for up to 6 months (Chapter 8). Yet, such plugs do not directly reflect the shape of the observed defects in patients as they are round, have a specific, relatively small diameter, and show a flat surface. Upscaling the size of implants results in individual challenges for the bone component (mechanical), the cartilage component (mechanical and biological), as well as challenges related to the combined osteochondral unit (fabrication of the patient-specific convex geometry).

Therefore, the aim of this study (Figure 1) was to scale-up the fabrication of from the relatively simple osteochondral plug to larger, more complex patient-specific implants, and subsequently demonstrate their load bearing properties under physiological loading conditions. We studied the effect of implant size (bone component only) on the mechanical properties of this bone component, but also the effect of implant size on cartilage-like tissue deposition. Additionally, to fabricate a patient-specific large osteochondral unit with a convex geometry, a semi-automatic software tool for resurfacing a complex-shaped bone-reflecting part of the joint structure has been achieved.

Materials and method

Cell harvest, expansion and culture conditions

Goat articular chondroprogenitor cells (ACPCs) were harvested from femur condyles, obtained from the local slaughterhouse, according to previously published protocols used for harvesting equine ACPCs.^[345,358] ACPCs were cultured in expansion medium until passage 5, after which they were embedded in the hydrogel and cultured in chondrogenic differentiation medium for 28 days. Expansion medium consisted of Dulbecco's modified eagle medium (31966, Thermo Fisher Scientific, USA) supplemented with 10% fetal bovine serum (Gibco, Thermo Fisher Scientific, USA), 1% penicillin-streptomycin (Gibco, Thermo Fisher Scientific, USA), 1% l-ascorbic acid-2-phosphate (0.2×10^3 M, Sigma Aldrich, USA), 1% non-essential amino acids (100X, Gibco, Thermo Fisher Scientific, USA), and 5 ng/mL bFGF (Preprotech, UK), and medium was refreshed twice per week. Chondrogenic differentiation medium

consisted of Dulbecco's modified eagle medium (31966, Thermo Fisher Scientific, USA) supplemented with 1% penicillin/streptomycin, 1% l-ascorbic acid-2-phosphate, 1% ITS + Premix Universal culture supplement (Corning, USA), 2.5% HEPES (1M, Gibco, Thermo Fisher Scientific, USA), 0.4% dexamethasone (0.1×10^{-6} M, Sigma Aldrich, USA) and 0.1% recombinant human transforming growth factor- β 1 (TGF- β 1) (10 ng/mL, Preprotech, UK). Medium was refreshed three times per week. All cultures were performed under sterile and normoxic culture conditions at a temperature of 37°C and 5% CO₂.

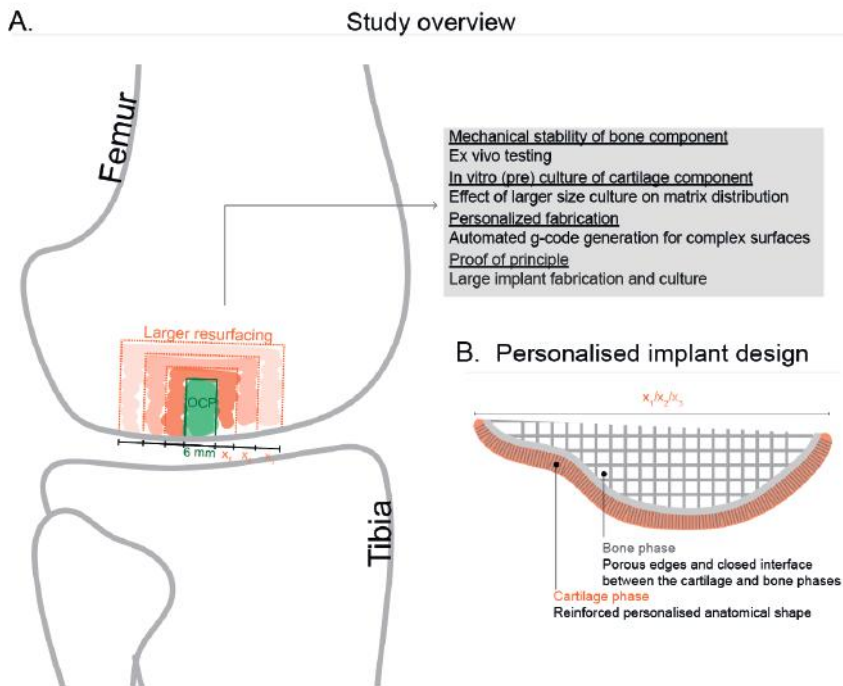


Figure 1. A) Study overview, highlighting the challenges that arise when transitioning from osteochondral plugs towards (partial) joint resurfacing. B) Personalised implant design highlighting side porosity in the bone phase and personalised anatomically-shaped reinforcement in the cartilage phase.

Implant fabrication

Bone component: Polycaprolactone (PCL, Purasorb PC12, Corbion, The Netherlands) was used as received. The PCL implants were printed via fused deposition modelling (FDM, 3D Discovery Evolution, regenHU, Switzerland). The cartridge temperature was set at 80°C, while the temperature of the nozzle was set at 90°C. The extrusion of the

melted PCL was controlled by a screw-system at a constant feed rate of 2 revs/min with a collector velocity of 2mm/min.

MgP-PCL was prepared as previously described^[255]. MgP-PCL implants were printed with a 3D-bioprinter (3DDiscovery Evolution, regenHU Ltd, Switzerland) using a conical shaped, 22 G nozzle (Nordson EFD, USA) at a velocity of 5 mm/min and a pressure ranging from 0.060 to 0.220 MPa, based on the viscosity of the MgP-PCL paste. The infill density of each layer was set at 35%, the overlapping perimeter at 15%, and the layer height at 0.2 mm. After printing, the dimensions of the generated implants were measured to assess shape fidelity of the printed implants. To eliminate solvents, the implants were washed in 70% ethanol for 6 hours and subsequently submerged in Milli-Q water for 24 hours.

Cartilage component: Gelatin methacryloyl (gelMA) was synthesized as previously described^[359,360]. Briefly, gelatin (type A, derived from porcine skin, 175 Bloom, Sigma Aldrich, The Netherlands) was dissolved at 10% w/v in phosphate-buffered-saline (PBS) at 60 °C after which 0.6 g methacrylic anhydride (Sigma Aldrich) was added per g of gelatin to achieve an 80% degree of functionalisation. Freeze-dried gelMA was diluted with PBS to obtain a final gelMA concentration of 10% w/v and subsequently placed in a 37°C incubator to ensure a homogeneous solution. To initiate the cross-linking reaction, a combination of 5mM sodium persulfate (Sigma Aldrich) and 0.5mM Tris(2,2'-bipyridyl) dichlororuthenium (II) hexahydrate (Sigma Aldrich) was added to the gelMA solution. Implants were crosslinked for 10 min under led light (20W LED, Jobmate, China)

Fibre reinforcing component: MEW was performed with PCL which was molten in a metallic cartridge at 80°C. The MEW head was translating in z- and y-direction whereas the high voltage collector plate was translating in x-direction. An air pressure of 110-125 kPa, voltage of 7-11 kV, collector velocity of 20 mm/s, and a constant collector to implant distance of 6 mm were applied to extrude the PCL fibres through a 24G nozzle.

Anatomically shaped implants:

To acquire the precise anatomy of the ovine stifle, micro-CT data were acquired at the Medical Engineering Research Facility (MERF) of Queensland University of Technology (QUT). From reconstructed CT models the tibia and the femur were segmented and subsequently exported into the Standard Tessellation Language (.STL) format. On the medial femoral condyle, three different sized defects, and subsequent implants, were generated by forming a 55° inclination with the horizontal plane (Autodesk

Netfabb Premium 2019, San Rafael, USA). The design of the implants was based on the principle of limiting cellular penetration from the bone compartment to the cartilage compartment and the knee-joint space, while allowing cell infiltration into the bone compartment.

Mechanical testing of printed implants under physiological loading

Two loading conditions were applied based on body weight & gait analysis of ovine^[361] that will be used for subsequent *in vivo* testing of the developed implants (average body weight 60kg, 2 years old). For the first loading condition (axial load), implants were fixed at a knee flexion angle of 55°, the angle at which maximum axial force is registered^[361], and cyclic compressed (6x) up to a maximum force of 2000N at a rate of 400N/s. These tests were performed on a universal testing machine (Instron 5967, US). For the second loading condition (flexion and extension), gait was resembled by allowing extension-flexion of femur and tibia vary between 50° - 60° at 5°/sec. Here, the axial load was kept constant at 400N (scaled due to the limitations of the unit cell available). For this second loading condition, a 5 degrees of freedom (DoF) robotic arm system was used (QUT, Australia). For both loading condition, a pre-load of 100 N was applied to ensure contact between the test samples and the opposing tibia. Implants composed of PCL and MgP-PCL with different sizes (small (S): 5 x 17 mm, medium (M): 10 x 17 mm, large (L): 15 x 17 mm) were studied. As a model joint (*i.e.*, tibia and femur compartments), a digital light processing (DLP)-fabricated patient-specific ovine joint was used (Non-deformable R05 material, Envisiontec, Germany) with defects that corresponded with the implant measurements.

For the mechanical analysis, stress-strain curves were calculated from the applied force and displacement data from the axial loading experiment. Here, stress is defined as the applied force divided by the implants' loaded area. Loaded area between implant and opposing tibia, was determined by stained paper positioned between implant and tibia. Strain was defined as the ratio between the initial implants thickness and the displacement of compression head. Implant stiffness was calculated from the slope of the engineered stress-strain curve near the maximum value of stress for each loading cycle. The implants that were tested in the flexion and extension experiment only reflect the maximum force as the contact area could not be determined (work in progress). In addition, all tested implants were measured before and after loading to quantify implants permanent deformation.

Automation of MEW printing path based on .STL file

A python program was written to automatically generate numerical control programming language (*i.e.*, g-code) from .STL files for the resurfacing movement

of the MEW head. A visual presentation of the printing trajectory was made with NC Viewer © 2018 Xander Luciano. Machine specific codes can be included in this program, or after extracting the g-code, to make this code more versatile for other machines. User input is only needed for parameters such as line spacing, collecting implant or printhead velocity, collector to implant distance and intended scaffold height. The python script runs through a series of events including importing the mesh and extracting coordinates of the .STL file, adjusting z-coordinates based on collecting implant to printhead distance, finding x- and y- values for the required line spacing, finding and combining the x-, y-, and z-trajectories, including machine specific input, and exporting the resulting g-code into a .txt file (Supplementary Figure 1). As a control mechanism, midpoint checks are added to the code to generate x-y-, y-z-, and x-z-scatterplots and histograms of the x-, y-, z- coordinates. In this code, the accuracy of the amount of steps made in x-, y-, and z-direction can be altered by changing the programmed trajectory accuracy (PTA) and a low input value reflects a higher accuracy. The average steps in x- and y- direction based on a low, medium, and high PTA was calculated based on all point in all lines for that specific direction. The effect of the PTA on the fibre diameter was measured with light microscopy (Olympus DP73, Olympus Nederland B.V., The Netherlands) and Fiji software (version 2.0.0-rc-54/1.51h). To measure the percentage of resurfacing of the implant, the deviation between the deposited MEW mesh and the edge of the implant was measured from a topview perspective.

***In vitro* culture**

To analyse the effect of implant size on *in vitro* cartilage-matrix deposition different diameter discs (diameter = 6, 12, 24 mm) were cultured in chondrogenic differentiation medium. Additionally, as osteochondral plugs, depending on the material used, may hamper the influx of nutrients and efflux of waste components during *in vitro* culture, the effect of a flat plate system (reflecting the same number of nutrient and waste exchange directions as the osteochondral plugs) as compared to a transwell system (reflecting the highest number of nutrient and waste directions during bulk static culture conditions) has been evaluated.

Biochemical evaluation of cartilage-like tissue formation

To quantify the amount of sulphated glycosaminoglycans (sGAGs) and correct them for DNA content, colorimetric dimethylmethylene blue (DMMB, Sigma Aldrich, USA) and fluorometric Picogreen (Quant-iT-Picogreen-dsDNA-kit, Invitrogen, USA) assays were performed, respectively. Prior to these assays, implants were enzymatically digested overnight at 60°C using a papain digestion solution.

Histological evaluation of cartilage-like tissue formation

Histological evaluation of the *in vitro* cultured constructs was performed to assess the distribution of cartilage-like matrix components. The constructs were formalin-fixed and embedded in paraffin. Tissue sections (thickness = 5 μ m) were deparaffinized with xylene and were rehydrated by gradual ethanol steps (100% - 70%) prior to staining. Safranin-O staining was used to visualize GAG distribution, combined with fast green (Sigma Aldrich, USA) to stain fibrous tissue, and haematoxylin (Sigma Aldrich, USA) to stain cell nuclei. Immunohistochemistry was performed to visualize type II collagen deposition. First, pronase (1 mg/mL, Roche, USA) and hyaluronidase (10 mg/ml, H2126, Sigma Aldrich, USA) were used for antigen retrieval, and sections were blocked with bovine serum albumin prior to primary antibody incubation II-II6B3 (DSHB, USA). IgG was used as negative control staining. Samples were incubated over night at 4°C, washed, incubated with matching secondary antibody (1:100, IgG HRP, P0447) for 1 hour at room temperature, and washed again. Subsequently, 3,3-diaminobenzidine-horseradish peroxidase (DAB, Sigma Aldrich, USA) was used to visualize the staining. After staining the cell nuclei with haematoxylin, pictures of histologically stained sections were made with a light microscope (Olympus BX51, The Netherlands).

SEM imaging

Scanning electron microscopy (SEM) (Phenom Pro Desktop SEM, Thermo Fischer Scientific, USA) was performed with an accelerating voltage of 10. Prior to imaging, samples were coated with 2 nm of gold to improve imaging quality.

Statistics

Data is presented as mean \pm standard deviation. Fibre diameters, inter-fibre spacings, and resurfacing percentages were measured on 5 samples per group. All *in vitro* culture studies were performed in triplicate, and mechanical analysis was performed with $n = 3$. To test the differences between groups, either an unpaired t-test, or an ANOVA with post hoc Bonferroni test was performed. Difference between groups was considered statistically significant if $p < 0.05$.

Results

Fabrication

Based on CT scans of ovine joints, Standard Tessellation (.STL) files were generated. In these .STL files, defects of 5 mm (S), 10 mm (M), and 15 mm (L) were made in the medial femoral condyle. Implants that were based on these defects presented

a contact surface area of 302, 459, and 469 mm² to fit into the 5 mm, 10 mm, and 15 mm defect, respectively (Figure 2A). The .STL files (Figure 2B) of the implants were used to design the bone component with a closed layer between the bone and cartilage interface and an open pore structure at the bottom and at the sides of the implant that will eventually interact with native tissues (Figure 2C-D). Printed implants showed a good fit in the DLP-fabricated model of the defect (Figure 2E).

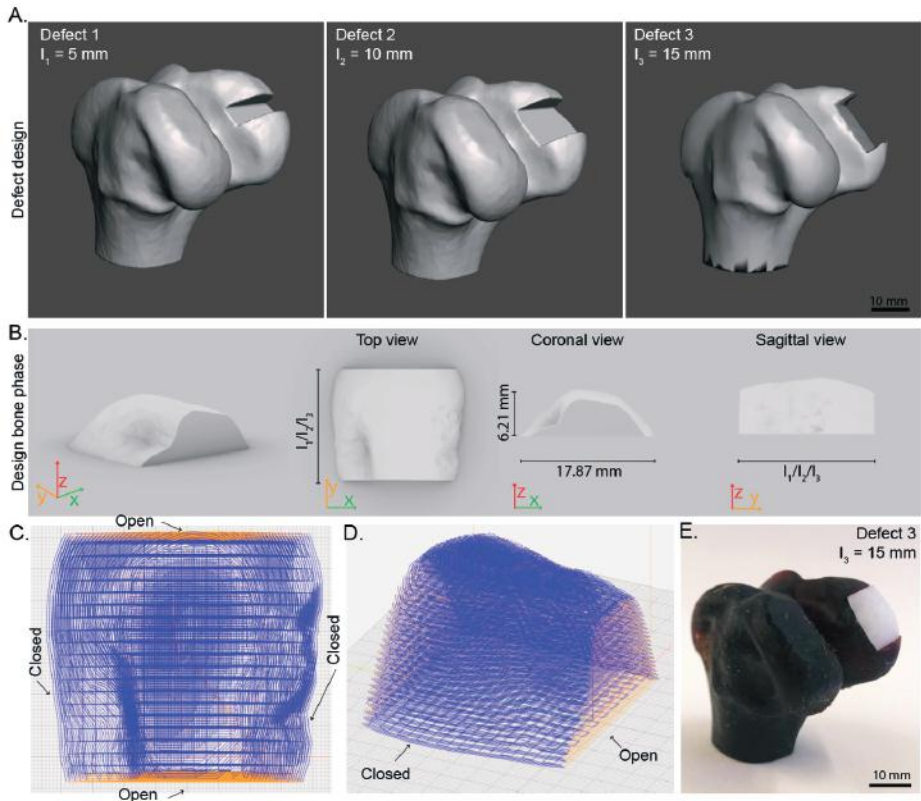


Figure 2. Implant design and printing trajectory of bone phase of the implant. A) Design of the defects with a difference in sagittal length (sagittal length $l_1 = 5$ mm (S), $l_2 = 10$ mm (M) and $l_3 = 15$ mm (L)). B) Rendering of implant reflecting complex shaped surface. C) Top view of the printing trajectory, with open pores (orange) on the connecting side and including 4 closing shells (blue) around the implant. D) Side view of printing trajectory. E) Digital Light Processing (DLP)-printed models that were used for digitally transferable *ex vivo* testing of implant, here filled with a PCL implant.

For the bone component, frequently used medical grade PCL was compared with magnesium phosphate enhanced PCL (MgP-PCL) implants. Both PCL and MgP-PCL showed a high shape fidelity after printing and successfully resolved the designed pore structure in the x-, y-, and z-direction (Figure 3A). MgP-PCL did show a higher

fibre diameter (PCL: $208 \mu\text{m} \pm 14 \mu\text{m}$, MgP-PCL: $300 \mu\text{m} \pm 20 \mu\text{m}$) and a lower inter-fibre spacing (PCL: $593 \mu\text{m} \pm 25 \mu\text{m}$, MgP-PCL: $424 \mu\text{m} \pm 28 \mu\text{m}$) as compared to PCL (Figure 3B, C). The inner pore structure of the first 4.7 mm was successfully achieved (Figure 3D-E). Printing of MgP-PCL implants showed high dimensional accuracy and reflected the STL file well. (Figure 3F-G).

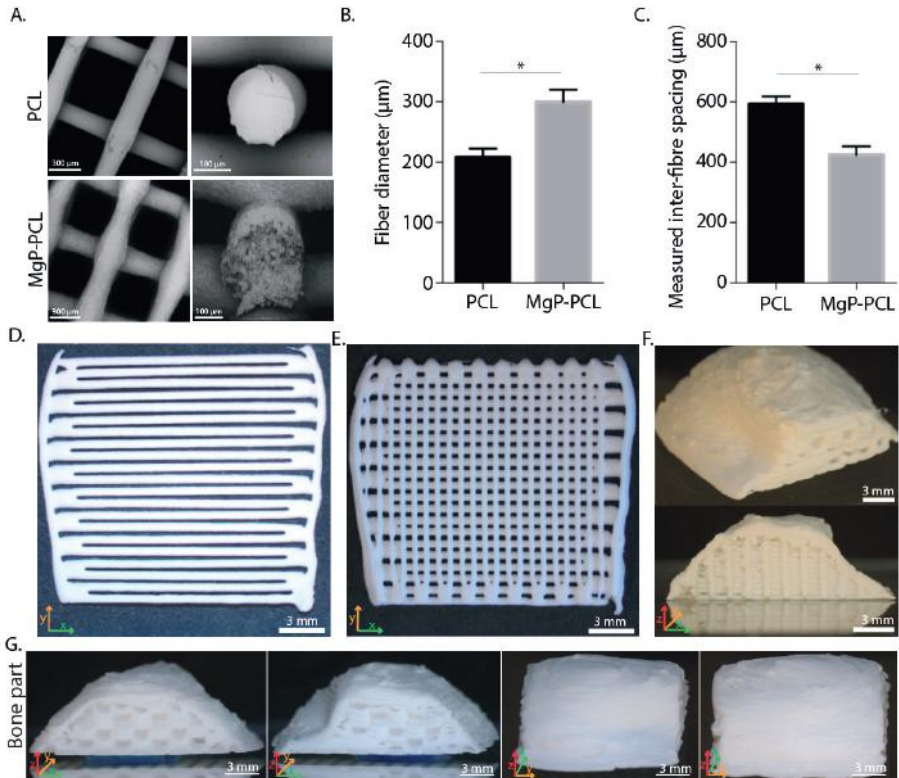


Figure 3. Details of PCL and MgP-PCL printed implants. A), Fibre morphology of PCL and MgP-PCL strands. B) Fibre diameter of PCL and MgP-PCL printed strands. C) Measured inter-fibre spacing of the PCL and MgP-PCL implants. D-E) Top view of the porous inner structure of the first 4.7 mm. F-G) MgP-PCL printed implant, representing the bone part from different angles. * = $p < 0.05$, t-test.

Mechanical testing

Uniaxial cyclic compression (Axial loading, Figure 4A) on the implants was performed with the opposing DLP fabricated tibia and yielded different stress strain curves for the small versus the large implant (Supplementary Figure 2). The implant stiffness of both small and large implants was increased per cycle (Figure 4B). The small implants yielded a significant higher stiffness compared to the large implants (Figure 4B). For the PCL implants, the implant thickness significantly decreased after compressive testing

for the medium (11 %) and large samples (13 %) (Figure 4C). When varying extension-flexion rotation at a constant axial compression (Figure 4D) larger PCL implant showed a lower maximum force compared to smaller implants with 76 N and 187 N after 5 cycles of compression, respectively (Figure 4E). After compression under flexion and extension, the medium (7 %) and large (10 %) implants showed a significant decrease in final implant thickness as compared to before compressive testing (Figure 4F).

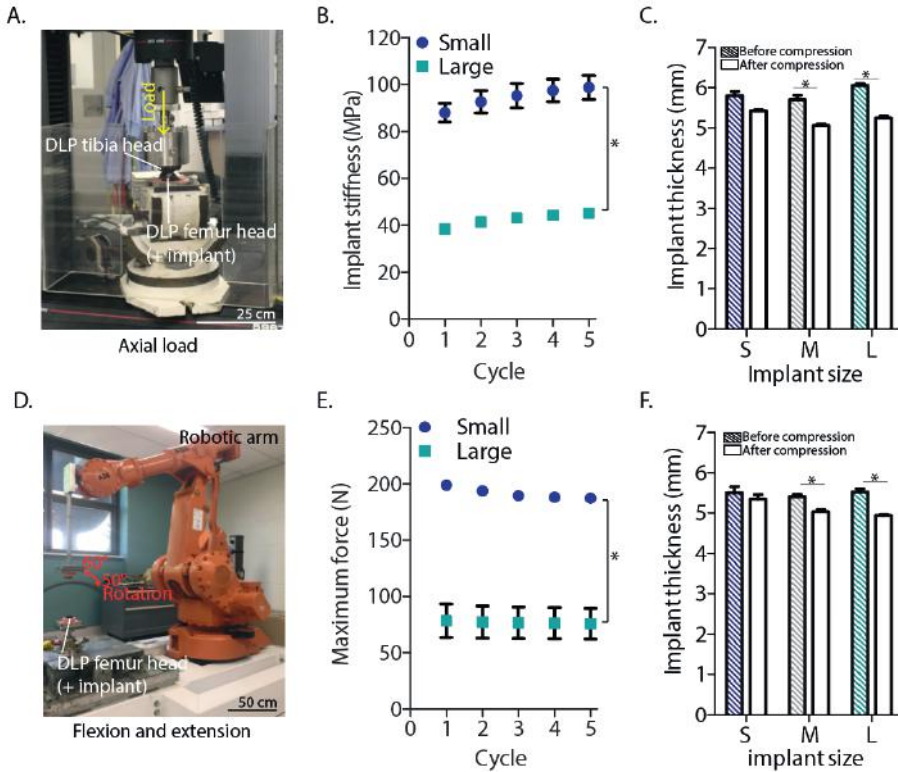


Figure 4. Mechanical evaluation of MgP-PCL and PCL implants under physiological loading. A) Axial loading condition. B) Stiffness of small and large PCL implants per cycle. C) Final implant thickness of different sized implants of PCL before and after 5 cycles of compression as a reflection of permanent deformation. D) Flexion and extension testing with a robotic arm system. E) Maximum force of small and large implants (Surface area was not determined, work in progress). F) Final implant thickness of different sized PCL implants before and after compression as a reflection of permanent deformation. * = $p < 0.05$, ANOVA post hoc Bonferroni.

In vitro culture

Caprine ACPCs showed slight positive staining for alizarin red, oil red O and safranin O staining (Figure 5A) after culture in adipogenic, osteogenic, and chondrogenic medium for 21, 28, and 28 days, respectively. Additionally, an increase in sGAGs per

DNA was found for all donors during 28 days of *in vitro* culture in 3D cell-laden hydrogel discs, a typically used 3D *in vitro* culture system for cartilage tissue engineering (Figure 5B). This increase was predominantly shown in the first 14 days of culture.

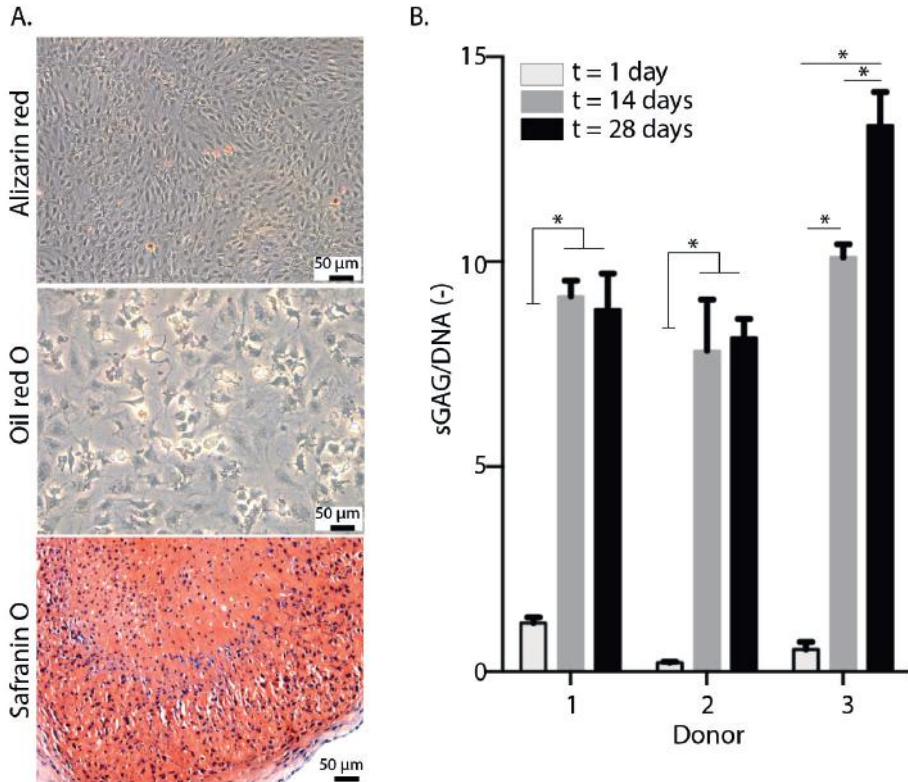


Figure 5. Caprine ACPCs. A) Tri-lineage assay shows that goat derived ACPCs are able to differentiate into the osteogenic, adipogenic, and chondrogenic lineage. B) Quantification of sGAG/DNA per donor over the course of 28 days of *in vitro* culture. * = $p < 0.05$, ANOVA, post hoc Bonferroni.

When assessing the effect of disc size (diameter = 6, 12, 24 mm, Figure 6A) on cartilage-like matrix distribution, all disc diameters showed an increase in sGAG/DNA after 14 and 28 days of culture (Figure 6B). After 28 days, a decrease in sGAG/DNA was observed with increasing disc diameters, with 81, 59, and 48 µg/µg sGAG/DNA for discs with a diameter of 6, 12, and 24 mm, respectively. A transition from a flat plate system (to reflect the same number of nutrient and waste exchange directions as engineered cartilage on osteochondral implants) to a transwell system (that reflects the highest number of nutrient and waste exchange directions for bulk static culture) (Figure 6C) did not affect sGAG/DNA, total sGAG or DNA content in the 6 or 24 mm diameter discs after 28 days of culture (Figure 6D).

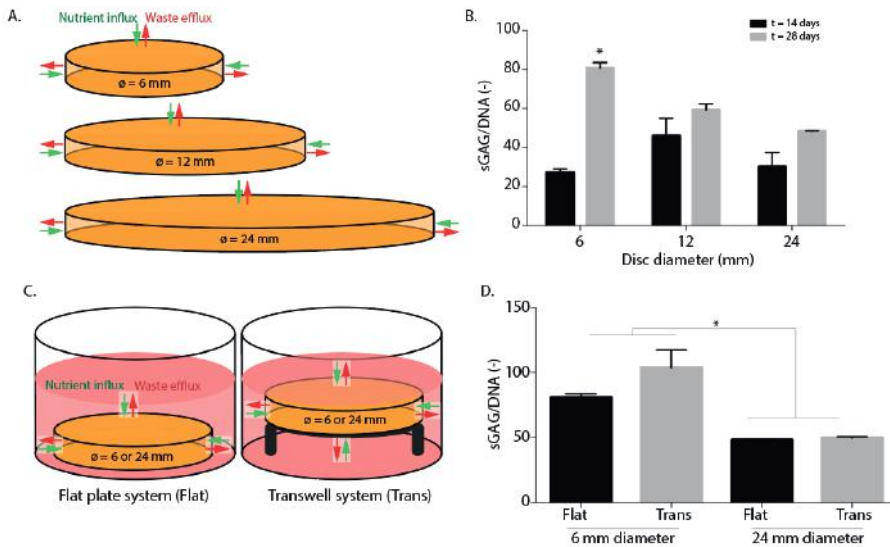


Figure 6. *In vitro* tissue culture. A-B) Effect of disc diameter (diameter = 6, 12, 24 mm, h = 2 mm) on cartilage like matrix formation in terms of sGAG/DNA. C-D) Effect of *in vitro* culture on a flat plate system as compared to on a transwell system with respect to cartilage-like matrix formation for 3D discs of 6 and 24 mm in diameter. * = $p < 0.05$, ANOVA, post hoc Bonferroni.

Automatic numerical control programming language (*i.e.*, g-code) generation

G-code generation to resurface the patient-specific .STL file, while keeping the distance between the collecting implant and the printing head equal by translating in z-direction, was successfully automated (Figure 7A). The number of steps along the length of a complete line in x-, or y- direction, depended on the difference in z-coordinates along this same x-, or y-trajectory and was determined as the Programmed Trajectory Accuracy (PTA) (Figure 7B). This PTA can be adjusted by the user and an increase in PTA included more steps in x-, and y- direction. Although a higher PTA involved an increased number of steps and therefore an increase in MEW jet disturbance by acceleration and deceleration in the motion pattern, only the high PTA printing condition showed a significant increase in fibre diameter as compared to the low and medium PTA (Figure 7C). Even though the lower PTA showed a lower resurfacing trajectory (Figure 7B), the measured resurfacing percentage was not affected by the PTA (Figure 7D). Irrespective of the amount of stacked MEW fibres, the measured resurfacing remained at around 71% (Figure 7E).

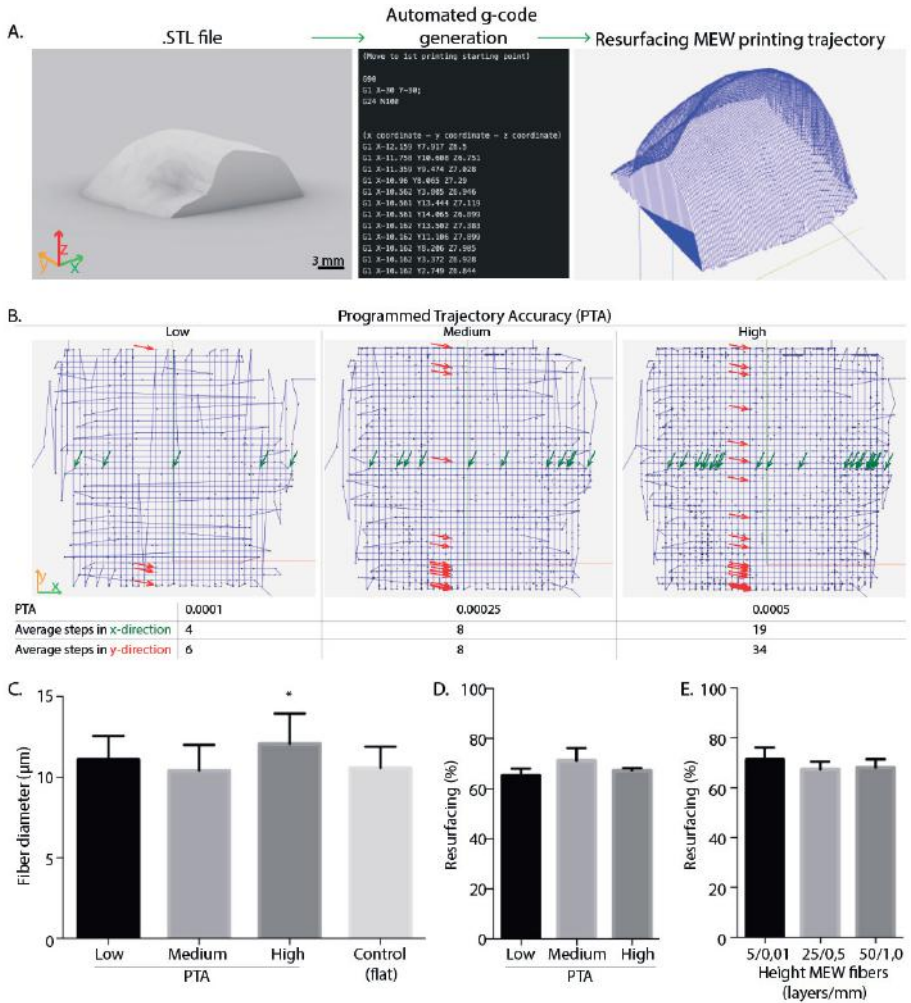


Figure 7. Automated g-code generation for MEW printing trajectory. A) Path from STL file to g-code to resurfacing trajectory. B) Top view of resurfacing MEW printing trajectory with low, medium, and high programmed trajectory accuracy (PTA). Green and red arrows indicate the specific points on 1 line where the printhead navigates to for the x, and y- direction, respectively. C) Effect of PTA on fibre diameter. D) Effect of PTA on measured % of resurfacing. E) Effect of MEW scaffolds height on measured % of resurfacing. * = $p < 0.05$, ANOVA, post hoc Bonferroni.

A

By adjusting the automatic printhead trajectory (Figure 8A) that followed the exact pattern of the .STL of the implant to an extended printhead trajectory (Figure 8B, C), where the printing trajectory is manually extended in the automatically generated g-code, the measured percentage of resurfacing was increased from 71% to 96% (Figure 8D). This increase was mainly found in the x-direction where the collecting implant showed more deviation in z-direction as compared to the y-direction (Figure 8E). The 71% of measured resurfacing for the automated printhead trajectory was affected by the geometry of the implant as the part where the geometry included the concave curvature ($x_{ii} - x_{iii}$) showed a lower percentage of resurfacing as compared to the part where the geometry only included the convex curvature ($x_i - x_{iii}$) (Figure 8F). Interestingly, incomplete resurfacing (71%) resulted in inaccurate fibre deposition and subsequent piling up of fibres at the top of the implant (Figure 8F-H). This effect was not found for the implants that were printed with the extended trajectory, where accurate fibre patterning was observed (Figure 8I-K, Supplementary Figure 3). Fibre deposition around the concave curvature (yellow arrow in Figure 8K) was less accurate as compared to fibre deposition at the convex curvatures.

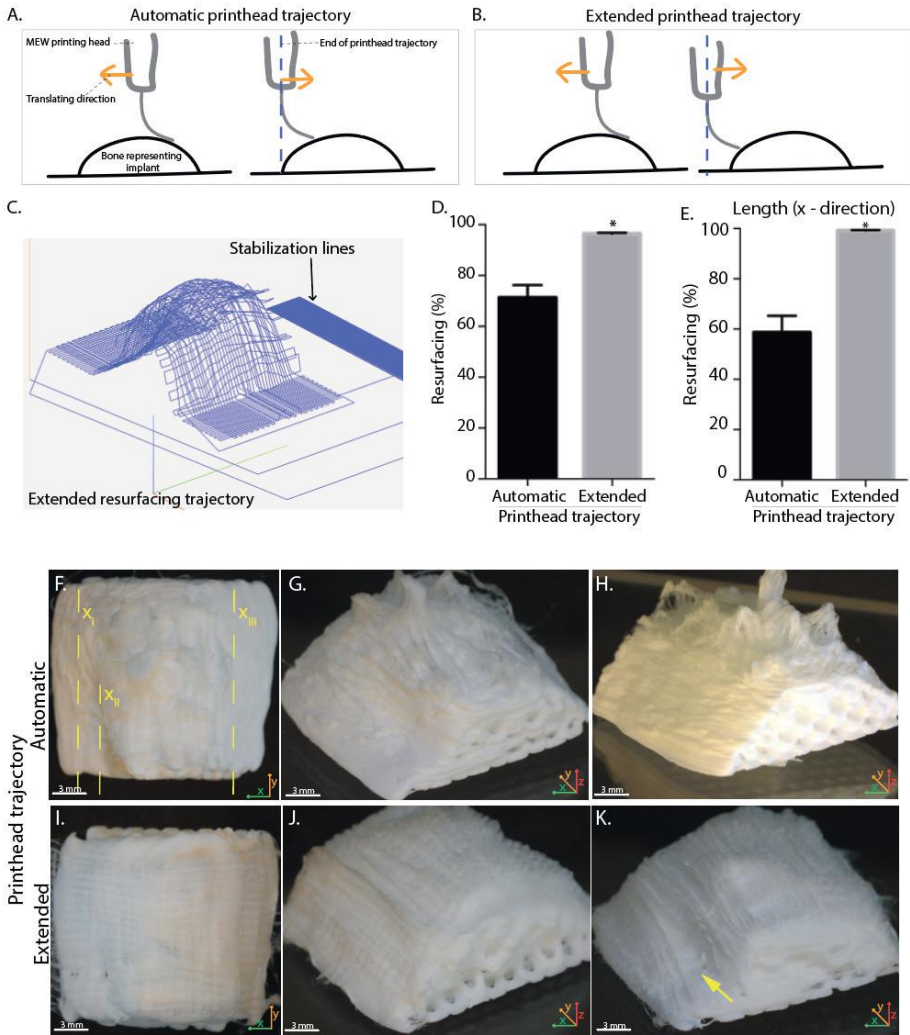


Figure 8. Extending the printhead trajectory. A) Automatically generated printhead trajectory stops resurfacing at the edge of the implants. B) Manually extended printhead trajectory moves beyond the edge of the implant. C) Simulation of the eventual printhead trajectory. D) Effect of manual extension of the printhead trajectory on the total measured % of resurfacing. E) Effect of manual extension of the printhead trajectory on the measured number of resurfacing in x-direction only. F-H) Macroscopic images of the implants that were resurfaced with the fully automated g-code. I-K) Macroscopic images of the implants that were resurfaced with the extended printhead trajectory. * = $p < 0.05$, unpaired t-test.

In vitro culture of completely resurfaced implants

As a proof-of-principle, the completely resurfaced implants (**Figure 9**) were cultured for 28 days. Directly after fabrication, macroscopic evaluation demonstrated that the implant showed a smooth surface and maintained integrity.

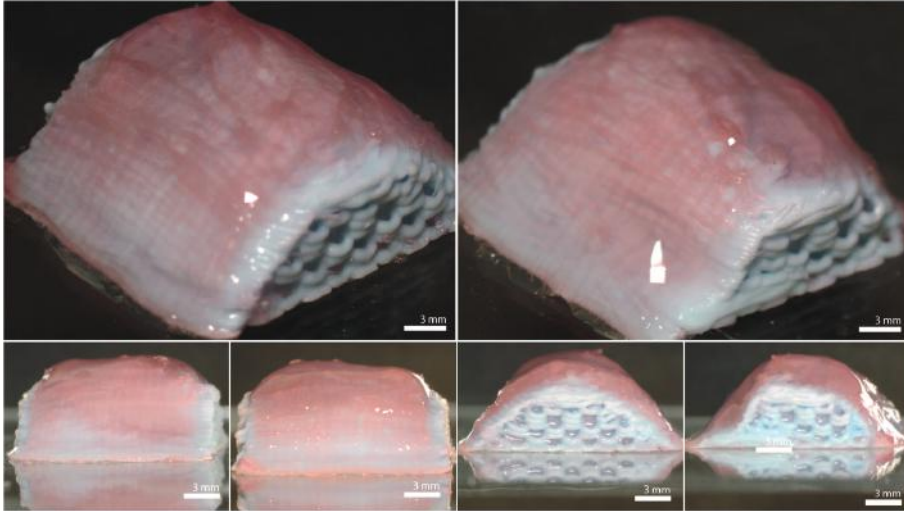


Figure 9. Completely resurfaced, large patient-specific, biofabricated implant.

Discussion

Current developments in (bio)fabrication technologies allow for multi-material and multi-scale fabrication resulting in tissue structures that more closely mimic native tissues.^[362–364] These developments have progressively improved the resolution of osteochondral plugs that are fabricated to treat AC and osteochondral defects.^[336,356,357] Although promising *in vitro* results have been shown, and mechanical stability of structurally strong plugs has been shown *in vivo*, these plugs are still relatively small and do not directly translate to patient-specific treatments. In this study, the first steps in the transition from the osteochondral plug towards larger, patient-specific and mechanical competent implants have been made.

Despite the fabrication challenges, engineering large tissue structures generally pose the challenge of nutrient and waste exchange to provide a biological environment in which the cells can produce matrix components and mature the engineered tissue.^[347,365] Multiple strategies to overcome this challenge have been tried such as incorporation of (micro-)channels within printed constructs^[366], controlled delivery mechanisms^[367], and modular scaffold designs^[368] to mature the tissue prior to

eventual assembly. The *in vitro* culture of this study shows that for the 2 mm thick cartilage layer, nutrient and waste exchange did not prevent matrix distribution in larger implants. Although there was less sGAG/DNA production for the 12 mm and 24 mm diameter constructs as compared to the 6 mm diameter construct, an increase in sGAGs was still found for all these constructs over the course of 28 days. Moreover, placing both the 6- and 24-mm constructs on a transwell culture system to allow nutrient and waste exchange from more directions, did not affect matrix deposition in these constructs as compared to the flat plate culture system that reflects the same amount of nutrient and waste exchange as engineered cartilage of an osteochondral implant has. This suggests that the 2 mm thickness is not a limiting factor for cartilage-like matrix formation. Multiple *in vitro* studies that use 2 mm thick discs as a culture system for articular cartilage-like tissue formation support this result.^[345,352,369] Additionally, in a study that used aggregates to resurface the large tibia plateau, ample matrix distribution and tissue maturation in terms of type II collagen alignment were shown.^[370] Although that study did not use a gel as a cell carrier, it does show that a 2 mm thick tissue does not have to be a limiting factor for articular cartilage-like tissue formation and maturation.

Another challenge of fabricating larger implants is the cell source and cell availability as cell-laden hydrogels generally use high cell densities to achieve matrix production throughout the entire construct. Achieving high cell numbers can be challenging with commonly used chondrocytes and MSCs as these loose chondrogenic potential after multiple proliferation cycles. Equine derived ACPCs do not show this limited proliferative capacity and can therefore be expanded to high cell quantities.^[345,358] An additional benefit of ACPCs as opposed to MSCs is that the former do not tend to go into hypertrophic growth and subsequent osteogenic lineage. The cells used in this study are caprine-derived cells from articular cartilage tissue that show the potential to differentiate into the adipogenic, osteogenic, and chondrogenic lineage. Although no specific ACPC markers are known, it is important to test the chondrogenic capacity of these cells after multiple proliferation cycles to more thoroughly understand if the behaviour of these cells is similar to that of equine-derived ACPCs. Other approaches to deal with the challenge of cell availability are by co-culture of different cell types^[371], use of extracellular vesicles that act as stimulating communication units between the cells^[372], or increasing cell-cell contact by aggregating^[370,373] and preculturing chondrocytes and use these as building blocks for tissue maturation.

In vivo implantation of osteochondral plugs at orthotopic locations that include high loading regimes commonly results in unexpected outcomes, even when using materials that have shown promise in *in vitro* studies as well as in ectopic *in vivo* studies

(Diloksumpan *et al.* *Under review*). The combination of loading and degradation of the material potentially induces micro-movements of the implant which subsequently results in bone resorption around it.^[374] Furthermore, if the implant loosens, this allows for infiltration of the synovial fluid to the bone tissue, which subsequently results in further bone degradation and thus intensifies the problem.^[375] To prevent micromovement and to further understand the role of mechanical loading on our implants, this study showed the effect of implant size on the mechanical properties of these implants under physiological loading conditions by using a DLP fabricated replica of the knee joint. Here, we show that an increase in implant size results in a decrease in implant stiffness during axial compression. Additionally, the maximum force of the implants decreased for larger implants as compared to smaller implants. Permanent deformation of the implants was both shown after axial compression and after flexion and extension. The 2-fold difference in stiffness between small and large implants during axial compression, and the 3-fold difference in maximum force during flexion-extension, highlight the importance of implant size as well as different testing regimes. In future research, this data can be incorporated in a finite element (FE) model that can be used to predict the mechanical loads on the implant and helps to improve the design of the bone component. This important step towards patient-specific implant stability, should also include the structural elements of the engineered cartilage component on top of the bone component as well.

To achieve larger patient-specific implants that include MEW fibres as the structural elements of the cartilage-component, it is important to maintain a constant electrical field strength by applying a constant collector to spinneret distance.^[376] Therefore, the curvature of the joint has to be followed with a constant distance between the collecting joint and the MEW printhead. As part of this study, a software tool has been developed to automatically generate a machine-specific g-code that accurately deposits MEW boxes on top of the complex MgP-PCL joint structure. The percentage of resurfacing was shown to be only 71% when exactly following the contours of the STL file, which can be explained by a deviation between the position of the printhead and the position where the actual fibre is deposited, caused by the viscoelastic behaviour of melt electrowritten PCL (also referred to as the “jetlag”). The piling up of fibres with this low percentage of resurfacing can be explained by the charge accumulation at the higher parts of the implant and the electrostatic autofocussing effect that favours vertical layer stacking.^[377] Manual extension of the printhead trajectory after automatic generation of g-code was performed to achieve 96% of resurfacing. This manual extension could potentially be avoided by direct feedback based on in-line monitoring of the jetlag and direct automatic extension of this printhead trajectory based on this jetlag. Additionally, although MEW onto the

convex geometries was shown to be accurate, the accuracy decreased for the concave geometries. As this study only included a correction in z-direction and used a 3-axis platform, this might be improved by including an extra rotational axis to achieve a jet that is always normal-to-surface. With a normal-to-surface jet, even more control over fibre positioning could be achieved and other MEW designs on non-planar surfaces could be explored. For example, by applying an offset in the printhead trajectory, out-of-plane, arched structures have been established.^[378] This approach can be explored to mimic the structurally important “Benninghoff arcades”^[341] and subsequently aid in further approximating the mechanical properties of AC tissue, which is a key requirement for regenerating AC tissue.^[379]

Conclusion

This study provides a roadmap for the successful scale-up from an osteochondral plug towards larger patient-specific implants for the treatment of joint damage. The mechanical characterization under physiological conditions shows that the implant size affects the stiffness of the implant (under axial loading) and maximum force (under flexion-extension). Large implants show lower stiffness, lower maximum force, and more permanent deformation as compared to small implants. Increased implant size did not limit cartilage-like tissue formation and additionally submerging the bottom of the construct in culture medium did not result in an increase in matrix production in neither the small or larger implants. This study provides an effective tool to automatically generate g-code to achieve a constant collecting implant to printhead distance. This allows for accurate MEW reinforcing fibre deposition on implants with patient-specific geometry. Manual extension of the printing trajectory in the direction that included most deflection in z-direction was needed to completely cover the bone-component with reinforcing MEW fibres. This study showed successful fabrication of a multi-scale, patient-specific, large, mechanically stable, osteochondral implant with a complex geometry and an ability to form cartilage like matrix close to currently used smaller sized implants. These first steps are imperative for moving towards mechanically stable, multi-scale patient-specific osteochondral implants for the treatment of clinically relevant (osteo)chondral defects.

Supplementary figures

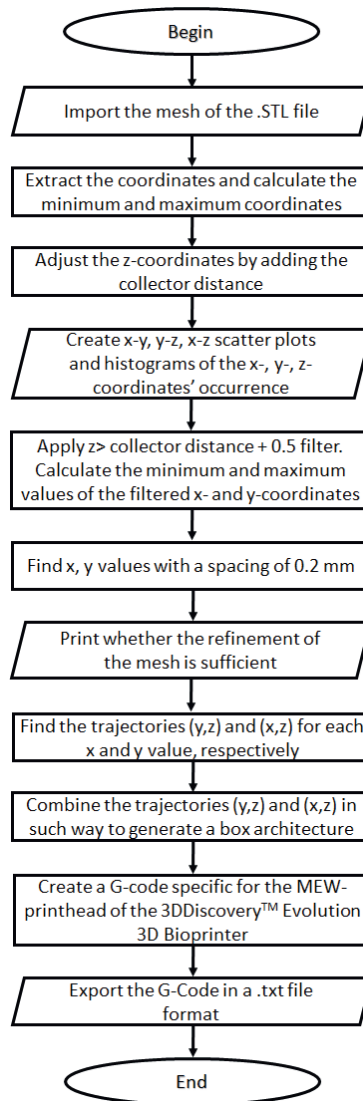


Figure S1. Flowchart of automatic g-code generation for MEW printhead trajectory.

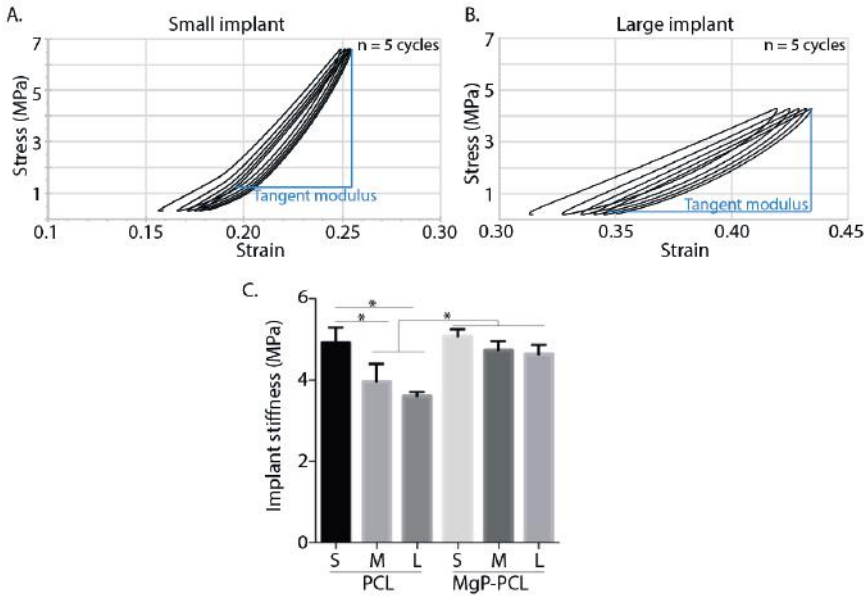


Figure S2. Stress-strain curves during cyclic axial compression. A) Small implant. B) Large implant.



Figure S3. Macroscopic images from all sides of the bone part and the resurfaced implants with the manually extended and fully automatic code.

Evaluation of the residual solvent concentrations in the MgP-based bioceramic biomaterial after the sterilization process

Introduction

The presence of solvents in the final MgP-based implants would hamper the clinical applications. The MgP-PCL biomaterial ink was prepared within a mixture of trisolvant. We assumed that the washing steps that are part of the sterilization process would remove any unwanted solvent. To evaluate this, proton nuclear magnetic resonance ($^1\text{H-NMR}$) was used to detect the residual solvents for the implants after the printing and sterilization process.

Method

The MgP bioceramics and PCL were dissolved in dichloromethane (DCM), 2-BU-1-(4- (diethylamino) anilino)-3-me-pyrido(1,2-a) benzimidazole - 4 – carbonitrile, and dibutyl phthalate (DBP) (Sigma-Aldrich, Germany) in a ratio of 10:2:1 wt.%. For the sterilization and washing process, the implants were washed for 24 hours in 100 v/v% ethanol followed by 24 hours in MQ water. Ethanol and MQ water were refreshed every 12 hours.

Two different implants immediately after the printing and after the washing steps were analyzed by Nuclear Magnetic Resonance ($^1\text{H-NMR}$), using an Agilent Technologies 400MR spectrometer (Santa Clara, CA, USA).

NMR samples are prepared by mixing ~5mg of sample with 800uL of CDCl_3 . The produced spectra were referenced against CDCl_3 (7.26 ppm).

Results

The characterization peaks of NMR for DCM are at 5.3 ppm, for dibutyl phthalate at 7.7 ppm; 7.53 ppm; 4.303 ppm; 1.7 ppm; 1.44 ppm; 97 ppm in CDCl_3 [380,381]. Immediately after the printing, the peaks for DCM and DBP were detected for the implants. However, after the washing steps, the peak of DCM disappeared and the peaks for DBP decreased significantly (Fig. 1). According to the general safety and performance requirements for the medical devices, substances having endocrine-disrupting properties such as phthalate should not be more than 0.1 w/w% [382]. In result, the NMR analysis showed that after the washing steps in ethanol and MQ water, the implants are safe to use as medical devices.

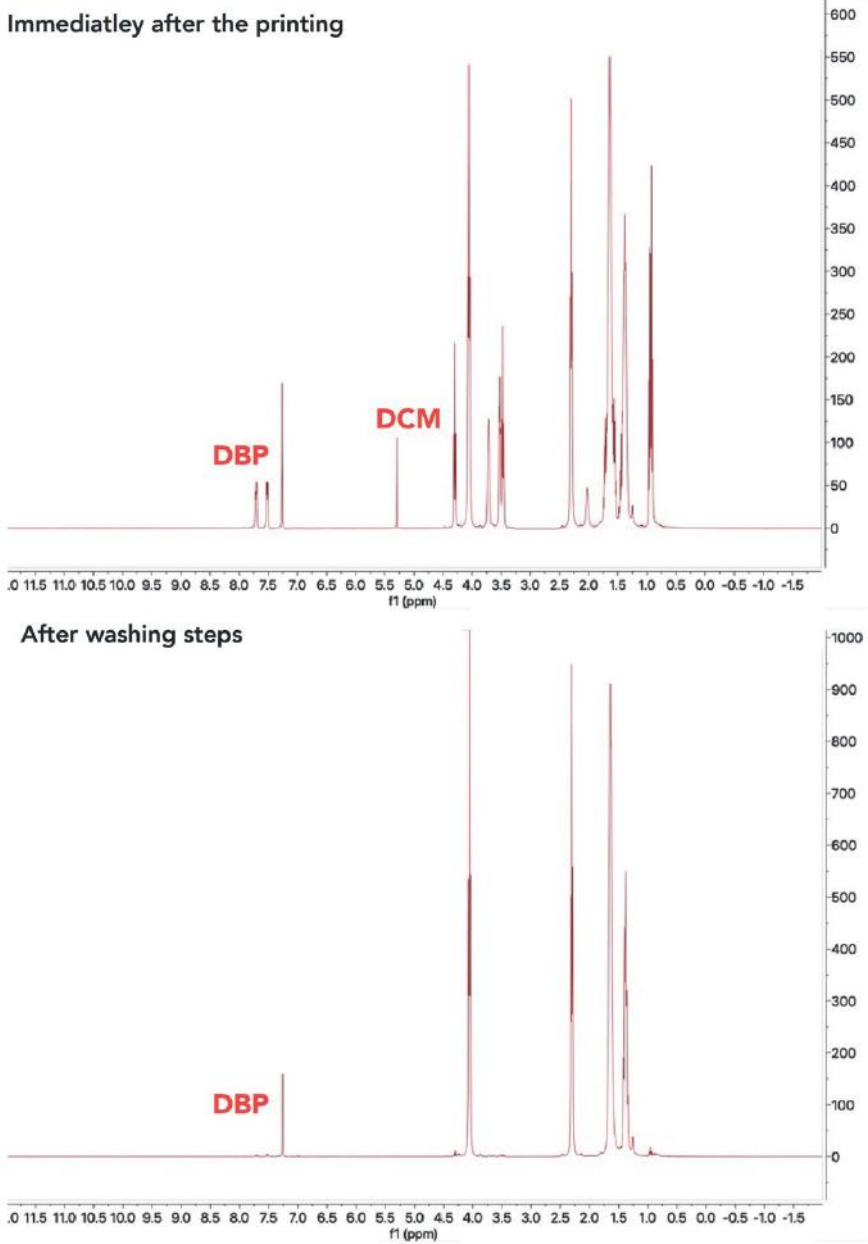
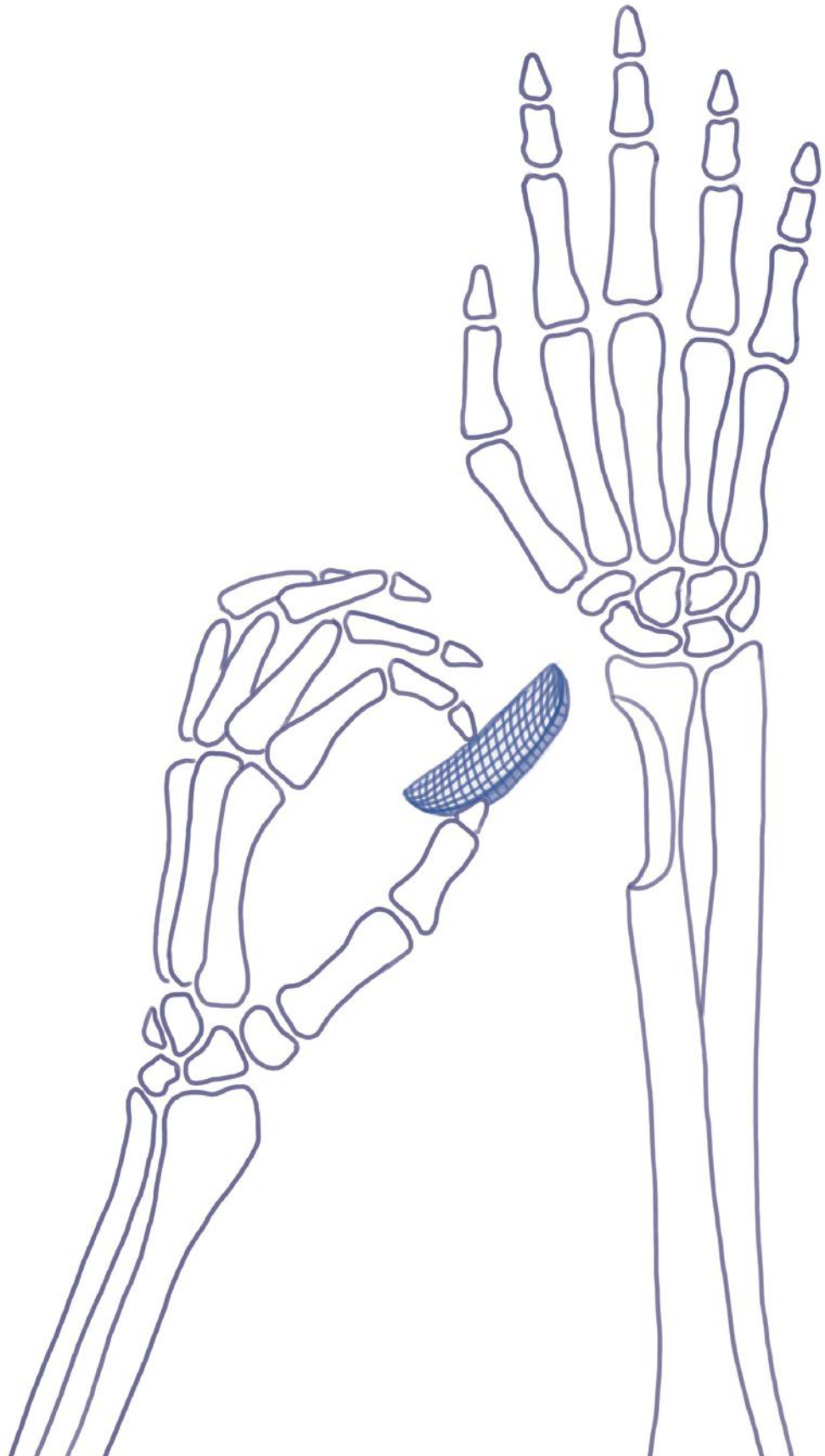


Figure 1. ¹H NMR analysis of MgP-PCL implants after the printing and washing steps.



References

- [1] N. Reznikov, R. Shahar, S. Weiner, In *Acta Biomaterialia*, Elsevier Ltd, **2014**, pp. 3815–3826.
- [2] N. Reznikov, M. Bilton, L. Lari, M. M. Stevens, R. Kröger, *Science (1979)* **2018**, 360.
- [3] R. Almany Magal, N. Reznikov, R. Shahar, S. Weiner, *J Struct Biol* **2014**, 186, 253.
- [4] A. R. Amini, C. T. Laurencin, S. P. Nukavarapu, *Crit Rev Biomed Eng* **2012**, 40, 363.
- [5] E. Fiume, J. Barberi, E. Verné, F. Baino, *Journal of Functional Biomaterials 2018, Vol. 9, Page 24* **2018**, 9, 24.
- [6] U. G. K. Wegst, H. Bai, E. Saiz, A. P. Tomsia, R. O. Ritchie, *NATURE MATERIALS* | **2015**, 14.
- [7] A.-M. Wu, C. Bisignano, S. L. James, G. G. Abady, A. Abedi, E. Abu-Gharbieh, R. K. Alhassan, V. Alipour, J. Arabloo, M. Asaad, W. N. Asmare, A. F. Awedew, M. Banach, S. K. Banerjee, A. Bijani, T. T. M. Birhanu, S. R. Bolla, L. A. Cámera, J.-C. Chang, D. Y. Cho, M. T. Chung, R. A. S. Couto, X. Dai, L. Dandona, R. Dandona, F. Farzadfar, I. Filip, F. Fischer, A. A. Fomenkov, T. K. Gill, B. Gupta, J. A. Haagsma, A. Haj-Mirzaian, S. Hamidi, S. I. Hay, I. M. Ilic, M. D. Ilic, R. Q. Ivers, M. Jürisson, R. Kalhor, T. Kanchan, T. Kavetsky, R. Khalilov, E. A. Khan, M. Khan, C. J. Kneib, V. Krishnamoorthy, G. A. Kumar, N. Kumar, R. Laloo, S. Lasrado, S. S. Lim, Z. Liu, A. Manafi, N. Manafi, R. G. Menezes, T. J. Meretoja, B. Miazgowski, T. R. Miller, Y. Mohammad, A. Mohammadian-Hafshejani, A. H. Mokdad, C. J. L. Murray, M. Naderi, M. D. Naimzada, V. C. Nayak, C. T. Nguyen, R. Nikbakhsh, A. T. Olagunju, N. Otstavnov, S. S. Otstavnov, J. R. Padubidri, J. Pereira, H. Q. Pham, M. Pinheiro, S. Polinder, H. Pourchamani, N. Rabiee, A. Radfar, M. H. U. Rahman, D. L. Rawaf, S. Rawaf, M. R. Saeb, A. M. Samy, L. Sanchez Riera, D. C. Schwebel, S. Shahabi, M. A. Shaikh, A. Soheili, R. Tabarés-Seisdedos, M. R. Tovani-Palone, B. X. Tran, R. S. Travillian, P. R. Valdez, T. J. Vasankari, D. Z. Velazquez, N. Venketasubramanian, G. T. Vu, Z.-J. Zhang, T. Vos, *Lancet Healthy Longev* **2021**, 2, e580.
- [8] N. K. Bakshi, J. T. Jolly, R. E. Debski, J. K. Sekiya, *Orthop J Sports Med* **2016**, 4.
- [9] S. Pun, *Curr Rev Musculoskelet Med* **2016**, 9, 427.
- [10] H. Shegarfi, O. Reikeras, *J Orthop Surg (Hong Kong)* **2009**, 17, 206.
- [11] M. R. Allen, D. B. Burr, *Basic and Applied Bone Biology* **2013**, 75.
- [12] E. Roddy, M. R. DeBaun, A. Daoud-Gray, Y. P. Yang, M. J. Gardner, *European Journal of Orthopaedic Surgery & Traumatology 2017 28:3* **2017**, 28, 351.
- [13] A. Nauth, E. Schemitsch, B. Norris, Z. Nollin, J. T. Watson, *J Orthop Trauma* **2018**, 32, S7.
- [14] K. Alvarez, H. Nakajima, *Materials* **2009**, 2, 790.
- [15] Albert Park Vet, *Hip Dysplasia*, **2021**.
- [16] cleft lip and palate, .
- [17] Richard Pallardy, *Bone fracture*.
- [18] Cleveland Clinic medical professional, *Bone cancer*.
- [19] M. Bohner, R. J. Miron, *Materials Today* **2019**, 22, 132.
- [20] G. Lalwani, M. D'Agati, B. Farshid, B. Sitharaman, *Nanocomposites for Musculoskeletal Tissue Regeneration* **2016**, 31.
- [21] N. Attias, A. M. Thabet, G. Prabhakar, J. A. Dollahite, R. J. Gehlert, T. A. DeCoster, *Bone Joint J* **2018**, 100-B, 646.
- [22] L. Williams, K. Fan, R. Bentley, *J Craniomaxillofac Surg* **2016**, 44, 789.

- [23] S. Das, *Indian Journal of Forensic Medicine & Toxicology* **2020**, *14*, 9183.
- [24] M. Bongio, J. J. P. van den Beucken, S. C. G. Leeuwenburgh, J. A. Jansen, *J Mater Chem* **2010**, *20*, 8747.
- [25] D. Zhao, T. Zhu, J. Li, L. Cui, Z. Zhang, X. Zhuang, J. Ding, *Bioact Mater* **2021**, *6*, 346.
- [26] J.-H. Shim, J.-B. Huh, J. Y. Park, Y.-C. Jeon, S. S. Kang, J. Y. Kim, J.-W. Rhie, D.-W. Cho, *Tissue Eng Part A* **2012**, *19*, 317.
- [27] Y. Lai, Y. Li, H. Cao, J. Long, X. Wang, L. Li, C. Li, Q. Jia, B. Teng, T. Tang, *Biomaterials* **2019**, *197*, 207.
- [28] Y. Chen, J. Xu, Z. Huang, M. Yu, Y. Zhang, H. Chen, Z. Ma, H. Liao, J. Hu, *Nature Publishing Group* **2017**.
- [29] S. Lin, L. Cui, G. Chen, J. Huang, Y. Yang, K. Zou, Y. Lai, X. Wang, L. Zou, T. Wu, J. C. Y. Cheng, G. Li, B. Wei, W. Y. W. Lee, *Biomaterials* **2019**, *196*, 109.
- [30] G. Qian, P. Fan, F. He, J. Ye, *Adv Healthc Mater* **2019**, *8*.
- [31] Y. Lai, Y. Li, H. Cao, J. Long, X. Wang, L. Li, C. Li, Q. Jia, B. Teng, T. Tang, J. Peng, D. Eglin, M. Alini, D. W. Grijpma, G. Richards, L. Qin, *Biomaterials* **2019**, *197*, 207.
- [32] S. S. Cao, S. Y. Li, Y. M. Geng, K. Kapat, S. bin Liu, F. H. Perera, Q. Li, H. Terheyden, G. Wu, Y. J. Che, P. Miranda, M. Zhou, *ACS Biomater Sci Eng* **2021**, *7*, 5727.
- [33] H. Zhu, K. Zheng, A. R. Boccaccini, *Acta Biomater* **2021**, *129*, 1.
- [34] L. Yang, B. Harink, P. Habibovic, *Comprehensive Biomaterials* **2011**, *1*, 299.
- [35] S. Gallinetti, C. Canal, M. P. Ginebra, *J Am Ceram Soc* **2014**, *97*, 1065.
- [36] A. Fuchs, D. Kreczy, T. Brückner, U. Gbureck, P. Stahlhut, M. Bengel, A. Hoess, B. Nies, J. Bator, U. Klammert, C. Linz, A. Ewald, *Clin Oral Investig* **2022**, *26*, 2619.
- [37] C. Moseke, K. Wimmer, M. Meiningner, J. Zerweck, C. Wolf-Brandstetter, U. Gbureck, A. Ewald, *Biomedizinische Technik* **2020**, *65*, 631.
- [38] X. Cao, H. Lu, J. Liu, W. Lu, L. Guo, M. Ma, B. Zhang, Y. Guo, *J Mater Sci Mater Med* **2019**, *30*.
- [39] J. Walker, S. Shadanbaz, T. B. F. Woodfield, M. P. Staiger, G. J. Dias, *J Biomed Mater Res B Appl Biomater* **2014**, *102*, 1316.
- [40] B. Kanter, A. Vikman, T. Brückner, M. Schamel, U. Gbureck, A. Ignatius, *Acta Biomater* **2018**, *69*, 352.
- [41] N. Ostrowski, A. Roy, P. N. Kumta, *ACS Biomater Sci Eng* **2016**, *2*, 1067.
- [42] H. Safiaghdam, H. Nokhbatolfoghahaei, A. Khojasteh, *Iran J Pharm Res* **2019**, *18*, 101.
- [43] C. Zhu, R. Cao, Y. Zhang, R. Chen, *Front Cell Dev Biol* **2021**, *9*, 707.
- [44] S. Vahabzadeh, M. Roy, S. Bose, *J Mater Chem B* **2015**, *3*, 8973.
- [45] A. Lode, C. Heiss, G. Knapp, J. Thomas, B. Nies, M. Gelinsky, M. Schumacher, *Acta Biomater* **2018**, *65*, 475.
- [46] Y. Li, E. Luo, S. Zhu, J. Li, L. Zhang, J. Hu, *J Appl Biomater Funct Mater* **2015**, *13*, 28.
- [47] F. Baines, G. Novajra, C. Vitale-Brovarone, *Front Bioeng Biotechnol* **2015**, *3*.
- [48] C. Cao, P. Huang, A. Prasopthum, A. J. Parsons, F. Ai, J. Yang, *Biomater Sci* **2021**, *10*, 138.
- [49] L. Chen, D. Zhai, Z. Huan, N. Ma, H. Zhu, C. Wu, J. Chang, *RSC Adv* **2015**, *5*, 37314.
- [50] K. Lawton, H. Le, C. Tredwin, R. D. Handy, *Int J Nanomedicine* **2019**, *14*, 7947.
- [51] L. A. dos Santos, R. Garcia Carrodéguas, A. Ortega Boschi, A. C. Fonseca De Arruda, *J Biomed Mater*

- Res A* **2003**, 65A, 244.
- [52] Mechanical evaluation of polylactic acid (PLA) based composites reinforced with different calcium phosphates, **2018**.
- [53] N. C. Bleach, S. N. Nazhat, K. E. Tanner, M. Kellomäki, P. Törmälä, *Biomaterials* **2002**, 23, 1579.
- [54] P. Habibovic, H. Yuan, M. van den Doel, T. M. Sees, C. A. van Blitterswijk, K. de Groot, *J Orthop Res* **2006**, 24, 867.
- [55] M. Bohner, R. J. Miron, *Materials Today* **2019**, 22, 132.
- [56] C. Gao, B. Yang, H. Hu, J. Liu, C. Shuai, S. Peng, *Mater Sci Eng C Mater Biol Appl* **2013**, 33, 3802.
- [57] L. Strobel, S. Rath, A. Maier, J. Beier, A. Arkudas, P. Greil, R. Horch, U. Kneser, *J Tissue Eng Regen Med* **2014**, 8, 176.
- [58] C. Schmidleithner, S. Malferrari, R. Palgrave, D. Bomze, M. Schwentenwein, D. M. Kalaskar, *Biomed Mater* **2019**, 14.
- [59] Y. Zhang, L. Xia, D. Zhai, M. Shi, Y. Luo, C. Feng, B. Fang, J. Yin, J. Chang, C. Wu, *Nanoscale* **2015**, 7, 19207.
- [60] K. Lin, R. Sheikh, S. Romanazzo, I. Roohani, *Materials* 2019, Vol. 12, Page 2660 **2019**, 12, 2660.
- [61] H. Elsayed, J. Schmidt, E. Bernardo, P. Colombo, *Adv Eng Mater* **2019**, 21, 1801160.
- [62] Z. Zhou, F. Buchanan, C. Mitchell, N. Dunne, *Materials Science and Engineering: C* **2014**, 38, 1.
- [63] M. Castilho, M. Dias, E. Vorndran, U. Gbureck, P. Fernandes, I. Pires, B. Gouveia, H. Armes, E. Pires, J. Rodrigues, *Biofabrication* **2014**, 6.
- [64] A. E. Jakus, A. L. Rutz, S. W. Jordan, A. Kannan, S. M. Mitchell, C. Yun, K. D. Koube, S. C. Yoo, H. E. Whiteley, C.-P. Richter, *Sci Transl Med* **2016**, 8, 358ra127.
- [65] Y. Zhang, J. Li, V. Hilda, M. Mouser, N. Roumans, L. Moroni, P. Habibovic, **2021**.
- [66] T. Jensen, T. Jakobsen, J. Baas, J. V Nygaard, A. Dolatshahi-pirouz, M. B. Hovgaard, M. Foss, C. Bu, F. Besenbacher, K. Søballe, **2010**, 665.
- [67] A. Dolatshahi-pirouz, T. H. L. Jensen, K. Kolind, C. Bünger, M. Kassem, **2011**, 84, 18.
- [68] T. Jensen, A. Dolatshahi-pirouz, M. Foss, J. Baas, J. Lovmand, M. Duch, F. Skou, M. Kassem, C. Bünger, K. Søballe, F. Besenbacher, **2010**, 75, 186.
- [69] M. Alehosseini, M. Roozbahani, M. Kharaziha, R. Emadi, *Materials Science and Engineering C* **2017**, 81, 10.
- [70] M. Kharaziha, H. Edris, M. Fathi, N. Golafshan, M. Alehosseini, *Macromol Biosci* **2018**, 18, 1800020.
- [71] L. Gineste, M. Gineste, X. Ranz, A. Elleferion, A. Guilhem, N. Rouquet, P. Frayssinet, *J Biomed Mater Res* **1999**, 48, 224.
- [72] I. Błaszczuk, E. Grucka-Mamczar, S. Kasperczyk, E. Birkner, *Biol Trace Elem Res* **2009**, 129, 229.
- [73] I. Błaszczuk, E. Grucka-Mamczar, S. Kasperczyk, E. Birkner, *Biol Trace Elem Res* **2009**, 129, 229.
- [74] K. A. Gross, K. A. Bhandang, *Biomaterials* **2004**, 25, 1395.
- [75] S. V Dorozhkin, M. Epple, *Angewandte Chemie International Edition* **2002**, 41, 3130.
- [76] S. Wu, X. Liu, K. W. K. Yeung, C. Liu, X. Yang, *Materials Science and Engineering: R: Reports* **2014**, 80, 1.
- [77] M. Kheradmandfard, M. H. Fathi, F. Ansari, T. Ahmadi, *Materials Science and Engineering: C* **2016**, 68, 136.
- [78] Z. Huang, F. Cui, Q. Feng, X. Guo, *Ceram Int* **2015**, 41, 8773.
- [79] D. J. Hickey, B. Ercan, L. Sun, T. J. Webster, *Acta Biomater* **2015**, 14, 175.

- [80] Y. Cai, S. Zhang, X. Zeng, Y. Wang, M. Qian, W. Weng, *Thin Solid Films* **2009**, *517*, 5347.
- [81] A. M. Pietak, J. W. Reid, M. J. Stott, M. Sayer, *Biomaterials* **2007**, *28*, 4023.
- [82] G. A. Fielding, A. Bandyopadhyay, S. Bose, *Dental Materials* **2012**, *28*, 113.
- [83] C. Wu, W. Fan, Y. Zhou, Y. Luo, M. Gelinsky, J. Chang, Y. Xiao, *J Mater Chem* **2012**, *22*, 12288.
- [84] A. Lode, C. Heiss, G. Knapp, J. Thomas, B. Nies, M. Gelinsky, M. Schumacher, *Acta Biomater* **2018**, *65*, 475.
- [85] Z. Y. Li, W. M. Lam, C. Yang, B. Xu, G. X. Ni, S. A. Abbah, K. M. C. Cheung, K. D. K. Luk, W. W. Lu, *Biomaterials* **2007**, *28*, 1452.
- [86] A. Goel, R. R. Rajagopal, J. M. F. Ferreira, *Acta Biomater* **2011**, *7*, 4071.
- [87] S. Tadier, R. Bareille, R. Siadous, O. Marsan, C. Charvillat, S. Cazalbou, J. Amédée, C. Rey, C. Combes, *J Biomed Mater Res B Appl Biomater* **2012**, *100*, 378.
- [88] J. Ran, P. Jiang, G. Sun, Z. Ma, J. Hu, X. Shen, H. Tong, *Mater. Chem. Front.* **2017**, *1*, 900.
- [89] M. A. Binsalah, S. Ramalingam, M. Alkindi, N. Nooh, K. Al-Hezaimi, *Journal of Investigative Surgery* **2019**, *32*, 456.
- [90] M. Hafezi, A. Reza Talebi, S. Mohsen Miresmaeili, F. Sadeghian, F. Fesahat, *Ceram Int* **2013**, *39*, 4575.
- [91] C. M. Cowan, O. O. Aalami, Y. Y. Shi, Y. F. Chou, C. Mari, R. Thomas, N. Quarto, R. P. Nacamuli, C. H. Contag, B. Wu, M. T. Longaker, *Tissue Eng* **2005**, *11*, 645.
- [92] T. Ahmadi, A. Monshi, V. Mortazavi, M. H. Fathi, S. Sharifi, B. Hashemi Beni, A. Moghare Abed, M. Kheradmandfard, A. Sharifnabi, *Ceram Int* **2014**, *40*, 8341.
- [93] Z. Y. Li, W. M. Lam, C. Yang, B. Xu, G. X. Ni, S. A. Abbah, K. M. C. Cheung, K. D. K. Luk, W. W. Lu, *Biomaterials* **2007**, *28*, 1452.
- [94] T. Ahmadi, A. Monshi, V. Mortazavi, M. H. Fathi, S. Sharifi, M. Kharaziha, L. Khazdooz, A. Zarei, M. Taghian Dehaghani, *Materials Science and Engineering C* **2020**, *106*, 110172.
- [95] I. R. Gibson, W. Bonfield, *J Biomed Mater Res* **2002**, *59*, 697.
- [96] H.-E. H.-W. Kim, H.-E. H.-W. Kim, J. C. Knowles, *Biomaterials* **2004**, *25*, 3351.
- [97] Z. Geng, Z. Cui, Z. Li, S. Zhu, Y. Liang, W. W. Lu, X. Yang, *J Mater Chem B* **2015**, *3*, 3738.
- [98] E. B. FLINK, H. V. DEDHIA, J. DINSMORE, H. M. DOSHI, D. BANKS, P. HSHIEH, *Crit Care Med* **1992**, *20*, 1692.
- [99] Strontium overload and toxicity: impact on renal osteodystrophy | Nephrology Dialysis Transplantation | Oxford Academic, .
- [100] W. Jahnen-Dechent, M. Ketteler, *Clin Kidney J* **2012**, *5*, i3.
- [101] D. J. Bellis, D. Li, Z. Chen, W. M. Gibson, P. J. Parsons, *J Anal At Spectrom* **2009**, *24*, 622.
- [102] I. Nishimura, R. Hisanaga, T. Sato, T. Arano, S. Nomoto, Y. Ikada, M. Yoshinari, *Regen Ther* **2015**, *2*, 24.
- [103] B. Kim, S. Yang, J. Yoon, J. Lee, *Clin Oral Implants Res* **2017**, *28*, 49.
- [104] T. C. Brennan, M. S. Rybchyn, W. Green, S. Atwa, A. D. Conigrave, R. S. Mason, *Br J Pharmacol* **2009**, *157*, 1291.
- [105] K. W. Yong, B. Pingguan-Murphy, F. Xu, W. A. B. W. Abas, J. R. Choi, S. Z. Omar, M. A. N. Azmi, K. H. Chua, W. K. Z. W. Safwani, *Sci Rep* **2015**, *5*, 9596.
- [106] A. K. Gaharwar, S. M. Mihaila, A. Swami, A. Patel, S. Sant, R. L. Reis, A. P. Marques, M. E. Gomes, A. Khademhosseini, *Advanced Materials* **2013**, *25*, 3329.

- [107] N. Tazi, Z. Zhang, Y. Messaddeq, L. Almeida-Lopes, L. M. Zanardi, D. Levinson, M. Rouabhia, *AMB Express* **2012**, *2*, 61.
- [108] A. Dolatshahi-Pirouz, M. Nikkhah, A. K. Gaharwar, B. Hashmi, E. Guermani, H. Aliabadi, G. Camci-Unal, T. Ferrante, M. Foss, D. E. Ingber, A. Khademhosseini, *Sci Rep* **2014**, *4*, 3896.
- [109] J.-H. Shim, J.-B. Huh, J. Y. Park, Y.-C. Jeon, S. S. Kang, J. Y. Kim, J.-W. Rhie, D.-W. Cho, *Tissue Eng Part A* **2012**, *19*, 317.
- [110] V. Nardone, R. Zonefrati, C. Mavilia, C. Romagnoli, S. Ciuffi, S. Fabbri, G. Palmiini, G. Galli, A. Tanini, M. L. Brandi, *Stem Cells Int* **2015**, 2015.
- [111] T. Y. Nguyen, C. G. Liew, H. Liu, *PLoS One* **2013**, *8*, e76547.
- [112] H. Zreiqat, C. R. Howlett, A. Zannettino, P. Evans, G. Schulze-Tanzil, C. Knabe, M. Shakibaei, *Journal of Biomedical Materials Research: An Official Journal of The Society for Biomaterials, The Japanese Society for Biomaterials, and The Australian Society for Biomaterials and the Korean Society for Biomaterials* **2002**, *62*, 175.
- [113] S. R. K. Meka, S. Jain, K. Chatterjee, *Colloids Surf B Biointerfaces* **2016**, *146*, 649.
- [114] K. Shin, A. C. Jayasuriya, D. H. Kohn, *J Biomed Mater Res A* **2007**, *83*, 1076.
- [115] B. Kim, S. Yang, J. Yoon, J. Lee, *Clin Oral Implants Res* **2017**, *28*, 49.
- [116] J. C. Le Huec, D. Clement, B. Brouillaud, N. Barthe, B. Dupuy, B. Foliguet, B. Basse-Cathalinat, *Biomaterials* **1998**, *19*, 733.
- [117] E. Luo, H. Liu, Q. Zhao, B. Shi, Q. Chen, .
- [118] F. C. Fierz, F. Beckmann, M. Huser, S. H. Irsen, B. Leukers, F. Witte, Ö. Degistirici, A. Andronache, M. Thie, B. Müller, *Biomaterials* **2008**, *29*, 3799.
- [119] D. Ke, S. Bose, *Addit Manuf* **2018**, *22*, 111.
- [120] Y. Ma, H. Dai, X. Huang, Y. Long, *J Mater Sci* **2019**, *54*, 10437.
- [121] J. Wang, C. Lin, X. Gao, Z. Zheng, M. Lv, J. Sun, Z. Zhang, **2018**.
- [122] A. Rakovsky, I. Gotman, E. Rabkin, E. Y. Gutmanas, *J Mech Behav Biomed Mater* **2014**, *32*, 89.
- [123] I. Sopyan, T. A. Rahim, *Materials and Manufacturing Processes* **2012**, *27*, 702.
- [124] Z. A. Shazni, M. Mariatti, A. Nurazreena, K. A. Razak, *Procedia Chem* **2016**, *19*, 174.
- [125] W. Chen, H. Zhou, M. Tang, M. D. Weir, C. Bao, H. H. K. Xu, *Tissue Eng Part A* **2012**, *18*, 816.
- [126] P. S. P. Poh, D. W. Hutmacher, B. M. Holzapfel, A. K. Solanki, M. M. Stevens, M. A. Woodruff, *Acta Biomater* **2016**, *30*, 319.
- [127] J. A. Inzana, D. Olvera, S. M. Fuller, J. P. Kelly, O. A. Graeve, E. M. Schwarz, S. L. Kates, H. A. Awad, *Biomaterials* **2014**, *35*, 4026.
- [128] T. Li, D. Zhai, B. Ma, J. Xue, P. Zhao, J. Chang, M. Gelinsky, C. Wu, *Advanced Science* **2019**, *6*, 1901146.
- [129] S. Meininger, S. Mandal, A. Kumar, J. Groll, B. Basu, U. Gbureck, *Acta Biomater* **2016**, *31*, 401.
- [130] M. Castilho, C. Moseke, A. Ewald, U. Gbureck, J. Groll, I. Pires, J. Teßmar, E. Vorndran, *Biofabrication* **2014**, *6*.
- [131] M. Castilho, J. Rodrigues, I. Pires, B. Gouveia, M. Pereira, C. Moseke, J. Groll, A. Ewald, E. Vorndran, *Biofabrication* **2015**, *7*.

- [132] S. Mohanty, M. Alm, M. Hemmingsen, A. Dolatshahi-Pirouz, J. Trifol, P. Thomsen, M. Dufva, A. Wolff, J. Emneus, *Biomacromolecules* **2016**, *17*, 1321.
- [133] M. Castilho, M. Dias, U. Gbureck, J. Groll, P. Fernandes, I. Pires, B. Gouveia, J. Rodrigues, E. Vorndran, *Biofabrication* **2013**, *5*.
- [134] C. Wu, W. Fan, Y. Zhou, Y. Luo, M. Gelinsky, J. Chang, Y. Xiao, *J Mater Chem* **2012**, *22*, 12288.
- [135] B. Kanter, A. Vikman, T. Brückner, M. Schamel, U. Gbureck, A. Ignatius, **2018**, *69*, 352.
- [136] J. A. Kim, J. Lim, R. Naren, H. S. Yun, E. K. Park, *Acta Biomater* **2016**, *44*, 155.
- [137] X. Yang, B. Xie, L. Wang, Y. Qin, J. Henneman, G. H. Nancollas, **2011**, 1153.
- [138] S. Choudhary, P. Halbout, C. Alander, L. Raisz, C. Pilbeam, **2007**, *22*, 1002.
- [139] H. Lariboisiere, *C. Cultures*, **1996**, *18*, 517.
- [140] S. Meininger, C. Moseke, K. Spatz, E. März, C. Blum, A. Ewald, E. Vorndran, **2019**.
- [141] A. Ribeiro, M. M. Blokzijl, R. Levato, C. W. Visser, M. Castilho, W. E. Hennink, T. Vermonden, J. Malda, *Biofabrication* **2017**, *10*, 14102.
- [142] M. Doube, M. M. Klosowski, I. Arganda-Carreras, F. P. Cordelières, R. P. Dougherty, J. S. Jackson, B. Schmid, J. R. Hutchinson, S. J. Shefelbine, *Bone* **2010**, *47*, 1076.
- [143] D. Gawlitta, K. E. M. Benders, J. Visser, A. S. Van Der Sar, D. H. R. Kempen, L. F. H. Theyse, J. Malda, W. J. A. Dhert, .
- [144] A. Kimura, H. Abe, S. Tsuruta, S. Chiba, Y. Fujii-Kuriyama, T. Sekiya, R. Morita, A. Yoshimura, *Int Immunol* **2014**, *26*, 209.
- [145] S. R. Aparicio, P. Marsden, *J Microsc* **1969**, *89*, 139.
- [146] S. Eshraghi, S. Das, *Acta Biomater* **2010**, *6*, 2467.
- [147] A. C. Jones, C. H. Arns, A. P. Sheppard, D. W. Hutmacher, B. K. Milthorpe, M. A. Knackstedt, *Biomaterials* **2007**, *28*, 2491.
- [148] L. Røhl, E. Larsen, F. Linde, A. Odgaard, J. Jørgensen, *J Biomech* **1991**, *24*, 1143.
- [149] D. L. Kopperdahl, T. M. Keaveny, *J Biomech* **1998**, *31*, 601.
- [150] J. W. Kim, K. H. Shin, Y. H. Koh, M. J. Hah, J. Moon, H. E. Kim, *Materials* **2017**, *10*.
- [151] K. J. Lewis, D. Frikha-Benayed, J. Louie, S. Stephen, D. C. Spray, M. M. Thi, Z. Seref-Ferlencez, R. J. Majeska, S. Weinbaum, M. B. Schaffler, *Proc Natl Acad Sci U S A* **2017**, *114*, 11775.
- [152] B. Huang, G. Caetano, C. Vyas, J. J. Blaker, C. Diver, P. Bártolo, *Materials* **2018**, *11*.
- [153] C. Spencer, P. Jonathan, M. Janice, S. Ralph, *Front Bioeng Biotechnol* **2016**, *4*.
- [154] E. Boanini, P. Torricelli, M. Fini, A. Bigi, *J Mater Sci Mater Med* **2011**, *22*, 2079.
- [155] Y. J. No, S. Roohaniesfahani, Z. Lu, J. Shi, H. Zreiqat, *Biomedical Materials (Bristol)* **2017**, *12*.
- [156] Y. Deng, M. Liu, X. Chen, M. Wang, X. Li, Y. Xiao, X. Zhang, *J Mater Chem B* **2018**, *6*, 6572.
- [157] P. Ducheyne, J. Beight, J. Cuckler, B. Evans, S. Radin, *Biomaterials* **1990**, *11*, 531.
- [158] Bioactive ceramic prosthetic coatings. - PubMed - NCBI, .
- [159] M. Sila-Asna, A. Bunyaratvej, S. Maeda, H. Kitaguchi, N. Bunyaratavej, *Kobe Journal of Medical Sciences* **2007**, *53*, 25.

- [160] B. Akar, A. M. Tatar, A. Sutradhar, H. Y. Hsiao, M. Miller, M. H. Cheng, A. G. Mikos, E. M. Brey, *Large Animal Models of an in Vivo Bioreactor for Engineering Vascularized Bone*, Vol. 24, Mary Ann Liebert Inc., **2018**, pp. 317–325.
- [161] M. Bohner, R. J. Miron, *A proposed mechanism for material-induced heterotopic ossification*, Vol. 22, Elsevier B.V., **2019**, pp. 132–141.
- [162] J. Lee, M. M. Farag, E. K. Park, J. Lim, H. S. Yun, *Materials Science and Engineering C* **2014**, *36*, 252.
- [163] J. Wei, J. Jia, F. Wu, S. Wei, H. Zhou, H. Zhang, J. W. Shin, C. Liu, *Biomaterials* **2010**, *31*, 1260.
- [164] U. Klammert, A. Ignatius, U. Wolfram, T. Reuther, U. Gbureck, *Acta Biomater* **2011**, *7*, 3469.
- [165] G. Yang, J. Liu, F. Li, Z. Pan, X. Ni, Y. Shen, H. Xu, Q. Huang, *Materials Science and Engineering C* **2014**, *35*, 70.
- [166] H. Zhou, A. K. Agarwal, V. K. Goel, S. B. Bhaduri, *Materials Science and Engineering C* **2013**, *33*, 4288.
- [167] S. Lee, M. Porter, S. Wasko, G. Lau, P. Y. Chen, E. E. Novitskaya, A. P. Tomsia, A. Almutairi, M. A. Meyers, J. McKittrick, *Materials Research Society Symposium Proceedings* **2012**, *1418*, 177.
- [168] E. Fiume, J. Barberi, E. Verné, F. Baino, *J Funct Biomater* **2018**, *9*.
- [169] S. Mohamed, B. H. Shamaz, *Int J Dent Oral Health* **2015**, *1*, 01.
- [170] S. on the Burden of Musculoskeletal Conditions at the Start of the New Millennium. (2003 : Geneva, *The burden of musculoskeletal conditions at the start of the new millenium : report of a WHO scientific group*, Geneve : World Health Organization, **2003**, p. 218 p.
- [171] S. R. Kingsbury, H. J. Gross, G. Isherwood, P. G. Conaghan, *Rheumatology (United Kingdom)* **2014**, *53*, 937.
- [172] S. Jacobsen, S. Sonne-Holm, *Rheumatology* **2005**, *44*, 211.
- [173] B. L. Gray, J. B. Stambough, G. R. Baca, P. L. Schoenecker, J. C. Clohisy, *Bone and Joint Journal* **2015**, *97-B*, 1322.
- [174] C. Pascual-Garrido, F. Guilak, M. F. Rai, M. D. Harris, M. J. Lopez, R. J. Todhunter, J. C. Clohisy, *Journal of Orthopaedic Research* **2018**, *36*, 1807.
- [175] R. Sakkers, V. Pollet, *The natural history of abnormal ultrasound findings in hips of infants under six months of age*, Vol. 12, British Editorial Society of Bone and Joint Surgery, **2018**, pp. 302–307.
- [176] R. Ganz, K. Klaue, T. S. Vinh, J. W. Mast, *Clin Orthop Relat Res* **1988**, *26*.
- [177] J. C. Clohisy, A. L. Schutz, L. St. John, P. L. Schoenecker, R. W. Wright, *Clin Orthop Relat Res* **2009**, *467*, 2041.
- [178] I. Zaltz, G. Baca, Y. J. Kim, P. Schoenecker, R. Trousdale, R. Sierra, D. Sucato, E. Sink, P. Beaulé, M. B. Millis, D. Podeszwa, J. C. Clohisy, *Journal of Bone and Joint Surgery - American Volume* **2014**, *96*, 1967.
- [179] D. R. Maldonado, V. Ortiz-Declet, A. W. Chen, A. C. Lall, M. R. Mohr, J. R. Laseter, B. G. Domb, *Arthrosc Tech* **2018**, *7*, e779.
- [180] K. Willemsen, C. J. Doelman, A. S. Y. Sam, P. R. Seevinck, R. J. B. Sakkers, H. Weinans, B. C. H. van Der Wal, *Acta Orthop* **2020**, *91*, 383.
- [181] N. Golafshan, E. Vorndran, S. Zaharievski, H. Brommer, F. B. Kadumudi, A. Dolatshahi-Pirouz, U. Gbureck, R. van Weeren, M. Castilho, J. Malda, *Biomaterials* **2020**, 120302.

- [182] ASTM C1161 - 02 Standard Test Method for Flexural Strength of Advanced Ceramics at Ambient Temperature, .
- [183] J. A. Inzana, D. Olvera, S. M. Fuller, J. P. Kelly, O. A. Graeve, E. M. Schwarz, S. L. Kates, H. A. Awad, *Biomaterials* **2014**, *35*, 4026.
- [184] L. Elomaa, S. Teixeira, R. Hakala, H. Korhonen, D. W. Grijpma, J. V. Seppälä, *Acta Biomater* **2011**, *7*, 3850.
- [185] K. Arcaute, B. Mann, R. Wicker, *Acta Biomater* **2010**, *6*, 1047.
- [186] G. N. Duda, E. Schneider, E. Y. S. Chao, *J Biomech* **1997**, *30*, 933.
- [187] A. Paknahad, N. W. Kucko, S. C. G. Leeuwenburgh, L. J. Sluys, *J Mech Behav Biomed Mater* **2020**, *103*, 103565.
- [188] S. de L. Schickert, J. A. Jansen, E. M. Bronkhorst, J. J. van den Beucken, S. C. Leeuwenburgh, *Acta Biomater* **2020**, *110*, 280.
- [189] N. R. Ordway, K. J. Ash, M. A. Miller, K. A. Mann, K. Hayashi, *Veterinary and Comparative Orthopaedics and Traumatology* **2019**, *32*, 369.
- [190] S. N. Sangiorgio, D. B. Longjohn, J. L. Lee, J. D. Alexander, L. D. Dorr, E. Ebramzadeh, *Journal of Applied Biomaterials and Biomechanics* **2008**, *6*, 72.
- [191] L. Mao, L. Xia, J. Chang, J. Liu, L. Jiang, C. Wu, B. Fang, *Acta Biomater* **2017**, *61*, 217.
- [192] S. Yoshizawa, A. Brown, A. Barchowsky, C. Sfeir, *Acta Biomater* **2014**, *10*, 2834.
- [193] A. F. Mavrogenis, A. D. Kanellopoulos, G. N. Nomikos, P. J. Papagelopoulos, P. N. Soucacos, *Clin Orthop Relat Res* **2009**, *467*, 1591.
- [194] N. G. Grün, P. L. Holweg, N. Donohue, T. Klestil, A. M. Weinberg, *Resorbable implants in pediatric fracture treatment*, Vol. 3, De Gruyter, **2020**, pp. 119–125.
- [195] K. Shi, J. Jing, L. Song, T. Su, Z. Wang, *Enzymatic hydrolysis of polyester: Degradation of poly(ϵ -caprolactone) by *Candida antarctica* lipase and *Fusarium solani* cutinase*, Vol. 144, Elsevier B.V, **2020**.
- [196] R. M. Felfel, I. Ahmed, A. J. Parsons, G. S. Walker, C. D. Rudd, *J Mech Behav Biomed Mater* **2011**, *4*, 1462.
- [197] A. A. Hofmann, R. D. Bloebaum, K. N. Bachus, **2009**.
- [198] H. Appel, S. Friberg, *Acta Orthop* **1972**, *43*, 558.
- [199] S. Ekhtiari, C. E. Haldane, D. de Sa, N. Simunovic, V. Musahl, O. R. Ayeni, *Journal of Bone and Joint Surgery - American Volume* **2016**, *98*, 1568.
- [200] P. Lobenhoffer, *Journal of Knee Surgery* **2017**, *30*, 769.
- [201] M. H. van Haeringen, P. P. F. M. Kuijjer, J. G. Daams, R. C. I. van Geenen, J. M. Brinkman, G. M. M. J. Kerkhoffs, R. J. van Heerwaarden, A. Hoorntje, *Knee Surgery, Sports Traumatology, Arthroscopy* **2022**.
- [202] Z. Wang, Y. Zeng, W. She, X. Luo, L. Cai, *Is opening-wedge high tibial osteotomy superior to closing-wedge high tibial osteotomy in treatment of unicompartmental osteoarthritis? A meta-analysis of randomized controlled trials*, Vol. 60, Elsevier Ltd, **2018**, pp. 153–163.
- [203] D. C. Lee, S. J. Byun, *Knee Surg Relat Res* **2012**, *24*, 61.

- [204] J. H. Han, H. J. Kim, J. G. Song, J. H. Yang, N. N. Bhandare, A. R. Fernandez, H. J. Park, K. W. Nha, *Knee Surg Relat Res* **2015**, 27, 207.
- [205] W. van Genechten, M. van den Bempt, W. van Tilborg, S. Bartholomeeusen, G. van den Bogaert, T. Claes, S. Claes, *Knee Surgery, Sports Traumatology, Arthroscopy* **2020**, 28, 3747.
- [206] Z. W. Cao, X. J. Mai, J. Wang, E. H. Feng, Y. M. Huang, *Journal of Arthroplasty* **2018**, 33, 952.
- [207] D. J. Chae, G. M. Shetty, D. B. Lee, H. W. Choi, S. B. Han, K. W. Nha, *Knee* **2008**, 15, 128.
- [208] J. S. Lee, Y. J. Park, L. Wang, Y. S. Chang, G. M. Shetty, K. W. Nha, *Knee Surg Relat Res* **2016**, 28, 277.
- [209] M. A. Kuremsky, T. M. Schaller, C. C. Hall, B. A. Roehr, J. L. Masonis, *Journal of Arthroplasty* **2010**, 25, 951.
- [210] A. Lode, K. Meissner, Y. Luo, F. Sonntag, S. Glorius, B. Nies, C. Vater, F. Despong, T. Hanke, M. Gelinsky, *J Tissue Eng Regen Med* **2014**, 8, 682.
- [211] N. M. Hooper, R. Schouten, G. J. Hooper, *Open Orthop J* **2013**, 7, 373.
- [212] M. Castilho, C. Moseke, A. Ewald, U. Gbureck, J. Groll, I. Pires, J. Teßmar, E. Vorndran, *Biofabrication* **2014**, 6.
- [213] X. Yang, B. Xie, L. Wang, Y. Qin, Z. J. Henneman, G. H. Nancollas, *CrystEngComm* **2011**, 13, 1153.
- [214] F. Yang, D. Yang, J. Tu, Q. Zheng, L. Cai, L. Wang, *Stem Cells* **2011**, 29, 981.
- [215] S. Reitmaier, A. Kovtun, J. Schuelke, B. Kanter, M. Lemm, A. Hoess, S. Heinemann, B. Nies, A. Ignatius, *Journal of Orthopaedic Research* **2018**, 36, 106.
- [216] A. Lode, C. Heiss, G. Knapp, J. Thomas, B. Nies, M. Gelinsky, M. Schumacher, *Acta Biomater* **2018**, 65, 475.
- [217] J. A. Kim, J. Lim, R. Naren, H. suk Yun, E. K. Park, *Acta Biomater* **2016**, 44, 155.
- [218] J. Jia, H. Zhou, J. Wei, X. Jiang, H. Hua, F. Chen, S. Wei, J. W. Shin, C. Liu, *J R Soc Interface* **2010**, 7, 1171.
- [219] N. Ostrowski, A. Roy, P. N. Kumta, *ACS Biomater Sci Eng* **2016**, 2, 1067.
- [220] N. Golafshan, E. Vorndran, S. Zaharievski, H. Brommer, F. B. Kadumudi, A. Dolatshahi-Pirouz, U. Gbureck, R. van Weeren, M. Castilho, J. Malda, *Biomaterials* **2020**, 261, 120302.
- [221] P. Lobenhoffer, J. D. Agneskirchner, *Knee Surgery, Sports Traumatology, Arthroscopy* **2003**, 11, 132.
- [222] S. Sasaki, A. Maeyama, T. Kiyama, S. Kamada, T. Kobayashi, S. Ishii, T. Yamamoto, *Asia Pac J Sports Med Arthrosc Rehabil Technol* **2022**, 29, 30.
- [223] Y. G. Koh, O. R. Kwon, Y. S. Kim, Y. J. Choi, *Arthroscopy - Journal of Arthroscopic and Related Surgery* **2014**, 30, 1453.
- [224] C. Chiari, L. Grgurevic, T. Bordukalo-Niksic, H. Oppermann, A. Valentinitich, E. Nemecek, K. Staats, M. Schreiner, C. Trost, A. Kolb, F. Kainberger, S. Pehar, M. Milosevic, S. Martinovic, M. Peric, T. K. Sampath, S. Vukicevic, R. Windhager, *Journal of Bone and Mineral Research* **2020**, 35, 1893.
- [225] L. C. Gerhardt, A. R. Boccaccini, *Materials* **2010**, 3, 3867.
- [226] L. A. Fortier, E. J. Strauss, D. O. Shepard, L. Beckett, J. G. Kennedy, *Journal of Knee Surgery* **2019**, 32, 2.
- [227] K. Willemsen, R. Nizak, H. J. Noordmans, R. M. Castelein, H. Weinans, M. C. Kruyt, *Lancet Digit Health* **2019**, 1, e163.

- [228] K. Willemsen, M. Tryfonidou, R. Sakkera, R. M. Castelein, A. A. Zadpoor, P. Seevinck, H. Weinans, B. Meij, B. C. H. Wal, *Journal of Orthopaedic Research* **2021**, 1.
- [229] W. Health Organization, .
- [230] V. di Nicola, *Regen Ther* **2020**, 15, 149.
- [231] Y. Zhang, D. Li, Z. Zhu, S. Chen, M. Lu, P. Cao, T. Chen, S. Li, S. Xue, J. Zhu, G. Ruan, C. Ding, *Osteoarthritis Cartilage* **2022**.
- [232] A. Anandacoomarasamy, L. March, <http://dx.doi.org/10.1177/1759720X09359889> **2010**, 2, 17.
- [233] S. Grässel, D. Muschter, *F1000Research* 2020 9:325 **2020**, 9, 325.
- [234] T. Pettit, T. Kolvek, M. Langworthy, *Phys Med Rehabil Res* **2017**, 2.
- [235] T. J. Lujan, C. J. Underwood, N. T. Jacobs, J. A. Weiss, *J Appl Physiol* **2009**, 106, 423.
- [236] L. Zhang, J. Hu, K. A. Athanasiou, *Critical Reviews™ in Biomedical Engineering* **2009**, 37, 1.
- [237] L. Roseti, G. Desando, C. Cavallo, M. Petretta, B. Grigolo, *Cells* **2019**, 8.
- [238] A. R. Martín, J. M. Patel, H. M. Zlotnick, J. L. Carey, R. L. Mauck, *npj Regenerative Medicine* 2019 4:1 **2019**, 4, 1.
- [239] C. H. Hulme, J. Perry, H. S. McCarthy, K. T. Wright, M. Snow, C. Mennan, S. Roberts, *Emerg Top Life Sci* **2021**, 5, 575.
- [240] I. Urlić, A. Ivković, *Cells* 2021, Vol. 10, Page 2496 **2021**, 10, 2496.
- [241] X. Wu, M. Zhou, F. Jiang, S. Yin, S. Lin, G. Yang, Y. Lu, W. Zhang, X. Jiang, *Bioact Mater* **2021**, 6, 3976.
- [242] F. Gao, Z. Xu, Q. Liang, H. Li, L. Peng, M. Wu, X. Zhao, X. Cui, C. Ruan, W. Liu, F. Gao, Z. Xu, H. Li, W. Liu, Q. Liang, L. Peng, M. Wu, X. Zhao, X. Cui, C. Ruan, *Advanced Science* **2019**, 6, 1900867.
- [243] H. Sodhi, A. Panitch, *Biomolecules* 2021, Vol. 11, Page 29 **2020**, 11, 29.
- [244] T. Wang, F. Yang, *Stem Cell Res Ther* **2017**, 8, 1.
- [245] M. T. Ross, D. Kilian, A. Lode, J. Ren, M. C. Allenby, M. Gelinsky, M. A. Woodruff, *Bioprinting* **2021**, 23, e00158.
- [246] M. Castilho, G. Hochleitner, W. Wilson, B. van Rietbergen, P. D. Dalton, J. Groll, J. Malda, K. Ito, *Sci Rep* **2018**, 8, 1245.
- [247] M. Castilho, V. Mouser, M. Chen, J. Malda, K. Ito, *Acta Biomater* **2019**, 95, 297.
- [248] Fabrication of MSC-laden composites of hyaluronic acid hydrogels reinforced with MEW scaffolds for cartilage repair, **2021**.
- [249] J. H. Galarraga, R. C. Locke, C. E. Witherel, al -, E. Hewitt, S. Mros, M. McConnell, **2020**.
- [250] I. A. D. Mancini, R. A. Vindas Bolaños, H. Brommer, M. Castilho, A. Ribeiro, J. P. A. M. van Loon, A. Mensinga, M. H. P. van Rijen, J. Malda, R. van Weeren, *Tissue Eng Part C Methods* **2017**, 23, 804.
- [251] D. Loessner, C. Meinert, E. Kaemmerer, L. C. Martine, K. Yue, P. A. Levett, T. J. Klein, F. P. W. Melchels, A. Khademhosseini, D. W. Huttmacher, *Nature Protocols* 2016 11:4 **2016**, 11, 727.
- [252] C. C. L. Schuurmans, A. J. Brouwer, J. A. W. Jong, G.-J. P. H. Boons, W. E. Hennink, T. Vermonden, **2021**.
- [253] M. Mihajlovic, M. Rikkers, M. Mihajlovic, M. Viola, G. Schuiringa, B. C. Ilochonwu, R. Masereeuw, L. Vonk, J. Malda, K. Ito, T. Vermonden, **2022**, 23, 1350.
- [254] A. Abbadessa, M. M. Blokzijl, V. H. M. Mouser, P. Marica, J. Malda, W. E. Hennink, T. Vermonden, *Carbohydr Polym* **2016**, 149, 163.

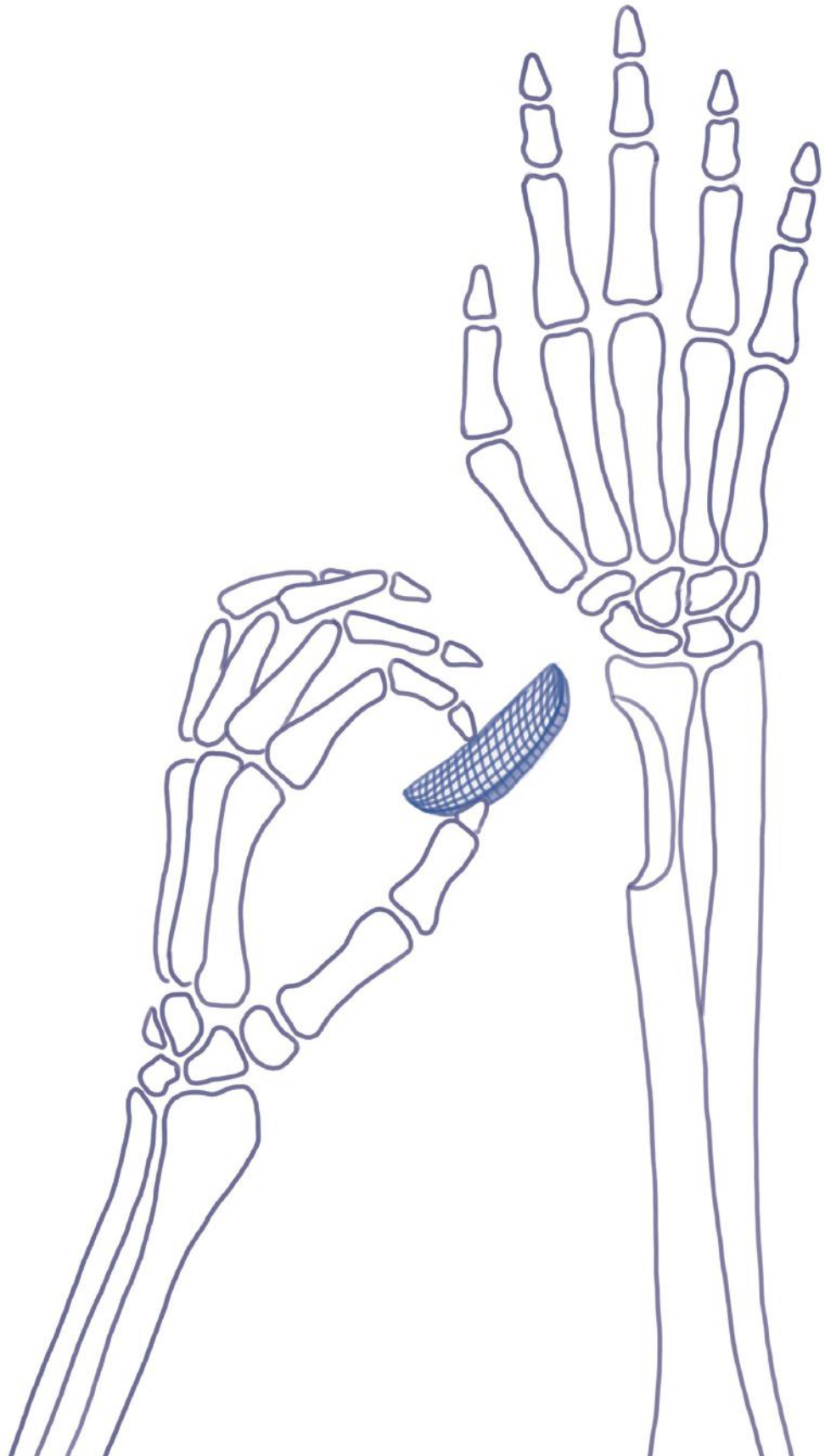
- [255] N. Golafshan, K. Willemsen, F. B. Kadumudi, E. Vorndran, A. Dolatshahi-Pirouz, H. Weinans, B. C. H. van der Wal, J. Malda, M. Castilho, *Adv Healthc Mater* **2021**, *10*.
- [256] B. J. Klotz, K. S. Lim, Y. X. Chang, B. G. Soliman, I. Pennings, F. P. W. Melchels, T. B. F. Woodfield, A. J. W. P. Rosenberg, J. Malda, D. Gawlitta, *Eur Cell Mater* **2018**, *35*, 335.
- [257] R. Zebaze, A. Ghasem-Zadeh, A. Mbala, E. Seeman, *Bone* **2013**, *54*, 8.
- [258] A. H. A. Damen, M. Nickien, K. Ito, C. C. van Donkelaar, *Clinical Biomechanics* **2020**, *79*, 105052.
- [259] R. Levato, W. R. Webb, I. A. Otto, A. Mensinga, Y. Zhang, M. van Rijen, R. van Weeren, I. M. Khan, J. Malda, *Acta Biomater* **2017**, *61*, 41.
- [260] D. E. T. Shepherd, B. B. Seedhom, *Ann Rheum Dis* **1999**, *58*, 27.
- [261] F. M. Wunner, M. L. Wille, T. G. Noonan, O. Bas, P. D. Dalton, E. M. De-Juan-Pardo, D. W. Hutmacher, *Advanced Materials* **2018**, *30*.
- [262] J. S. Jurvelin, M. D. Buschmann, E. B. Hunziker, *Proc Inst Mech Eng H* **2003**, *217*, 215.
- [263] M. Charlebois, M. D. McKee, M. D. Buschmann, *J Biomech Eng* **2004**, *126*, 129.
- [264] A. H. A. Damen, C. C. van Donkelaar, R. M. Cardinaels, J. M. Brandt, T. A. Schmidt, K. Ito, *Osteoarthritis Cartilage* **2021**, *29*, 894.
- [265] T. Wang, J. H. Lai, F. Yang, *Tissue Eng Part A* **2016**, *22*, 1348.
- [266] R. Subramani, A. Izquierdo-Alvarez, P. Bhattacharya, M. Meerts, P. Moldenaers, H. Ramon, H. van Oosterwyck, *Front Mater* **2020**, *7*, 212.
- [267] T. Lei, T. Zhang, W. Ju, X. Chen, B. C. Heng, W. Shen, Z. Yin, *Bioact Mater* **2021**, *6*, 2491.
- [268] P. J. Yang, J. S. Temenoff, *Engineering Orthopedic Tissue Interfaces*.
- [269] C. H. Park, H. F. Rios, Q. Jin, M. E. Bland, C. L. Flanagan, S. J. Hollister, W. v. Giannobile, *Biomaterials* **2010**, *31*, 5945.
- [270] G. Criscenti, A. Longoni, A. di Luca, C. de Maria, C. A. van Blitterswijk, G. Vozzi, L. Moroni, *Biofabrication* **2016**, *8*.
- [271] Y. Liang, X. Luan, X. Liu, *Bioact Mater* **2020**, *5*, 297.
- [272] C. H. Lee, J. Hajibandeh, T. Suzuki, A. Fan, P. Shang, J. J. Mao, *Tissue Eng Part A* **2014**, *20*, 1342.
- [273] P. I. Eke, L. Wei, W. S. Borgnakke, G. Thornton-Evans, X. Zhang, H. Lu, L. C. McGuire, R. J. Genco, *Periodontol 2000* **2016**, *72*, 76.
- [274] WHO, .
- [275] S. Amar, K. M. Chung, S. H. Nam, S. Karatzas, F. Myokai, T. E. van Dyke, *J Periodontol Res* **1997**, *32*, 148.
- [276] J. Dai, J. Si, N. Ouyang, J. Zhang, D. Wu, X. Wang, G. Shen, *Mol Med Rep* **2017**, *15*, 2443.
- [277] M. C. Bottino, V. Thomas, G. Schmidt, Y. K. Vohra, T. M. G. Chu, M. J. Kowolik, G. M. Janowski, *Dental Materials* **2012**, *28*, 703.
- [278] J. Liu, J. Ruan, M. D. Weir, K. Ren, A. Schneider, P. Wang, T. W. Oates, X. Chang, H. H. K. Xu, *Cells* **2019**, *8*, 537.
- [279] M. C. Bottino, D. Pankajakshan, J. E. Nör, *Dent Clin North Am* **2017**, *61*, 689.
- [280] Analysis of the in vitro degradation and the in vivo tissue response to bi-layered 3D-printed scaffolds combining PLA and biphasic PLA/bioglass components - Guidance of the inflammatory response as basis for osteochondral regeneration | Elsevier Enhanced Reader, .

- [281] Stratified scaffold design for engineering composite tissues | Elsevier Enhanced Reader, .
- [282] N. Dubey, J. A. Ferreira, A. Dagherery, Z. Aytac, J. Malda, S. B. Bhaduri, M. C. Bottino, *Acta Biomater* **2020**, *113*, 164.
- [283] S. Samavedi, P. Vaidya, P. Gaddam, A. R. Whittington, A. S. Goldstein, *Biotechnol Bioeng* **2014**, *111*, 2549.
- [284] A. Dagherery, J. A. Ferreira, J. Xu, N. Golafshan, D. Kaigler, S. B. Bhaduri, J. Malda, M. Castilho, M. C. Bottino, *Bioact Mater* **2023**, *19*, 268.
- [285] A. Dagherery, J. A. Ferreira, I. J. de Souza Araújo, B. H. Clarkson, G. J. Eckert, S. B. Bhaduri, J. Malda, M. C. Bottino, *Adv Healthc Mater* **2021**, *10*.
- [286] F. B. Kadumudi, M. Jahanshahi, M. Mehrali, T.-G. Zsuzsán, N. Taebnia, M. Hasany, S. Mohanty, A. Knott, B. Godau, M. Akbari, A. Dolatshahi-Pirouz, *Advanced Science* **2019**, *6*, 1801241.
- [287] M. v J Braham, M. C. Minnema, T. Aarts, Z. Sebestyén, T. Straetemans, A. Vyborova, J. Kuball, F. Cumhuri Öner, C. Robin, J. Alblas, by Taylor, F. Cumhuri, **2018**.
- [288] S. N. Rampersad, *Sensors (Basel)* **2012**, *12*, 12347.
- [289] A. A. de Oliveira, F. Priviero, R. C. Tostes, R. C. Webb, K. P. Nunes, *Sci Rep* **2021**, *11*.
- [290] M. Castilho, D. Feyen, M. Flandes-Iparraguirre, G. Hochleitner, J. Groll, P. A. F. Doevendans, T. Vermonden, K. Ito, J. P. G. Sluijter, J. Malda, **2017**.
- [291] J. C. Kade, P. D. Dalton, *Adv Healthc Mater* **2021**, *10*, 2001232.
- [292] N. Abbasi, S. Hamlet, V. T. Dau, N. T. Nguyen, *Journal of Science: Advanced Materials and Devices* **2020**, *5*, 30.
- [293] K. F. Eichholz, S. von Euw, R. Burdis, D. J. Kelly, D. A. Hoey, *Adv Healthc Mater* **2020**, *9*, 2001102.
- [294] P. S. P. Poh, D. W. Hutmacher, M. M. Stevens, M. A. Woodruff, *Biofabrication* **2013**, *5*, 045005.
- [295] J. Ren, K. A. Blackwood, A. Doustgani, P. P. Poh, R. Steck, M. M. Stevens, M. A. Woodruff, *J Biomed Mater Res A* **2014**, *102*, 3140.
- [296] M. Nabyouni, T. Brueckner, H. Zhou, U. Gbureck, S. B. Bhaduri, *Acta Biomater* **2018**, *66*, 23.
- [297] M. Gupta, W. L. E. Wong, *Mater Charact* **2015**, *105*, 30.
- [298] H. Zreiqat, C. R. Howlett, A. Zannettino, P. Evans, G. Schulze-Tanzil, C. Knabe, M. Shakibaei, *Journal of Biomedical Materials Research: An Official Journal of The Society for Biomaterials, The Japanese Society for Biomaterials, and The Australian Society for Biomaterials and the Korean Society for Biomaterials* **2002**, *62*, 175.
- [299] K. F. Eichholz, S. von Euw, R. Burdis, D. J. Kelly, D. A. Hoey, *Adv Healthc Mater* **2020**, *9*, 2001102.
- [300] T. L. Jenkins, D. Little, *npj Regenerative Medicine* **2019**, *4*, 1.
- [301] R. A. Thibault, A. G. Mikos, F. K. Kasper, *Adv Healthc Mater* **2013**, *2*, 13.
- [302] S. Ali, Z. Khatri, K. W. Oh, I. S. Kim, S. H. Kim, *Macromolecular Research* **2014**, *22*, 562.
- [303] I. Calejo, R. Costa-Almeida, R. L. Reis, M. E. Gomes, *Adv Healthc Mater* **2019**, *8*, 1900200.
- [304] W. Jiang, L. Li, D. Zhang, S. Huang, Z. Jing, Y. Wu, Z. Zhao, L. Zhao, S. Zhou, *Acta Biomater* **2015**, *25*, 240.
- [305] W. Wang, J. He, B. Feng, Z. Zhang, W. Zhang, G. Zhou, Y. Cao, W. Fu, W. Liu, <https://doi.org/10.2217/nnm.16.24> **2016**, *11*, 1055.
- [306] R. Staples, S. Ivanovski, C. Vaquette, *Acta Biomater* **2022**, *150*, 221.

- [307] M. Komaki, K. Iwasaki, H. Arzate, A. S. Narayanan, Y. Izumi, I. Morita, *J Cell Physiol* **2012**, *227*, 649.
- [308] B. L. Foster, M. Ao, C. R. Salmon, M. B. Chavez, T. N. Kolli, A. B. Tran, E. Y. Chu, K. R. Kantovitz, M. Yadav, S. Narisawa, J. L. Millán, F. H. Nociti, M. J. Somerman, *Bone* **2018**, *107*, 196.
- [309] J. Du, M. Li, *Cellular and Molecular Life Sciences* **2017**, *74*, 4279.
- [310] C. Yang, H. Ma, Z. Wang, M. R. Younis, C. Liu, C. Wu, Y. Luo, P. Huang, *Advanced Science* **2021**, *8*.
- [311] S. Yoshizawa, A. Brown, A. Barchowsky, C. Sfeir, S. Yoshizawa, A. Brown, A. Barchowsky, C. Sfeir, S. Yoshizawa, A. Brown, A. Barchowsky, C. Sfeir, **2014**, 8207.
- [312] J. Zarins, M. Pilmane, E. Sidhoma, I. Salma, **2017**, 2016, 17.
- [313] H. Safiaghdam, H. Nokhbatolfoghahaei, A. Khojasteh, *Iranian Journal of Pharmaceutical Research* **2019**, *18*, 101.
- [314] E. M. Carlisle, *Science* **1972**, *178*, 619.
- [315] Y. H. Lin, A. K. X. Lee, C. C. Ho, M. J. Fang, T. Y. Kuo, M. Y. Shie, *Biomaterials Advances* **2022**, *133*, 112660.
- [316] R. Taktak, A. Elghazel, J. Bouaziz, S. Charfi, H. Keskes, *Materials Science and Engineering: C* **2018**, *86*, 121.
- [317] W. Qiao, Q. Liu, Z. Li, H. Zhang, Z. Chen, *Sci Technol Adv Mater* **2017**, *18*, 110.
- [318] H. Zhou, B. Liang, H. Jiang, Z. Deng, K. Yu, *Journal of Magnesium and Alloys* **2021**, *9*, 779.
- [319] G. Borciani, G. Ciapetti, C. Vitale-Brovarone, N. Baldini, *Materials* **2022**, *Vol. 15*, Page 1724 **2022**, *15*, 1724.
- [320] W. Habraken, P. Habibovic, M. Epple, M. Bohner, *Materials Today* **2016**, *19*, 69.
- [321] M. Bohner, *Injury* **2000**, *31*, D37.
- [322] M. Nabiyouni, T. Brückner, H. Zhou, U. Gbureck, S. B. Bhaduri, *Acta Biomater* **2018**, *66*, 23.
- [323] F. Tamimi, D. le Nihouannen, D. C. Bassett, S. Ibasco, U. Gbureck, J. Knowles, A. Wright, A. Flynn, S. v. Komarova, J. E. Barralet, *Acta Biomater* **2011**, *7*, 2678.
- [324] S. v. Dorozhkin, *Materials* **2013**, *Vol. 6*, Pages 3840-3942 **2013**, *6*, 3840.
- [325] C. Zhou, L. Liu, W. Wang, L. Zhao, M. Li, J. Li, B. Zhang, Y. Han, L. Wang, Z. Zhang, *Nanotechnol Rev* **2021**, *10*, 1359.
- [326] A. di Luca, B. Ostrowska, I. Lorenzo-Moldero, A. Lepedda, W. Swieszkowski, C. van Blitterswijk, L. Moroni, **2016**.
- [327] T. Albrektsson, W. Becker, P. Coli, T. Jemt, J. Mölne, L. Sennerby, *Clin Implant Dent Relat Res* **2019**, *21*, 786.
- [328] C. P. Kruize, S. Panahkhah, N. E. Putra, P. Diaz-Payno, G. van Osch, A. A. Zadpoor, M. J. Mirzaali, **2021**.
- [329] N. T. Saidy, T. Shabab, O. Bas, D. M. Rojas-González, M. Menne, T. Henry, D. W. Hutmacher, P. Mela, E. M. De-Juan-Pardo, *Front Bioeng Biotechnol* **2020**, *8*, 793.
- [330] J. A. Buckwalter, H. J. Mankin, *Instr Course Lect* **1998**, *47*, 487—504.
- [331] J. Buckwalter, *Journal of Orthopaedic & Sport Physical Therapy* **1998**, *28*, 192.
- [332] L. P. M. Brittberg, A. Lindahl, A. Nilsson, C. Ohlsson, O. Isaksson, *N Engl J Med* **1994**, *331*, 889.
- [333] W. Hunter, *Philos Trans R Soc Lond* **1743**, *42b*, 514.
- [334] G. Pisanu, U. Cottino, F. Rosso, D. Blonna, A. G. Marmotti, C. Bertolo, R. Rossi, D. E. Bonasia, *Joints* **2018**, *6*, 42.

- [335] J. Groll, T. Boland, T. Blunk, J. A. Burdick, D. W. Cho, P. D. Dalton, B. Derby, G. Forgacs, Q. Li, V. A. Mironov, L. Moroni, M. Nakamura, W. Shu, S. Takeuchi, G. Vozzi, T. B. F. Woodfield, T. Xu, J. J. Yoo, J. Malda, *Biofabrication* **2016**, 8.
- [336] A. C. Daly, F. E. Freeman, T. Gonzalez-Fernandez, S. E. Critchley, J. Nulty, D. J. Kelly, *Adv Healthc Mater* **2017**, 6, 1.
- [337] I. A. D. D. Mancini, R. A. Vindas Bolaños, H. Brommer, M. Castilho, A. Ribeiro, J. P. A. M. A. M. Van Loon, A. Mensinga, M. H. P. P. Van Rijen, J. Malda, R. van Weeren, *Tissue Eng Part C Methods* **2017**, 23, 804.
- [338] J. Golafshan, Nasim; Vorndran, Elke; Zaharievski, Stefan; Brommer, Harold; Babu Kadumudi, Firoz; Dolatshahi-Pirouz, Alireza; Gbureck, Uwe; van Weeren, René; Castilho, Miguel; Malda, *Under review*.
- [339] T. J. Klein, D. Ph, J. Malda, D. Ph, R. L. Sah, D. Sc, D. W. Hutmacher, D. Ph, **2009**, 15.
- [340] A. R. Poole, T. Kojima, T. Yasuda, F. Mwale, M. Kobayashi, S. Laverty, *Clin Orthop Relat Res* **2001**, 26.
- [341] A. Benninghoff, **1925**.
- [342] M. A. MacCONAILL, *J Bone Joint Surg Br* **1951**, 33B, 251.
- [343] P. A. Levett, F. P. W. Melchels, K. Schrobback, D. W. Hutmacher, J. Malda, T. J. Klein, *J Biomed Mater Res A* **2014**, 102, 2544.
- [344] V. H. M. Mouser, R. Levato, A. Mensinga, W. J. A. Dhert, D. Gawlitta, J. Malda, *Connect Tissue Res* **2018**, 00, 1.
- [345] R. Levato, W. R. Webb, I. A. Otto, A. Mensinga, Y. Zhang, M. van Rijen, R. van Weeren, I. M. Khan, J. Malda, *Acta Biomater* **2017**, 61, 41.
- [346] W. Schuurman, V. Khristov, M. W. Pot, P. R. Van Weeren, W. J. A. Dhert, J. Malda, *Biofabrication* **2011**, 3.
- [347] H.-W. Kang, S. J. Lee, I. K. Ko, C. Kengla, J. J. Yoo, A. Atala, *Nat Biotechnol* **2016**, 34, 312.
- [348] S. Critchley, E. J. Sheehy, G. Cunniffe, P. Diaz-Payno, S. F. Carroll, O. Jeon, E. Alsberg, P. A. J. Brama, D. J. Kelly, *Acta Biomater* **2020**.
- [349] R. Schipani, S. Scheurer, R. Florentin, S. E. Critchley, D. J. Kelly, *Biofabrication* **2020**.
- [350] P. D. Dalton, *Curr Opin Biomed Eng* **2017**, 2, 49.
- [351] T. M. Robinson, D. W. Hutmacher, P. D. Dalton, *Adv Funct Mater* **2019**, 29.
- [352] J. Visser, F. P. W. Melchels, J. E. Jeon, E. M. Van Bussel, L. S. Kimpton, H. M. Byrne, W. J. A. Dhert, P. D. Dalton, D. W. Hutmacher, J. Malda, *Nat Commun* **2015**, 6, 1.
- [353] O. Bas, D.-J.-P. Elena M, C. Meinert, D. D'Angella, J. G. Baldwin, L. J. Bray, R. M. Wellard, S. Kollmannsberger, E. Rank, C. Werner, T. J. Klein, I. Catelas, D. W. Hutmacher, *Biofabrication* **2017**.
- [354] M. Castilho, G. Hochleitner, W. Wilson, B. van Rietbergen, P. D. Dalton, J. Groll, J. Malda, K. Ito, *Sci Rep* **2018**, 8, 1.
- [355] M. de Ruijter, A. Hrynevich, J. N. Haigh, G. Hochleitner, M. Castilho, J. Groll, J. Malda, P. D. Dalton, *Small* **2018**, 14, 1.
- [356] M. de Ruijter, A. Ribeiro, I. Dokter, M. Castilho, J. Malda, *Adv Healthc Mater* **2018**, 1800418, 1800418.
- [357] P. Diloksumpan, M. de Ruijter, M. Castilho, U. Gbureck, T. Vermonden, P. R. van Weeren, J. Malda, R. Levato, *Biofabrication* **2020**, 12, 025014.

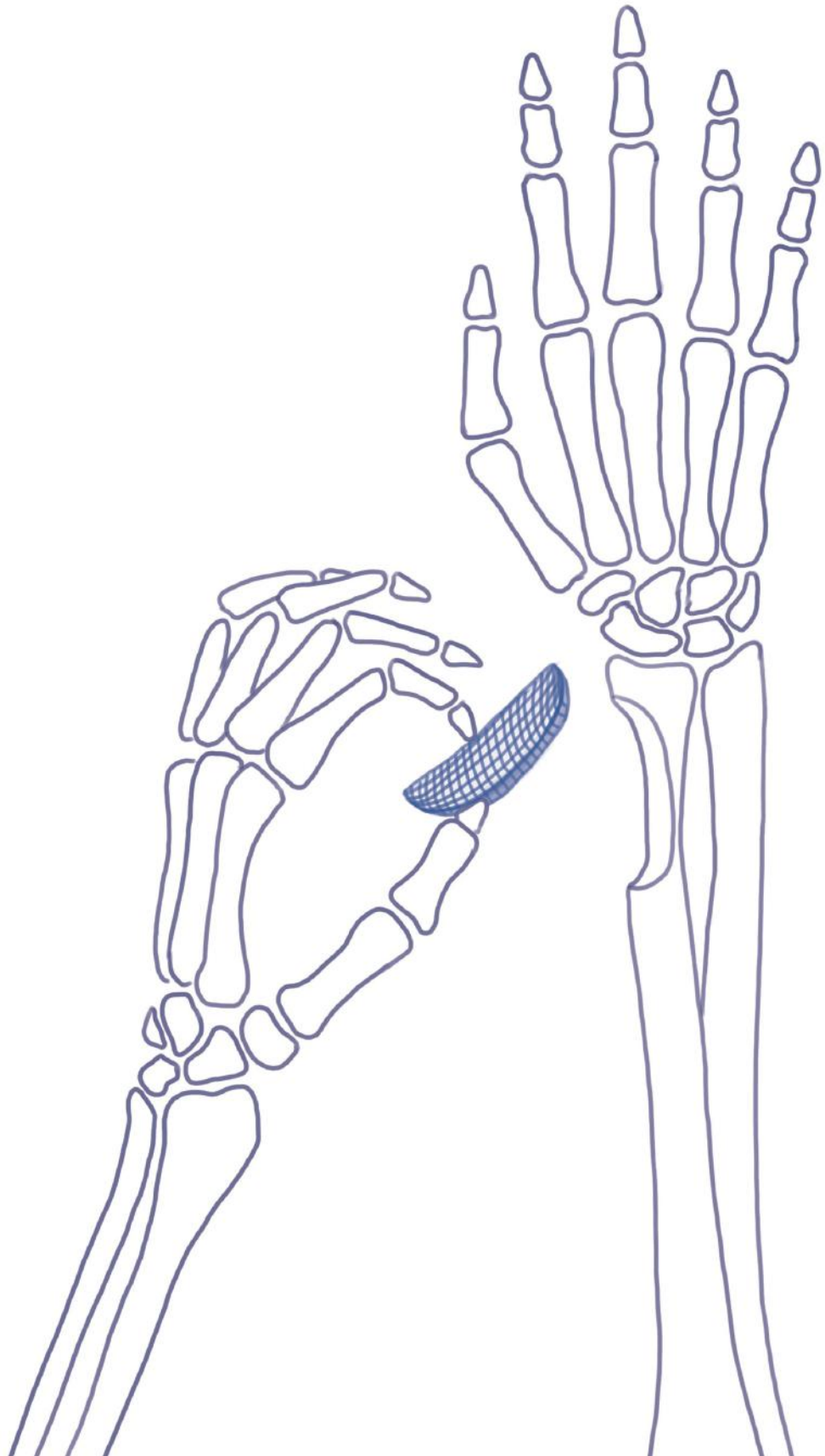
- [358] R. Williams, I. M. Khan, K. Richardson, L. Nelson, H. E. McCarthy, T. Analbelsi, S. K. Singhrao, G. P. Dowthwaite, R. E. Jones, D. M. Baird, H. Lewis, S. Roberts, H. M. Shaw, J. Dudhia, J. Fairclough, T. Briggs, C. W. Archer, *PLoS One* **2010**, 5.
- [359] F. P. W. W. Melchels, W. J. A. A. Dhert, D. W. Hutmacher, J. Malda, *J Mater Chem B* **2014**, 2, 2282.
- [360] A. I. Van Den Bulcke, B. Bogdanov, N. De Rooze, E. H. Schacht, M. Cornelissen, H. Berghmans, *Biomacromolecules* **2000**, 1, 31.
- [361] W. R. Taylor, R. M. Ehrig, M. O. Heller, H. Schell, P. Seebeck, G. N. Duda, *J Biomech* **2006**, 39, 791.
- [362] M. Castilho, M. De Ruijter, S. Beirne, C. C. Villette, K. Ito, G. G. Wallace, J. Malda, *Trends Biotechnol* **2020**, 1.
- [363] P. D. Dalton, T. B. F. Woodfield, V. Mironov, J. Groll, *Adv Sci (Weinh)* **2020**, 7, 1902953.
- [364] R. Levato, T. Jungst, R. G. Scheuring, T. Blunk, J. Groll, J. Malda, *Advanced Materials* **2020**, 32, 1906423.
- [365] E. B. C. Standards, K. Willson, D. Ke, C. Kengla, A. Atala, S. V. Murphy, 2140.
- [366] D. B. Kolesky, R. L. Truby, A. S. Gladman, T. A. Busbee, K. A. Homan, J. A. Lewis, *Advanced Materials* **2014**, 26, 3124.
- [367] M. T. Poldervaart, H. Wang, J. van der Stok, H. Weinans, S. C. G. Leeuwenburgh, F. C. Öner, W. J. A. Dhert, J. Alblas, *PLoS One* **2013**, 8, e72610.
- [368] I. A. Otto, F. P. W. Melchels, X. Zhao, M. A. Randolph, M. Kon, C. C. Breugem, J. Malda, *Biofabrication* **2015**, 7, 32001.
- [369] M. Castilho, V. Mouser, M. Chen, J. Malda, K. Ito, *Acta Biomater* **2019**, 95, 297.
- [370] A. C. Daly, D. J. Kelly, *Biomaterials* **2019**, 197, 194.
- [371] T. S. de Windt, L. A. Vonk, I. C. M. Slaper-Cortenbach, M. P. H. van den Broek, R. Nizak, M. H. P. van Rijen, R. A. de Weger, W. J. A. Dhert, D. B. F. Saris, *Stem Cells* **2017**, 35, 256.
- [372] L. A. Vonk, S. F. J. van Dooremalen, N. Liv, J. Klumperman, P. J. Coffer, D. B. F. Saris, M. J. Lorenowicz, *Theranostics* **2018**, 8, 906.
- [373] L. S. Moreira Teixeira, J. C. H. Leijten, J. Sobral, R. Jin, A. A. van Apeldoorn, J. Feijen, C. van Blitterswijk, P. J. Dijkstra, M. Karperien, *Eur Cell Mater* **2012**, 23, 387.
- [374] T. Albrektsson, W. Becker, P. Coli, T. Jemt, J. Mölne, L. Sennerby, *Clin Implant Dent Relat Res* **2019**, 21, 786.
- [375] S. E. Kold, J. Hickman, F. Melsen, *Equine Vet J* **1986**, 18, 18.
- [376] C. M. Peiffer Q.C., de Ruijter M., van Duijn J., Crottet D., Dominic E., Malda J., *Under review*.
- [377] F. M. Wunner, M. L. Wille, T. G. Noonan, O. Bas, P. D. Dalton, E. M. De-Juan-Pardo, D. W. Hutmacher, *Advanced Materials* **2018**, 1706570, 1.
- [378] I. Liashenko, A. Hrynevich, P. D. Dalton, *Adv Mater* **2020**, e2001874.
- [379] J. Malda, J. Groll, P. R. van Weeren, *Nat Rev Rheumatol* **2019**, 15, 571.
- [380] Dichloromethane - ¹H NMR - Chemical Shifts - SpectraBase, .
- [381] Dibutyl phthalate (84-74-2) ¹H NMR spectrum, .
- [382] Annex I (MDR): General safety and performance requirements - Medical Device Regulation WebApp english language, .



List of Abbreviations

3D print	Three-dimensional print
3DPP	Three-dimensional powder print
AC	Articular cartilage
ALP	Alkaline phosphate
AM	Additive manufacturing
aMEM	Minimal Essential Medium
ARed	Alizarin Red
ASAP	Ascorbic acid
BCIP/NBT	(5-Bromo-4-chloro-3-indolyl phosphate/Nitro blue tetrazolium
BCP	Biphasic calcium phosphate
BGP	<i>β-glycerophosphate</i>
BMC	Bone marrow concentrate
CAD	computer-aided design
CaP	Calcium phosphate
CDHA	calcium-deficient hydroxyapatite
ACPCs	chondroprogenitor Cells
CPC	Calcium phosphate cement
CT	Computed tomography
DAB	3,3-diaminobenzidine-horseradish peroxidase
DoF	degrees of freedom
DIW	Direct ink writing
DLP	Digital light processing
DMEM	Dulbecco's Modified Eagle Medium
DMMB	dimethylmethylene blue
DMSO	Dimethyl sulfoxide
EDX	Energy-dispersive X-ray spectroscopy
eMSCs	Equine mesenchymal stem cells
FAp	Fluorapatite
FBS	Fetal bovine serum
FDM	Fused deposition model
FTIR	Fourier-transform infrared spectroscopy
G code	Geometric Code
GelMA	Gelatin methacrylated
HA	Hydroxy apatite
HE	<i>hematoxylin and eosin</i>
hMSCs	Human mesenchymal stem cells
hNMR	Proton nuclear magnetic resonance
ICP-MS	Inductively coupled plasma mass spectrometry
IFS	Interfibre spacing

MEW	Melt electrowriting
MgP	Magnesium phosphate
MgPSr	Magnesium strontium phosphate
MPC	Magnesium phosphate cement
OA	Osteoarthritis
OCN	Osteonectin
OWO	open-wedge osteotomy
PCL	polycaprolactone
PDLA	Poly(DL-lactide)
Pen strep	Penicillin-Streptomycin
PLGA	poly(lactic-co-glycolic acid)
pNPP	p-Nitrophenyl Phosphate, Disodium Salt
PTA	programmed trajectory accuracy (PTA)
SEM	Scanning electron microscope
STL	3D-standard tessellation language
sGAGs	sulphated glycosaminoglycans
TCP	Tri calcium phosphate
TEM	Transmission electron microscopy
VEGF	Vascular endothelial growth factor
XRD	X-Ray Diffraction



Summary

Samenvatting

Summary

The development of the degradable bone implants has gained a great attention during the last years. This need comes from the fact that autologous bone transplantation, which is the current standard and most effective treatment of bone defects, is associated with severe drawbacks regarding donor site morbidity and limited availability. However, there is a lack of synthetic materials that are degradable, osteopromotive and mechanically competent at the same time. Further, materials processing and the implantation of the scaffolds in the body are also an important challenge. In this thesis, by using advanced 3D printing technologies, the fabrication of biodegradable, patient-specific, and mechanically competent MgP-based implants has been explored to treat critical-sized bone defects. The developed MgP-based biomaterial is inspired by the composition of native bone tissue and can be degraded in the body and subsequently be replaced by native bone.

In the past decade, important contributions to the field of synthetic bone substitutes have been made by the development of CaP ceramic materials. Although some CaP bioceramics are known as osteopromotive materials, the most widely used like HA do not fully dissolve within the physiologically environment. However, by addition of the osteoinductive metallic ions, such as Mg^{2+} and Sr^{2+} , through a mechanical alloying technique, the osteogenic properties of CaP-based bioceramics (FAp) can be significantly improved (**Chapter 2**). More specifically, improved bone formation was observed in a defect model of femur rats after 3 weeks using FAp bioceramics that contain Mg^{2+} and Sr^{2+} .

Building on these findings, an osteopromotive ink with high content of MgP-based bioceramics was developed (**Chapter 3**). The ink was composed of 70 wt.% MgP and 30 wt.% PCL polymers, while the MgP particles were not fully encapsulated and the bioceramic was still exposed. Printability assessment confirmed that the MgP-based ink showed appropriate shape fidelity among the other compositions; as the ink has shown the less deviation from computational designed implants. The ink was printable into regular geometries with controlled internal architectures (i.e. pore size and interconnectivity) using the extrusion-based printers. The mechanical behavior of the scaffolds under compression loading such as elastic modulus were within the same range as the compressive properties of trabecular bone. The 3D printed MgP-based scaffolds were implanted in a critical sized-defect created in the tubercosxae of ponies. The *in vivo* results did confirm that the 3D printed scaffolds are capable of inducing bone formation within critical size defects after 6 months implantation

To investigate the possibility to fabricate more complex, patient-specific, and geometries, a scaffold to treat dysplastic hip in canines was developed based on actual CT scans of patients. Further, in order to evaluate if the designed scaffolds could provide a stable restoration of the hip socket, they were investigated by three-point flexure and compression mechanical tests. Finally, to anticipate the *in vivo* mechanical performance of the resorbable, patient specific scaffolds, implants were loaded under physiological loading conditions using a custom-built bioreactor system and after exposed to accelerated *in vitro* enzymatic degradation (**Chapter 4**).

Then, the application of the material was further evaluated in a procedure for the correction of the alignment of the leg in knee surgery (osteotomy). After the correction of the leg, an open wedge will typically be left open. This can cause pain for the patients. To address this, CT scans were obtained of the human's cadaver leg and different implants were designed based on different corrective knee osteotomy procedures. Implants were fabricated using the osteogenic MgP-based biomaterial ink, and the wedges were implemented into the osteotomy wedge in the human cadaveric legs (**Chapter 5**).

Further, degradable osteochondral scaffolds were fabricated using the CaP-based bioceramics as the bone anchor and the MEW fibres for the chondral zone. The polysaccharide hydrogel was casted into the MEW PCL fibres and the osmotic swelling were investigated to enhance the cartilage regeneration (**Chapter 6**).

Building on the findings above, the next challenge addressed in this thesis was to advance the biomaterial ink and 3D printing technology to fabricate highly resolved scaffolds which can facilitate integration of bone scaffolds with surrounding connective tissues. To achieve this, the compositionally and structurally tailored multilayered MgP-based scaffolds were processed by MeltElectro Writing (MEW) to develop a graded implant to regenerate both the bone and ligament. The high-resolution scaffolds showed great potential to better resemble bone microenvironments and regenerate bone. The regeneration capacity of the scaffolds for bone and ligament was evaluated in the fenestration defects of the rats over 6 weeks (**Chapter 7**).

To upscale the osteochondral scaffolds to patient-specific scaffolds, it has been shown that the full joint of the patient from MgP-based ink can be printed by using the extrusion-based printer. Also, a new design can generate the cartilage zone of the joint by resurfacing of patient-specific geometries (**Annex I**).

This thesis underscores the substantial progress made towards the clinical translation of fully mechanically competent and osteopromotive, patient-specific bone scaffolds, which can be generated through extrusion- and MEW-based printing processes. It particularly showed that the MgP-based bioceramics can be integrated with other biomaterials through 3D printing and regenerate the bone in contact with various connective tissues, such as ligament and cartilage, to form mechanically stable scaffolds for interface tissue engineering. Nevertheless, there are several challenges that still need to be explored further, especially regarding the development of the biomaterials with mechanical properties for proper durability under full load bearing conditions without loss of guidance or mechanical support. A summary of these challenges and contributions of this thesis is presented schematically in Fig. 1.

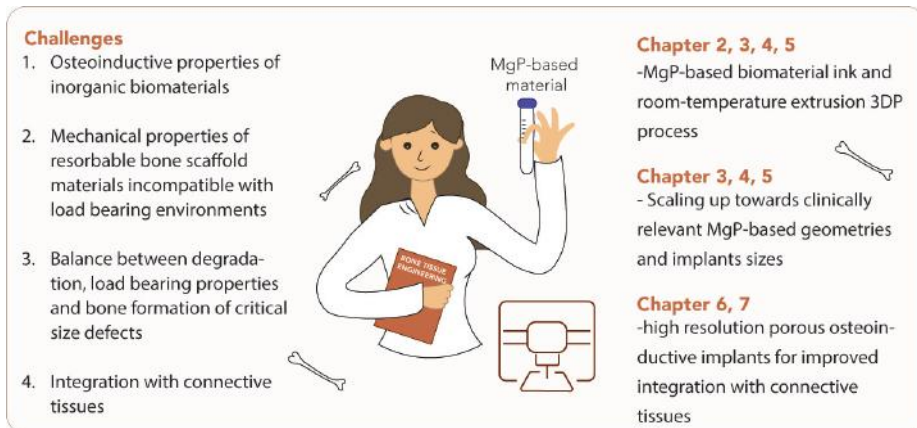


Figure 1. A summary of the thesis chapters, and how they relate to the open challenges in bone tissue engineering.

Samenvatting

De ontwikkeling van de afbreekbare botimplantaten heeft de laatste jaren veel aandacht gekregen. Deze behoefte komt voort uit het feit dat autologe bottransplantatie, de huidige standaard en meest effectieve behandeling van botdefecten, gepaard gaat met ernstige nadelen wat betreft morbiditeit op de donorplaats en beperkte beschikbaarheid. Er is echter een gebrek aan synthetische materialen die tegelijkertijd afbreekbaar, osteobevorderend en mechanisch competent zijn. Verder vormen ook de materiaalverwerking en de implantatie van de scaffolds in het lichaam een belangrijke uitdaging. In dit proefschrift is, door gebruik te maken van geavanceerde 3D-printtechnologieën, de fabricage van biologisch afbreekbare, patiëntspecifieke en mechanisch competente MgP-gebaseerde implantaten onderzocht om botdefecten van kritische grootte te behandelen. Het ontwikkelde op MgP gebaseerde biomateriaal is geïnspireerd op de samenstelling van aangeboren botweefsel en kan in het lichaam worden afgebroken en vervolgens worden vervangen door aangeboren bot.

In het afgelopen decennium zijn belangrijke bijdragen op het gebied van synthetische botvervangers geleverd door de ontwikkeling van CaP-keramische materialen. Hoewel sommige CaP-biokeramische materialen bekend staan als osteobevorderende materialen, lossen de meest gebruikte zoals HA niet volledig op in de fysiologische omgeving. Echter, door toevoeging van de osteo-inductieve metaalionen, zoals Mg^{2+} en Sr^{2+} , via een mechanische legeringstechniek, kunnen de osteogene eigenschappen van op CaP gebaseerde biokeramiek (FAP) aanzienlijk worden verbeterd (**Hoofdstuk 2**). Meer specifiek werd een verbeterde botvorming waargenomen in een defectmodel van dijbeenratten na 3 weken gebruik van FAP-biokeramiek die Mg^{2+} en Sr^{2+} bevatten.

Voortbouwend op deze bevindingen werd een osteopromotorische inkt met een hoog gehalte aan op MgP gebaseerde biokeramiek ontwikkeld (**Hoofdstuk 3**). De inkt was samengesteld uit 70 gew.% MgP en 30 gew.% PCL-polymeren, terwijl de MgP-deeltjes niet volledig waren ingekapseld en het biokeramiek nog zichtbaar was. Bedrukbaarheidsbeoordeling bevestigde dat de op MgP gebaseerde inkt de juiste vormgetrouwheid vertoonde tussen de andere samenstellingen; omdat de inkt de minste afwijking heeft laten zien van door computers ontworpen implantaten. De inkt was bedrukbaar tot regelmatige geometrieën met gecontroleerde interne architecturen (d.w.z. poriegrootte en onderlinge verbondenheid) met behulp van op extrusie gebaseerde printers. Het mechanische gedrag van de scaffolds onder compressiebelasting, zoals elastische modulus, lag binnen hetzelfde bereik als de

compressie-eigenschappen van trabeculair bot. De 3D-geprinte op MgP gebaseerde steigers werden geïmplant in een defect van kritieke grootte dat was ontstaan in de tubercosae van pony's. De in vivo resultaten bevestigden dat de 3D-geprinte scaffolds na 6 maanden implantatie in staat zijn om botvorming te induceren binnen kritische grootte-defecten

Om de mogelijkheid te onderzoeken om meer complexe, patiëntspecifieke en geometrieën te fabriceren, werd een scaffold voor de behandeling van dysplastische heup bij hoektanden ontwikkeld op basis van daadwerkelijke CT-scans van patiënten. Verder, om te evalueren of de ontworpen steigers een stabiel herstel van de heupkom konden bieden, werden ze onderzocht door mechanische driepuntsbuig- en compressietests. Ten slotte werden de implantaten, om te anticiperen op de in vivo mechanische prestaties van de resorbeerbare, patiëntspecifieke scaffolds, geladen onder fysiologische belastingsomstandigheden met behulp van een op maat gemaakt bioreactorsysteem en na blootstelling aan versnelde in vitro enzymatische afbraak (**Hoofdstuk 4**).

Vervolgens werd de toepassing van het materiaal verder geëvalueerd in een procedure voor de correctie van de uitlijning van het been bij knieoperaties (osteotomie). Na de correctie van het been wordt een open wig doorgaans opengelaten. Dit kan pijn veroorzaken bij de patiënten. Om dit aan te pakken, werden CT-scans gemaakt van het kadaverbeen van de mens en werden verschillende implantaten ontworpen op basis van verschillende corrigerende knie-osteotomieprocedures. Implantaten werden vervaardigd met behulp van de osteogene MgP-gebaseerde biomateriaalinkt, en de wiggan werden in de osteotomiewig in de menselijke kadaverpoten geplaatst (**Hoofdstuk 5**).

Verder werden afbreekbare osteochondrale scaffolds vervaardigd met behulp van de op CaP gebaseerde biokeramiek als botanker en de MEW-vezels voor de chondrale zone. De polysaccharide hydrogel werd in de MEW PCL-vezels gegoten en de osmotische zwelling werd onderzocht om de kraakbeenregeneratie te bevorderen (**Hoofdstuk 6**).

Om de osteochondrale scaffolds op te schalen naar patiëntspecifieke scaffolds, is aangetoond dat het volledige gewricht van de patiënt van MgP-gebaseerde inkt kan worden geprint met behulp van de extrusie-gebaseerde printer. Ook kan een nieuw ontwerp de kraakbeenzone van het gewricht genereren door patiëntspecifieke geometrieën weer aan de oppervlakte te brengen (**bijlage I**).

Dit proefschrift onderstreept de substantiële vooruitgang die is geboekt in de richting van de klinische vertaling van volledig mechanisch competente en osteobevorderende, patiëntspecifieke botsteigers, die kunnen worden gegenereerd door middel van extrusie- en MEW-gebaseerde printprocessen. Het toonde met name aan dat de op MgP gebaseerde biokeramiek kan worden geïntegreerd met andere biomaterialen door middel van 3D-printen en het bot regeneert dat in contact komt met verschillende bindweefsels, zoals ligament en kraakbeen, om mechanisch stabiele steigers te vormen voor interface tissue engineering. Desalniettemin zijn er verschillende uitdagingen die nog verder moeten worden onderzocht, vooral met betrekking tot de ontwikkeling van de biomaterialen met mechanische eigenschappen voor een goede duurzaamheid onder volledige belasting zonder verlies van geleiding of mechanische ondersteuning. Een samenvatting van deze uitdagingen en bijdragen van dit proefschrift wordt schematisch weergegeven in **figuur 1**.



Figuur 1. Een samenvatting van de hoofdstukken van het proefschrift, en hoe deze zich verhouden tot de openstaande uitdagingen in de botweefselmanipulatie.

پیشرفت ایمپلنت‌های استخوانی تخریب‌پذیر در سال‌های اخیر مورد توجه بسیاری قرار گرفته است. این توجه به این دلیل است که استفاده از پیوند استخوان که روشی موثر برای درمان عیوب استخوانی است، دارای محدودیت‌های مهمی است. از جمله این محدودیت‌ها می‌توان به میزان محدود بافت استخوان و همچنین نگهداری از بافت مانند عفونت پس از جراحی اشاره کرد. برای ترمیم عیوب استخوان، همچنین از موادی مانند فلزات و سرامیک‌ها و پلیمرها نیز استفاده می‌کنند. اما ایمپلنت‌های استخوانی موجود توسط مواد سنتزی، همچنان محدودیت‌هایی از جمله غیرتخریب‌پذیر بودن، عدم پیوند با استخوان، و خواص مکانیکی نامتناسب با بافت اصلی استخوان را دارند. همچنین فرآیند ساخت ایمپلنت‌ها و کاشتن آن‌ها در بدن نیز از چالش‌های اساسی در حین جراحی است. در تز پیش رو، با استفاده از تکنولوژی پرینتر سه بعدی، ساخت ایمپلنت‌های تخریب‌پذیر، با توجه به آناتومی بیمار با خواص مکانیکی شبیه بافت استخوان مورد بررسی قرار گرفته است. ایمپلنت‌های استخوانی ساخته شده برای درمان عیوب بحرانی استخوان (عیوبی که استخوان به صورت خود به خود نمی‌تواند خود را ترمیم کند) ساخته شده‌اند. ساخت ایمپلنت‌های بر پایه سرامیک منیزیم فسفات در این تز (از جمله بایوسرامیک‌های مورد استفاده در پزشکی) با توجه به ساختار اصلی استخوان طراحی و ساخته شده که می‌تواند در محیط فیوزیولوژی بدن تخریب شود و با بافت استخوان جایگزین شود. این دسته از ایمپلنت‌های استخوانی بر خلاف ایمپلنت‌های فلزی تیتانیومی نیازی به جایگزینی پس از مدت زمانی را نداشته، و می‌توانند محدودیت‌های در رابطه با ایمپلنت‌های فلزی را برطرف کنند.

در دهه اخیر پیشرفت در زمینه استفاده از مواد سنتزی تخریب‌پذیر برای بافت استخوان به صورت عمده با استفاده از سرامیک‌های کلسیم فسفات انجام شد. با وجودی که کلسیم فسفات به عنوان موادی با خاصیت رشد استخوان شناخته می‌شوند، اما مهمترین مواد از خانواده کلسیم فسفات‌ها که به هیدروکسی‌آپاتیت معروف است، به صورت کامل نمی‌تواند در بدن تخریب شود. اما با اضافه کردن یون‌های فلزی مانند منیزیم و استرانسیوم به ساختار مواد سرامیکی کلسیم فسفات، نشان داده شد که خاصیت استخوان‌سازی سرامیک‌ها شامل یون‌های منیزیم و استرانسیوم افزایش یافت (فصل ۲). به طور دقیقتر، تشکیل استخوان در عیوبی در استخوان ران موش‌ها در طی سه هفته مورد بررسی قرار گرفت.

با توجه به این نتایج، جوهر استخوان ساز با درصد وزنی بالای سرامیک بر پایه منیزیم فسفات همانطور که در فصل ۳ توضیح داده شده است، ساخته شد. این جوهر از ۷۰ درصد وزنی منیزیم فسفات و ۳۰ درصد پلیمر پلی‌کاپرولاکتون تشکیل شده است. درصد بالای منیزیم فسفات باعث می‌شود تا ذرات سرامیکی منیزیم فسفات توسط پلیمر محصور نشوند و خاصیت استخوان‌سازی آن‌ها به قوت باقی بماند. توانایی پرینت شدن این جوهر نشان داد که این ترکیب می‌تواند پس از پرینت شدن شکل خود را به خوبی حفظ کند. این تست با توجه به مقایسه شکل نهایی ایمپلنت پرینت شده و فایل طراحی انجام شد. این جوهر امکان پرینت شدن به شکل‌های هندسی مختلف با حفظ تخلخل ایمپلنت را داراست. این تخلخل‌ها برای کمک به ترمیم بافت استخوان مورد نیاز می‌باشد و اندازه تخلخل‌ها نیز در موثر بودن رشد استخوان نقش مهمی را ایفا می‌کند. خواص مکانیکی ایمپلنت‌های پرینت شده تحت نیروی فشاری نشان می‌دهد که خواص مکانیکی این ایمپلنت‌ها از جمله مدول الاستیک شبیه مدول الاستیک بافت استخوان متخلخل است. ایمپلنت‌های بر پایه منیزیم

فسفات، برای عیوب استخوانی با اندازه بحرانی برای اسب های پونی طراحی شده و در استخوان لگن اسب ها به مدت ۶ ماه مورد آزمایش قرار گرفت. نتایج تست حیوانی پس از ۶ ماه نشان داد که ایمپلنت های پرینت شده توانایی تولید استخوان را برای عیوب با اندازه بحرانی را دارند. قابل ذکر است که بافت استخوان بافتی است که در هنگام ایجاد آسیب های کوچک می تواند خود را ترمیم کند، اما زمانی که این آسیب ها به صورت جدی باشند، استخوان دیگر نمی تواند خود را ترمیم کند، این آسیب ها عیوب بحرانی نامیده میشوند.

بررسی پرینت کردن ایمپلنت های استخوانی با ساختار پیچیده، و با توجه به نیاز بیمار برای درمان هیپ دیسپلیسیا (در جایی که ناحیه لگن به خوبی استخوان بلند ران را احاطه نکرده است) مورد بررسی قرار گرفت. برای این کار استخوان لگن سگ را که دچار هیپ دیسپلیسیا بودن اسکن شده، و با توجه به آناتومی هر سگ، ایمپلنتی برای لگن سگ طراحی شد. طراحی این ایمپلنت به این صورت است که قسمتی از استخوان بلند ران را که توسط لگن احاطه نشده است را، می پوشاند تا بتواند استخوان ران را در جای ثابت نگه دارد. دلیل استفاده از نمونه سگ برای این ریسک این است که آناتومی لگن سگ ها به آناتومی لگن انسان شبیه است. تست های مکانیکی تحت نیروی خمشی و فشاری برای این ایمپلنت ها با میزان تخلخل متفاوت انجام شد. در نهایت برای پیش بینی عملکرد این ایمپلنت ها در محیط بدن، سیستم مکانیکی به صورت شبیه سازی ناحیه لگن ساخته شد و ایمپلنت ها در این دستگاه مورد آزمایش قرار گرفتند. همچنین این ایمپلنت ها پس از تخریب در محیط آزمایشی نیز مورد بررسی قرار گرفتند تا نشان داده شود که حتی پس از تخریب نیز این ایمپلنت ها ساختار اصلی خود را حفظ خواهند کرد (فصل ۴).

برای یک گام جلوتر و به کارگیری این بایومتریال در کلینیک، ایمپلنت های شخصی سازی شده برای جراحی زانو پرینت شده و مورد بررسی قرار گرفتند. این جراحی زانو که به استئوتومی معروف است، در زمانی انجام می شود که زاویه پاهای بیمار به صورت صحیح قرار نگرفته است. در نتیجه پزشک برای جلوگیری از تخریب غضروف، با بریدن قطعه ای از زانو، زاویه پاها را به صورت صحیح تنظیم می کند. این جای برش عموماً پس از جراحی باز باقی می ماند که باعث نشت مغز استخوان و ایجاد درد برای بیمار است. در فصل ۵ زانو پس از جراحی اسکن شده و با توجه به اسکن زانو بیمار، ایمپلنت های شخصی برای زانو بیمار پرینت شد. این ایمپلنت ها در زانو و قسمت قاج خورده زانو مدل کاداور انسان (جسد انسان) قرار گرفت. بررسی لازم برای ارزیابی آنها در حین جراحی به عمل آمد.

ایمپلنت های استئوکندرال (یا به طور دقیق تر، اسکفولدهای قسمتی از زانو شامل استخوان و غضروف) توسط مواد کلسیم فسفات با پرینتر اکستروژن برای استخوان، و فایبرهای پلیمری با پرینتر ملت الکترورایتینگ برای ناحیه غضروف ساخته شد. هایدروژل پلی ساکاراید درون فایبرهای ملت الکترورایتینگ تزریق شده و به این طریق تورم اسموتیک هایدروژل کنترل شد. این کنترل کمک می کند تا به صورت موثری بافت غضروف ترمیم شود (فصل ۶).

استخوان بافتی است که توسط بافت های همبند دیگر مانند غضروف و لیگامنت محاصره شده است. برای ترمیم این بافت های همبند، ترمیم ناحیه استخوان در مجاورت این بافت ها نیز مورد اهمیت هست. با توجه به نتایج به دست آمده، چالش دیگری که در این تز بررسی شده است، پرینت ایمپلنت با رزولوشن بالا برای بافت استخوان و بافت های مجاور آن است. ایمپلنت ها با رزولوشن بالا ماتریکس خارج سلولی را به صورت موثری شبیه سازی می کنند. برای این منظور در فصل ۷ ایمپلنت چند لایه با ساختار و ترکیب مختلف توسط پرینتر ملت الکترورایتینگ ساخته شد. این ایمپلنت چند لایه برای ترمیم ناحیه استخوان و لیگامنت با رزولوشن بالا طراحی و ساخته شده اند. این ایمپلنت ها با رزولوشن

بالا توانایی لازم برای شبیه سازی ماتریکس خارج سلولی را دارا هستند و باعث ترمیم بافت می شوند. توانایی ترمیم این ایمپلنت های چند لایه در عیب فستریشن در ناحیه دندان موش ها برای مدت ۶ هفته بررسی شد (فصل ۷).

ایمپلنت های استیوکندرال قسمتی از آنو هستند که شامل استخوان و غضروف می باشند. برای نشان دادن اینکه این ایمپلنت ها می توانند با ابعاد بزرگتر و با توجه به آناتومی بیمار ساخته شوند؛ زانو بیمار اسکن شده و با جوهر بر پایه منیزیم فسفات پرینت شد. با استفاده از پرینتر ملت الکترورایتینگ قسمت غضروف زانو نیز توسط طی کردن جت پرینتر بر سطح ایمپلنت استخوان ساخته شد (انکس ۱).

تزی پیش رو؛ پیشرفت اساسی به سمت استفاده کلینیکی ایمپلنت های تخریب پذیر با خواص مکانیکی مناسب را مورد بحث قرار می دهد. این ایمپلنت ها توسط پرینترهای سه بعدی ساخته شده اند. به صورت اختصاصی در این تز نشان داده شده است که جوهر بر پایه منیزیم فسفات همچنین می تواند با دیگر بایومتریال ها برای ساخت ایمپلنت های استخوانی که در تماس با بافت های همبند مجاور مانند غضروف و لیگامنت هستند، مورد استفاده قرار گیرد. استفاده از این گونه ایمپلنت ها باعث می شود تا بافت های در مجاورت استخوان بتوانند پیوند مکانیکی مستحکم تری را برقرار کنند.

با این وجود همچنان چالش هایی در این زمینه وجود دارد که نیازمند تحقیق بیشتر در این زمینه هست. برای مثال خواص مکانیکی این دسته از مواد تخریب پذیر می توانند بهبود یابد تا برای استفاده از محیط تحت باری مانند استخوان، به صورت قابل اطمینانی مورد استفاده قرار گیرد. خلاصه ای از چالش ها و نقش هر چپتر در بررسی این چالش ها برای مهندسی بافت استخوان در شکل ۱ نشان داده شده است.

بخش ۲، ۳، ۴ و ۵

بایومتریال پرینت شونده در دمای محیط بر پایه منیزیم فسفات

بخش ۳، ۴ و ۵

ساخت ایمپلنت های استخوان با مقیاس و هندسه مطابق با نمونه های کلینیکی

بخش ۶ و ۷

ایمپلنت های با رزولوشن بالا و شبیه ماتریکس سلولی برای افزایش اتصال با بافت های همبند مانند غضروف و لیگامنت

چالش ها

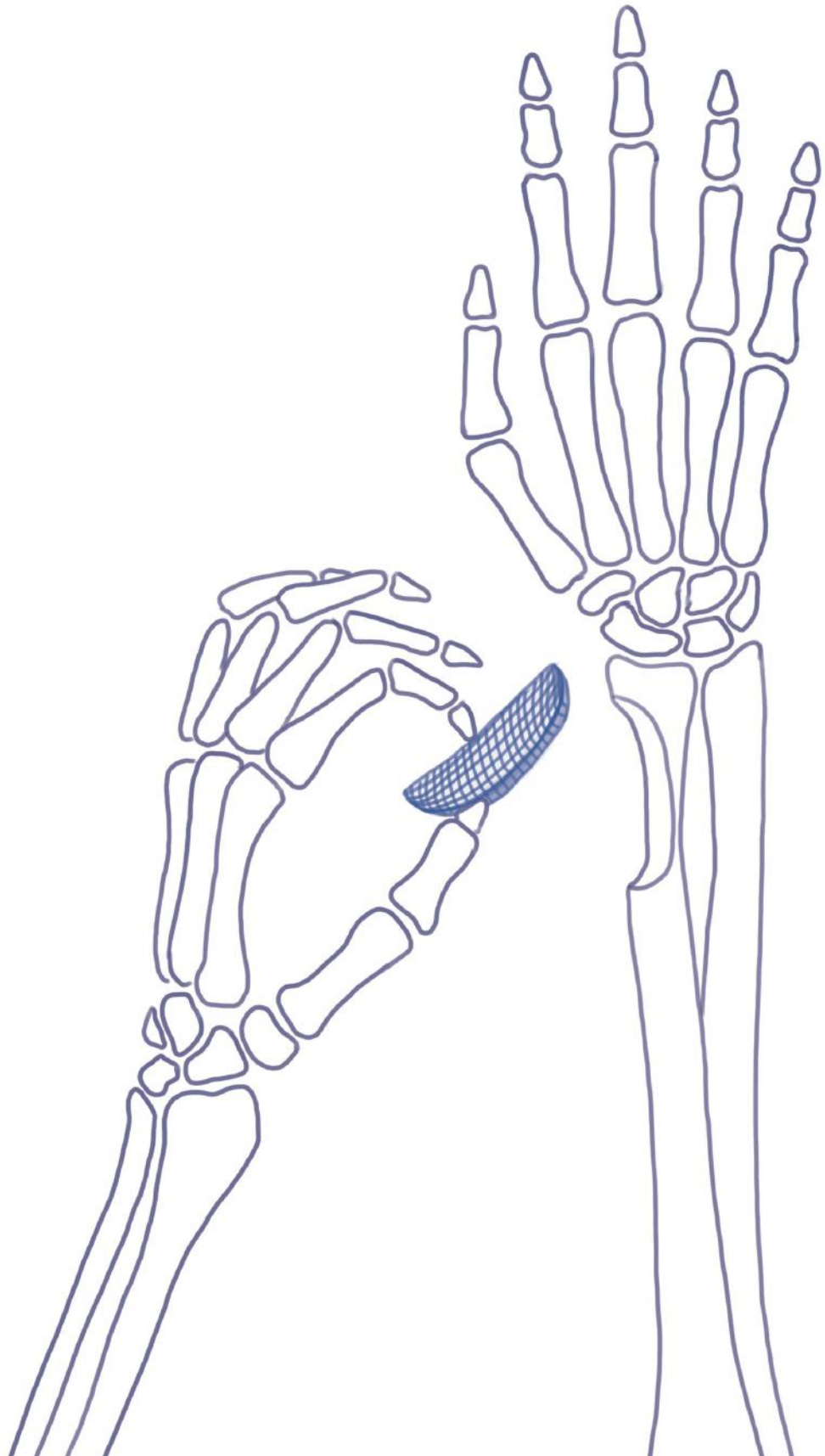
۱- مواد غیرآلی با خاصیت استخوان سازی

۲- مطابقت خواص مکانیکی ایمپلنت های استخوانی با بافت استخوان

۳- وجود ایمپلنت هایی با خواص تخریب پذیری و استخوان سازی مناسب برای عیوب استخوان که به خودی خود ترمیم میشوند

۴- اتصال استخوان با بافت های همبند

شکل ۱. خلاصه ای از فصل های تزی پیش رو و ارتباط آن ها با چالش های مهندسی بافت استخوان.



Acknowledgments

Promoter and co-promoter

Dear Professor dr. ir. **Malda**,

My heartfelt gratitude for giving me the chance to pursue my dreams towards PhD study. I should say your support has been instrumental in shaping me into the researcher I am today. You challenged me to push the boundaries of my knowledge, to ask tough questions, think critically, and to pursue my research with passion and dedication. Your insights and advice were always spot-on, and your ability to guide me through the complexities of the research process was truly invaluable. I am grateful to providing me the opportunity to participate in the meetings with clinicians as an engineer. This experience opened my eyes to the importance of understanding patient needs in developing biomedical solutions. Without your encouragement, I could not have imagined making the transition towards working on patient-specific implants for bone tissue engineering, which I am proud to have achieved as one of the pioneers in the field.

Beyond all your scholarly prowess, what I truly appreciated about working with you was your patience. I am so grateful to have had the opportunity to work under your mentorship, and I feel incredibly fortunate to have you as a role model. Thank you for everything Jos, and I wish you all the best in your future endeavors.

Dear dr. ir. **Castilho**,

Since I had started my PhD, you have been a source of inspiration and motivation, always pushing me to do my best and encouraging me to aim higher.

Even during the moments when I felt discouraged, you always made time to brainstorm ideas with me and provided constructive feedback on my research. Your mentorship has been invaluable in teaching me how to transform simple ideas into groundbreaking and impactful work. I am proud of our joint achievements in the field of bone regeneration, particularly our success in translating degradable materials for clinical use. I appreciate all the discussion we had about the mechanics and the designing of the implants to reach the requirements for personalized implants for bone tissue engineering.

Your expertise, patience, and kindness have made this journey so much easier and more enjoyable than I ever thought possible. I have learned so much from you, not just about the academic world, but also about the importance of hard work, dedication, and perseverance.

Review committee

I would like to express my sincere gratitude to **Prof. dr. ir. S.C.G. Leeuwenburgh**, **Prof. dr. J.M. Beekman**, **Prof. dr. F.C. Oner**, **Prof. dr. B.P. Meij**, and **dr. S. Hofmann** for the support and enthusiasm throughout the evaluation of this thesis. It is a great honor for me to have the opportunity to discuss my research findings with esteemed scientists of your caliber, and your invaluable feedback has contributed immensely to the quality of this work. Thank you for taking the time to evaluate this thesis.

Collaborators

UMC Utrecht and Utrecht University team

Prof. dr. ir. Harrie Weinans and **Dr. Bart van der Wal**, your insights and feedback in the hip dysplasia project have been instrumental in helping me to think and communicate more effectively in academic settings.

Dear **Prof. dr. René van Weeren**, I am deeply grateful for the opportunity to work with you and to contribute my engineering expertise to the clinical science field.

Technical University of Denmark team

Dear **Dr. Alireza Dolatshahi-Pirouz**, thank you for the great time I've had during my research stay in Copenhagen. I am grateful for the guidance you have provided me in thinking straight and communicating openly in academic settings. Your mentorship has been invaluable in teaching me how to approach academic work with clarity and openness in my thinking and communication. Special thanks to **Dr. Firoz Babu Kadumudi**, and **Dr. Morteza Alehosseini** to assist me during my PhD study, I already missed the great discussion we had.

University of Michigan team

Despite never having met in person, I have thoroughly enjoyed working alongside you, **Dr. Marco C. Bottino**, and have found our scientific discussions on the creation of implants for periodontal defects to be both engaging and illuminating. Thank you for always making time even when you were super busy at work. Special thanks to **Dr. Arwa Dagherery** for her input and great work in the animal study. I am deeply grateful for your contributions to my growth and development.

Wurzburg University team

Dear **Dr. Elke Vorndran**, thank you for your support towards reaching your interesting research in MgP-based bioceramics. Your support during my PhD guided me through the achieving the goals to the employment of MgP-based bioceramics in patient-specific designs for bone regeneration.

Colleagues from UMC Utrecht and Utrecht University

My PhD journey would not have been the same without the wonderful colleagues who have supported and encouraged me along the way. To each and every one of you, I want to express my heartfelt thanks for making this experience such a memorable one.

My gratitude goes out to my friends and colleagues at UMC Utrecht, including **Fatemeh Jahanmard, Mylene de Ruijter, Koen Willemsen, Martina Viola, Quentin Peiffer, Maria Fugazzola, Lizette Utomo, Saber Amin Yavari, Azin Khodaei, Maaike Braham, Lotte Groen, and Margot Rikkers.**

It is with deep gratitude that I acknowledge the contributions of **Saskia Plomp, Mattie van Rijen, and Anneloes Mensinga** to my research. Your energy and supporting of you made this journey for me so enjoyable. Your willingness to help and the constant support at RMCU and department of clinical sciences have been invaluable.

Paranymphs

I would like to express my deepest appreciation to my friends, **Martina** and **Pardis**, for your kind support and guidance throughout my academic journey. Your encouragement, advice, and willingness to lend an ear when needed have been invaluable, and I truly appreciate your presence in my life. Thank you for standing by my side as my paranymphs, and for making this experience so much richer and more rewarding.

Students

I want to give a big shout-out to the former amazing master students! You guys have done a great job with your enthusiasm, creativity, and hard work. Whether we were diving deep into complex theories or just having a laugh, you always brought your bests.

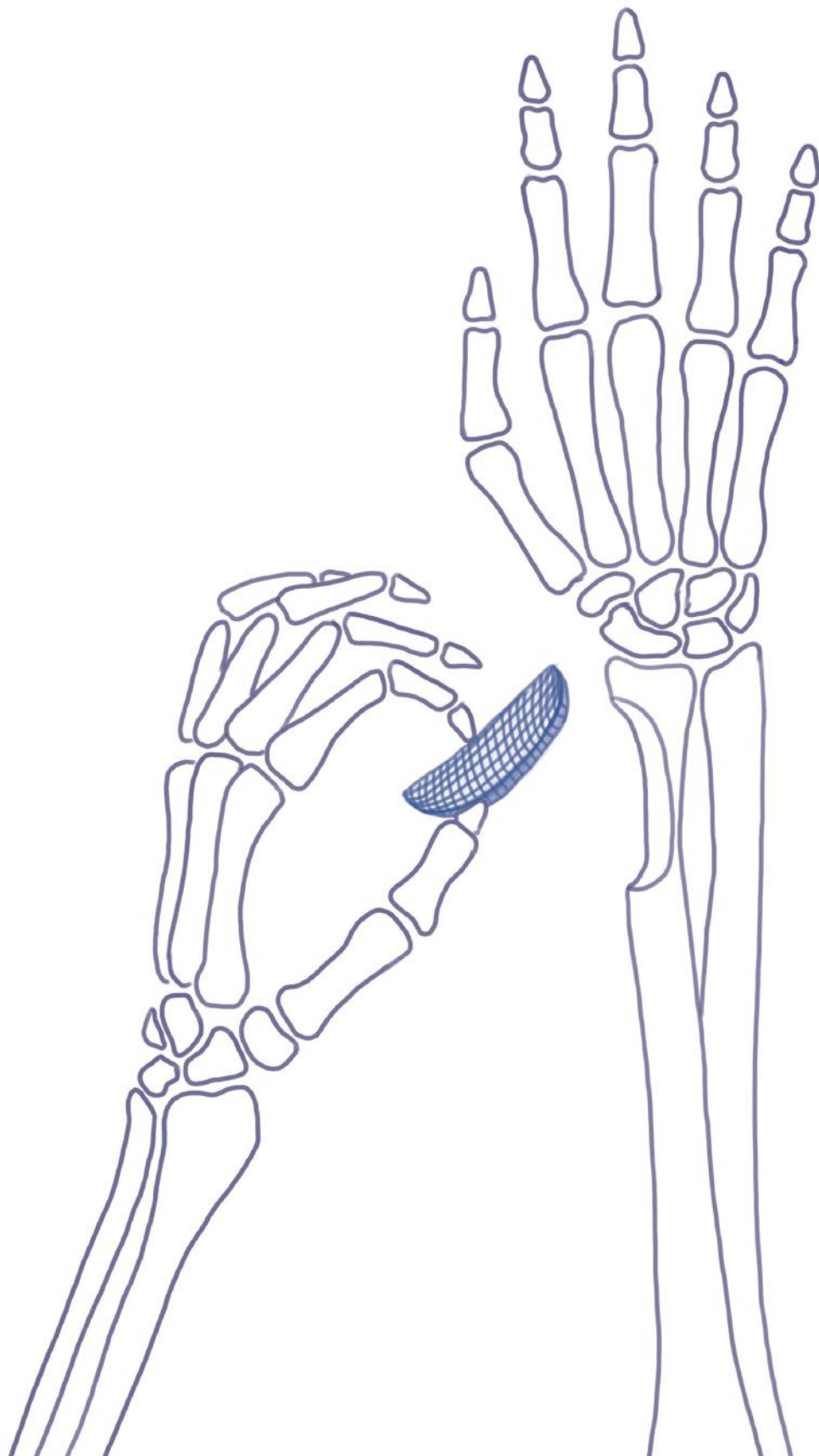
I've learned just as much from you as I hope you've learned from me. From all the hard working on 3D printing of natural-based hydrogels by **Diogo** Sabino, MEW for MgP-based materials by **Konstantinos** Krikonis specially during the Covid lockdown, and the synthesis of personalized hydrogels from natural bone by **Tom** van de Kemp, we've been through it all together, and I couldn't be prouder of the incredible progress you've made. So, here's to you– without you guys, my PhD journey would not have been such a fulfilling and unforgettable experience.

Family and friends

برای مادر مهربانم و پدر عزیزم، هر چند که سال‌هاست از شما دورم ولی عشق و یاد شما همیشه در قلب و وجودم جاریست. این که حالا من به دنبال آرزوها و خواسته‌هایم هستم را مدیون شما هستم؛ که راه و روش خواستن و تلاش کردن را به من آموختید. شما بودید که به من یاد دادید برای خواسته‌هایم بکنم و در لحظات شکست، زمانی که شکست‌ناپذیری ممکن نبود صبور باشم. هر چه بزرگتر شدم بیشتر فهمیدم که چگونه به من آموختید هر چه از قلبم بگذرد بر سر راهم قرار می‌گیرد. ممنون برای زندگی و تربیتی که به من بخشیدید.

To my dear sister, **Shamim**, I just wanted to let you know how much you mean to me. You've been not just a sister but also a true friend who I can always rely on, someone who knows me inside and out, and who supports me no matter what. Even though we're miles apart, you always manage to bring joy to my life and make me feel loved. I'm so grateful to have you in my life, Shamim. Thank you for being the best sister anyone could ask for.

To my very best friends, thank you for being a part of my life's journey and for bringing so much laughter, fun, and love into it. **Fateme**, I cannot thank you enough for being my greatest supporter and for always being there for me. I am constantly inspired by your hard work, creativity, and resilience, and I feel fortunate to have you as a friend who challenges me to be a better person every day. **Narges**, despite the distance between us, you have shown me how to be fully present and involved in a great friendship, supporting each other through ups and downs. **Morteza**, I appreciate our friendship which helps me shape my professional and personal growth. **Azin**, your remarkable patience in listening and supporting me through my challenges has been truly unbelievable. **Pardis**, you are the most energized and motivating person I have ever known, thank you for inspiring me. And **Atefeh**, your kindness and empathy have made a profound impact on my life, and I am so grateful to have you as my friend. From the moments we were working together at the Biomaterials laboratory at IUT, to all the moments we shared our knowledge in the biomedical field together from far distance, I have always felt your support and encouragement. Your kindness and empathy have made a profound impact on my life, and I am so grateful to have you all in my life.



List of publications

This thesis is based upon the following publications

Combinatorial fluorapatite-based scaffolds substituted with strontium, magnesium and silicon ions for mending bone defects

N. Golafshan, M. Alehosseini, T. Ahmadi, A. Talebi, M. Fathi, M. Kharaziha, G. Orive, M. Castilho, A. Dolatshahi-Pirouz
Journal Materials Science and Engineering: C, Jan 2021; **DOI:** 10.1016/j.msec.2020.111611

Tough magnesium phosphate-based 3D-printed implants induce bone regeneration in an equine defect model

N. Golafshan, E. Vorndran, S. Zaharievski, H. Brommer, F. Kadumudi, A. Dolatshahi-Pirouz, U. Gbureck, R. V. Weeren, M. Castilho, J. Malda
Biomaterials, Dec 2020; **DOI:** 10.1016/j.biomaterials.2020.120302

3D-Printed Regenerative Magnesium Phosphate Implant Ensures Stability and Restoration of Hip Dysplasia

N. Golafshan, K. Willemsen, F. Kadumudi, E. Vorndran, A. Dolatshahi-Pirouz, H. Weinans, B. van der Wal, J. Malda, M. Castilho
Advanced Healthcare Materials, Nov 2021; **DOI:** 10.1002/adhm.202101051

A Patient-Specific, Regenerative Implant for Open-Wedge Osteotomy - From Scan to Surgery

M. Rikkers, **N. Golafshan**, M. HC. Nguyen, M De Ruijter, M Castilho, N Van Egmond, LA. Vonk, RJH. Custers, J. Malda
Journal of Cartilage & Joint Preservation, Feb 2023, **DOI:** 10.1016/j.jcjp.2023.100117

Composite graded melt electrowritten scaffolds for regeneration of the periodontal ligament-to-bone interface

N. Golafshan, M. Castilho, A. Daghreery, M. Alehosseini, F. Kadumudi, K Krikonis, R. Dal-Fabbro, A. Dolatshahi-Pirouz, M. C. Bottino, J. Malda
ACS Appl. Mater. Interfaces, Jan 2023, **DOI:** 10.1021/acsami.2c21256

Influence of osmotic swelling restriction on load bearing properties and neo-cartilage matrix formation on osteochondral implant

N. Golafshan, M. Castilho, M. Jiménez, I. Pennings, M. Chen, A. Damen, K. Ito, T. Vermonden, J. Malda
 Manuscript is in preparation

Scaling up from osteochondral plug to patient-specific condyle resurfacing: fabrication, in vitro characterization, and mechanical characterization under physiological conditions of clinically relevant osteochondral implants

M. d. Ruijter, **N. Golafshan**, I. Dokter, I. Gkoni, R. Verberne, J. Garcia, L. Creemers, P. R v. Weeren, P. A.J. Brama, D. J Kelly, K. Ito, P. Little, P. Pivonka, J. Malda, M. Castilho
Manuscript is in preparation

Publications that are not listed in this thesis:

Stable and Antibacterial Magnesium–Graphene Nanocomposite-Based Implants for Bone Repair

N. Golafshan, N. Safari, M. Kharaziha, M. Toroghinejad, L. Utomo, J. Malda, M. Castilho, *ACS Biomaterials Science & Engineering*, **2020**.

DOI: 10.1021/acsbiomaterials.0c00613

Tissue-specific melt electrowritten polymeric scaffolds for coordinated regeneration of soft and hard periodontal tissues

A. Dagherery, J. Ferreira, J. Xu, **N. Golafshan**, D. Kaigler, S. B. Bhaduri, J. Malda, M. Castilho, M. C Bottino, *Bioactive Materials*. Jan 2023;

DOI: 10.1016/j.bioactmat.2022.04.013

Hemocompatible and bioactive heparin-loaded PCL- α -TCP fibrous membranes for bone tissue engineering

M. Alehosseini, **N. Golafshan**, M. Kharaziha, M. Fathi, H. Edris, *Macromolecular Bioscience*, **2018**.

DOI: 10.1002/mabi.201800020

Nanoclay Reinforced Biomaterials for Mending Musculoskeletal Tissue Disorders

I. Erezuma, T. Eufrazio-da-Silva, **N. Golafshan**, K. Deo, Y. Kumar Mishra, M. Castilho, A. K Gaharwar, S. Leeuwenburgh, A. Dolatshahi-Pirouz, G. Orive, *Advanced Healthcare Materials*, **2018**.

DOI: 10.1002/adhm.202100217

Conference participation and award

N. Golafshan, 2022 Winner of Mimics Innovation Award (MIA) for the research in personalized implants, 3D-Printed Regenerative Magnesium Phosphate Implant Ensures Stability and Restoration of Hip Dysplasia, Materialise NV, Leuven, Belgium.

N. Golafshan, et. al., A 3D printed bone implant for hip dysplasia treatment: Combining shape and mechanical function in a fully resorbable implant, Termis 2021, Maastricht, the Netherlands, Poster presentation.

N. Golafshan, et. al., Combining shape and mechanical function in a fully resorbable 3D-printed bone implant for hip dysplasia treatment, European Society of Biomaterials 2021, Porto, Oral presentation.

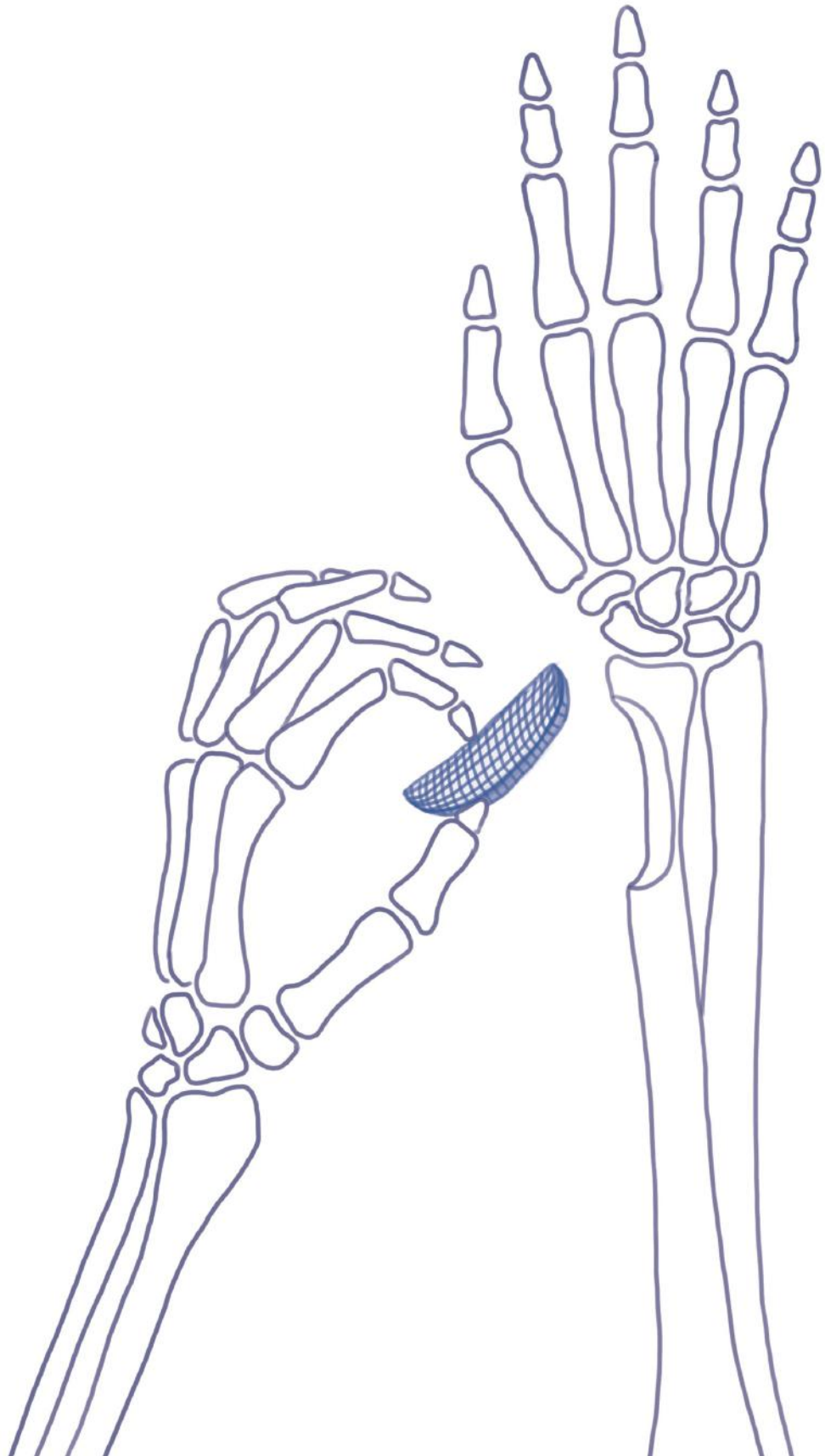
N. Golafshan, et. al., 3D printed tough magnesium phosphate-based implants induce bone regeneration in an equine defect model, World Biomaterials Congress (WBC) 2020, Glasgow, Scotland, Oral presentation.

N. Golafshan, et. al., Design and fabrication of 3D printed magnesium phosphate-based scaffolds to repair, RegMed 2020, Utrecht, the Netherlands, Poster presentation.

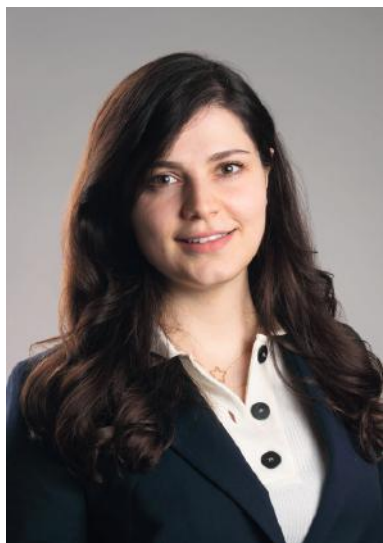
N. Golafshan, et. al., A Bone Substitute with High Bioactivity, strength, and Porosity for Repairing Large Bone Defects, European Society for Biomaterials (ESB) 2019, Dresden, Germany, Poster presentation.

N. Golafshan, et. al., Manufacturing of biologically active bone implants by extrusion 3D printing, Biofabrication 2018, Wurzburg, Germany, Poster presentation.





Curriculum Vitae



Nasim Golafshan was born on 25th of September 1990 in Isfahan, Iran. After finishing high school in 2009, she started her education in materials science at Isfahan University of Technology. During her bachelor, she gained interest in tissue engineering and the development of biomaterials to regenerate tissues. In particular, her interest in the field of tissue engineering was sparked by a research project at Materials and Research Laboratory, where she focused on the synthesis of biodegradable polymers. In 2014, Nasim continued her education within a master's program (materials science, Isfahan University of Technology) and during this time, she focused on developing and fabrication

of the degradable implants for tissue engineering. She gained experience-in the fabrication of hydrogel-based materials and electrospinning techniques to develop nerve guidance conduits. After obtaining her master's degree in 2016, she started to work as a research assistant in the cell culture laboratories at Isfahan University of Technology and Isfahan University. Her PhD work started in 2018 at the department of Orthopedics (UMC Utrecht, the Netherlands) and was part of two larger projects called 3D-JOINT (funded by the European Research Council) and RegMed XB. Nasim was supervised by dr. ir. Miguel Castilho and prof. dr. ir. Jos Malda for her PhD program. Her research focused on developing of advanced bioactive materials for musculoskeletal tissue and fabrication technologies. As part of her PhD project, she continued a pre-existent collaboration with the University of Würzburg, Technical University of Denmark and later on expanded her projects by collaborating with the University of Michigan, School of Dentistry. The outcome of her PhD research is presented and discussed in this thesis. Nasim presented her research at several international conferences. She was awarded the Mimics Innovation Award 2022 for her work on degradable personalized hip implants. After submitting her thesis, Nasim started as a postdoctoral researcher at the University of Denmark to expand her training in smart biomaterials science and processing.

